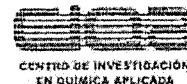


**GOBIERNO DE  
MÉXICO**



**CONAHCYT**  
CONSEJO NACIONAL DE CIENCIAS BIOLÓGICAS,  
QUÍMICAS Y TECNOLÓGICAS



**CENTRO DE INVESTIGACIÓN  
EN QUÍMICA APLICADA**

Saltillo, Coahuila a 03 de septiembre de 2024

Coordinación de Posgrado

Presente

Por este conducto nos permitimos informar a esta coordinación que, el documento de Tesis preparado por CAROLINA VENTURA HUNTER titulado **Hemagglutinin-derived peptides and their conjugation with block copolymers (Péptidos derivados de la hemaglutinina y su conjugación con copolímeros en bloques)** el cual fue presentado el día 30 de agosto de 2024, ha sido modificado de acuerdo a las observaciones, comentarios y sugerencias, realizadas por el Comité Evaluador asignado. Por tal motivo, avalamos que el documento adjunto corresponde a la versión final del documento de Tesis.

Atentamente,

**SINODALES**

Dr. Luis-Ernesto Elizalde Herrera  
Presidente

Dra. Abril Fonseca García  
Secretario

Dr. Roberto Yáñez Macías  
Primer Vocal

Dra. Guadalupe Ayora Talavera  
Segundo Vocal

Dr. Gonzalo Ramírez García  
Tercer Vocal

Vo. Bo. ASESORES

Dr. Enrique Saldivar Guerra

Dr. Carlos Guerrero Sánchez

## TESIS CON CARACTER ABIERTO

PROGRAMA: DOCTORADO EN TECNOLOGÍA DE POLÍMEROS

---

AUTOR: CAROLINA VENTURA HUNTER

FIRMA



TITULO: Hemagglutinin-derived peptides and their conjugation with block copolymers (Péptidos derivados de la hemaglutinina y su conjugación con copolímeros en bloques).

ASESORES: Dr. Enrique Saldivar Guerra

FIRMA



Dr. Carlos Guerrero Sánchez

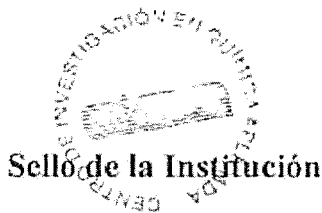
FIRMA



El Centro de Investigación en Química Aplicada clasifica el presente documento de tesis como ABIERTO.

Un documento clasificado como Abierto se expone en los estantes del Centro de Información para su consulta. Dicho documento no puede ser copiado en ninguna modalidad sin autorización por escrito del Titular del Centro de Información o del Director General del CIQA.

Saltillo, Coahuila, a 30 de agosto de 2024



  
Dra. Julieta Torres González  
Directora General del CIQA



**CENTRO DE INVESTIGACIÓN EN QUÍMICA APLICADA**  
**Programa de Doctorado en Tecnología de Polímeros**

***TESIS***

**Hemagglutinin-derived peptides and their conjugation with block copolymers**  
**(Péptidos derivados de la hemaglutinina y su conjugación con copolímeros en bloques)**

***Presentada por:***

**CAROLINA VENTURA HUNTER**

***Para obtener el grado de:***

**Doctor en Tecnología de Polímeros**

***Asesorada por:***

**Dr. Enrique Saldívar Guerra**  
**Dr. Carlos Guerrero Sánchez**

**Agosto, 2024**

**CENTRO DE INVESTIGACIÓN EN QUÍMICA APLICADA**  
**Programa de Doctorado en Tecnología de Polímeros**

**TESIS**

**Hemagglutinin-derived peptides and their conjugation with block copolymers**  
**(Péptidos derivados de la hemaglutinina y su conjugación con copolímeros en bloques)**

*Presentada por:*

**CAROLINA VENTURA HUNTER**

*Para obtener el grado de:*

**Doctor en Tecnología de Polímeros**


*Asesorada por:*

**Dr. Enrique Saldivar Guerra**  
**Dr. Carlos Guerrero Sánchez**

**SINODALES**

  
\_\_\_\_\_  
**Dr. Luis Ernesto Elizalde Herrera**  
**Presidente**

  
\_\_\_\_\_  
**Dra. Abril Fonseca García**  
**Secretario**

  
\_\_\_\_\_  
**Dr. Roberto Yañez Macías**  
**Primer Vocal**

  
\_\_\_\_\_  
**Dra. Guadalupe Ayora Talavera**  
**Segundo Vocal**

  
\_\_\_\_\_  
**Dr. Gonzalo Ramírez García**  
**Tercer Vocal**

## DECLARACIÓN

Declaro que la información contenida en la Parte Experimental así como en la Parte de Resultados y Discusiones de este documento y que forman parte de las actividades de investigación y desarrollo realizadas durante el período que se me asignó para llevar a cabo mi trabajo de tesis, será propiedad del Centro de Investigación en Química Aplicada.

Saltillo, Coahuila a 30 de agosto de 2024



CAROLINA VENTURA HUNTER

Nombre y Firma



Hemagglutinin-derived peptides and their conjugation  
with block copolymers.

Carolina Ventura Hunter

Dissertation Prepared for the Degree of  
DOCTOR OF POLYMER TECHNOLOGY

Supervisors

Dr. Enrique Saldívar Guerra

Dr. Carlos Guerrero Sánchez

Centro de Investigación en Química Aplicada (Mexico) &  
Friedrich-Schiller University Jena (Germany).

August 2024

## CONTENTS

CONTENTS .....	2
Abstract .....	14
Thesis Outline .....	15
Chapter 1 Introduction .....	16
1.1 Introduction to reversible deactivation radical polymerizations .....	16
1.2 RAFT polymerization: Mechanism and RAFT agent selection .....	17
1.2.1 RAFT mechanism .....	17
1.2.2 RAFT agent selection.....	18
1.3 Microstructure of RAFT polymers.....	18
1.3.1 Statistical and gradient copolymers.....	19
1.3.2 Block copolymers.....	20
1.3.3 Brush and Graft polymers .....	20
1.4 Self-assembly of amphiphilic block copolymers in solution .....	21
1.5 Applications of polymer materials in biomedicine .....	22
1.5.1 Conceptualization and main definitions .....	22
1.5.2 Bioconjugation of synthetic polymer with biomolecules.....	24
1.5.3 Bioconjugation strategies .....	25
1.6 Peptides in nanomedicine.....	29
1.6.1 Types of peptides to functionalize polymers.....	29
1.6.2 Peptides derived from the HA protein of the influenza virus.....	31
1.7 PEG and PGMMA as biocompatible polymers and their application in bioconjugate chemistry.....	32
1.7.1 Poly(ethylene glycol) (PEG) .....	32
1.7.2 Poly(glycerol mono-methacrylate) (PGMMA) .....	34
1.8 Fluorescence spectroscopy and fluorescent biomolecules .....	34
1.9 Cytotoxicity assays.....	37
1.10 Physicochemical properties of peptides and proteins.....	38
1.11 Hypothesis.....	40
1.12 Aim of this work .....	40
Chapter 2 Materials and characterization methods .....	41
2.1 Materials.....	41
2.2 Characterization methods.....	41
Chapter 3 . Glycerol methacrylate-based copolymers: Reactivity ratios, physicochemical characterization, and cytotoxicity .....	43
3.1 Introduction.....	43
3.2 Determination of reactivity ratios: using the terminal model.....	45
3.3 Experimentation .....	46

3.3.1	General procedure for the synthesis of GMMA copolymers .....	46
3.3.2	Synthesis of PNIPAM homopolymer (B6) .....	51
3.3.3	Cell viability assay on L929 cell line .....	51
3.4	Results and discussion.....	52
3.4.1	Synthesis of GMMA-based statistical copolymers via RAFT polymerization. ....	52
3.4.2	Estimation of reactivity ratios for the copolymerization systems GMMA with NHSMA, NIPAM and BuA, and estimation of the sequence length distribution.....	62
3.4.3	DSC investigations and theoretical estimations of Tg. ....	70
3.4.4	TGA investigations .....	74
3.4.5	Light transmission measurements and cell viability .....	75
3.5	Conclusions and outlook .....	77
Chapter 4	Bioconjugation of amphiphilic copolymers with peptides derived from HA protein.      78	
4.1	Introduction.....	78
4.2	Experimentation .....	79
4.2.1	Synthesis of PFP-CPAD. ....	79
4.2.2	Synthesis of P(OEGMEMA -stat-FLUMA) with PFP-CPAD (P10 macro RAFT agent).....	79
4.2.3	Synthesis of block copolymer P(OEGMEMA-stat-FLUMA)-b-P(BMA) (P20). ....	80
4.2.4	Synthesis of P(BMA) macro-CTA (P30). ....	80
4.2.5	Synthesis of P(BMA)-b-P(GMMA)-b-P(GMMA-stat-NHSMA-stat-FLUMA) (P40). ....	81
4.2.6	Synthesis of peptide-bioconjugated copolymer. ....	82
4.2.7	Evaluations of potential cytotoxic effects of peptides and peptide-polymer conjugates .....	83
4.2.8	Cell-uptake experiments and flow cytometry quantification .....	84
4.3	Synthesis and characterization of amphiphilic block copolymers based on GMMA and OEGMEMA .....	85
4.4	Characterization of peptides PC1-PC3.....	91
4.4.1	Physicochemical properties of PC1-PC3 peptides .....	91
4.4.2	Characterization of PC1-PC3, PC1-5FAM and PC3-5FAM peptides by NMR .....	94
4.4.3	Fluorescence properties of the investigated peptides .....	94
4.5	Conjugation of peptides with amphiphilic block copolymers.....	100
4.6	Polymer nanoparticles decorated with peptides derived from the HA protein of the influenza A virus .....	111
4.7	Cell viability and cellular internalization of polymer nanoparticles decorated with peptides derived from the HA protein of the influenza virus.....	117
4.7.1	Cell viability and internalization of peptides in MDCK cell line.....	117
4.7.2	Comparison of cell viability of the MDCK cell line vs HuH7 and HEPG2 cell lines in the presence of the investigated copolymers and derivative conjugates. ....	121



4.8 Conclusion and outlook.....	123
Chapter 5 Conclusions, recommendations publications- congresses and references.....	125
5.1 Conclusions.....	125
5.2 Recommendations.....	126
5.3 Publications and congresses.....	126
5.4 Appendix.....	128
5.5 References.....	130

## List of figures

Figure 1.1 Mechanism of the reversible addition–fragmentation chain transfer polymerization.[6].....	17
Figure 1.2 Topologies, compositions, and functionalities accessible through the RAFT polymerization technique.[11] .....	19
Figure 1.3 Morphologies obtained via self-assembly in solution.[17].....	21
Figure 1.4 Schematic representation of the bioconjugation process between synthetic polymers and biological molecules.[36] .....	25
Figure 1.5 Schematic representation of the bioconjugation of synthetic polymers using activated esters.[40].....	27
Figure 1.6 Schematic representations of post-modification strategies for RAFT polymers. [35] .....	29
Figure 1.7 Schematic representation of two approaches to design peptides and their coupling onto a nanoparticle.[46] .....	30
Figure 1.8 Schematic representation of the advantages of the PEGylation of proteins.[87].....	33
Figure 1.9 Reduction of resazurin (AlamarBlue) to resorufin.[126].....	38
Figure 3.1. NMR spectrum of purified copolymer A1 and A2. A. <sup>1</sup> H-NMR spectrum of purified copolymer A1 (Table 3.1) in DMSO- <i>d</i> <sub>6</sub> (top), and equation for estimation of cumulative copolymer composition (bottom). B. Quantitative <sup>13</sup> C spectrum (Inverse-Gated Decoupling) of purified copolymer A2 (Table 3.1) in DMSO- <i>d</i> <sub>6</sub> (top), and equation for estimation of cumulative copolymer composition (bottom). .....	49

Figure 3.2 <sup>1</sup>H-NMR spectrum of B1 purified copolymer in MeOD-*d*<sub>4</sub> (top), and their equation for estimation of cumulative copolymer composition (bottom)..... 50

Figure 3.3 <sup>1</sup>H-NMR spectrum of C4 purified copolymer in DMF-*d*<sub>7</sub> (bottom), and their equation for estimation of cumulative copolymer composition (top). ..... 50

Figure 3.4 Semi-logarithmic kinetic plots for A1-A5. Monomer conversions were calculated from <sup>1</sup>H-NMR spectra. .... 55

Figure 3.5 Semi-logarithmic kinetic plots for B0-B5. Monomer conversions were calculated from <sup>1</sup>H-NMR spectra. .... 56

Figure 3.6 Semi-logarithmic kinetic plots for C1-C6. Monomer conversions were calculated from <sup>1</sup>H-NMR spectra. .... 57

Figure 3.7 Evolution of molar mass and dispersities, estimated by SEC, as a function of the overall monomer conversion of A1-A5, B0-B5 and C1-C6. .... 58

Figure 3.8 SEC chromatograms of copolymers A1-A4 and poly(N-hydroxysuccinimide methacrylate) (PNHSMA) A5 in eluent DMAc + 0.21 % LiCl, RI detection and calibrated against PMMA standards. .... 60

Figure 3.9 SEC chromatograms of PGMMA homopolymer B0, copolymers B1-B5 and PNIPAM homopolymer B6, determined by SEC, eluent DMAc + 0.21 % LiCl, RI detection, calibrated against PMMA standards. .... 61

Figure 3.10 Gel permeation chromatograms of copolymers C1-C5 and homopolymer C6 (poly(butyl acrylate) (PBuA) determined by SEC, eluent DMAc + 0.21 % LiCl, RI detection, calibrated against PMMA standards. .... 62

Figure 3.11 Joint confidence and monomer fraction  $f_{\text{NHSMA}}$  and copolymer fraction  $F_{\text{NHSMA}}$  plots. Fig. A shows joint confidence regions for the estimated reactivity ratios of the system GMMA/NHSMA. Green 50%, blue 70%, orange 90% and red 95% probabilities.  $r_{\text{NHSMA}}=1.01$  and  $r_{\text{GMMA}}=0.32$ . Figures B and C compare the monomer fraction  $f_{\text{NHSMA}}$  and copolymer fraction  $F_{\text{NHSMA}}$  as a function of conversion with the corresponding experimental values obtained by NMR. .... 64

Figure 3.12 Sequence length distribution for the copolymerization of the system  
 MMA/NHSMA (A1-A4) at different monomers fractions  $f_{0(\text{NHSMA})}$ . The vertical axis  
 represents the percentage of a determined mean sequence length N (Figure A for NHSMA  
 and Figure B for MMA) and one of the horizontal axes the corresponding sequence of  
 length x. Please note that sequences are only shown up to heptads but other sequences  
 could be present..... 66

Figure 3.13 A) and B) compare the instantaneous NIPAM fraction ( $f_{\text{NIPAM}}$ ) and the cumulative  
 NIPAM fraction in the copolymer ( $F_{\text{NIPAM}}$ ) for different comonomer compositions (see  
 Table 1) as a function of the overall monomer conversion for both theoretical estimations  
 and the corresponding experimental values as determined by <sup>1</sup>H-NMR. C) shows the joint  
 confidence region for the estimated reactivity ratios. Green 50%, blue 70%, orange 90%  
 and red 95%;  $r_{\text{NIPAM}} = 0.11$  and  $r_{\text{MMA}} = 2.55$ . ..... 67

Figure 3.14 Sequence length distribution for the copolymerization of the system  
 MMA/NIPAM (samples B1-B5 in Table 1) at different NIPAM fractions in the feed  
 ( $f_{\text{NIPAM},0}$ ). The vertical axis represents the percentage of a determined mean sequence length  
 N (A) for NIPAM and B) for MMA) and one of the horizontal axes the corresponding  
 sequence of length x. Please note that sequences are only shown up to heptads, but other  
 sequences could be present. .... 68

Figure 3.15 Monomer fraction  $f_{\text{BuA}}$  and copolymer fraction  $F_{\text{BuA}}$ . and joint confidence plots.  
 Figures A and B compare the monomer fraction  $f_{\text{BuA}}$  and copolymer fraction  $F_{\text{BuA}}$  as a  
 function of conversion with the corresponding experimental values obtained by NMR for  
 the copolymerization of the system MMA/BuA. Figure C shows joint confidence regions  
 for the estimated reactivity ratios. Green 50%, blue 70%, orange 90% and red 95%  
 probabilities joint confidence regions for the estimated reactivity ratios.  $r_{\text{BuA}}=0.66$  and  
 $r_{\text{MMA}}=3.31$  ..... 69

Figure 3.16 Sequence length distribution for the copolymerization of the system MMA/BuA at  
 different monomers fractions  $f_0(\text{BuA})$ . The vertical axis represents the percentage of a  
 determined mean sequence length N (Figure A for BuA and Figure B for MMA) in

percentage and one of the horizontal axes the corresponding sequence of length  $x$ . Please note that sequences are only shown up to heptads but other sequences could be present... 70

Figure 3.17 DSC Analysis of B0-B6 and C1-C6 copolymers. A) DSC thermograms of homopolymers B0 and B6, and copolymers B1-B5, determination of the  $T_g$ . B) Thermodynamic transition observed around 20 °C. C) DSC thermograms of C6 homopolymer and C1-C5 copolymers. The DSC curves have been shifted (y-axis) to facilitate their interpretation. .... 72

Figure 3.18 Area values (J/g) of polymers B0-B5 calculated by integration of DSC thermograms at the transition around 20 °C..... 72

Figure 3.19 Experimental  $T_g$  values and  $T_g$  values estimated with the Fox, Kwei, and Brostow equations A) homopolymers B0 and B6 and copolymers B1-B5,  $K_{kwei} = 5.92$ ,  $q^{G^{MMA-NIPAM}} = 18.70$ ,  $a_0 = -15.82$ ,  $a_1 = -30.56$  and  $a_2 = -21.82$ . B) homopolymers C0 and C6 and copolymers C1-C5,  $K_{kwei} = 0.45$ ,  $q^{G^{MMA-BuA}} = 4.55$ ,  $a_0 = 134.34$  and  $a_1 = 61.09$ . .... 74

Figure 3.20 TGA thermograms of A) homopolymer A5 and copolymers A2-A4; B) homopolymers B0 and B6, and copolymers B1-B5; C) homopolymers C6 and copolymers C1-C5. .... 75

Figure 3.21 A) Light transmission measurements of homopolymer B6 and copolymers B4-B5. B) Cell viability of homopolymers B0 and B6 and copolymers B4-B5. .... 76

Figure 4.1.  $^{19}F$ -NMR spectra of (A) purified PFP-CTAP, (B) P10 and (C) P20 in  $CDCl_3$  (300 MHz). .... 86

Figure 4.2.  $^1H$ -NMR spectrum of the synthesized P(OEGMEMA-*stat*-FLUMA) (copolymer P10) in  $CDCl_3$  (300 MHz)..... 87

Figure 4.3  $^1H$ -NMR spectrum of the synthesized P(OEGMEMA-*stat*-FLUMA)-*b*-P(BMA) (copolymer P20) in  $CDCl_3$  (300 MHz). .... 87

Figure 4.4.  $^1H$ -NMR spectrum of synthesized PBMA (homopolymer P30) in  $CDCl_3$  (300 MHz) ..... 89

Figure 4.5  $^1H$ -NMR spectrum of P(BMA)-*b*-P(GMMA)-*b*-P(GMMA-*stat*-NHSMA-*stat*-FLUMA) (copolymer P40) in  $DMF-d_7$  (300 MHz)..... 89

Figure 4.6 <sup>13</sup> C NMR spectrum (using the Inverse-Gated Decoupling technique) of P(BMA)- <i>b</i> -P(GMMA)- <i>b</i> -P(GMMA- <i>stat</i> -NHSMA- <i>stat</i> -FLUMA) (copolymer P40) in DMF- <i>d</i> <sub>7</sub> utilized for a quantitative analysis.....	90
Figure 4.7 Elemental analysis results for copolymer P40. ....	90
Figure 4.8 SEC chromatograms of the investigated polymers A) P10 copolymer and corresponding P20 block copolymer. B) P30 macro-RAFT and corresponding P40 copolymer. The SEC equipment utilized DMAc + 0.21 wt% LiCl was used as an eluent, refractive index (RI) detection and a calibration curve prepared from P(methyl methacrylate) (PMMA) standards of narrow dispersity.....	91
Figure 4.9 Secondary structure of the investigated peptides generated with the PEP-FOLD3 and I-TASSER platforms. * Prediction of secondary structure and confidence scores were computed by the iterative threading assembly refinement (I-TASSER) server, H: Helix; S: Strand; C: Coil. (Zhang Lab, University of Michigan (2018) I-TASSER Protein Structure and Function Predictions [Internet]. <a href="https://zhanglab.ccmb.med.umich.edu/I-TASSER/">https://zhanglab.ccmb.med.umich.edu/I-TASSER/</a> . Accessed 06 December 2021) ** Three-dimensional (3D) models were predicted by the PEP-FOLD3 platform using 100 simulations. ***The local structure predictions were generated with PEP-FOLD3 platform; the color code corresponds to red: helical, green: extended, and blue: coil.....	93
Figure 4.10 3D Fluorescence spectra plots of the investigated peptides in DMSO at <i>T</i> = 25 °C. A) PC1 (1.6 μM; 0.002 mg mL <sup>-1</sup> ). B) PC2 (3.2 μM; 0.004 mg mL <sup>-1</sup> ). C) PC3 (2.57 μM; 0.004 mg mL <sup>-1</sup> ). D) PC1-5FAM (2.49 μM; 0.002 mg mL <sup>-1</sup> ). E) PC3-5FAM (2.09 μM; 0.004 mg mL <sup>-1</sup> ).....	95
Figure 4.11 Excitation-emission contour plots of investigated peptides in physiological solution at pH 7.4 (PBS) and <i>T</i> = 25 °C. A) PC1 (3.21 μM). B) PC1-5FAM (2.49 μM). C) PC3 (2,57 μM). D) PC3-5FAM (2.09 μM).....	97
Figure 4.12 Fluorescence spectra of investigated peptides in PBS at <i>T</i> = 25 °C and 4 μg mL <sup>-1</sup> . A) PC1 (3.2 μM). B) PC1-5FAM (2.5 μM). C) PC3 (2.57 μM) and D) PC3-5FAM (2.1 μM). ....	97

Figure 4.13 Excitation-emission contour plots of investigated peptides in DMSO at 4 $\mu\text{g mL}^{-1}$ and $T=25^\circ\text{C}$ . A) PC1. B) PC1-5FAM. C) PC3. D) PC3-5FAM. ....	98
Figure 4.14 Fluorescence spectra of peptides PC1 to PC3 in anhydrous DMSO using a $\lambda_{\text{ex}} = 360$ nm at different concentrations (ca 90.04, 80.03, 70.18, 60.13, 50.13, 40.06, 29.91, 20.18, 10.18, 8.11, 6.13 and 3.99 $\mu\text{g mL}^{-1}$ ) (A, C and E). Generated calibration calibration plots of fluorescence intensity vs concentration (B, D and F).....	99
Figure 4.15 2D DOSY spectra of A) P20 and B) P40 in DMF- $d_7$ (400 MHz, RT).....	102
Figure 4.16 2D DOSY spectra in DMF- $d_7$ (400 MHz, RT). A) PC1 peptide, b) B1 conjugate, C) PC3 peptide and D) B2 conjugate. ....	103
Figure 4.17 2D DOSY spectra in DMF- $d_7$ (400 MHz, RT). A) PC1 peptide, b) B3 conjugate, C) PC3 peptide and D) B4 conjugate. ....	104
Figure 4.18. 3D fluorescence spectra at 0.2 mg mL $^{-1}$ of A) P20 copolymer in PBS, B) P20 copolymer in DMSO, C) conjugate B1 in DMSO and D) conjugate B2 in DMSO.....	109
Figure 4.19. 3D- fluorescence spectra at 0.2 mg mL $^{-1}$ of A) P40 copolymer in PBS, B) P40 copolymer in DMSO, C) conjugate B3 in DMSO and D) conjugate B4 in DMSO.....	110
Figure 4.20. 3D fluorescence spectrum of the utilized DMSO solvent. ....	110
Figure 4.21. DLS size distribution plots, measurements performed using deionized water at room temperature. A) DLS plots of copolymer P20 (1 and 5 mg mL $^{-1}$ ), and conjugates B1 (3 mg mL $^{-1}$ ) and B2 (3 mg mL $^{-1}$ ). B) DLS plots of copolymer P40 (0.5 and 1.5 mg mL $^{-1}$ ), and conjugates B3 (2 mg mL $^{-1}$ ), and B4 (2 mg mL $^{-1}$ ). ....	114
Figure 4.22. Cryo-TEM micrographs of copolymers P20 and P40 and their corresponding conjugates; the analysis was performed using deionized water at room temperature. Shape changes from micelles to vesicles were observed with an increase in P20 concentration. A) Copolymer P20 at 0.4 mg mL $^{-1}$ . B) Copolymer P20 at 5 mg mL $^{-1}$ . Conjugate of P20 with PC1 peptide forms micelle in aqueous media. C) Conjugate B1 at 5 mg mL $^{-1}$ . Shape changes from worms, micelles and vesicles to vesicles were observed with an increase in P40 concentration. D) Copolymer P40 at 0.5 mg mL $^{-1}$ . E) Copolymer P40 at 1.5 mg mL $^{-1}$ .	

Conjugate of P40 with PC1 peptide forms mainly micelle nanostructure F) Conjugate B3 at 2 mg mL <sup>-1</sup> .....	115
Figure 4.23 Cryo-TEM micrographs of copolymers P20 and P40 in aqueous media. A) Co-existence of vesicles and micelles using P20 at 5 mg mL <sup>-1</sup> . B-C) Formation of vesicles using P40 at 1.5 mg mL <sup>-1</sup> . .....	116
Figure 4.24. A) Relative cell viability of MDCK cells in the presence of 4-500 µg mL <sup>-1</sup> of PC1-PC3, PC1-5FAM, and PC3-5FAM as determined by Alamar Blue measurements after 24 h. Microscope was used at Ex 560/ Em 590 nm. B) Cellular uptake peptides-labeled 5FAM at different concentrations (n = 4) quenched by trypan blue and without pretreatment. C) Confocal images of the MDCK cells exposed to PC1-5FAM and PC3-5FAM peptides (250 µg mL <sup>-1</sup> ), the nuclei of the cells were stained with Hoechst dye. ....	119
Figure 4.25. A) Relative cell viability of MDCK cells exposed at a polymer / nanoparticle concentration of 100 µg mL <sup>-1</sup> as determined by Alamar Blue measurements after 24 h using wavelengths of Ex 560/ Em 590 nm, and methodologies A and B for the analyses. B) Cell v viability of MDCK, HuH7 and HEPG2 cell lines in the presence of copolymers P20 and P40 and conjugates B1-B4 at a material concentration of 200 µg mL <sup>-1</sup> .....	120
Figure 4.26. Cell viability of the MDCK, HuH7 and HEPG2 cell lines in presence of copolymers P20 and P40, and conjugates B1-B4 at a material concentration of 100 µg mL <sup>-1</sup> . .....	122
Figure 4.27. Cellular uptake of block copolymers conjugated with peptides PC1 and PC3 quenched by trypan blue and without pretreatment at material concentrations of 50 and 100 µg mL <sup>-1</sup> . A) Copolymer P20 and its corresponding conjugates B1 and B2. B) Copolymer P40 and its corresponding conjugates B3 and B4. ....	123
Figure 5.1 <sup>1</sup> H-NMR spectrum of PC1 (in DMSO- <i>d</i> <sub>6</sub> , 300 MHz) .....	128
Figure 5.2 <sup>1</sup> H-NMR spectrum of PC1-5FAM (in DMSO- <i>d</i> <sub>6</sub> , 300 MHz) .....	129
Figure 5.3 <sup>1</sup> H-NMR spectrum of PC2 (in DMSO- <i>d</i> <sub>6</sub> , 300 MHz) .....	129
Figure 5.4 <sup>1</sup> H-NMR spectrum of PC3 (in DMSO- <i>d</i> <sub>6</sub> , 300 MHz) .....	130
Figure 5.5 <sup>1</sup> H-NMR spectrum of PC3-5FAM (in DMSO- <i>d</i> <sub>6</sub> , 300 MHz) .....	130

## List of Schemes

Scheme 1.1 Schematic representation of thesis.....	16
Scheme 3.1 Schematic representation of GMMA-based copolymers and their synthesis via RAFT copolymerization using 4-cyano-4-(phenylcarbonothioylthio)pentanoic acid (CPAD) and 4-cyano-4-[(dodecylsulfanylthiocarbonyl)sulfanyl]pentanoic acid (CDTPA) RAFT agents, and 4,4'-azobis(4-cyanopentanoic acid) (ACVA) as a thermal radical initiator.....	52
Scheme 4.1 Scheme 4.1. Synthesis of amphiphilic block copolymers via RAFT Polymerization (A) Synthesis of functionalized PFP-CTAP RAFT agent. (B) Synthesis of P(OEGMEMA- <i>stat</i> -FLUMA)- <i>b</i> -P(BMA) (P20), (C) Synthesis of P(BMA)- <i>b</i> -P(GMMA)- <i>b</i> -P(GMMA- <i>stat</i> -NHSMA- <i>stat</i> -FLUMA) (P40).....	86
Scheme 4.2 Conjugation route of peptides derived from HA and amphiphilic block copolymers. A) Aminolysis of PFP-CTAP in P(OEGMEMA- <i>stat</i> -FLUMA)- <i>b</i> -P(BMA) (P20) and peptides. B) Synthesis of P(BMA)- <i>b</i> -P(GMMA)- <i>b</i> -P(GMMA- <i>stat</i> -NHSMA- <i>stat</i> -FLUMA)-peptide (P40-peptide) conjugate via aminolysis of NHSMA. C) Scheme of peptide-polymer conjugation.....	100

## List of tables

Table 1.1 List of cell penetrating peptides commonly used in nanomedicine.....	30
Table 1.2 List of cell targeting peptides and their corresponding cell receptors.....	31
Table 1.3 Spectroscopy properties of fluorescent amino acids.[115] .....	35
Table 3.1. $f_n$ and estimated $F_n$ for GMMA-based copolymerizations obtained by $^1\text{H-NMR}$ .....	53
Table 3.2. Summary of the reaction conditions of GMMA and NHSMA copolymerization in DMF.....	53
Table 3.3. Summary of the reaction conditions of GMMA and NIPAM copolymerization in DMF.....	53
Table 3.4. Summary of the reaction conditions of GMMA and BuA copolymerization in DMF.....	53
Table 4.1 Summary of some physicochemical properties of polymers P10 to P40.....	91



Table 4.2 Theoretical physicochemical properties of peptides PC1-PC3, PC1-5FAM, and PC3-5FAM. ....	92
Table 4.3 Summary of $\lambda_{ex} / \lambda_{em}$ signal of the investigated peptides in DMSO and PBS.....	95
Table 4.4 Summary of the properties of bioconjugates and peptides.....	101
Table 4.5 Physicochemical properties of the investigated copolymer and conjugates derived thereof. ....	112

## List of Abbreviations

ACVA	4,4'-azobis(4-cyanopentanoic acid)
AIBN	Azobisisobutyronitrile
ATRP	Atom transfer radical polymerization
BMA	Butyl methacrylate
BuA	Butyl acrylate
CDCl <sub>3</sub>	Deuterated chloroform
CDTPA	4-cyano-4-[(dodecylsulfanylthiocarbonyl)sulfanyl]pentanoic acid
CPAD	4-cyano-4-(phenylcarbonothioylthio)pentanoic acid
CPPs	Cell-penetrating peptides
CTA	Chain transfer agent
CTPs	Cell targeting peptides
<i>D</i>	Diffusion coefficient
<i>D</i>	Dispersity
DCM	Dichloromethane
DIC	N,N'-Diisopropylcarbodiimid
DLS	Dynamic light scattering
DMAc	Dimethylacetamide
DMAP	4-Dimethylaminopyridine
DMF	N,N- dimethylformamide
DMSO	Dimethyl sulfoxide
DNA	Deoxyribonucleic acid
DSC	Differential scanning calorimetry
FDA	Food and Drug Administration
FLUMA	Fluorescein <i>O</i> -methacrylate
$f_n$ and $F_n$	Initial comonomer composition ( $f_n$ ) and final copolymer composition ( $F_n$ )
GMMA	Glycerol mono-methacrylate/poly(2,4-Dihydroxypropyl methacrylate)
GRAVY	Grand average of hydrophaticity index
HA	Hemagglutinin protein
HTE	High-throughput experimentation
<sup>1</sup> H-NMR	Proton nuclear magnetic resonance
LCST	lower critical solution temperature
MDCK	Madin-Darby canine kidney

NHS	N-hydroxysuccinimide
NHSMA	N-succinimidyl methacrylate
NIPAM	N-isopropylacrylamide
NMP	Nitroxide-mediated polymerization
NMR	Nuclear Magnetic Resonance
OEGMEMA	Oligoethylene glycol methyl ether methacrylate Mn 500 gmol <sup>-1</sup> ,
PBuA	Poly(butyl acrylate)
PEG	Poly(ethylene glycol)
PFP	pentafluorophenyl
PFP-CPAD	Pentafluorophenyl-(4-phenylthiocarbonylthio-4-cyanovalerate)
PGMMA	Poly(glycerol mono-methacrylate) or poly(2,3-dihydroxypropyl methacrylate)
Phe	Phenylalanine
PIGMA	Poly(isopropylidenglycerol methacrylate)
PMMA	Poly(methyl methacrylate)
PNIPAM	Poly(N-isopropylacrylamide)
PNHSMA	Poly(N-hydroxysuccinimide methacrylate)
POEGMEMA	Poly(oligo(ethylene glycol) methyl ether methacrylate)
PyMA	Pyrene methacrylate
SEC	Size exclusion chromatography
r	Reactivity ratios
RAFT	Reversible addition–fragmentation chain transfer
RDRP	Reversible deactivation radical polymerization
RNA	Ribonucleic acid
SEC	Size exclusion chromatography
T <sub>cp</sub>	Cloud point temperature
TEA	Triethylamine
TEM	Transmission electron microscopy
T <sub>g</sub>	Glass transition temperatures
TGA	Thermogravimetical analysis
Trp	Tryptophan
Tyr	Tyrosine
UCST	Upper critical solution temperature
UV	Ultraviolet
5-FAM	5-Carboxyfluorescein

## Abstract

This work investigates the conjugation process of polymer nanoparticles with peptides derived from the hemagglutinin (HA) protein of the influenza A virus. Two amphiphilic copolymer systems, one based on polyethylene glycol (PEG) and the other one on glycerol mono-methacrylate (GMMA) units, were considered for the formulation of the nanoparticles. An important part of this investigation was the synthesis of novel block copolymers with a precise macromolecular structure via the reversible addition–fragmentation chain transfer (RAFT) polymerization technique, the polymer structure was elucidated with the aid of proton nuclear magnetic resonance ( $^1\text{H-NMR}$ ) spectroscopy and size exclusion chromatography (SEC) techniques.

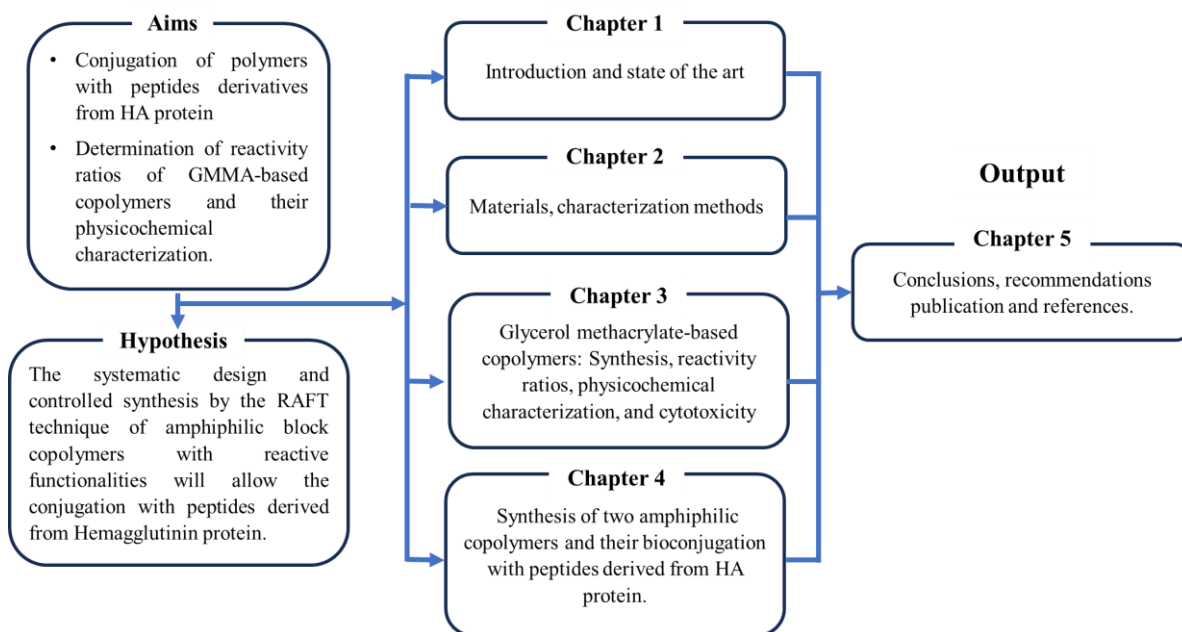
Copolymers based on the GMMA monomer are generally less explored systems in biomedical applications. Therefore, the copolymerization of GMMA with the comonomers *N*-succinimidyl methacrylate (NHSMA), *N*-isopropylacrylamide (NIPAM) and butyl acrylate (BuA) was investigated in more detail using high-throughput experimentation (HTE). The experimental results of this work enabled the determination of the reactivity ratios, the distribution of comonomer sequence lengths and the thermal properties (via differential scanning calorimetry (DSC) and thermogravimetric analysis (TGA)) of the investigated comonomer systems.

The selected conjugation pathway was via nucleophilic aminolysis of primary and secondary amines, which allowed the incorporation of the peptide units onto the copolymer chains. The obtained copolymer precursors and the peptide-copolymer conjugates tend to self-assemble in water due to their amphiphilic nature, enabling the formation of different nanostructures featuring morphologies such as micelles and vesicles as revealed by dynamic light scattering (DLS) and transmission electron microscopy (TEM) investigations. The preparation of polymer nanoparticles conjugated with the peptides was further analyzed and quantified via fluorescence spectroscopy. Finally, the cytotoxicity of both the copolymer precursors and the peptide-copolymer conjugates as well as their internalization into Madin-Darby canine kidney (MDCK) cells were evaluated via presto blue assay and flow cytometry, respectively.

## Thesis Outline

The main goal of the present thesis was the conjugation of polymers with peptides derived from the HA protein. The elucidation of the macromolecular architecture of the selected polymer platforms, some of them based on GMMA copolymer systems, was supported by the determination of the respective reactivity ratios using the RAFT polymerization technique. Two main polymeric systems were synthesized, the first one was based on GMMA, whereas the second one on PEG. Thereafter, peptides derived from the HA protein were conjugated with both polymeric systems and the obtained conjugates were evaluated in different epithelial cell lines.

The organization of this thesis is summarized in **Scheme 1.1**. Briefly, the first chapter provides the reader with the aim of this thesis as well as an introduction, antecedents and definitions of the main topics relevant to this investigation. The second chapter describes the experimental details and methods utilized for this research work. In the third chapter, the reactivity ratios and some physicochemical properties of some of the investigated and new copolymer systems based on the GMMA monomer are discussed. The fourth chapter deals with the synthesis and characterization of amphiphilic block copolymer systems via a reversible deactivation radical polymerization technique (*i.e.*, RAFT polymerization) as well as their self-assembly into nanostructures in aqueous media, followed by the characterization of the selected peptides derived from the HA protein of the influenza A virus and the conjugation of such block copolymers with the investigated peptides. The last section of chapter 4 focuses on the evaluation of the cytotoxicity and cellular internalization of the peptide precursors and respective copolymer conjugates. Finally, the last chapter provides conclusions, recommendations, a list of publications achieved during the course of this research project and participations in conferences, and references.



**Scheme 1.1** Schematic representation of the organization of this thesis.

## Chapter 1 Introduction

### 1.1 Introduction to reversible deactivation radical polymerizations

Controlled radical polymerization also known as reversible deactivation radical polymerization (RDRP) provides both the characteristics of a “living” polymerization and the versatility of a free-radical process.[1,2] RDRP entails equilibria between active and dormant chains through two processes called (1) reversible deactivation and (2) degenerative transfer. RDRP has aided in the development of well-defined polymers with predictable molar mass, low molar mass dispersity, high end-group fidelity, and the ability to be chain-extended.[3] To date, the most common RDRPs include nitroxide-mediated polymerization (NMP)[4], atom transfer radical polymerization (ATRP)[5] and RAFT polymerization.[6]

Thiocarbonylthio compounds are employed in RAFT polymerizations as reversible chain transfer agents (CTAs). The advantages of RAFT over other RDRP techniques are tolerance to many functionalized monomers and the possibility to use aqueous solutions and various organic solvents as a reaction medium.[6] Although there are some limitations inherent to the RAFT process, which include the difficulty to access high

molar mass and the necessity of an oxygen-free reaction medium to prevent retardation or inhibition during the polymerization reactions. Moreover, RAFT also requires an external and continuous source of radicals, which also leads to bimolecular termination reactions.[6,7]

## 1.2 RAFT polymerization: Mechanism and RAFT agent selection

### 1.2.1 RAFT mechanism

To carry out a RAFT polymerization, a radical initiator is required. The initiation step proceeds as in a typical radical polymerization (see **Figure 1.1**). First, the homolytic decomposition of the initiator provides a source of free radicals (I), the free radical adds to the  $\pi$ -bond of a vinyl monomer to form a propagating radical ( $P_n^\bullet$ ) (II), then the  $P_n^\bullet$  adds to the thiocarbonylthio compound in the RAFT agent (1) to form a radical intermediate (2), which later experiments a fragmentation yielding a polymeric thiocarbonylthio compound (3) and a new radical ( $R^\bullet$ ). Subsequently, the radical  $R^\bullet$  reinitiates the polymerization reacting with monomer units to form a new propagating radical ( $P_m^\bullet$ ) (III). Thereafter, the activation-deactivation equilibrium between the propagating and dormant polymeric chains is maintained ( $P_n^\bullet$  and  $P_m^\bullet$ ) (V). However, undesirable termination reactions cannot be suppressed and are directly related to the initiator concentration.[2,6]

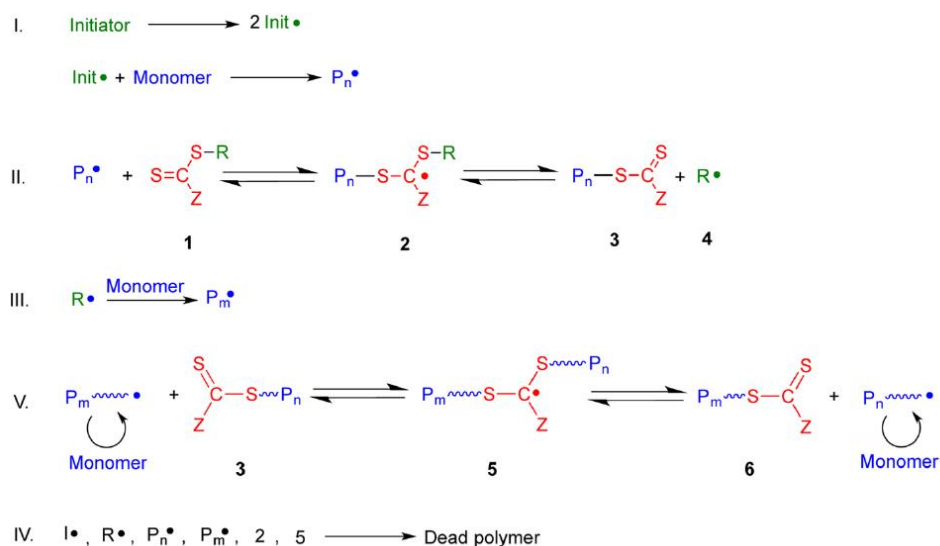


**Figure 1.1** Mechanism of the reversible addition–fragmentation chain transfer polymerization.[6]

### 1.2.2 RAFT agent selection

The selection of a suitable RAFT agent depends on the type of monomer. Vinyl monomers can be classified in two types according to their reactivity: (1) "More activated monomers" (MAMs) and (2) "Less activated" (LAMs). MAMs have the vinyl group conjugated to an aromatic ring or to a carbonyl group (*e.g.* (meth)acrylates and (meth)acrylamides), or as double bonds as in conjugated dienes. On the other hand, the double bond in LAMs are adjacent to saturated carbon, or to oxygen, nitrogen, and sulfur lone pairs atoms (*e.g.*, *N*-vinylpyrrolidone, vinyl acetate, etc.).[2] Dithiocarbamate and xanthate RAFT agents are more suitable for the polymerization of LAMs as dithioesters deliver long inhibition times and broad molar mass distributions.[8] In the case of MAMs, dithioesters or trithiocarbonates are used to obtain a good control over the corresponding polymerization reaction.

RAFT agents include Z and R groups in their chemical structure, which play different roles in the RAFT polymerization mechanism. The Z group is associated with the reactivity of the C=S bond in the thiocarbonyl and also relates to the lifetime of the intermediate radical (see 2 and 5 in **Figure 1.1**).[6] For example, *N*-vinyl monomers (LAMs) have a poor leaving group, thus, electron-donating groups are required in the Z moiety (as *O*-alkyl substituents) to destabilize the RAFT adduct radical (5) and increase the rate of the fragmentation reaction. In contrast, MAMs are characterized by having good leaving groups and generating propagating radicals that are less reactive than LAMs in the radical addition reaction, hence, more active RAFT agents with electron-withdrawing groups in the Z group are necessary to increase the rate of addition.[8–10] On the other hand, R must be a leaving group capable of effectively reinitiating radical polymerization. Steric factors and type of substituents (electron-withdrawing or electron-donating) in the R group have both an influence on the rates of addition and fragmentation to the thiocarbonyl group.[10]

## 1.3 Microstructure of RAFT polymers

RAFT polymerization might enable the precise design of complex polymer architectures and specific topology as depicted in **Figure 1.2**. Accessible topologies include linear, star, brush, network, hyperbranched, etc. Such polymers may also contain different functionalities.[11] Polymers formed of one single monomer are known as homopolymers, whereas those prepared from two or more comonomers are known as

copolymers. The synthesis of statistical, gradient, block or grafted copolymers might be also synthesized by controlling the addition of monomer or modifying the chemical structure of the macro-CTA.

The terminology for defining the different types of copolymers could be confusing, thus, definitions provided by the International Union of Pure and Applied Chemistry (IUPAC) are addressed herein. The following paragraphs briefly explain the basic aspects for the synthesis of these copolymers as well as their applications.

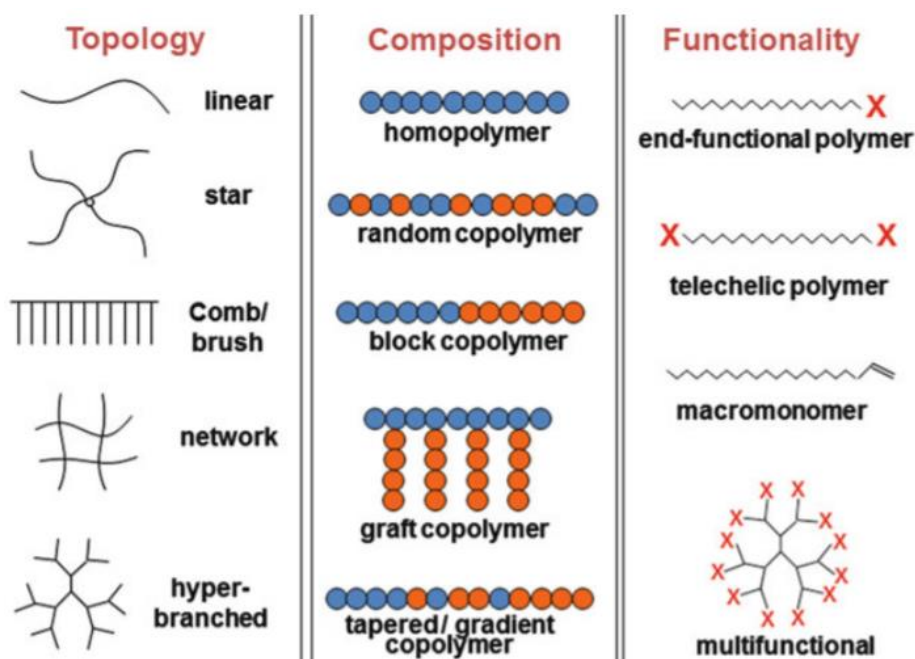


**Figure 1.2** Topologies, compositions, and functionalities accessible through the RAFT polymerization technique.[11]

### 1.3.1 Statistical and gradient copolymers

A target monomer composition is required in a copolymer to define a range of specific properties. In addition, it is necessary to know where the monomer units are located along the polymeric chain, *i.e.*, their microstructure.[12] The copolymerization of two monomers, M1 and M2, yields a distribution of sequence lengths along the polymeric chain. A great variety of statistical, random, alternating or gradient copolymers can be synthesized by RDRP techniques and used in diverse applications.

As indicated by IUPAC, a statistical copolymer is *a copolymer consisting of macromolecules in which the sequential distribution of the monomeric units obeys known statistical laws*.[13] An example of a statistical copolymer is the random copolymer that proceeds from a Bernoullian process, the IUPAC defines it as *a copolymer consisting of*



*macromolecules in which the probability of finding a given monomeric unit at any given site in the chain is independent of the nature of the adjacent units.*[13] Another interesting type of copolymers is known as tapered (gradient), such copolymers present a gradient of the same repeating unit throughout a part of the polymeric chain length (see **Figure 1.2**). Those types of copolymers are the result of the differences in the reactivity of the propagating chains when two or more monomers are added; this topic is explained in detail in section 1.5.

### *1.3.2 Block copolymers*

Block copolymers are formed by two or more blocks where each block can have unique characteristics such as hydrophobicity, hydrophilicity, biocompatibility, ions, etc. The synthesis of block copolymers can be performed by different pathways using RAFT polymerization, the two most common ones are explained next.

The first includes the synthesis of a pre-polymer bearing the RAFT moiety as an end group (also known as a macro-RAFT). Thereafter, the extension of the macro-RAFT chain by a sequential addition of other monomer units enables the construction of the second block; this step is repeated until the desired number of blocks is obtained. In this approach, it is essential to consider that dead chains derived from termination reactions cannot be extended; termination reactions might be minimized if the polymerization is stopped at low monomer conversion. The integrity of the RAFT group must be also kept as this would be critical to perform a proper chain extension.[14]

The second method includes the synthesis of two pre-polymers with terminal functional groups; thereafter, the linking of those blocks can be performed via a post-modification reaction. For example, RAFT agents with a carboxyl end group (from the R group) can be modified by amidation or esterification reactions.[2]

### *1.3.3 Brush and Graft polymers*

Graft polymers are similar to brush/comb polymers (*i.e.*, a backbone with branches). However, comb polymers have a higher density of side chains. Synthesis of both types of these polymers follows similar pathways that are described in several research works [15,16]; some of these strategies include the statistical copolymerization of macro-monomers and/or monomers bearing post-modifiable functional groups, as well as the attachment of a RAFT agent to a polymeric backbone and the post-modification of the R

or Z groups. Another interesting approach within this context refers to combinations of RAFT with other RDRP techniques. [14]

#### 1.4 Self-assembly of amphiphilic block copolymers in solution

Amphiphilic block copolymers have been particularly valued because of their ability to self-organize in bulk or solution. Bulk self-assembly is mainly governed by parameters such as copolymer composition, number of repeating units and Flory-Huggins interaction parameters; combinations of these parameters will lead to the formation of different morphologies such as body-centered cubic phases, hexagonal-packed cylinders, helices, or lamellae.[17] Although bulk self-assembly has been studied since 1960's, self-assembly in solution has gained importance in recent years due to its potential applications in biomedicine. Nanostructured morphologies in solution include spheres, vesicles, cylinders, nanofibers, worm-like micelles and others (see **Figure 1.3**). These morphologies may be predicted by the packing parameter ( $p=v/a_0l_c$ ), where  $v$  and  $l_c$  are the volume and length of the hydrophobic segment, respectively, and  $a_0$  is the interfacial area between two different phases.[17,18] The solution conditions, such as co-solvent ratios, pH, temperature, ionic strength, etc. can be modulated to trigger the formation of different nanostructures.[19] However, the copolymer composition and degree of polymerization of the blocks are the most critical factors in self-assembly processes.[20]

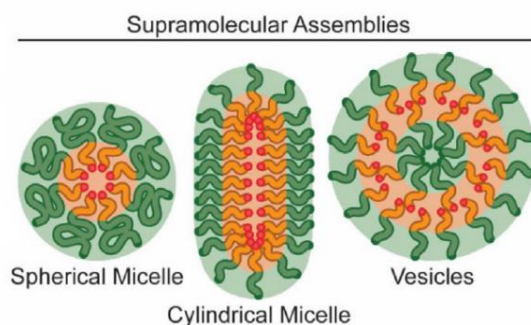


**Figure 1.3** Morphologies obtained via self-assembly in solution.[17]

From the thermodynamic point of view, the self-assembly of amphiphilic block copolymers in aqueous media is an entropy-driven process.[21] The main forces driving this phenomenon are (1) the ability of the hydrophobic segment of the polymer chains to stretch to potentially form the core of a nanostructure, which is driven by entropic energy, (2) the interfacial tension between the core and the solvent driven by enthalpy, and (3),

due to the potential presence of ionic groups and/or bulky substituents, repulsive interactions might also occur within the hydrophilic segment via non-covalent interactions such as electrostatic forces or steric interactions.[19]

Different approaches to promote the self-assembly of block copolymers have been developed. Notwithstanding, the most popular technique is dissolving the copolymer material in a good solvent for both blocks followed by the slow and selective addition of a non-solvent for one of the blocks (to promote the formation of the core of the nanostructure). To reach the final self-assembly, the initial good solvent is then removed from the system by dialysis or evaporation. This method is known as nanoprecipitation when nano-objects are generated.[22,23] In an alternative approach, the copolymer sample is dissolved, with the aid of, for instance, a thermal treatment or ultrasonic agitation in a selective and good solvent for one of the segments to promote self-assembly.[24]

## **1.5 Applications of polymer materials in biomedicine**

### *1.5.1 Conceptualization and main definitions*

Polymers are versatile materials with several potential applications in biomedicine. For instance, numerous articles and reviews describe their use in tissue engineering,[25] drug delivery,[26] coatings for medical devices,[27] among others.[28] To understand the role of polymers in biomedicine is essential to be familiar with the definitions of several terms, such as biomaterial, biopolymer, biocompatibility, cytotoxicity and/or biodegradation. Even though the vocabulary in this field is extensive, the definitions of these concepts is necessary to better understand the main goals of this project.

Biomaterial is referred by IUPAC [29] as a *material exploited in contact with living tissues, organisms, or microorganisms*. IUPAC recommends the use of the term “polymeric biomaterial” for the case where such material is a polymer. At the same time, it describes that a biopolymer is composed of one type of biomacromolecule such as proteins, nucleic acids, polysaccharides, etc.[29]

Currently, various definitions of biocompatibility have been coined, and this project takes the one proposed by Williams, D.F.: *Biocompatibility refers to the ability of a biomaterial to perform its desired function with respect to a medical therapy, without eliciting any undesirable local or systemic effects in the recipient or beneficiary of that therapy, but*

*generating the most appropriate beneficial cellular or tissue response in that specific situation, and optimising the clinically relevant performance of that therapy.*[30] Cell viability assays are usually performed with the aid of indicator dyes that undergo changes due to biochemical events occurring in their surroundings or in living cells.[31]

In addition, another useful concept to describe the characteristics of polymeric biomaterials is biodegradability, which refers to their degradation and elimination into / from the body, for instance, via a hydrolysis or an enzymatic activity.[30] Polymers employed in biomedicine must be also non-cytotoxic, non-mutagenic, and non-immunogenic. Cytotoxicity testing involves a biological evaluation *in vitro* of cell growth, reproduction and morphological effects upon adding and/or in contact with an external substance.[32] Regarding immunogenicity and mutagenicity, the first term refers to the *ability of a material or substance to elicit a cellular immune response and/or antibody production* (IUPAC, 2009)[29], whereas mutagenicity implies genotoxic effects and specifically refers to *the ability of a compound to induce point mutations* (Snodin 2020)[33].

Having introduced some terms useful for describing polymeric biomaterials in the previous paragraphs, some advantages and disadvantages of using such materials in biomedicine are briefly mentioned next.

Modern synthetic methods for the preparation of polymeric materials can offer the possibility to control, for instance, their molecular architecture, degradation, immunogenicity, molar mass, among other properties.[34] A such polymers offer “unlimited” combinations of a wide range of physical, chemical and biological properties for the development of materials with complex and advanced shapes that can undergo changes with temperature, pH, magnetic fields, light, etc. The degradation of synthetic polymers mainly depends on the chemical structure of their monomeric units, for example, polyesters bearing aliphatic glycolic and lactic acid units are some of the most common examples that exhibit this property; however, the range of degradable synthetic polymers still remains limited nowadays.[25,28]

In general, the toxicity of synthetic polymers is usually related to impurities remaining from their synthesis and/or formulation processes, which can include residual monomers, organic solvents, catalysts, etc. It may also come from other additives such as plasticizers. Likewise, the degradation mechanisms of several synthetic polymers and the

corresponding toxicity of the generated degradation by-products (*e.g.*, monomer units) are aspects that still remain unclear.

#### *1.5.2 Bioconjugation of synthetic polymer with biomolecules*

Synthetic polymers coupled to biomolecules via covalent bonds or electrostatic interactions can be referred as polymer bioconjugates. The incorporation of polymers endows biomolecules with unprecedented properties, such as stimuli responsiveness, improved thermal stability, self-assembly capabilities, etc.[35] Hence, peptides, proteins, oligonucleotides, nucleic acids, lipids, sugars and/or carbohydrates can be attached to synthetic/artificial polymers to form hybrid macromolecules (see **Figure 1.4**).[36]

For example, biomolecules such as deoxyribonucleic acid (DNA) and ribonucleic acid (RNA) have extraordinary molecular recognition capabilities. Furthermore, polysaccharides and carbohydrates play important roles in living organisms, such as expression of glycoproteins and glycolipids that bind to the surface of cells bearing cellular recognition targets. All in all, these mentioned abilities can imprint biocompatibility and cell-recognition properties to synthetic polymers.

On other hand, it is also possible to covalently attach therapeutic agents to polymeric materials to form drug-polymer conjugates. For instance, peptides are usually used as bioactive linkers in bioconjugate therapeutics. From this point of view, a proper design of bioconjugate must take into account the presence of functional and suitable chemical groups necessary to attach into specific polymeric chains without detriment of the efficiency of the corresponding drug.[37]

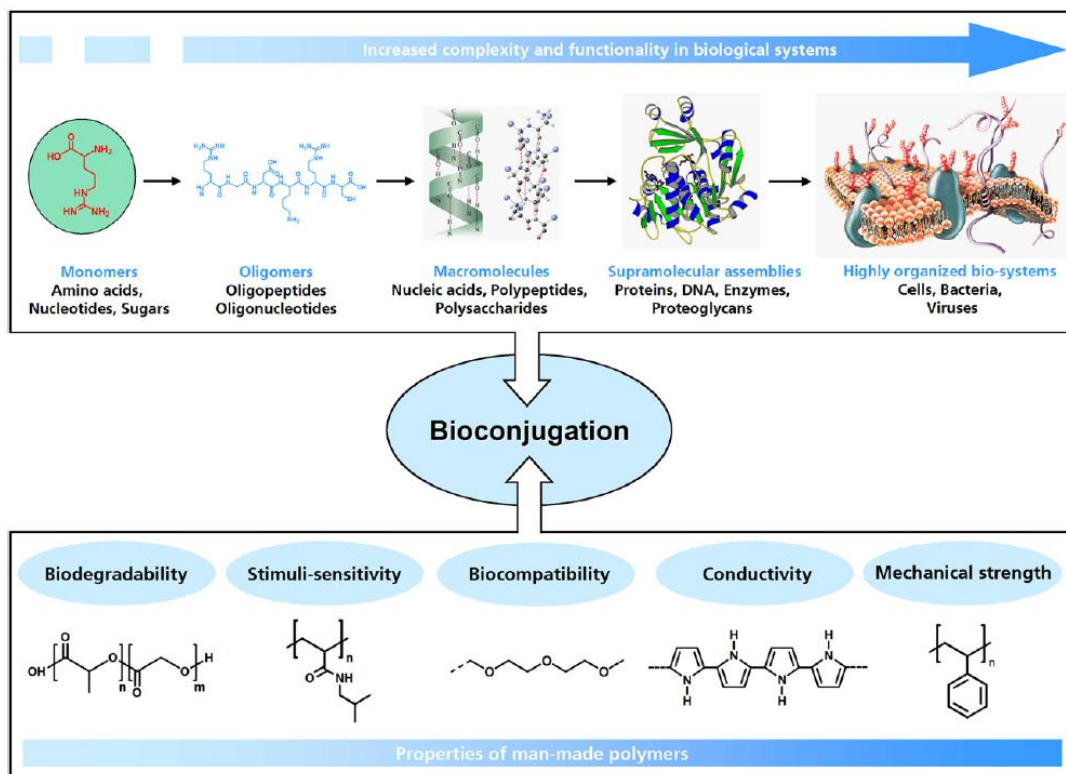


**Figure 1.4** Schematic representation of the bioconjugation process between synthetic polymers and biological molecules.[36]

Conjugation of proteins/peptides are of particular interest in biomolecule-polymer bioconjugates because proteins fulfill essential tasks in many biological processes, such as bio-catalysis (enzymes) or immune system functions (immunoglobulins). The conditions to successfully achieve this type of bioconjugations must be carefully analyzed and/or optimized to avoid the denaturation of the proteins during the synthesis process as their corresponding bioactivity might be compromised. However, denatured proteins may be still utilized to increase biocompatibility and promote cellular uptake. In contrast, peptides have shorter amino acid chain lengths than proteins as well as lower molar mass and less complex tertiary structures. For this reason, peptides are good potential candidates to form bioconjugates as compared to entire protein.[38]

### 1.5.3 Bioconjugation strategies

A coupling between biomolecules and synthetic polymers can be performed via three strategies: (I) *Grafting to* allows the attachment of pre-synthesized polymers to biomolecules, (II) *grafting from* refers to an *in situ* polymer growth from a biomolecule (macroinitiator); alternatively, it is also possible the synthesis of biomolecules utilizing a pre-synthesized polymer as a precursor (technique also known as inverse bioconjugation),

and (III) *grafting through* where the synthesis of grafted copolymers is carried out with monomers bearing reactive functional groups that enable the insertion of biomolecules in a post-modification reaction; with this approach, it is also possible to perform a copolymerization reaction with macromonomers that already contain the biomolecule of interest.[36,38]

To properly select a suitable conjugation strategy for a specific purpose, it is important to understand the advantages and disadvantages of each approach. *Grafting to* provides low bioconjugation yields as compared to *grafting from* due to a potential steric hindrance between the synthetic polymer and the biomolecule. An extensive polymer characterization may be required for the *grafting to* process, whereas the *grafting from* approach may allow for a more precise characterization of the generated biomacromolecule. In terms of purification of the generated bioconjugates, *grafting from* has an advantage since the removal of unreacted monomer can be achieved in a final stage. *Grafting through* offers a quantitative functionalization in a rather uncomplicated way. However, the synthesis of specific macromonomers can be challenging; also, the polymerization macromonomer may require the protection/deprotection of certain functional groups prior/post the polymerization reaction.[39]

The first approaches established for bioconjugation chemistry were based on active esters (see **Figure 1.5**), in which polymers with modulated chemical properties were attached to proteins/peptides via lysine and histidine residues or the *N*-terminus. This strategy is considered as non-selective due to the large number of lysine groups available in different proteins/peptides; nonetheless, the method is still widely used.

Active ester chemistry has also enabled to couple antibodies, sugars, drugs, etc. to different polymeric materials. For instance, *N*-hydroxysuccinimide (NHS) ester is the most used activated ester in the production of polyacrylamide derivatives. The solubility of NHS (meth)acrylates homopolymers is limited to solvents such as dimethyl sulfoxide (DMSO) and *N,N*-dimethylformamide (DMF); however, NHS monomers can be copolymerized with other monomers to improve solubility in other solvents such as dioxane, toluene, tetrahydrofuran (THF), etc. An additional limitation related to the usage of polymers bearing NHS units is the presence of side reactions during the aminolysis step.[40,41]

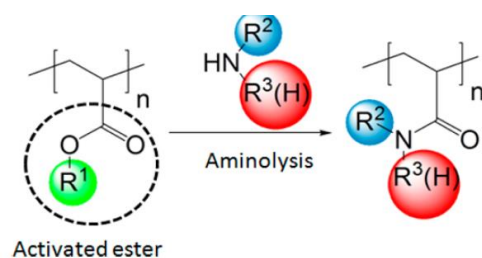


**Figure 1.5** Schematic representation of the bioconjugation of synthetic polymers using activated esters.[40]

In another approach, Eberhardt and Theato[42] performed the homopolymerization and post-functionalization of pentafluorophenyl (PFP) ester-based (meth)acrylates (PFPMA and PFPA). PFP ester-based polymers were suitable for performing the nucleophilic aminolysis of primary and secondary amines; although a hydroxyl functionalization is also possible, yields are rather low when using both monomers. Post-functionalization reactions are carried out under mild conditions, in general PFPA is more reactivity than PFPMA and, moreover, the conjugation reaction can be monitored by fluorine-19 nuclear magnetic resonance spectroscopy ( $^{19}\text{F}$  NMR). The polymerization of PFPA and PFPMA monomers can be performed in conventional solvents such as dioxane, acrylonitrile or DMF[43].

NHS and PFP-containing polymers have both low coupling yields with aromatic amines. On the other hand, PFP esters have shown higher reactivities than their NHS esters counterparts under similar reaction conditions.[42]

For protein/peptide bioconjugates, research on regioselective reactions that focus on specific targeting residues such as cysteine, tyrosine, tryptophan, arginine, etc. has currently attracted more interest. For these approaches, it is possible to insert desired residue sequences into biomolecules to direct bioconjugation reactions. For example, for cysteine residues, conjugation is conducted based on pyridyl disulfide–thiol, thiol-ene and/or thio- Michael reactions.[38] Similarly, ‘click’ chemistry is also one of the most promising methods for bioconjugate chemistry. ‘Click’ reactions are highly efficient and selective, and can be carried out with organo-azide and triphenylphosphines (Staudinger ligation), or as copper catalyzed Huisgen cycloadditions of azides and alkynes.[39]

Some of the advantages of RAFT polymerizations are mentioned above in Section 1.4. RAFT polymers contain R and Z groups derived from the corresponding RAFT agent also denominated, which are often referred as alpha and omega end groups, respectively.



Bioconjugation strategies for RAFT polymers are mainly based on post-polymerization procedures (*grafting to* and *grafting through*; see **Figure 1.6**) and via *in situ* polymerizations (*grafting from*). A post-modification of polymer chains is possible via (i) a reaction of a thiocarbonylthio end-group in a polymeric chain with a thiol-reactive reagent, (ii) coupling of a reactive biomolecules with functionalized RAFT agents (the alpha R group is usually utilized in this approach as several RAFT agents have a carboxylic acid functionality, so polymers prepared from such RAFT agents can react with amino or hydroxyl groups to form amide or ester bonds; it is also common in this approach to activate the end-chain with a reactive ester prior the bioconjugation reaction), and (iii) “*grafting through*” is possible via RAFT homopolymerization or copolymerization reactions with (co)monomers bearing reactive functionalities. To avoid secondary reactions with the RAFT agent, the protection of functional groups might be necessary considered prior the polymerization reaction. For *in situ* bioconjugations, such strategies include *grafting to* and *biomolecule-based monomers*, which both require protecting functional groups of the biomolecule and a careful selection of polymerization conditions to prevent degradation of the biomolecule.[35]

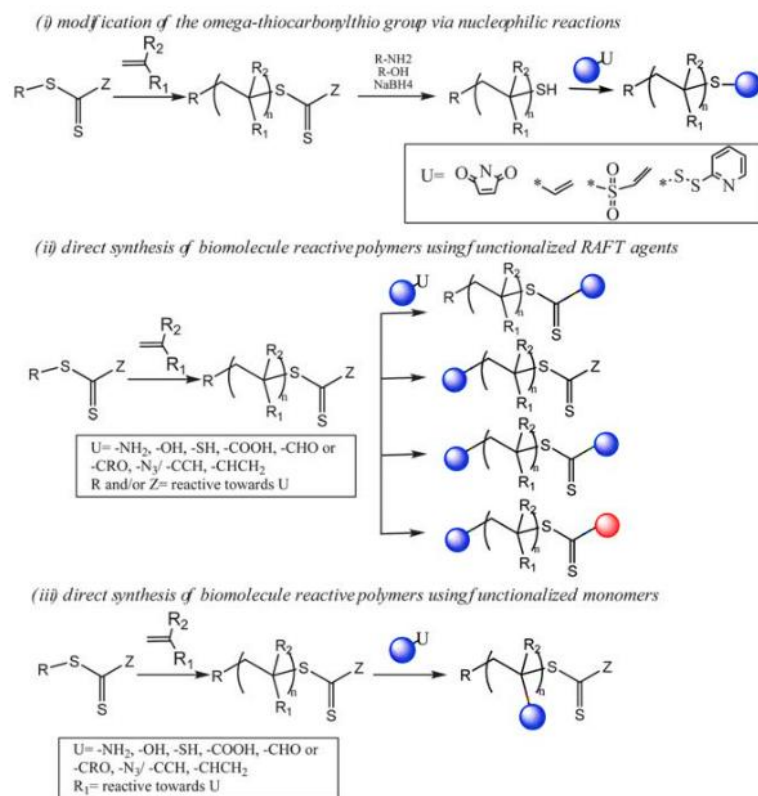


**Figure 1.6** Schematic representations of post-modification strategies for RAFT polymers. [35]

## 1.6 Peptides in nanomedicine

### 1.6.1 Types of peptides to functionalize polymers.

Peptides in nanomedicine have been explored for different purposes, some possess antibacterial properties[44] while others are effective in trespassing biological membranes. Peptides used to penetrate the biological barriers are generally classified as (i) cell-penetrating peptides (CPPs), which facilitate cell entry, (ii) cell targeting peptides (CTPs), which target specific cell-receptors, (iii) endosome-disruptive peptides, and (iv) nuclear localization signal peptides.[45] Currently, the development of peptide sequences is performed in two ways (1) by building and screening random amino acids sequences (top-down approach), or (2) by mimicking biologically active sequences of specific proteins (bottom-up approach).[46]

Based on the remarkable advantages offered by peptides, the development and design of new peptide-conjugates has been extended to peptide-drug[47], organometallic-peptide[48] and peptide-nanoparticle conjugates (which include polymer, inorganic and hybrid nanoparticles). Peptide-nanoparticle conjugates bear peptides onto the surface of nanoparticles to enhance their bioavailability (see **Figure**

1.7). Size is one of the most important parameters of nanoparticles, for example, for drug delivery applications, nanoparticles of small size (<200 nm) and large surface area might improve drug solubility and the ability to cross the blood-brain barrier (BBB).[49] Despite the different advantages offered by peptides, they may still show some limitations such as lower affinity for proteins when compared to proteins, short circulating half-life times, susceptibility to protease digestion in different biological environments, etc. [46]

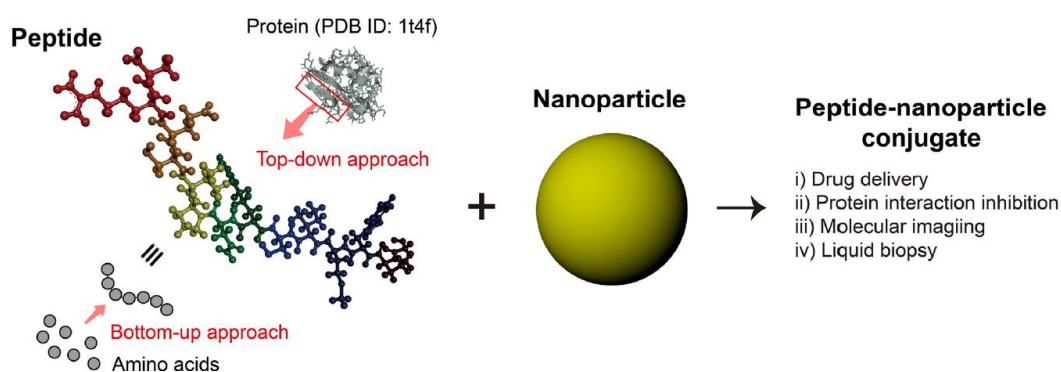


**Figure 1.7** Schematic representation of two approaches to design peptides and their coupling onto a nanoparticle.[46]

As mentioned before, CPPs offer high transduction efficiencies and can be classified as (1) cationic, identified by the presence of arginine and lysine residues, (2) amphipathic formed by hydrophobic and hydrophilic amino acid, and (3) hydrophobic, composed of residues such as alanine, leucine, isoleucine, methionine or valine.[50] The mechanism of internalization of CPPs through cell membranes usually undergoes via two pathways. The first one is energy-independent via direct penetration, which generally is driven by electrostatic interactions between the phospholipid bilayer of membranes and the CPPs. The second pathway is referred as energy-dependent via an endocytosis.[51] **Table 1.1** summarizes some of the most commonly CPPs used in nanomedicine.

**Table 1.1** List of cell penetrating peptides commonly used in nanomedicine.

Name	Origen	Amino acid sequence	Ref.
<i>Cationic</i>			
TAT	Human immunodeficiency virus (HIV)-TAT protein	RKKRRQRRRHRRKRR	[52]
8-Arginine	Synthetic	RRRRRRRR	[53]
8-Lysine	Synthetic	KKKKKKKK	[54]
Penetratin (pAntp)	Antennapedia Drosophila Melanogaster	RQIKIWFQNRRMKWKK	[55]
R6H4	Synthetic	RRRRRRHHHH	[56]
M918	Tumor suppressor protein p14ARF	MVTVLFRRLRIRRACGPPRVRV-NH <sub>2</sub>	[57]
<i>Amphipathic</i>			
ARF(1–22)	p14ARF Protein	MVRRFLVTLRIRRACGPPRVRV	[58]
VP22	Herpes virus	NAATATRGRSAASRPTQR	[59]

		PRAPARSASRPRRPVQ	
Transportan 10 (TP10)	Neuropeptide galanin (1-12) and mastoparan, connected via lysine.	AGYLLGKINLKALAALAKKIL-amide	[60]
Pep-1	Simian virus 40 (SV40)	KETWWETWWTEWSQPKKRKRK	[61]
pVEC	Murine vascular endothelium cadherin	LLIILRRRIRKQAHHSK-amide	[62]
MAP	Synthetic	KLALKLALKALKAAALKLA-amide	[63]
MPG	HIV gp41 and SV40 large T antigen domains	GALFLGFLGAAGSTMGAWSQP-KSKRKRK	[64]
VT5	Synthetic	DPKGDGPKGVTVTVTVTVTGKGDGPKPD-NH <sub>2</sub>	[65]
<i>Hydrophobic</i>			
PFV	C105Y, a synthetic peptide	PFVYLI	[66]
FGF	Cellular and viral proteins	PIEVCMYREP	[67]
SG3	Randomized peptide library	RLSGMNEVLSFRW	[68]

In contrast to CPPs, CTPs penetrate into the cell using a selective binding to a receptor. Several short peptides have been identified as CTPs and used to improve drug therapeutic efficacy, in particular in cancer therapies. [69] A few examples of CTPs and their corresponding cell-surface receptors are listed in **Table 1.2**. However, there are many more examples reported in the literature, for instance, as reviewed by Kang *et al.*[45] with focus on the application of CPPs and CTPs in gene therapies.

**Table 1.2 List of cell targeting peptides and their corresponding cell receptors.**

Name	Receptor	Amino acid sequence	Ref.
RGD	Integrin receptors	RGD peptide derivates	[70]
REDV	Integrin receptors	REDV	[71]
YIGSR	Laminin receptor	YIGSR	[72]
GE11	Epidermal growth factor receptor (EGFR)	YHWYGYTPQNVIGRC	[73]
Angiopep-2	Low density lipoprotein receptor-related protein (LRP-1)	TFFYGGSRGKRNNFKTEEY	[74]
MQLPLAT	Fibroblast growth factor receptor (FGFR)	MQLPLAT	[75]
CAGW	Endothelial cells (Ecs)	CAGW	[76]

### 1.6.2 Peptides derived from the HA protein of the influenza virus

Up to this point, types of peptides and their main characteristics relevant to nanomedicine have been introduced. In this section, specific examples of relevant peptides derived from proteins of influenza viruses are described. In this regard, the HA protein is a trimeric surface glycoprotein of the influenza virus and mediates binding of the virus to the specific sialic acid moieties located on the surface of the cell membrane. From its original conformation HA0, this protein can be divided into HA1 and HA2 subunits, which contain a receptor-binding domain and a fusogenic domain, respectively.[77,78] Activation models suggest that structural dynamic changes in the HA protein occur under

acid conditions; this can lead to an exposition of the fusion peptide of the HA2 subunit, which occurs in parallel to the endocytosis step[79].

In 1987 Ohnishi *et al.* studied the peptide GLFGAIAGFIENGWEGMIDG derived from the *N*-terminal segment of the HA2 subunit of the HA protein of the influenza virus; this short and hydrophobic sequence exhibited a pH-response under acid conditions.[80] Subsequently, peptide sequences contained in the HA2 subunit showing a larger capability to penetrate endosomal membranes were further investigated. For instance, it was found that the INF7 (GLFEAIEGFIENGWEGMIDGWYG) and H5WYG (GLFHAI AHFIHGGWHGLIHGWYG) peptides also have the ability to penetrate cell membranes under acid conditions.[81,82]

On the other hand, conserved HA peptide sequences have been proposed as adjuvants (*i.e.*, substances that increase vaccine efficacy) in vaccine formulations. Darji *et al.* utilized the peptide sequence NG34 (NSDNGTCYPGDFIDYEELREQLSSVSSFERFEIF) from the strain A/California/04/09(H1N1)pdm09 of the Influenza A virus as an adjuvant for the development of a vaccine formulation for swine immunization.[83,84] Subsequently, the HA1 segment SVIEKMNTQFTA VGKE from the strain A/New Caledonia/20/99 of the H1N1 virus, which also elicit an immune response, was investigated.[85] Furthermore, in 2018, Lohia and Baranwal[86] conducted immune reactivity studies in-vitro and in-silico (using molecular docking approaches) of the conserved sequences STDTVDTVLEKNVTVTHSVNL (H1) and KVNSVIEKMNTQFTA VGKEF (H2) as candidates for vaccine formulations.

## **1.7 PEG and PGMA as biocompatible polymers and their application in bioconjugate chemistry**

### *1.7.1 Poly(ethylene glycol) (PEG)*

Poly(ethylene oxide) (PEO) (also known as poly(ethylene glycol) (PEG) is the most investigated polymer in nanomedicine. The term PEGylation (a specific type of bioconjugation) has been used to refer to a covalent or a non-covalent linkage of PEG to different bioactive molecules, such as proteins, peptides, lipids, drugs, oligonucleotides, liposomes, nanocarriers, etc.[87] PEG is a non-toxic, highly biocompatible and water-soluble material approved by the US Food and Drug Administration (FDA).[88] As

depicted in **Figure 1.8**, PEGylation can increase thermal stability and the absorption half-life time of proteins, as well as their resistance to degradation, for instance, by proteolytic enzymes. Moreover, after PEGylation, an increase in the molecular size (hydrodynamic volume) of the conjugated molecule is observed, which can contribute to decrease its renal clearance as a consequence of an increase of the half-life time in the bloodstream.[89] In contrast, renal clearance and immunogenic response can decrease when hiding latent antigenic sites.[90]

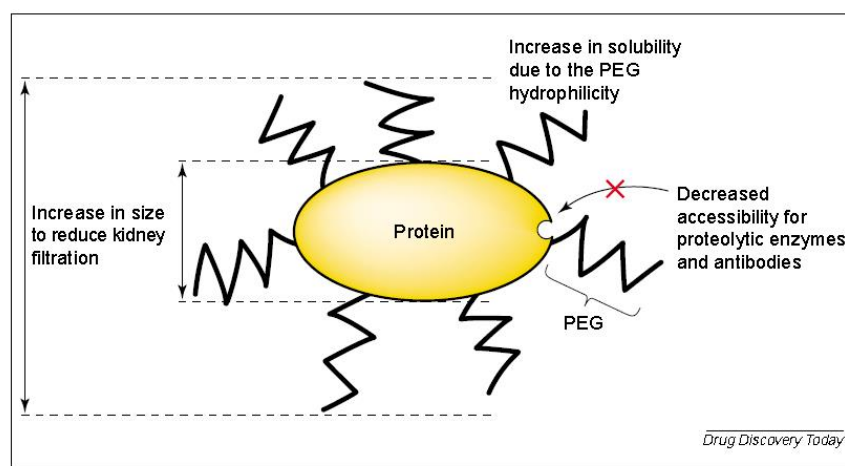


**Figure 1.8** Schematic representation of the advantages of the PEGylation of proteins.[87]

There is a wide range of synthetic routes and topologies of PEG derivatives documented in the literature.[87–92] PEG derivatives can feature different molecular architectures such as hyperbranched, star, comb, brush, network, and linear topologies (as mentioned in section 1.4).[93] For example, the synthesis of linear PEG is conventionally performed via the anionic ring-opening polymerization of ethylene oxide (EO). Furthermore, the use of PEG derivative monomers bearing reactive groups such as (meth)acrylates enables the synthesis of polymers with comb-like and brush-like topologies via radical polymerization.[91]

The literature describing PEG conjugates is extensive; there are several articles and reviews available discussing bioconjugation reactions in detail based on the strategies mentioned in section 1.6.3. The most representative reaction used for the synthesis of PEG conjugates is via the formation of an amide bond derived from an active ester (*i.e.*, based on a succinimide moiety or, more recently, the highly efficient pentafluorophenyl ester).[43,91,94,95]

### 1.7.2 Poly(glycerol mono-methacrylate) (PGMMA)

An interesting and less explored alternative to PEG to carry out the bioconjugation reactions is poly(2,4-dihydroxypropyl methacrylate), commonly known as poly(glycerol mono-methacrylate) (PGMMA), which also displays hydrophilic and biocompatible properties, a "stealth" effect (*i.e.*, protein-repellent properties or low protein adsorption)[96,97] and has been proposed to develop drug-delivery carriers.[98] The hydroxyl-rich chemical structure of PGMMA promotes a high solubility in water and protic solvents such as methanol and ethanol. PGMMA can be synthesized via RDRP techniques such as ATRP and RAFT.[99,100] Other synthetic route to obtain PGMMA is based on the polymerization of solketal methacrylate followed by hydrolysis of the acetal groups in post-polymerization reaction.[101]

Recently, PGMMA homopolymers have been utilized as hydrophilic precursors and macro-CTAs in the polymerization-induced self-assembly (PISA) RAFT technique.[102] Other applications of PGMMA also include contact lenses,[103] drug-delivery systems,[104][105] coatings for glucose sensors,[106] hydrogels,[107][108][109] and preparation of surfaces with reduced cell adhesion.[110]

The bioconjugation of PGMMA can be achieved via (1) a modification of its diol group to link, for example, drugs[98] or mannose[111], or (2) using other reactive groups in the polymeric chain or CTA. For instance, based on the second approach, Lamm *et al.* proposed adding a NHS ester reactive comonomer to a hydrophilic block composed of GMMA and 2-hydroxyethyl methacrylate (HEMA) to enable the bioconjugation of a fibrin-binding peptide.[112]

## 1.8 Fluorescence spectroscopy and fluorescent biomolecules

In this section, the main concepts of fluorescence spectroscopy are briefly introduced as well as some examples of fluorescent biomolecules.

IUPAC[29] defines a fluorophore as a *molecular entity (often organic) that emits fluorescence*, and a chromophore as *the part (atom or group of atoms) of a molecular entity in which the electronic transition responsible for a given spectral band is approximately localized*. The latter term arose from the dyestuff industry, referring originally to the chemical groups in a certain molecule that are responsible for the color of a dye.

Fluorescent moieties (fluorophores) absorb light (photons) of a specific wavelength ( $\lambda_{\text{Ex}}$ ), and after a short interval, also known as the fluorescence lifetime ( $\tau$ ), energy is emitted at a wavelength ( $\lambda_{\text{Em}}$ ).[113] In other words, the absorption of light of a chromophore involves the electron movement from the single ground electronic level  $S_0$  to an excited state  $S_n$  ( $n > 1$ ), whereas the emission process refers to the return to the ground state. The absorption energy is higher than the emission energy.[114]

**Table 1.3 Spectroscopy properties of fluorescent amino acids.**[115]

	Lifetime ( $\tau$ )	Absorption		Fluorescence	
	(ns)	$\lambda$ (nm)	Absorptivity ( $\epsilon$ )	$\lambda$ (nm)	Quantum Yield ( $\Phi_F$ )
Tryptophan	3.1 (mean)	280	5600	348	0.2
Tyrosine	3.6	274	1400	303	0.14
Phenyl alanine	6.4	257	200	282	0.04

Fluorophores can be categorized into intrinsic and extrinsic. Intrinsic fluorophores occur naturally such as peptides and proteins. In contrast, compounds lacking of fluorescence require the addition of extrinsic fluorophores to become fluorescence or modify their spectral properties (*e.g.*, compounds bearing fluorescein, rhodamine or dansyl groups).[116] Intrinsic protein fluorescence mainly derives from three aromatic amino acids: Tyrosine (Tyr), tryptophan (Trp) and phenylalanine (Phe). Nonetheless, the contribution of phenylalanine is negligible due to its low absorptivity and low quantum yield (see **Table 1.3**). Tyrosine has a quantum yield close to that of tryptophan and higher than that of phenylalanine; its wavelength scale is also narrower than that of tryptophan. The fact that tyrosine fluorescence can be quenched (*e.i.*, decrease in fluorescence intensity) in proteins may ascribed to its intermolecular interactions with other moieties and/or energy transfer to tryptophan.[116]

In proteins the indole group of tryptophan is the major source of UV absorbance at ~280 nm and emission at ~350 nm (see **Table 1.3**). However, its spectroscopy properties are mainly governed by interactions with the surroundings (local environment). For this reason, changes in protein conformation and/or interactions with ligands could provoke its quenching or wavelength shift; moreover, the nearby presence of electron-deficient groups also decreases its fluorescence.[115,116] Examples of intrinsic fluorophores are: the green fluorescent protein (GFP) from jellyfish *Aequorea Victoria*, coenzymes such as



nicotinamide adenine dinucleotide (NADH), flavin mononucleotide (FMN) and flavin adenine dinucleotide (FAD), and also other biomolecules such as riboflavin (known as vitamin B<sub>2</sub>).[116]

Common dyes used to label biomolecules are fluorescein and its derivatives. Fluorescein fluorescence studies demonstrated an increase in the hydrogen-bonding power of solvents leads to a shift of the fluorescence signals to shorter wavelengths in the absorption and fluorescence spectra. The intensity of the fluorescence signal also decreases when the hydrogen bonding power decreases. In DMSO, the absorption and fluorescence signals are centered at 520 and 543 nm, respectively. [117]

In a neutral aqueous solution (pH 6.86) fluorescein absorbs around 495 nm; however, its intensity ratios increase with increasing pH, which may be ascribed to its two fluorescent forms causing absorption and emission spectral changes. In nonpolar solvents, such as isopropanol and cyclohexane, the non-fluorescent lactone form is typically found.[118][116]

The formation of fluorescein species is pH dependent; in the case of fluorescein diacetate hydrolyzate at pH 7.4 the dianion form is mainly present (84%). Noticeable changes in absorption spectra, *e.g.*, intensity decrease and redshift ( $\lambda_{\text{Max}} = 490$  nm at pH 7.4) can occur. Acidic conditions promote the formation of a weak association of a non-fluorescent complex between the fluorescein and tryptophan. However, this non-fluorescent complex can be also found in no acidic conditions.[119]

Sjöback *et al.* [120] observed that the dianion yields its main absorption signal at 490 nm with a shoulder around 475 nm. It shows a very weak absorption in the 350-440 nm region and a distinct absorption signal in the UV region at 322, 283 and 239 nm. The anion has a somewhat weaker absorption in the visible region with signals at 472 nm of roughly the same molar absorptivity. It also absorbs weakly in the near UV region and displays signals at 310 and 273 nm.

Marmé *et al.* observed the formation of a non-fluorescent complex between tryptophan and fluorescein in a buffer solution of pH=7.4. They reported that fluorescein quenching is both static and dynamic and that the contact between tryptophan and the chromophore is essential for an efficient quenching. Furthermore, tryptophan containing peptides in labeled with fluorescein did not decrease their quantum yield and half-life time.[121]

Vaiana *et al.* performed fluorescence spectroscopic and molecular dynamics investigations about the interactions between dyes and tryptophan where rhodamine 6G and an oxazine derivative were used as model dyes. The quenching distance was  $\sim 5.5 \text{ \AA}$  for both dyes, which is in the range of a van der Waals contact.[122]

## 1.9 Cytotoxicity assays

As mentioned in section 1.7.1, cytotoxicity assays provide information about the damage of cells under their exposition to certain substances. Materials designed for biomedical applications might be tested in different cell lines *in vitro* to confirm that their presence do not inhibit the cell growth or compromise biological components or functions, such as membrane integrity, enzyme activity and production, cell adherence, ATP production, nucleotide uptake activity, etc.[123] Membrane integrity is usually tested with propidium iodide[124] and Trypan blue[125] dyes, which cannot internalize into viable cells (*i.e.*, they only penetrate cells with a damaged membrane). Regarding metabolically active cells, the most common tests are redox assays using tetrazolium salts and resazurin dye; these compounds are initially colorless and become colored once they are reduced by nicotinamide adenine dinucleotides ( $\text{NAD}^+/\text{NADH}$ ) and their phosphorylated derivatives ( $\text{NADP}^+/\text{NADPH}$ ).

The reduction of 3-(4,5-dimethylthiazol-2-yl)-2,5-diphenyltetrazolium bromide (*i.e.*, MTT assay) to formazan has been extensively reported due to its low cost and practical advantages. In particular, the MTT assay yields an insoluble formazan (detected at 578 nm). Alternatively, tetrazolium salts, whose formazan derivatives are water-soluble compounds, have been also proposed. In this regard, some bacteria (or other microorganisms) lack the ability to reduce tetrazolim to formazan, whereas others become unviable in the presence of tetrazolim-based dyes. Resazurin trademarks are AlamarBlue<sup>TM</sup>, PrestoBlue, and UptiBlue, which are very sensitive in fluorescence spectroscopic methods. The reduction of resazurin to resorufin (change of color from blue to violet) can be correlated to oxygen consumption (see **Figure 1.9**), for this reason, anaerobic microorganisms might not be suitable for reducing resazurin.[126]

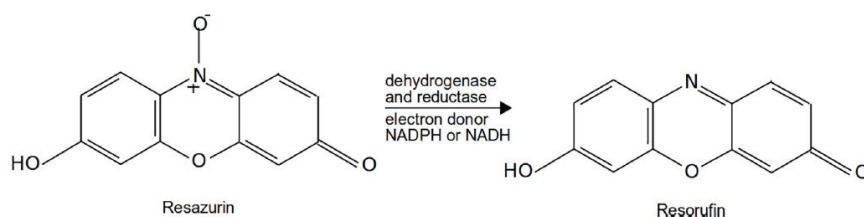


**Figure 1.9** Reduction of resazurin (AlamarBlue) to resorufin.[126]

Xu *et al.* compared PrestoBlue, AlamarBlue and MTT assays in human corneal epithelial cells and demonstrated that PrestoBlue and alamarBlue are more sensitive methods than MTT, which was ascribed to two reasons. The first aspect suggests that the reduction of the tetrazolium derivate is mainly performed by NADH, whereas PrestoBlue and AlamarBlue utilize more mitochondrial enzymes and electron acceptors. The second reason is associated with the methodology itself because the poor solubility of the formazan product in the MTT assays requires a dissolution in a suitable organic solvent prior the measurement; this additional step can increase the standard deviation of the experiment and negatively impact the sensitivity of the method.[127]

PrestoBlue and AlamarBlue were evaluated utilizing different organisms and cell lines, for example, *Streptococcus mutans*, *Prevotella intermedia* and *Mycobacterium tuberculosis*; a response (*i.e.*, a color change) was first detected in PrestoBlue and later on in Alamarblue.[128] On the contrary, in the evaluation of the metabolic activity of the *Acanthamoeba* pathogen, similar results were obtained for both compounds.[129] Although PrestoBlue is considered to have some advantages over the Alamarblue and MTT assays, such as shorter incubation times and higher sensitivity, the literature reports evidence that the performance of PrestoBlue depends on the type of microorganisms and cell lines utilized for the evaluations. In this research project PrestoBlue was selected to evaluate viability of epithelial cell lines.

### 1.10 Physicochemical properties of peptides and proteins

Various physicochemical properties of peptides and proteins can be calculated using their primary molecular structure as discussed in more detail next.

The structure, stability, solubility and function of proteins and peptides are influenced by the ionization state of the individual residues,[130] which also determines their net charge. For instance, the pH value where the net charge is zero is known as the isoelectric point (pI), which can be theoretically estimated from the pK values of each ionizable group; it

is useful to determine this parameter since the solubility of proteins decreases near their pI.[131]

Furthermore, the grand average of the hydropathicity index (GRAVY) can be estimated via the sum of the hydropathy values (from Kyte and Doolittle) of each amino acid divided by the total length of the peptide (n).[132] Positive and negative GRAVY values provide with an indication of the hydrophobic and hydrophilic nature of the protein/peptide, respectively.

The instability index (II) was introduced by Guruprasad *et al.*[133] in 1990 and is calculated according to equation 1.1. This statistical method considers the presence of certain dipeptides in the primary structure of peptides/proteins and associated with their instability (or stability) behavior.

$$\text{II} = (10/L) \sum_{i=1}^{L-1} \text{DIWV}(x_i y_{i+1}) \quad \text{Equation 1.1}$$

where DIWV is the dipeptide instability weight value,  $x_i y_{i+1}$  is the dipeptide, L is the length of the sequence and 10 provides with a scaling factor. Sequences with an II value > 40 are considered unstable, whereas stable sequences have an II value < 40.

On the other hand, the aliphatic index is defined as the relative volume occupied by the aliphatic side chains (alanine, valine, isoleucine, and leucine).[134] Globular proteins with a high value of aliphatic index are associated with a higher thermostability. The aliphatic index is calculated according to equation 1.2.

$$\text{Aliphatic Index} = x_A + ax_v + b(x_I + x_L) \quad \text{Equation 1.2}$$

Where  $x_A$ ,  $x_v$ ,  $x_I$ , and  $x_L$  are mol % of alanine, valine, isoleucine and leucine, respectively. The values of the coefficients  $a$  and  $b$  are  $2.1 \pm 0.1$  and  $3.9 \pm 0.1$ , respectively.

## **1.11 Hypothesis**

The functionalization of biocompatible amphiphilic block copolymers with peptides derived from the Hemagglutinin protein of the influenza A virus will increase the cell internalization capacity and viability of self-assembled nanoparticles prepared from such polymeric platforms, turning them into good drug carrier candidates for biomedical applications. The access to such advanced polymeric platforms can be achieved via a systematic design and controlled synthesis using the RAFT polymerization technique, which will enable the preparation of amphiphilic block copolymers derived from biocompatible monomers and bearing activated ester-based functionalities that will allow post-polymerization modifications (via amine groups) to covalently bind peptides derived from the Hemagglutinin protein onto the polymer chains. Thereafter, such well-defined macromolecular structures can self-assemble into nanoparticles in aqueous media and be further investigated as cell targeting nanocarriers for the development of new biomedical therapies.

## **1.12 Aim of this work**

Conjugation of biomolecules with polymers is a useful technique for providing these conventional materials with specific cell-targeting capabilities and/or enhancing their biocompatibility; such materials are potential candidates for use in nanomedicine.

To this end, a preliminary objective of this work was to determine the reactivity ratios of one of the selected, and less explored in nanomedicine, biocompatible monomers (*i.e.*, MMA) when copolymerized with other comonomers such as NHSMA, NIPAM and BuA. Consequently, the cytotoxicity of these obtained copolymers had also to be assessed to determine their biocompatibility and further use in the preparation of bioconjugated polymer materials.

Hence, the main objective of this research project was to synthesize and evaluate the conjugation of amphiphilic and biocompatible block copolymers with two peptides derived from the HA protein of the influenza A virus. Thereafter, and due to their amphiphilic nature, the self-assembly processes of such block copolymers and the

corresponding conjugates into nanostructures in aqueous media was investigated as a prerequisite for relevant and subsequent biological evaluations to prove our hypothesis and the functionality of the proposed materials (*i.e.*, cytotoxicological and cellular internalization effects due to the incorporation of peptides onto the chains of the prepared polymer materials).

## Chapter 2 Materials and characterization methods

### 2.1 Materials

4-cyano-4-(phenylcarbonothioylthio)pentanoic acid (CPAD, 97 % STREAM Chemicals), 4-cyano-4-[(dodecylsulfanylthiocarbonyl)sulfanyl]pentanoic acid (CDTPA, 97 % Boron Molecular), pentafluorophenol (PF, > 98.0 % TCI), 4-Dimethylaminopyridine (DMAP, > 99 % Sigma-Aldrich), *N,N'*-Diisopropylcarbodiimid (DIC, MERCK Germany), 4,4'-azobis(4-cyanopentanoic acid) (ACVA,  $\geq 98$  % Sigma-Aldrich), 1,1'-Azobis(cyclohexanecarbonitrile) (V88, 98 % Sigma Aldrich), Fluorescein O-methacrylate (FLUMA, 99 %, Sigma Aldrich), *N*-succinimidyl methacrylate (NHSMA,  $> 98$  %, TCI), triethylamine (TEA, 99.5 %, Sigma Aldrich), amino-2-propanol (93 %, Sigma-Aldrich), anisole (99 % Alfa Aesar), 1,4-dioxane (Alfa Aesar, anhydrous, 99.8%), dimethyl sulfoxide (DMSO, anhydrous,  $\geq 99.9$  % Sigma-Aldrich) and 1,3,5-trioxane ( $\geq 99$  % Aldrich) were used as received. Oligoethylene glycol methyl ether methacrylate (OEGMEMA  $M_n$  500  $\text{g mol}^{-1}$ , Sigma-Aldrich), butyl acrylate (BuA,  $\geq 99\%$  Sigma-Aldrich) and glycerol mono-methacrylate (GMMA, 95 %, Polysciences, Inc) were purified by stirring in the presence of inhibitor removers beads (for hydroquinone and monomethyl ether hydroquinone, Sigma Aldrich). Azobisisobutyronitrile (AIBN) was recrystallized from *n*-methanol whereas *N*-isopropylacrylamide (NIPAM,  $> 98$  % TCI) was recrystallized from *n*-hexane prior to use. *N,N*- dimethylformamide (DMF) and dichloromethane (DCM) were obtained from a solvent purification system (MB-SPS-800 by MBraun) and stored under argon. PC1-PC3, PC1-5FAM and PC3-5FAM were purchased from Pepmic Co. (China).

### 2.2 Characterization methods

Size exclusion chromatography (SEC) measurements of the (co)polymers were performed on an Agilent system, equipped with a G1329A Autosampler, a G1310A pump,

a G1362A refractive index detector and a PSS (Polymer Standards Service GmbH, Mainz, Germany) GRAM column with a solution of dimethylacetamide (DMAc) + 0.21 wt. % LiCl as an eluent at a flow rate of 1 mL min<sup>-1</sup> at 40 °C. The relative molar mass calculations were estimated against a poly(methyl methacrylate) (PMMA) as calibration curve built with standards of narrow dispersity ( $\mathcal{D}$ ).

Proton nuclear magnetic resonance (<sup>1</sup>H-NMR) spectroscopy was used to estimate the monomer conversion and the copolymer composition. The spectra were recorded at room temperature using a 300 MHz Bruker Avance I spectrometer equipped with a dual <sup>1</sup>H and <sup>13</sup>C probe head and a 120 × BACS automatic sample changer. DOSY and Fluorine nuclear magnetic resonance (<sup>19</sup>F NMR) were measured on a 400 MHz Bruker Avance III spectrometer with a BBFO probe head and a 60× SampleXpress automatic sample changer. The samples were measured in DMF-d<sub>7</sub>, DMSO-d<sub>6</sub> and CDCl<sub>3</sub> at room temperature.

The T<sub>cp</sub> of the aqueous polymer solutions were recorded using a Crystal 16<sup>®</sup> multiple-reactor system by Avantium Technologies with magnetic stirrer bars at 700 rpm and using a heating/cooling ramp of 1 °C min<sup>-1</sup>. The T<sub>CP</sub> of the solutions (10 mg mL<sup>-1</sup>) were recorded at a value of 50% transmittance. DSC investigations were performed on a Netzsch DSC 204 F1 Phoenix calorimeter under inert atmosphere using a heating/cooling rate of 20 °C min<sup>-1</sup> and a temperature range from -110 to 200 °C. TGA measurements were performed using a NETZSCH TG 209F1 Libra equipment with a heating rate of 20 °C min<sup>-1</sup> and a temperature range from 25 to 600 °C.

A Zetasizer Nano ZS from Malvern Instruments (Herrenberg, Germany) was used for dynamic light scattering (DLS) in UV-Vis cuvettes made of polystyrene (Brand). The DLS was operated with a He–Ne laser at a wavelength of  $\lambda = 633$  nm. The hydrodynamic diameter was approximated as the effective (z-average) diameter and the width of the distribution as the polydispersity index (PDI) of the NPs obtained by the cumulants method assuming a spherical particle model.

Cryo-TEM images were acquired on a FEI Tecnai G2 20 TEM. Samples were prepared on Quantifoil grids (Quantifoil R2/2), which were hydrophilized prior to use by a treatment with Ar plasma for 2 min. 8.5  $\mu$ L of the NP suspension were blotted onto the grid and plunged into liquid ethane, which served as the cryogen. The vitrification was performed with a Vitrobot Mark IV. After vitrification, the grids were transferred into the

cryo-holder (Gatan 626) utilizing a Gatan cryo transfer stage and were measured at an acceleration voltage of 200 kV. Samples were maintained at a temperature below  $-175\text{ }^{\circ}\text{C}$  for all steps after the vitrification process. Images were recorded with a CCD camera system (Olympus Soft Imaging Systems, Megaview G2,  $1376 \times 1024$  pixels).

A TECAN Infinite M200 Pro microplate reader was used for fluorescence measurements in cell lines and to prepare a standard peptide calibration.

## **Chapter 3. Glycerol methacrylate-based copolymers: Reactivity ratios, physicochemical characterization, and cytotoxicity**

### **3.1 Introduction**

Biocompatible (co)polymers based on PEG derivatives are usually considered as the “gold standard” for diverse biomedical applications. However, hypersensitivity in humans has been documented for these materials.[135–137] Hence, several polymers have been proposed as potential alternatives to PEG being PGMA, a very promising candidate. PGMA is a hydrophilic, biocompatible, and non-toxic polymer that has been utilized in diverse applications.[103] [104,105][110] [106] [107–109]

Polymers can be conjugated to different biofunctional molecules such as drugs, peptides or proteins following different synthetic strategies. One conjugation approach involves the copolymerization of a biocompatible monomer with a reactive comonomer, which can be later linked to the targeted biofunctional molecule. For instance, monomers containing NHS or PFP ester reactive groups are subjected to aminolysis reactions with functionalized primary or secondary amines to access the corresponding functionalized polymer derivatives.[40,41] NHS-based polymers are commonly soluble in DMF and DMSO, and are quite resistant to hydrolysis[138]. Additionally, the aforementioned post-polymerization conjugation strategies can be effectively performed under relatively mild reaction conditions. For instance, Lamm *et al.*, reported a statistical copolymer system based on MMA and the reactive comonomer NHSMA, which was employed in a fibrin-binding peptide conjugation.[112]



The composition of a copolymer is a crucial factor for diverse applications. As such, knowledge about the reactivity ratios of a specific copolymer system is fundamental as it can be used to predict or design the final composition of a certain material.[139,140] Experimental kinetic data along with linear and nonlinear mathematical methods are commonly employed for the determination of these kinetic parameters.[141]

Other interesting polymer materials, known as smart materials, can show a reversible change in their physical properties as a response to an external stimuli such as pH, temperature, light, etc. [142] For instance, thermoresponsive polymers can possess the so-called lower critical solution temperature (LCST), upper critical solution temperature (UCST) or both depending on the nature of its constituents. The LCST corresponds to the temperature at which a polymer monophasic system (*i.e.*, a solution) separates in two immiscible phases.[143] In this regard, poly(N-isopropylacrylamide) (PNIPAM) is a widely known thermoresponsive polymer, whose LCST can be modulated to match, for instance, the temperature of the human body. For example, statistical copolymers of NIPAM and GMMA have been post-functionalized to obtain copolymers featuring pH-responsive and degradability properties as well as low cytotoxicity.[108]

Armes *et al.*, determined of the reactivity ratios of the GMMA and pyrene methacrylate (PyMA) copolymerization system using RAFT-mediated copolymerization mechanism, where a pyrene-containing macro chain transfer agent (macro-CTA) was employed for the synthesis of pH-responsive block copolymers.[144] Inspired by this latter contribution, in the estimation of reactivity ratios and some physicochemical properties of the three GMMA-based copolymer systems depicted in **Scheme 3.1**, which encompass the functional comonomers: NIPAM (thermoresponsive), butyl methacrylate (BuA) (hydrophobic) and NHSMA (ester-reactive) were performed in this research work. The reactivity ratios were estimated from kinetic data obtained via high-throughput experimentation and applied to a non-linear mathematical model reported elsewhere.[141] Likewise, thermal analyses (*i.e.*, DSC for the determination of glass transition temperatures ( $T_g$ ) and TGA) and cytotoxicity studies of the obtained materials covering a broad copolymer composition range, as well as the determination of the cloud point temperature ( $T_{cp}$ ) via light transmittance measurements for aqueous solutions of the thermoresponsive GMMA/NIPAM copolymer system, are also reported.

### 3.2 Determination of reactivity ratios: using the terminal model

The composition of a copolymer constituted by two different monomers,  $M_1$  and  $M_2$ , at any instant during the copolymerization reaction can be calculated with the *copolymerization equation* (Equation 3.1) derived from the terminal model, which considers that the chemical reactivity of the propagating polymer chain (i.e, free radical, carbocation or carbanion) is only influenced by the last monomer unit incorporated into the respective polymer chain.[12]

$$\frac{d[M_1]}{d[M_2]} = \frac{[M_1](r_1[M_1] + [M_2])}{[M_2]([M_1] + r_2[M_2])} \text{ Equation 3.1}$$

where the  $d[M_1]/d[M_2]$  is the copolymer composition,  $[M_1]$  and  $[M_2]$  correspond to the concentration of the respective monomers in the feed, and  $r_1$  and  $r_2$  are the monomer reactivity ratios. The determination of the reactivity ratios  $r_1$  and  $r_2$  involves the rate constant of the different chain propagation reactions occurring during the copolymerization,  $k_{11}$ ,  $k_{12}$ ,  $k_{22}$ ,  $k_{21}$  (Equation 3.2).

$$r_1 = \frac{k_{11}}{k_{12}} \quad \text{and} \quad r_2 = \frac{k_{22}}{k_{21}} \text{ Equation 3.2}$$

Hence, the values of  $r_1$  and  $r_2$  provide information about how the monomer units are incorporated into the formed polymer chains (i.e., copolymer composition). For example, when  $r_1 \cdot r_2 \approx 1$  the copolymerization system is referred as "*ideal*", which means that the propagating polymer chains have the same preference to add either of the two monomers. Instead, alternating copolymers are distinguished by  $r_1 \cdot r_2 \approx 0$ . If one of the two monomers has a reactivity ratio value greater than 1 and that of the other monomer is less than 1, the formed copolymer chains are abundant in the monomer with  $r > 1$  at the initial stage of the copolymerization reaction as the monomer with  $r < 1$  prefers cross-propagation but the one with  $r > 1$  has tendency to homopropagation.[12]

For the determination of reactivity ratios in copolymerization systems, there are available different linear and non-linear methods. [145] The Mayo-Lewis equation is one of the most popular mathematical expressions to estimate the values of  $r_1$  and  $r_2$ , which can be solved using, for instance, a nonlinear least squares regression [146] and experimental data of the mole fraction value of each monomer contained in the copolymer chains ( $F_1$  and  $F_2$ ) and mole fraction value of each monomer in the copolymerization reaction feed ( $f_1$  and  $f_2$ ) as is showed in the Equation 3.3.

$$F_1 = \frac{r_1 f_1^2 + f_1 f_2}{r_1 f_1^2 + 2 f_1 f_2 + r_2 f_2^2} \text{ Equation 3.3}$$

In this research work, the terminal model as used in the Mayo-Lewis equation was utilized to estimate the reactivity ratios values of the copolymerization of GMMA with three different monomers (*i.e.*, NHSMA, NIPAM and BuA).

### 3.3 Experimentation

#### 3.3.1 General procedure for the synthesis of GMMA copolymers

Copolymerization reactions were performed in a commercially available automated parallel synthesizer (ASW-2000) from Chemspeed Technologies (Switzerland). The synthesizer was equipped with a reactor block consisting of 16 glass reaction vessels (13 mL) with thermal jackets connected in series to a heating/cooling system (Huber, from -20 to 140 °C), and a vortex mixer (up to 1400 rpm). Additionally, each reaction vessel was equipped with a cold-finger reflux condenser (5 °C). An automated liquid handling system composed of a needle head (NH) was used for dispensing reagents and sampling into/from the reactor vessels. The NH was connected to a solvent reservoir bottle for needle rinsing after each liquid transfer. Before each experiment, a nitrogen atmosphere was applied to stock solutions and reaction vessels to deplete moisture and oxygen, according to previous procedures reported elsewhere.[147] After this pre-treatment, RAFT polymerizations were performed according to the procedures described next.

The use and advantages of automated parallel synthesizers and/or high-throughput / high-output experimental techniques for performing kinetic investigations and determination of reactivity ratios in (co)polymerization reactions has been well-documented in the last two decades.[43,148–151] In general, these experimental approaches offer cost-effective methods for screening of reaction parameters and preparing (co)polymer libraries with systematic variations of properties (*e.g.*, molar mass, composition, functionality, architecture and others) for different applications.[151–155]

A series of GMMA-based copolymers with different comonomers and compositions were obtained using the following experimental conditions. Using previously prepared stock solutions and the automated liquid handling of the system, a total monomer concentration was adjusted to 1 M per reaction and the ratio of [monomer]:[RAFT agent]:[initiator] to [50]:[1]:[0.1]. Because of solubility and reactivity of a RAFT agent mainly depend on the R and Z groups (see **Sections 1.4** and **1.6.3** for more details), different RAFT agents are

more suitable for specific types of monomers as widely discussed elsewhere.[10,156,157] In general, CPAD is a suitable RAFT agent to polymerize methacrylate- and methacrylamide-based monomers, but it is less effective for the polymerization of acrylate- and acrylamide-based monomers; for the latter, a better selection would be CDTPA.[157] Thus, in this contribution, the utilized RAFT agent for the NHSMA copolymer system was CPAD, whereas for the NIPAM and BuA copolymerizations was CDTPA. The reaction mixtures were degassed by sparging N<sub>2</sub> gas for 20 min. Subsequently, the reactor block was sealed under a N<sub>2</sub> atmosphere and heated to 70 °C. The onset of the polymerization was considered once the reaction temperature was reached. Each reaction was periodically monitored by sampling aliquots from the reactors (0.2 mL) under an inert N<sub>2</sub> flow.  $f_n$  and monomer conversion were determined by means of <sup>1</sup>H-NMR in deuterated DMSO-*d*<sub>6</sub>; the signal range selected for the determination of NIPAM conversion was  $\delta = 5.49\text{-}5.59$  ppm, for BuA  $\delta = 5.87\text{-}5.97$  ppm and for NHSMA  $\delta = 6.31\text{-}6.37$  ppm. As an internal standard, 1,3,5-trioxane (5.12 ppm) was used for the NHSMA copolymerization and anisole (6.93 ppm) for the NIPAM and BuA copolymer systems; both references are inert and stable under the utilized reaction conditions. Likewise,  $F_n$  was determined by <sup>1</sup>H-NMR in DMSO-*d*<sub>6</sub>, DMF-*d*<sub>7</sub> or MeOD-*d*<sub>4</sub> through the signal integration shown in **Figures 3.1-3.3**. The  $f_n$  and  $F_n$  values of the investigated systems are summarized Table 2.1. Note that there is an overlapping of signals in the <sup>1</sup>H-NMR spectra of the GMMA / NHSMA copolymer system (**Figure 3.1**) that may turn the integration of the corresponding signals more challenging for quantification purposes of the final copolymer composition. To support the “reliability” of this utilized quantification method for the specific case of the P(GMMA-*stat*-NHSMA) copolymer system, a selected <sup>13</sup>C-NMR experiment was additionally performed (not shown) with the so-called Inverse-Gated Decoupling (IGD) technique, which is suitable for quantification purposes of polymer materials.[158] Nonetheless, these measurements are experimentally more demanding (as compared to “conventional” <sup>1</sup>H-NMR measurements) because they require several hours to obtain sufficient signal-to-noise that allows for the integration of spectra.[158] Hence, in this investigation, the quantified <sup>13</sup>C-NMR measurement performed with the IGD technique was compared to a “conventional” <sup>1</sup>H-NMR measurement of the same copolymer sample. The copolymer composition results obtained from these two measurements were very comparable to each other (See **Fig. 3.1B**), which supports to the “reliability” of the utilized and less demanding <sup>1</sup>H-NMR analysis method. However, and because of this overlapping of signals, these results must

be taken with care and other technique may be additionally considered for this purpose, such as elemental analysis via nitrogen quantification (not performed).

The signals of vinylic protons of GMMA at 5.71-5.63 ppm include their two overlapping isomers,[99,159] 2,3-dihydroxypropyl methacrylate and 1,3-dihydroxypropyl methacrylate. The commercial GMMA employed in this investigation contains 78 mol % of 2,3-dihydroxypropyl methacrylate and 22 mol % of 1,3-dihydroxypropyl methacrylate estimated by <sup>1</sup>H-NMR.

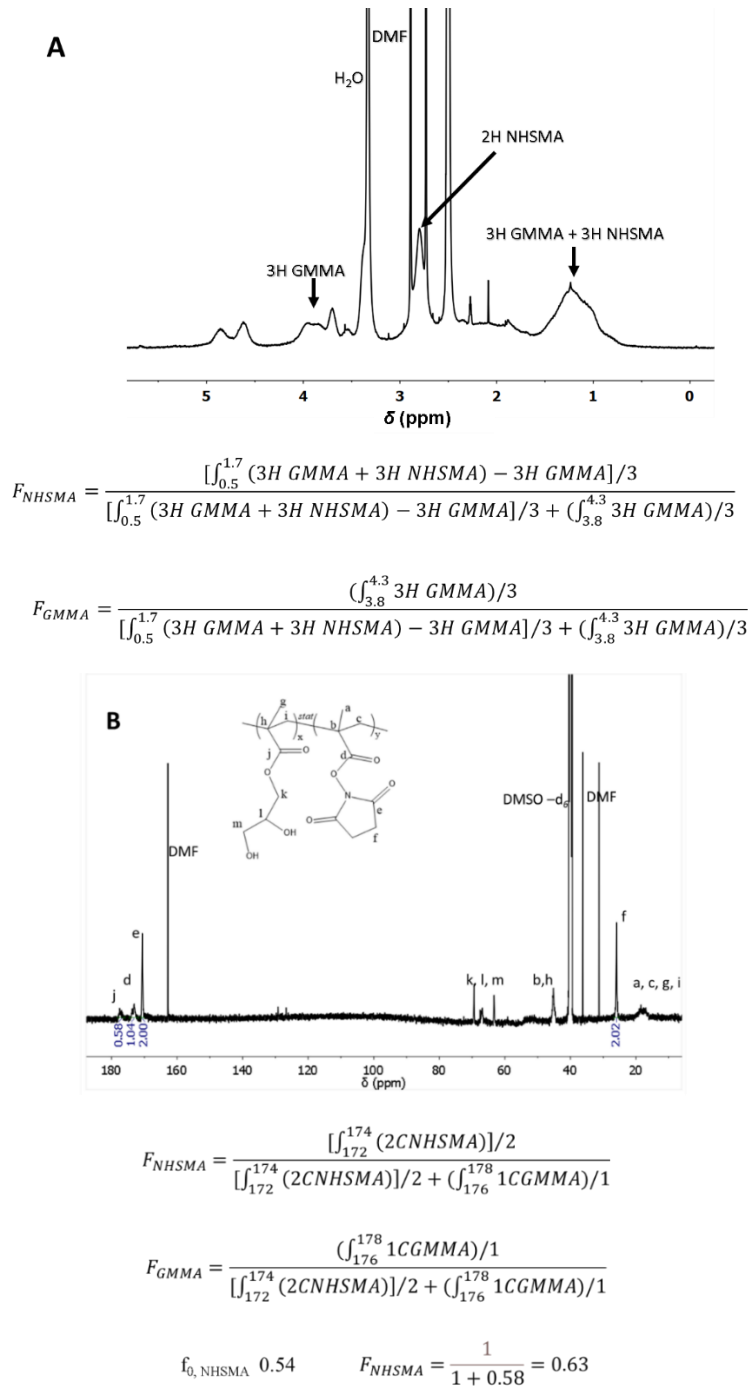
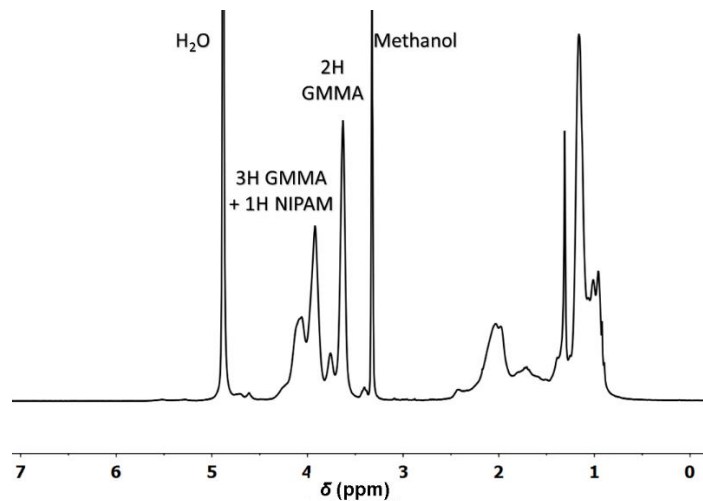


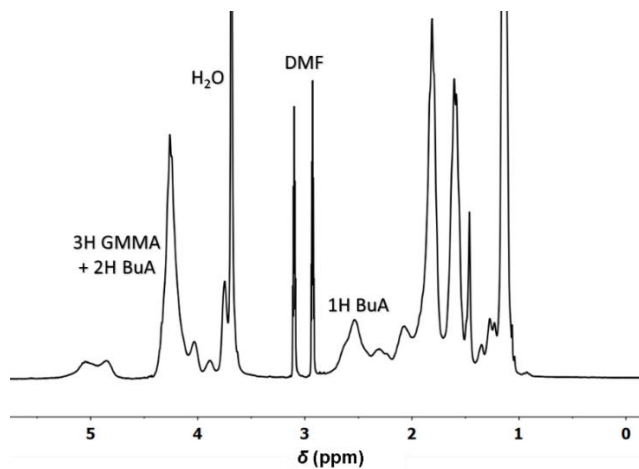
**Figure 3.1.** NMR spectrum of purified copolymer A1 and A2. A.  $^1\text{H}$ -NMR spectrum of purified copolymer A1 (Table 3.1) in  $\text{DMSO-}d_6$  (top), and equation for estimation of cumulative copolymer composition (bottom). B. Quantitative  $^{13}\text{C}$  spectrum (Inverse-Gated Decoupling) of purified copolymer A2 (Table 3.1) in  $\text{DMSO-}d_6$  (top), and equation for estimation of cumulative copolymer composition (bottom).



$$F_{NIPAM} = \frac{[\int_{3.8}^{4.4} (3H\ GMMA + 1H\ NIPAM) - 3H\ GMMA]/1}{[\int_{3.8}^{4.4} (3H\ GMMA + 1H\ NIPAM) - 3H\ GMMA]/1 + (\int_{3.5}^{3.7} 2H\ GMMA)/2}$$

$$F_{GMMA} = \frac{(\int_{3.5}^{3.7} 2H\ GMMA)/2}{[\int_{3.8}^{4.4} (3H\ GMMA + 1H\ NIPAM) - 3H\ GMMA]/1 + (\int_{3.5}^{3.7} 2H\ GMMA)/2}$$

**Figure 3.2** <sup>1</sup>H-NMR spectrum of B1 purified copolymer in MeOD-*d*<sub>4</sub> (top), and their equation for estimation of cumulative copolymer composition (bottom).



$$F_{BuA} = \frac{\int_{2.4}^{2.8} (1H\ BuA)}{[\int_{3.8}^{4.5} (3H\ GMMA + 2H\ BuA) - 2 \int_{2.4}^{2.8} (1H\ BuA)]/3 + \int_{2.4}^{2.8} (1H\ BuA)}$$

$$F_{GMMA} = \frac{[\int_{3.8}^{4.5} (3H\ GMMA + 2H\ BuA) - 2 \int_{2.4}^{2.8} (1H\ BuA)]/3}{[\int_{3.8}^{4.5} (3H\ GMMA + 2H\ BuA) - 2 \int_{2.4}^{2.8} (1H\ BuA)]/3 + \int_{2.4}^{2.8} (1H\ BuA)}$$

**Figure 3.3** <sup>1</sup>H-NMR spectrum of C4 purified copolymer in DMF-*d*<sub>7</sub> (bottom), and their equation for estimation of cumulative copolymer composition (top).

### 3.3.2 Synthesis of PNIPAM homopolymer (B6)

NIPAM (2 g, 17.7 mmol) was polymerized in 7 mL of 1,4-dioxane in the presence of CDTPA (71.3 mg, 177  $\mu\text{mol}$ ) as CTA, ACVA (4.9 mg, 17.7  $\mu\text{mol}$ ) as initiator (NIPAM:CTA:ACVA = 100:1:0.1 mole ratio) and anisole (80  $\mu\text{L}$ , 733  $\mu\text{mol}$ ) as an internal standard for  $^1\text{H-NMR}$  measurements. This solution was degassed for 30 min by sparging  $\text{N}_2$  gas and subsequently placed in a preheated oil bath at 70  $^\circ\text{C}$ . The reaction run for 4 h and thereafter was quenched by cooling in an ice bath. The polymer was isolated by precipitation in cold diethyl ether ( $\times 4$ ) and dried under vacuum at 40  $^\circ\text{C}$  for 48 h. The obtained monomer conversion was 93 % as calculated via  $^1\text{H-NMR}$ ; size exclusion chromatography (SEC) revealed a number average molar mass ( $M_{n,SEC}$ ) = 21000  $\text{g mol}^{-1}$  and a  $D$  value = 1.09.

### 3.3.3 Cell viability assay on L929 cell line

Fibroblasts cell culture. L929 cells were cultivated in Dulbecco's modified eagle's medium with 10 % fetal bovine serum (Capricorn, Germany) and 1% Penicillin / Streptomycin (Gibco; Germany) The cells were maintained under conditions of 5%  $\text{CO}_2$  at 37  $^\circ\text{C}$ .

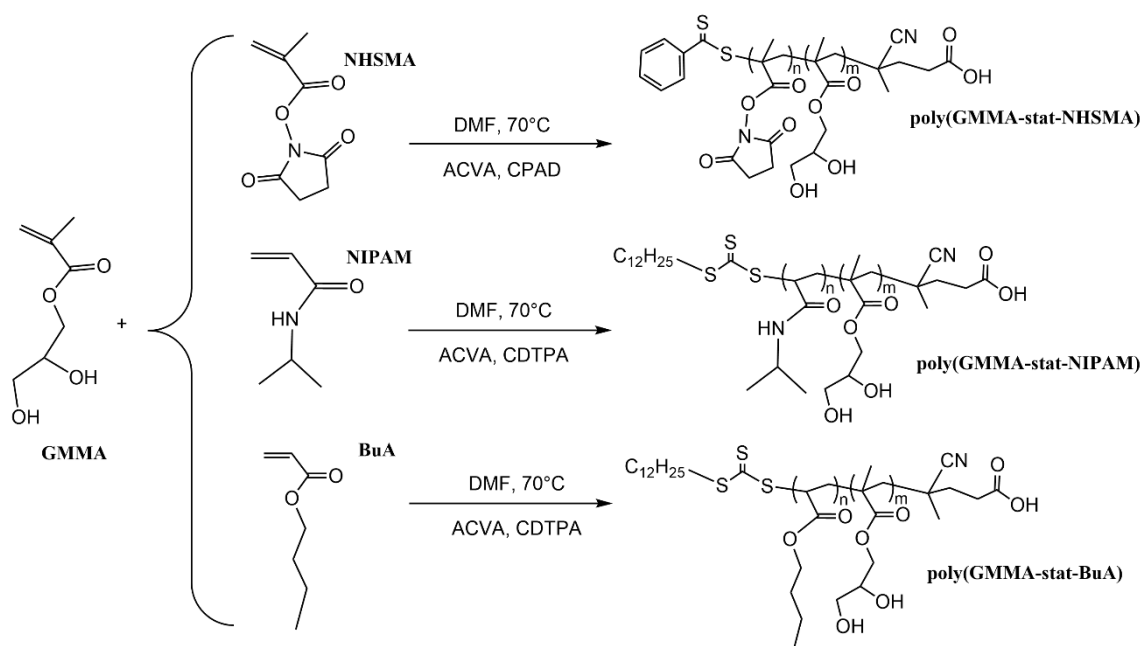
Evaluation of cytotoxicity. Cytotoxicity was evaluated using L929 mouse fibroblast cell line (CCL-1, ATCC) based on the standard ISO10993-5. The cells were sampled at a density of 105 cells  $\text{mL}^{-1}$  in 96-well plates and grown for 24 h. No cells were seeded in outer wells. After 24 h, several concentrations of each polymer sample (in the range from 0 to 200  $\mu\text{g mL}^{-1}$ ) were prepared in Dulbecco's modified eagle's medium with 10 % fetal bovine serum (Capricorn, Germany) and 1% Penicillin / Streptomycin (Gibco; Germany) media and 100  $\mu\text{L}$  of each dilution were added into different wells containing cells. Control cells were incubated with fresh culture media. In addition, as the analyzed samples were dissolved in DMSO solutions, we also included DMSO as a control to demonstrate that the utilized DMSO amounts does not have any effect on the evaluated cytotoxicity. After further 24 h of incubation time, the media was changed to PrestoBlue and mixed with culture media according to the manufacturers' description (Invitrogen, Germany). After 45 min with PrestoBlue, fluorescence was measured at the wavelengths of Ex 560/ Em 590 nm. Samples with cell viability values higher than 80 % were considered non-cytotoxic. All these experiments were performed in triplicate.



## 3.4 Results and discussion

### 3.4.1 Synthesis of GMMA-based statistical copolymers via RAFT polymerization.

NHSMA, NIPAM, and BuA comonomers were independently copolymerized in the presence of GMMA using an automated parallel synthesizer and the RAFT polymerization technique (**Scheme 3.1**). The obtained results for monomer conversion, initial comonomer composition ( $f_n$ ) and final copolymer composition ( $F_n$ ) are summarized in **Tables 3.1-3.4**.  $^1\text{H-NMR}$  spectra of final copolymers and the utilized procedures for determined copolymer composition for each system are shown in **Figures 3.1-3.3**. The polymerization of GMMA has been reported in methanol, ethanol or water; however, in this research, these solvents were discarded due to their low miscibility with the utilized comonomers. Thus, DMF was selected as the polymerization media for all 3 investigated copolymer systems.



**Scheme 3.1** Schematic representation of GMMA-based copolymers and their synthesis via RAFT copolymerization using 4-cyano-4-(phenylcarbonothioylthio)pentanoic acid (CPAD) and 4-cyano-4-[(dodecylsulfanylthiocarbonyl)sulfanyl]pentanoic acid (CDTPA) RAFT agents, and 4,4'-azobis(4-cyanopentanoic acid) (ACVA) as a thermal radical initiator.

**Table 3.1.**  $f_n$  and estimated  $F_n$  for GMMA-based copolymerizations obtained by  $^1\text{H-NMR}$ .

Entry	$[f_{\text{GMMA}}] :$ $[f_{\text{NHSMA}}]$	$[F_{\text{GMMA}}] :$ $[F_{\text{NHSMA}}]$	Entry	$[f_{\text{GMMA}}] :$ $[f_{\text{NIPAM}}]$	$[F_{\text{GMMA}}] :$ $[F_{\text{NIPAM}}]$	Entry	$[f_{\text{GMMA}}] :$ $[f_{\text{BuA}}]$	$[F_{\text{GMMA}}] :$ $[F_{\text{BuA}}]$
<b>A1</b>	71 : 29	54 : 46	<b>B0</b>	100 : 0	100 : 0	<b>C1</b>	80 : 20	84 : 16
<b>A2</b>	46 : 54	38 : 62	<b>B1</b>	84 : 16	87 : 13	<b>C2</b>	62 : 38	73 : 27
<b>A3</b>	26 : 74	24 : 76	<b>B2</b>	65 : 35	73 : 27	<b>C3</b>	39 : 61	45 : 55
<b>A4</b>	13 : 87	12 : 88	<b>B3</b>	44 : 56	50 : 50	<b>C4</b>	19 : 81	21 : 79
<b>A5</b>	0 : 100	0 : 100	<b>B4</b>	22 : 78	26 : 74	<b>C5</b>	09 : 81	10 : 90
			<b>B5</b>	11 : 89	13 : 87	<b>C6</b>	0 : 100	0 : 100
			<b>B6</b>	0 : 100	0 : 100			

**Table 3.2.** Summary of the reaction conditions of GMMA and NHSMA copolymerization in DMF.

Entry	$f_{\text{GMMA}}^{\text{a}}$	$f_{\text{NHSMA}}^{\text{a}}$	$F_{\text{GMMA}}^{\text{a}}$	$F_{\text{NHSMA}}^{\text{a}}$	Overall Conv. <sup>b</sup> [%]	$M_{n,\text{theo}}^{\text{c}}$ [kg mol <sup>-1</sup> ]	$M_{n,\text{SEC}}^{\text{d}}$ [kg mol <sup>-1</sup> ]	$\bar{D}^{\text{d}}$	$T_{\text{g,DSC}}^{\text{e}}$ (°C)	$T_{\text{d,TGA}}^{\text{e}}$ (°C)
<b>A1</b>	0.71	0.29	0.54	0.46	21	2.2	11.15	1.17	IS	IS
<b>A2</b>	0.46	0.54	0.38	0.62	29	3.1	13.12	1.28	124.0	208
<b>A3</b>	0.26	0.74	0.24	0.76	40	4.1	15.57	1.38	146.3	231
<b>A4</b>	0.13	0.87	0.12	0.88	52	5.4	18.05	1.47	157.8	230
<b>A5</b>	0	1	0	1	56	5.8	20.05	1.65	158.6	200

For the copolymerization of GMMA/NHSMA (A1-A4) the ratio of [monomer]:[RAFT agent]:[initiator] correspond to [50]:[1]:[0.1] carried out at 70°C and 1M. <sup>a</sup> initial monomer mol feed ratio of GMMA with respect to NHSMA determined by  $^1\text{H-NMR}$  <sup>b</sup> calculated by  $^1\text{H-NMR}$ ; <sup>c</sup>determined from  $M_{n,\text{theo.}} = ([\text{Monomer}]_0 / [\text{CTA}]_0 \times \text{Conv.} \times M_M) + M_{\text{CTA}}$ ; <sup>d</sup> determined by SEC, eluent DMAc + 0.21 wt% LiCl, RI detection, calibrated against PMMA standards <sup>e</sup> Decomposition temperature ( $T_d$ ) at 5% weight loss. IS: Insufficient sample for measurement.

**Table 3.3.** Summary of the reaction conditions of GMMA and NIPAM copolymerization in DMF.

Entry	$f_{\text{GMMA}}^{\text{a}}$	$f_{\text{NIPAM}}^{\text{a}}$	$F_{\text{GMMA}}^{\text{a}}$	$F_{\text{NIPAM}}^{\text{a}}$	Overall Conv. <sup>b</sup> [%]	$M_{n,\text{theo}}^{\text{c}}$ [kg mol <sup>-1</sup> ]	$M_{n,\text{SEC}}^{\text{d}}$ [kg mol <sup>-1</sup> ]	$\bar{D}^{\text{d}}$	$T_{\text{g,DSC}}^{\text{e}}$ (°C)	$T_{\text{d,TGA}}^{\text{e}}$ (°C)
<b>B0</b>	1	0	1	0	99	8.4	22.1	1.54	107.7	199
<b>B1</b>	0.84	0.16	0.87	0.13	94	8.1	19.9	1.30	109	279
<b>B2</b>	0.65	0.35	0.73	0.27	92	7.1	17.5	1.23	112.5	267
<b>B3</b>	0.44	0.78	0.50	0.50	89	6.5	15.0	1.16	114.7	257
<b>B4</b>	0.22	0.78	0.26	0.74	87	5.9	12.4	1.12	117.3	256
<b>B5</b>	0.11	0.89	0.13	0.87	87	5.5	10.4	1.16	121.3	249
<b>B6</b>	0	1	0	1	93	10.9	21.0	1.09	132.1	246

For the copolymerization of GMMA/NIPAM (B1-B5) the ratio of [monomer]:[RAFT agent]:[initiator] correspond to [50]:[1]:[0.1] carried out at 70°C and 1M. <sup>a</sup> initial monomer mol feed ratio of GMMA with respect to NIPAM determined by  $^1\text{H-NMR}$  <sup>b</sup> calculated by  $^1\text{H-NMR}$ ; <sup>c</sup>determined from  $M_{n,\text{theo.}} = ([\text{Monomer}]_0 / [\text{CTA}]_0 \times \text{Conv.} \times M_M) + M_{\text{CTA}}$ ; <sup>d</sup> determined by SEC, eluent DMAc + 0.21 % LiCl, RI detection, calibrated against PMMA standards <sup>e</sup> Decomposition temperature ( $T_d$ ) at 5% weight loss.

**Table 3.4.** Summary of the reaction conditions of GMMA and BuA copolymerization in DMF.

Entry	$f_{\text{GMMA}}^{\text{a}}$	$F_{\text{BuA}}^{\text{a}}$	$F_{\text{GMMA}}^{\text{a}}$	$F_{\text{BuA}}^{\text{a}}$	Overall Conv. <sup>b</sup> [%]	$M_{n,\text{theo}}^{\text{c}}$ [kg mol <sup>-1</sup> ]	$M_{n,\text{SEC}}^{\text{d}}$ [kg mol <sup>-1</sup> ]	$\bar{D}^{\text{d}}$	$T_{\text{g,DSC}}^{\text{e}}$ (°C)	$T_{\text{d,TGA}}^{\text{e}}$ (°C)
<b>C1</b>	0.8	0.2	0.84	0.16	92	7.6	18.0	1.27	71.1	275
<b>C2</b>	0.62	0.35	0.73	0.27	92	7.2	16.7	1.21	54.0	300
<b>C3</b>	0.39	0.78	0.45	0.55	94	7.1	13.5	1.20	-2.9	297
<b>C4</b>	0.19	0.81	0.21	0.79	88	6.4	10.8	1.19	-24.8	297

<b>C5</b>	0.9	0.91	0.1	0.9	87	6.1	8.7	1.20	-38.4	295
<b>C6</b>	0	1	1	0	1	5.9	5.7	1.18	-52.4	298

For the copolymerization of GMMA/BuA (C1-C5) the ratio of [monomer]:[RAFT agent]:[initiator] correspond to [50]:[1]:[0.1] carried out at 70°C and 1M, f is the composition initial, and F is composition final. <sup>a)</sup> initial monomer mol feed ratio of GMMA with respect to BuA determined by <sup>1</sup>H-NMR <sup>b)</sup> calculated by <sup>1</sup>H-NMR; <sup>c)</sup> determined from  $M_{n,theo} = ([Monomer]_0/[CTA]_0 \times Conv. \times M_M) + M_{CTA}$ ; <sup>d)</sup> determined by SEC, eluent DMAc + 0.21 % LiCl, RI detection, calibrated against PMMA standards <sup>e)</sup> decomposition temperature (T<sub>d</sub>) at 5% weight loss.

The kinetic investigations of the copolymerization of GMMA and NHSMA revealed that NHSMA was consumed faster than GMMA (**Figure 3.4**). In agreement with Lamm *et al.*, the preparation of P(NHSMA-*stat*-GMMA) with a NHSMA content of 20 mol % in dimethylacetamide (DMAc) as reaction solvent showed a similar kinetic behavior to that observed in this research.[112] In contrast, the incorporation of GMMA was faster than the NIPAM and BuA comonomers in the corresponding copolymerization systems (**Figures 3.5 and 3.6**). This suggests that the GMMA content in the formed copolymers is higher at the beginning of the copolymerization reactions and decreases as the reaction progresses. These observations are in agreement with predicted monomer fractions as a function of monomer conversion as discussed in more detail next.

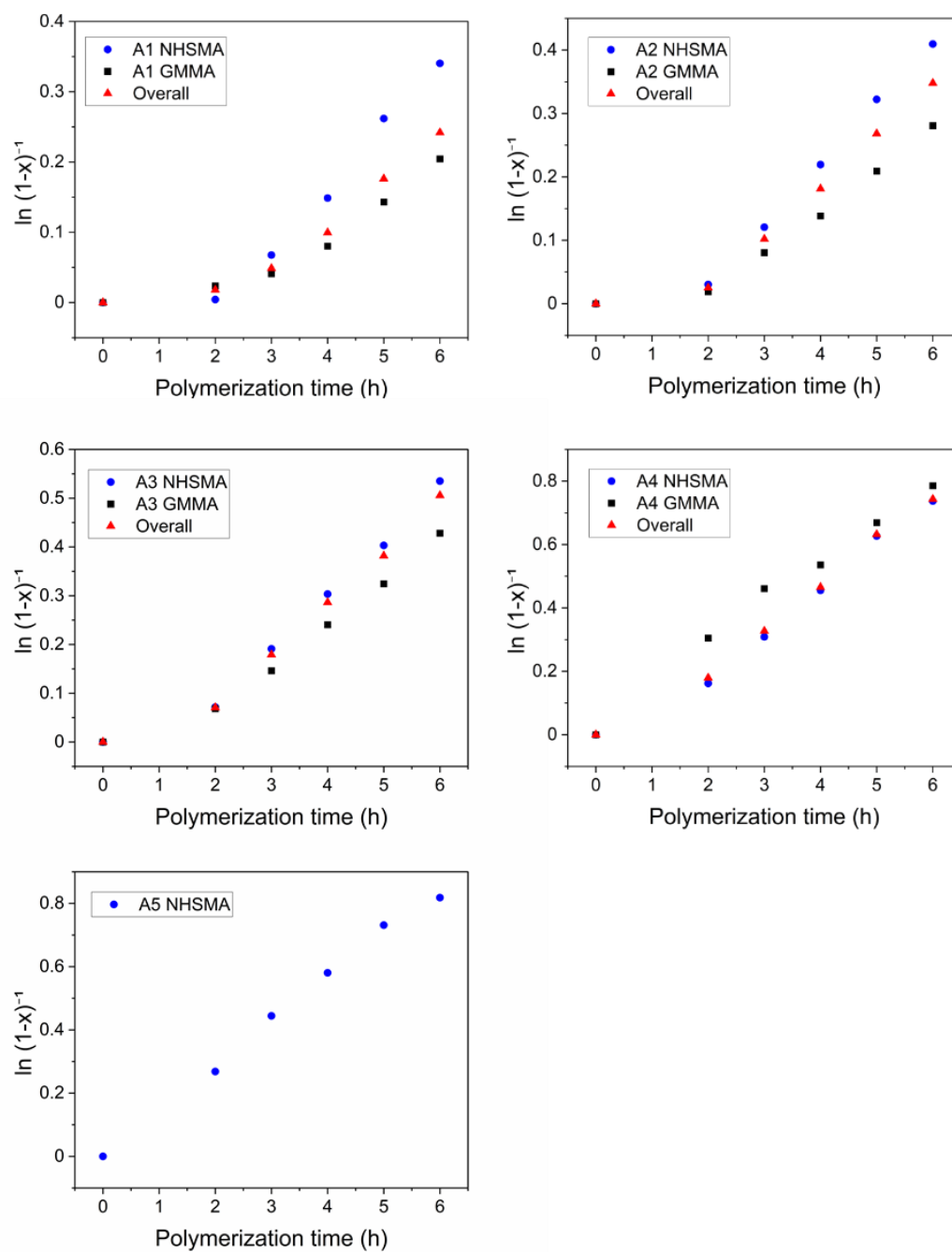


**Figure 3.4** Semi-logarithmic kinetic plots for **A1-A5**. Monomer conversions were calculated from  $^1\text{H}$ -NMR spectra.

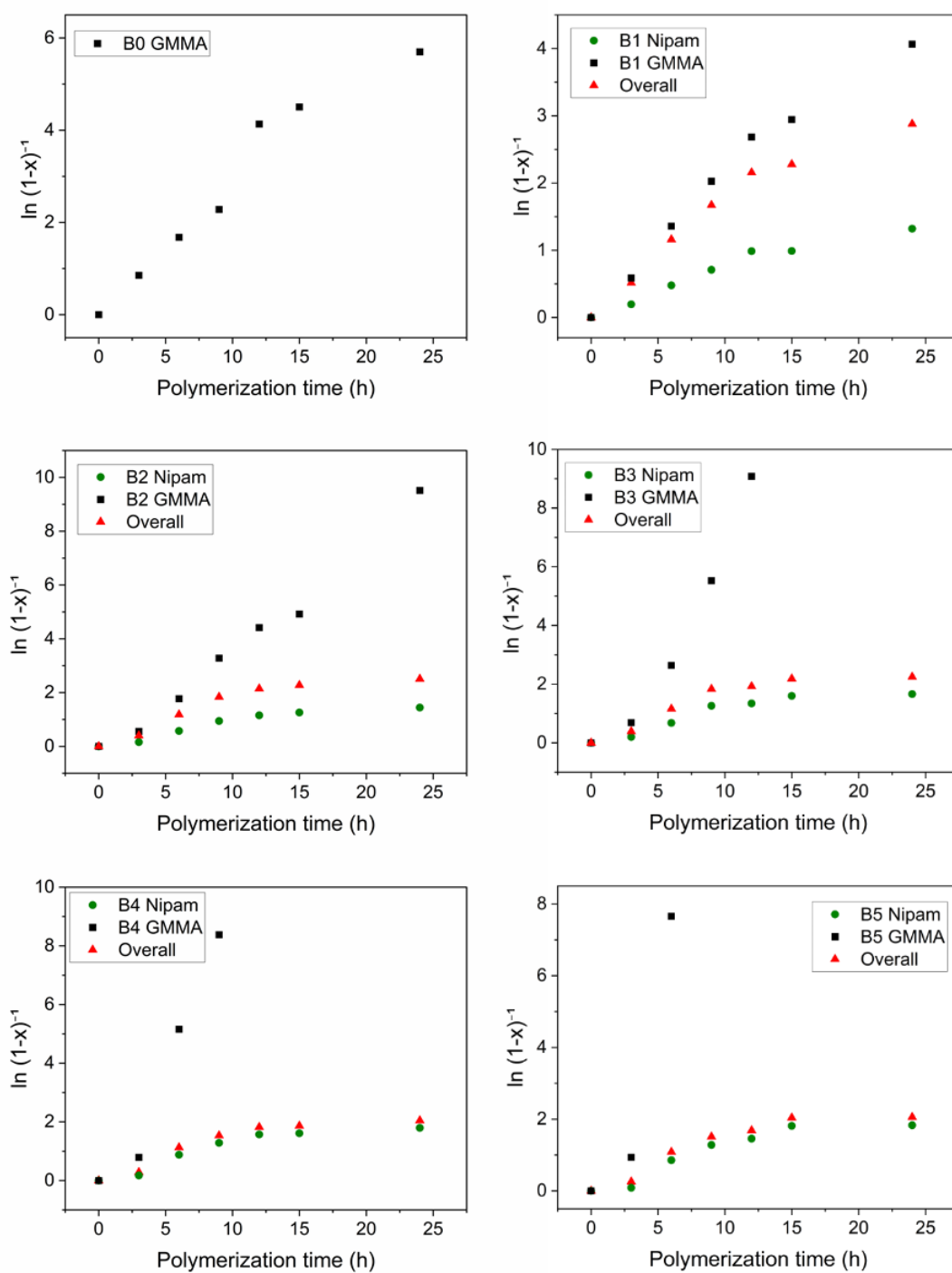


**Figure 3.5** Semi-logarithmic kinetic plots for **B0-B5**. Monomer conversions were calculated from  $^1\text{H-NMR}$  spectra.

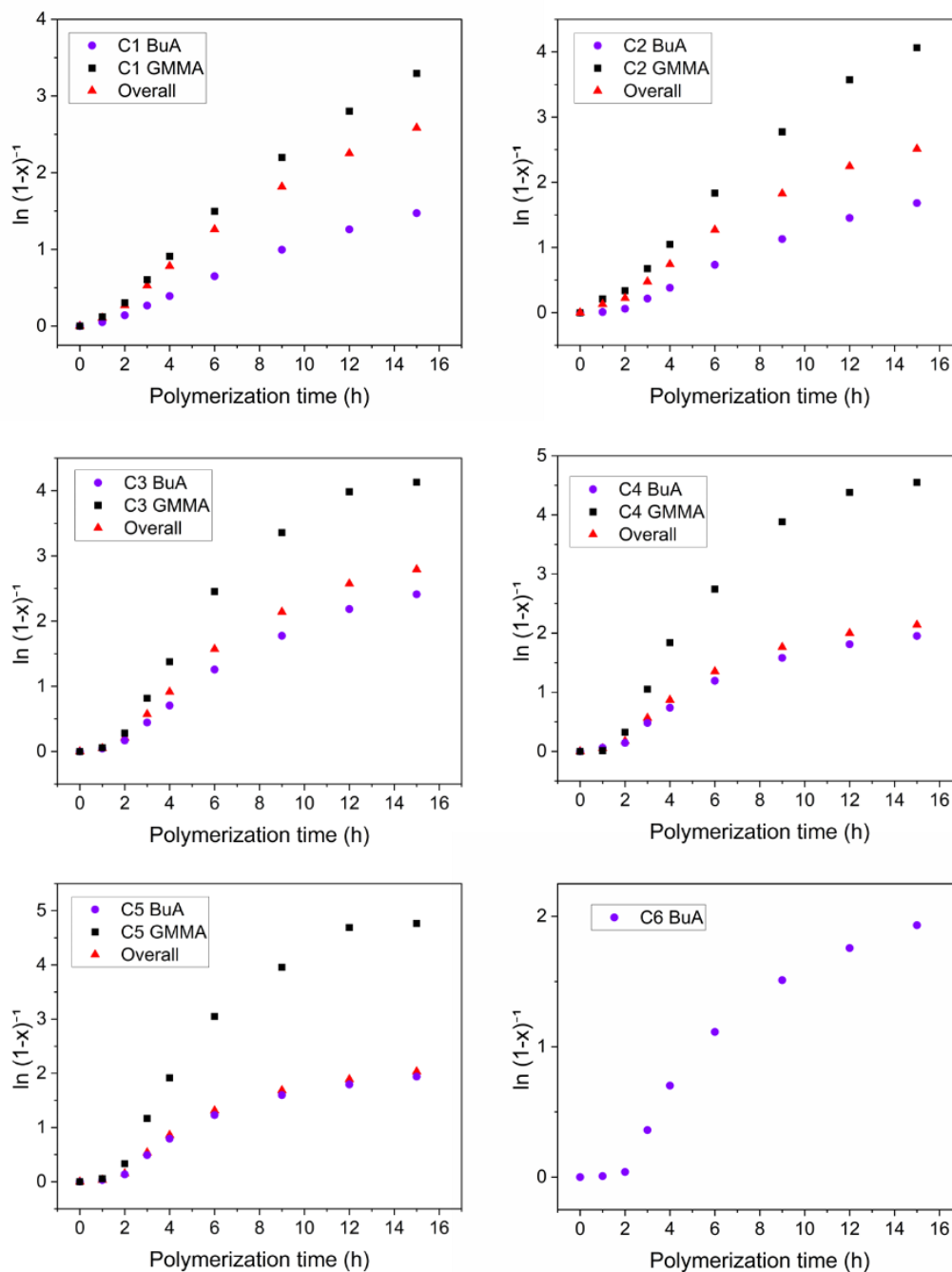


**Figure 3.6** Semi-logarithmic kinetic plots for **C1-C6**. Monomer conversions were calculated from  $^1\text{H-NMR}$  spectra.

$M_n$  and  $\mathcal{D}$  values of PGMMA homopolymer (sample B0 in **Table 3.1**) were determined by SEC. A linear increase of  $M_n$  vs. *monomer conversion* was observed suggesting a limited control over the polymerization reaction (sample B0, **Figure 3.7**); the overlaid SEC chromatograms corresponding to this polymerization series only revealed a slight displacement towards higher  $M_n$  values as a function of polymerization time (sample B0, **Figure 3.9**). Moreover, significant differences between the theoretical ( $M_{n, \text{theo}}$ ) and the

experimental ( $M_{n,SEC}$ ) molar masses were observed (**Table 3.3**), which can be ascribed to differences in hydrodynamic volume between the polymer chains of PGMMA and PMMA standards utilized for the SEC calibration.

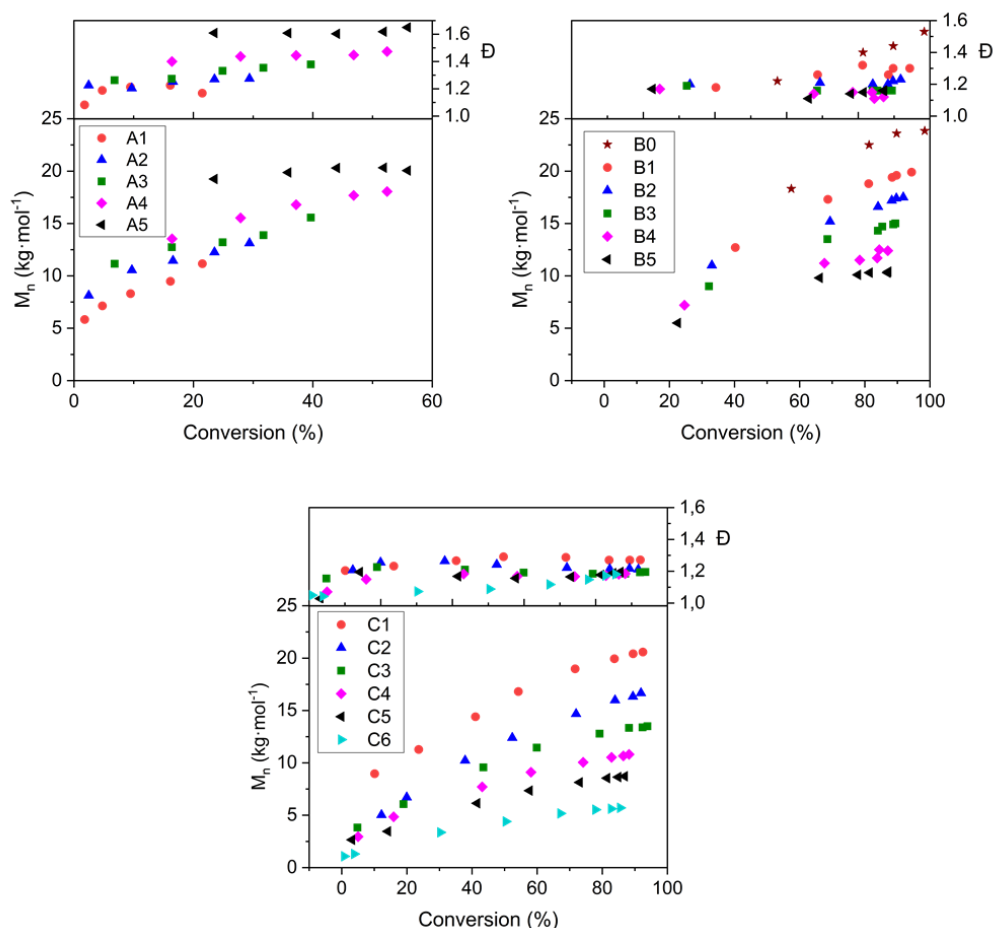


**Figure 3.7** Evolution of molar mass and dispersities, estimated by SEC, as a function of the overall monomer conversion of A1-A5, B0-B5 and C1-C6.

NHSMA can be homo- and co-polymerized in DMF and DMSO using reversible deactivation radical polymerization techniques.[160] Schilli *et al.*, described the RAFT polymerization of NHSMA in DMF using different CTA's where polymers with a broad dispersity ( $\bar{D} \leq 2.34$ ) were obtained when using high CTA concentrations. In addition, considerable differences between the target and experimental molar masses have been reported for this polymerization system.[161] These results already suggest that only a limited control over the homopolymerization of NHSMA could be achieved under those reported experimental conditions. In contrast, other studies describing the preparation of NHSMA-based copolymers have reported materials with lower  $\bar{D}$  values, in particular for low NHSMA contents, denoting that the addition of NHSMA as a comonomer has a

significant influence on the copolymer chain growth during the RAFT process.[162–164] In agreement with Schilli *et al.*, poly(N-hydroxysuccinimide methacrylate) (PNHSMA) obtained homopolymer (sample A5, **Figure 3.8**) revealed relatively high  $\mathcal{D}$  values ( $\leq 1.65$ ), although a gradual decrease in the  $\mathcal{D}$  values of the obtained materials was observed when NHSMA was copolymerized with GMMA and the GMMA content was increased (samples A1-A4, **Fig. 3.8** and **Table 3.2**).

For P(GMMA-*stat*-NIPAM) (samples B1-B5, **Figure 3.9** and **Table 3.3**) and P(GMMA-*stat*-BuA) (C1-C5, **Figure 3.10** and **Table 3.4**) copolymers,  $M_n$  increased with monomer conversion and, for both systems, the obtained  $\mathcal{D}$  values were relatively low ( $\mathcal{D} < 1.33$ ) (**Figure 3.7**, and **Tables 3.3-3.4**). The shoulder observed in the low molar mass region of some the SEC chromatograms corresponding to samples C1-C5 were ascribed to the presence of unreacted monomer (see **Figure 3.10**). Significant deviations between the  $M_{n, \text{theo}}$  and  $M_{n, \text{SEC}}$  values for both copolymerization systems were observed (*ca.* two-fold for copolymers B1-B5, whereas such discrepancies decreased for samples C1-C5 as the GMMA content was reduced). These observed deviations can be ascribed to different intrinsic factors related to the SEC technique as briefly described next.

SEC characterization is based on the difference in hydrodynamic volume of a sample and a reference (or standard), as such, different factors such as the molar mass of the sample, have a direct influence on its hydrodynamic volume in solution. Furthermore, the formation of aggregates triggered by intermolecular interactions can also contribute to the hydrodynamic volume of a certain sample.[165] For instance, SEC investigations of cellulose and polysaccharides in DMF or DMAc usually utilize small amounts of LiCl or LiBr to screen solvent-solute or column-solute interactions.[166,167] These studies reported the formation of complexes between C-OH hydroxy groups and LiCl or LiBr molecules, as well as intramolecular hydrogen bonds between monomer units and adjacent polymer chains. [168] Similarly, Armes *et al.*, synthesized a PGMMA of relatively high molar mass via the acidic hydrolysis of poly(isopropylidenglycerol methacrylate) (PIGMA) and reported that  $M_{n, \text{SEC}}$  of PGMMA (DMF with 10 mM LiBr was used as eluent) was higher than its PIGMA precursor even though the molar mass of the monomeric unit decreased ( $M_w^{\text{GMMA}} < M_w^{\text{IGMA}}$ ). The authors attributed this behavior to differences in solubility of the polymers in the utilized SEC eluent which might lead to changes in the hydrodynamic volume.[169] These latter investigations next to the SEC results obtained in this research suggest three possibilities to explain the observed



differences between  $M_{n,theo}$  and  $M_{n,SEC}$ : (1) a potential loss of the thiocarbonylthio group (from the RAFT agent) during the (co)polymerizations might lead to the formation of (co)polymers of higher molar mass; *i.e.*, a decrease in the number of “living” polymer chains, [3] (2) changes in the elution behavior of the copolymers caused by intermolecular interactions between hydroxy groups of the same (co)polymer chain and/or between hydroxy groups of PGMMA chains with LiCl contained in the DMAc SEC eluent[168,170] (or even with the material of the SEC chromatographic column) and, (3) an increase in the hydrodynamic volume due to intramolecular formation of hydrogen bonds between the different pendant groups (*i.e.*, hydroxyl, amide and succinimide groups) of adjacent (co)polymer chains.

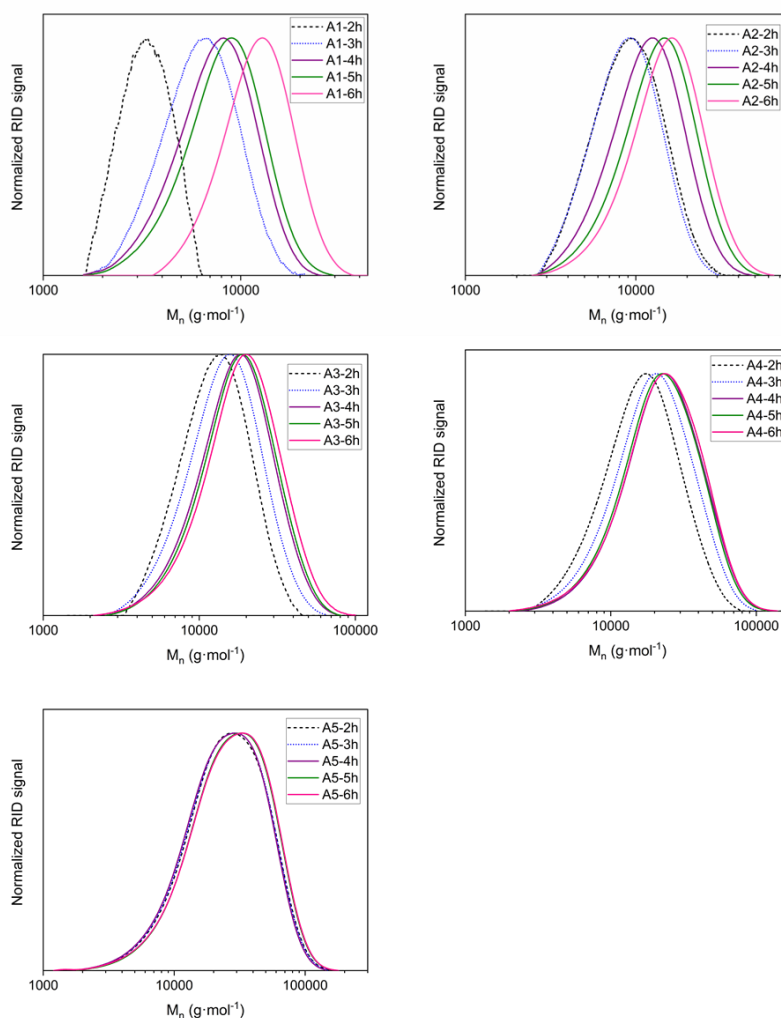


**Figure 3.8** SEC chromatograms of copolymers A1-A4 and poly(N-hydroxysuccinimide methacrylate) (PNHSMA) A5 in eluent DMAc + 0.21 % LiCl, RI detection and calibrated against PMMA standards.

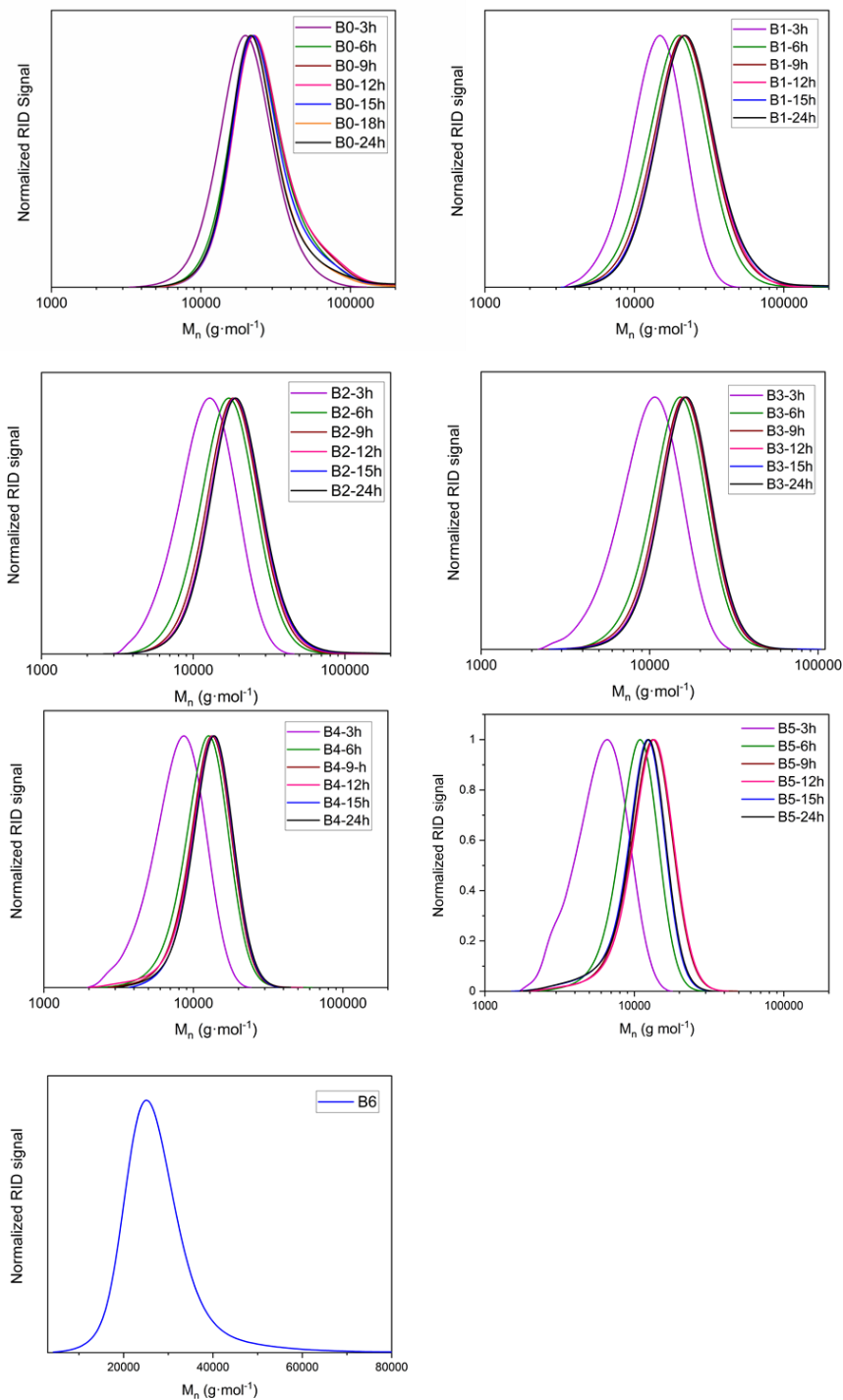


**Figure 3.9** SEC chromatograms of PGMMA homopolymer B0, copolymers B1-B5 and PNIPAM homopolymer B6, determined by SEC, eluent DMAc + 0.21 % LiCl, RI detection, calibrated against PMMA standards.

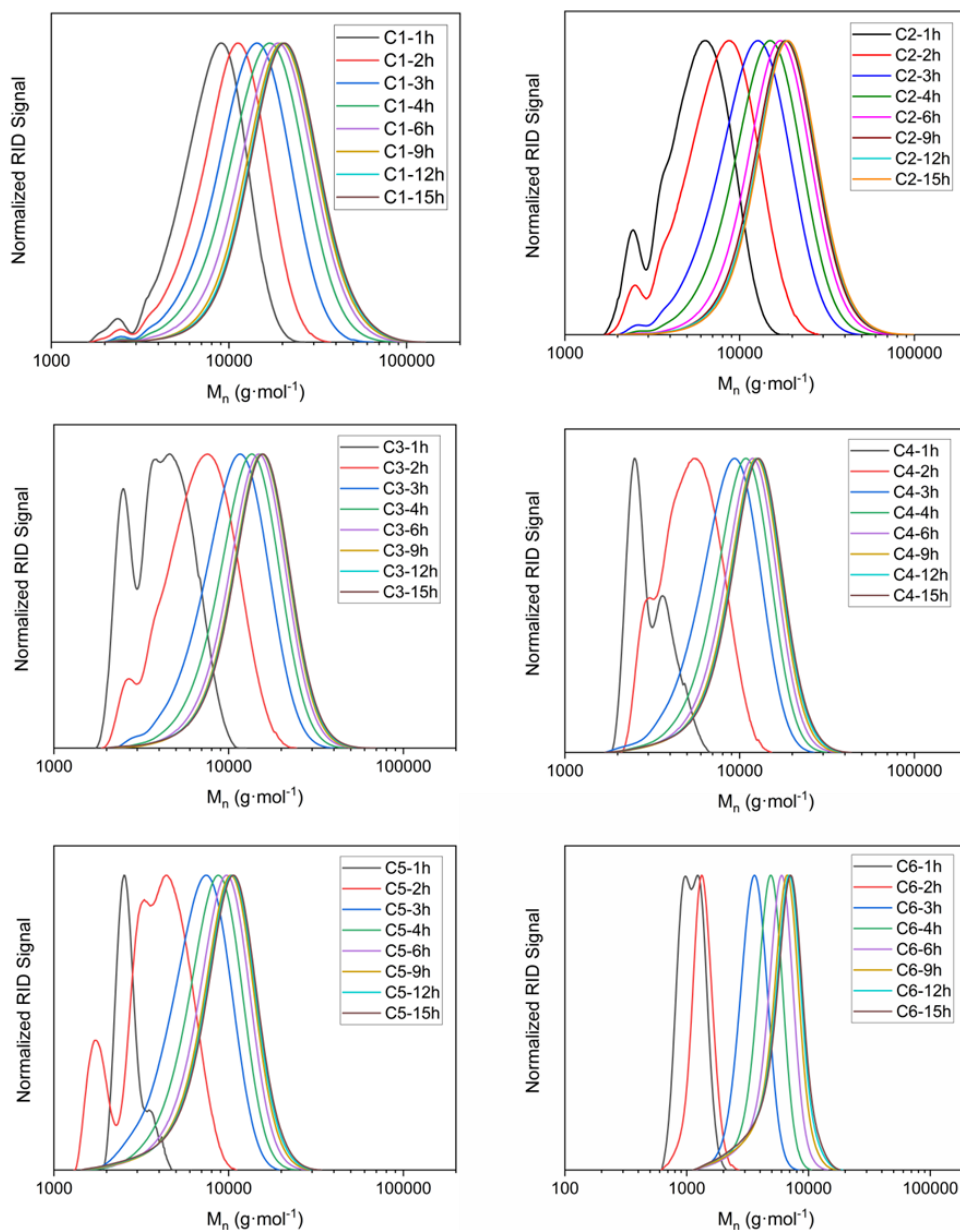


**Figure 3.10** Gel permeation chromatograms of copolymers C1-C5 and homopolymer C6 (poly(butyl acrylate) (PBuA) determined by SEC, eluent DMAc + 0.21 % LiCl, RI detection, calibrated against PMMA standards.

### 3.4.2 Estimation of reactivity ratios for the copolymerization systems GMMA with NHSMA, NIPAM and BuA, and estimation of the sequence length distribution

The reactivity ratios values for GMMA with the three different comonomers NHSMA, NIPAM and BuA were estimated using the integrated form of the copolymerization equation and performing a nonlinear regression by visualization of the residual space.[171] GMMA is generally a mixture of two isomers, 2,3-dihydroxypropyl methacrylate and 1,3-dihydroxypropyl methacrylate; the relative reactivity of both

isomers was reported by Madsen *et al.* [144] In that investigation the reported reactivities were 0.7, and 1.6 for 2,3-dihydroxypropyl methacrylate (92 mol %) and 1,3-dihydroxypropyl methacrylate (8 mol %), respectively. The reactivity ratios for the GMMA / pyrene methacrylate (PyMA) comonomer system were also determined in the same study assuming a non-terminal model (where the reactivity only depends on the monomer structure and not on the polymer radical chain-end). For these calculations, the utilized integral value of the GMMA signal in high pressure liquid chromatography (HPLC) measurements combined the signals of both GMMA isomers. Hence, the reported value of the reactivity ratio for GMMA was 0.7 and, in contrast, for PyMA, different values were reported ranging from 1.2 and 1.16 suggesting that the utilized non-terminal model may not be suitable for this case. [144]

Similarly, in this work, the integral values of the  $^1\text{H-NMR}$  signals ascribed to GMMA isomers during the performed kinetic investigations (*i.e.*, measurements of monomer conversion in time) were utilized for the calculation of the reactivity ratios values with the comonomers NHSMA, NIPAM and BuA. The reactivity ratios of these copolymerization systems have not been previously reported.

The obtained reactivity ratios values for the GMMA/NHSMA comonomer system ( $r_{\text{NHSMA}} = 1.01$  and  $r_{\text{GMMA}} = 0.32$ ) suggest that a polymer chain radical of NHSMA has no preference to add either a GMMA or NHSMA monomer units, whereas a GMMA-terminated radical would be prone to a cross-propagation. **Figure 3.11A** displays the corresponding joint confidence regions with 50, 70, 90 and 95 % probabilities utilized for the estimation of these reactivity ratios values. In addition, by using the estimated reactivity ratios in combination with the differential form of the copolymerization equation (Mayo-Lewis equation), predictions of the monomer and copolymer compositions can be made as a function of monomer conversion as shown in **Figures 3.11B** and **C**; a good agreement can be observed between the theoretical calculations and the experimental results.

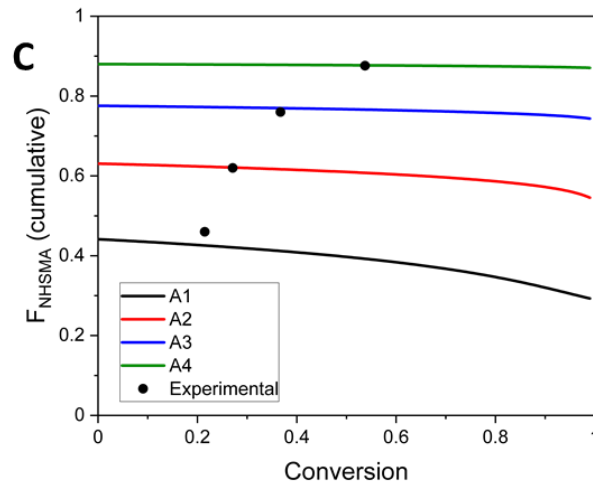
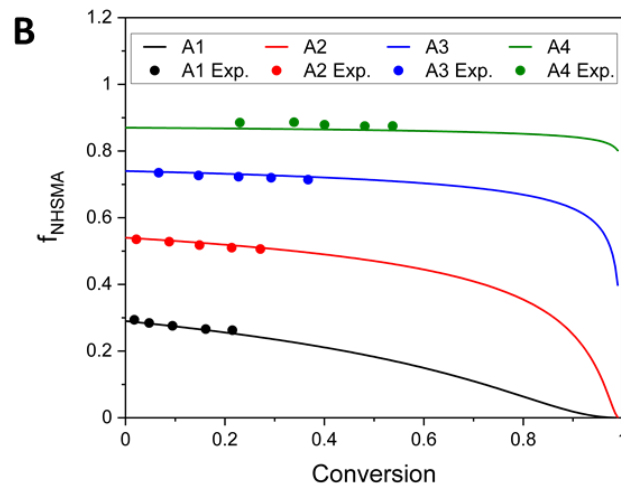
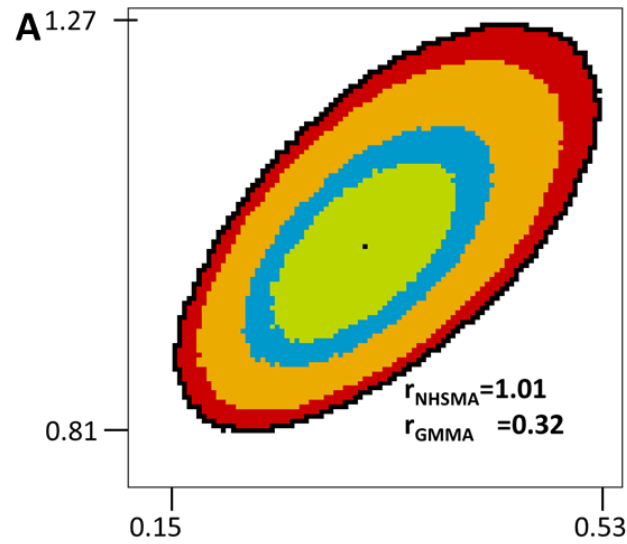


**Figure 3.11** Joint confidence and monomer fraction  $f_{\text{NHSMA}}$  and copolymer fraction  $F_{\text{NHSMA}}$  plots. Fig. A shows joint confidence regions for the estimated reactivity ratios of the system GMMA/NHSMA. Green 50%, blue 70%, orange 90% and red 95% probabilities.  $r_{\text{NHSMA}}=1.01$  and  $r_{\text{GMMA}}=0.32$ . Figures B and C compare the monomer fraction  $f_{\text{NHSMA}}$  and copolymer fraction  $F_{\text{NHSMA}}$  as a function of conversion with the corresponding experimental values obtained by NMR.

The microstructure of a determined copolymer can be defined in terms of the distribution of the various lengths of sequences of the monomer units A and B, known as the sequence length distribution,  $(N_A)_x$  and  $(N_B)_x$ , respectively. These quantities represent the probability of forming A and B sequences of length  $x$ . [172] In this regard, the calculated instantaneous sequence length distribution for the copolymer system GMMA/NHSMA is displayed in **Figure 3.12**. For  $N_{(NHSMA)_x}$ , **Figure 3.12A**, it can be observed that the instantaneous sequences of the form GMMA-NHSMA-GMMA (12.9 %) are comparable to other sequences such as dyads (11.2 %), triads (9.8 %) and tetrads (8.5 %) for a NHSMA fraction in the feed ( $f_{NHSMA,0} = 0.87$  (sample A4)). As the  $f_{NHSMA,0}$  decreases, the sequences of the form GMMA-NHSMA-GMMA can increase up to 78.8 % for a  $f_{NHSMA,0} = 0.29$  (sample A1). Similar analyses of other sequences of NHSMA show that dyads reach a maximum of 24.6 % for a  $f_{NHSMA,0} = 0.54$  (sample A2) while triads reach a maximum of 14.8 % for a  $f_{NHSMA,0} = 0.74$  (sample A3). In the case of the GMMA monomer, sequences of the form NHSMA-GMMA-NHSMA represent 95.4 % for a  $f_{NHSMA,0} = 0.87$  (sample A4) and decrease to a minimum of 11 % when  $f_{NHSMA,0} = 0.29$  (sample A1). Other GMMA sequences yield important percentages, such as dyads (22.7%) for a  $f_{NHSMA,0} = 0.74$  (sample A3) and triads (14.3 %) for a  $f_{NHSMA,0} = 0.54$  (sample A2); for this same monomer fraction, tetrads (10.5 %), pentads (7.8 %), hexads (5.7 %) and heptads (4.2 %) also appear.

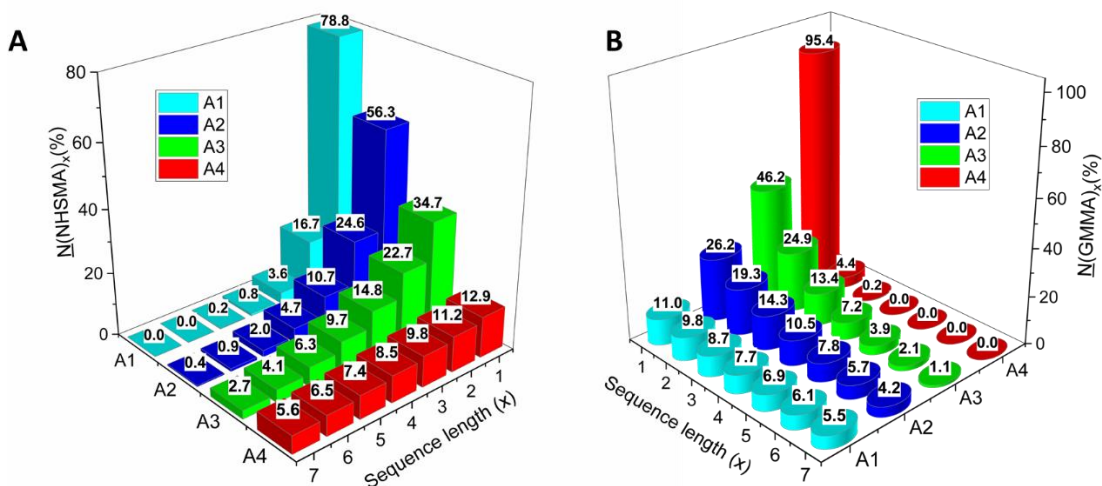


**Figure 3.12** Sequence length distribution for the copolymerization of the system GMMA/NHSMA (A1-A4) at different monomers fractions  $f_{0(\text{NHSMA})}$ . The vertical axis represents the percentage of a determined mean sequence length  $N$  (Figure A for NHSMA and Figure B for GMMA) and one of the horizontal axes the corresponding sequence of length  $x$ . Please note that sequences are only shown up to heptads but other sequences could be present.

NIPAM is a well-known monomer that forms thermo-responsive polymers [173] and has a relatively low reactivity when copolymerized with other comonomers.[174] This does not differ too much from the copolymer system investigated in this contribution where  $r_{\text{NIPAM}} = 0.11$  and  $r_{\text{GMMA}} = 2.55$ . This essentially means that a NIPAM terminal unit in a given copolymer chain will prefer cross propagation in contrast to a GMMA terminal unit that will prefer to react with another GMMA monomeric unit (homopolymerization). This is consistent with the observed rapid consumption of GMMA and the corresponding compositional drift for high values of NIPAM fraction in the feed ( $f_{\text{NIPAM},0}$ ) as the copolymerization proceeds, see **Figure 3.13A**. Theoretical and experimental copolymer compositions are also in good agreement with each other at the corresponding monomer conversion as shown in **Figure 3.13B**. The corresponding joint confidence regions for the estimation of the reactivity ratios are displayed in **Figure 3.13C**.

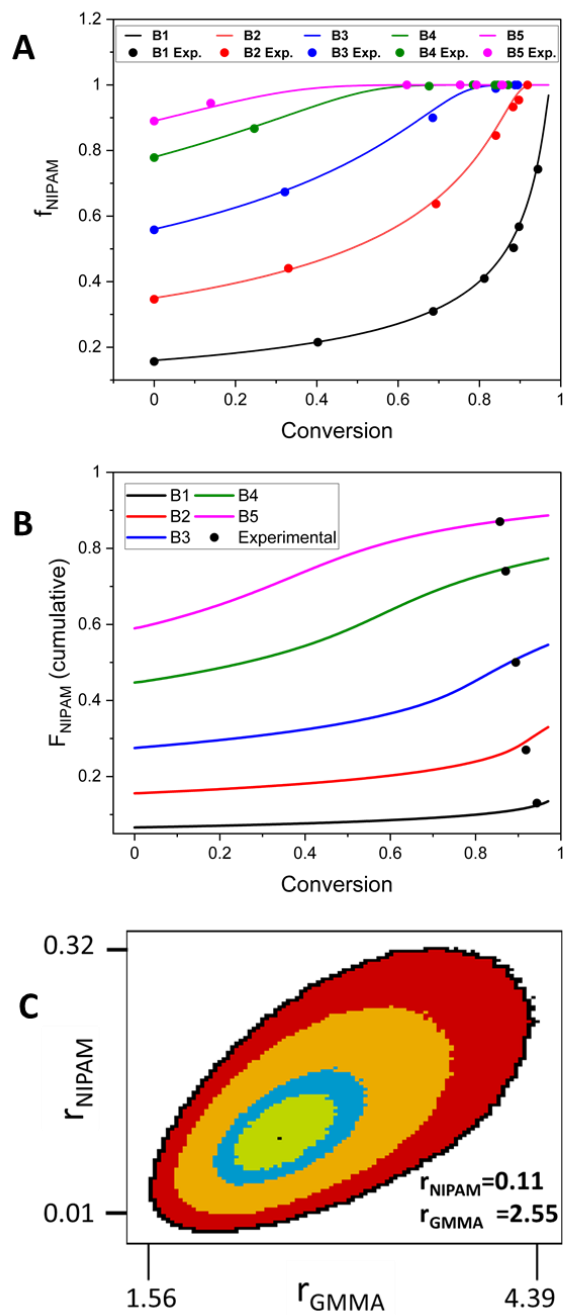


**Figure 3.13** A) and B) compare the instantaneous NIPAM fraction ( $f_{\text{NIPAM}}$ ) and the cumulative NIPAM fraction in the copolymer ( $F_{\text{NIPAM}}$ ) for different comonomer compositions (see Table 1) as a function of the overall monomer conversion for both theoretical estimations and the corresponding experimental values as determined by  $^1\text{H-NMR}$ . C) shows the joint confidence region for the estimated reactivity ratios. Green 50%, blue 70%, orange 90% and red 95%;  $r_{\text{NIPAM}} = 0.11$  and  $r_{\text{GMMA}} = 2.55$ .



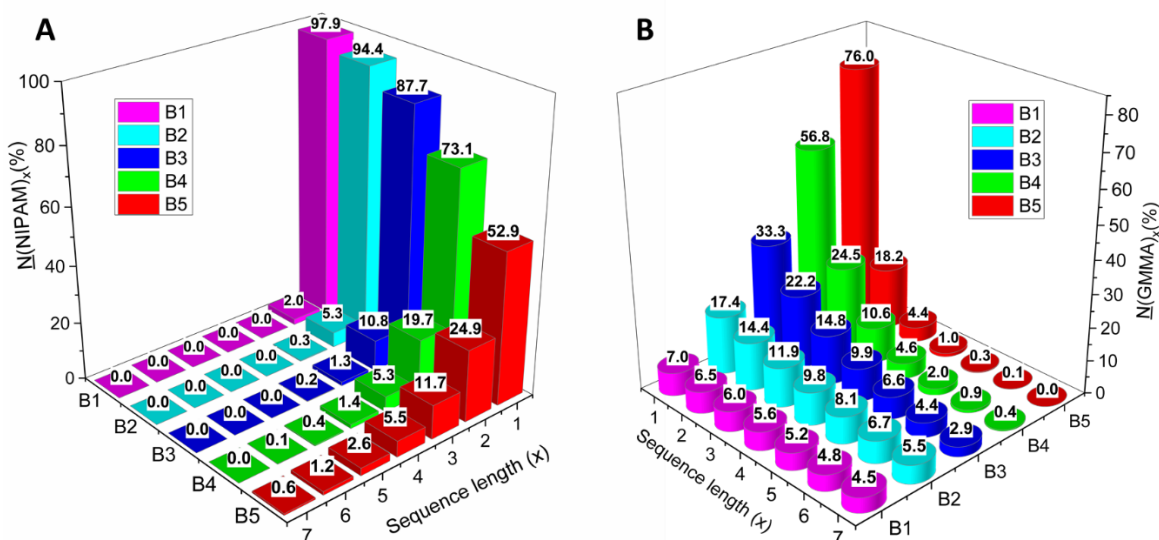


**Figure 3.14** Sequence length distribution for the copolymerization of the system GMMA/NIPAM (samples B1-B5 in Table 1) at different NIPAM fractions in the feed ( $f_{\text{NIPAM},0}$ ). The vertical axis represents the percentage of a determined mean sequence length  $\bar{N}$  (A) for NIPAM and B) for GMMA) and one of the horizontal axes the corresponding sequence of length  $x$ . Please note that sequences are only shown up to heptads, but other sequences could be present.

Utilizing the estimated reactivity ratios, one can calculate the expected instantaneous sequences for this copolymer system are shown in **Figure 3.14** for both monomers. As observed, the most abundant sequence (52.9 %) was GMMA-NIPAM-GMMA for a  $f_{\text{NIPAM},0} = 0.89$  (sample B5). For this same comonomer composition, we can also observe dyads and triads of NIPAM at the range of 24.9% and 11.7%, respectively. As  $f_{\text{NIPAM},0}$  decreases, it is expected an increased proportion of sequences in the form GMMA-NIPAM-GMMA as NIPAM is more prone to cross-propagate. In fact, for a  $f_{\text{NIPAM},0} = 0.16$  (sample B1), this kind of sequences represent a very large proportion (97.9 %), whereas the rest of the sequences are very close to zero (see **Figure 3.14A**). For GMMA, the behavior contrasts with the previous case according to **Figure 3.14B**. The sequences of the form NIPAM-GMMA-NIPAM decrease from 76% to 7% when  $f_{\text{NIPAM},0}$  changes from 0.89 (sample B5) to 0.16 (sample B1). In this case, other sequences of GMMA become also more significant; the proportion of dyads, triads, tetrads, pentads, hexads and heptads sequences increase when  $f_{\text{NIPAM},0}$  decreases (GMMA increases) from 0.89 (sample B5) to 0.16 (sample B1).

For the GMMA/BuA copolymer system, the estimated values of reactivity ratios ( $r_{\text{BuA}} = 0.66$  and  $r_{\text{GMMA}} = 3.31$ ) also suggest a preference for cross-propagation for BuA, whereas GMMA prefers to homopolymerize. Predictions of the monomer composition match very well the corresponding experimental values for monomer conversions below 0.5 (see **Figure 3.15A**). However, some deviations can be observed at higher monomer

conversion, in particular for  $f_{\text{BuA},0}$  values of 0.2, 0.8 and 0.9. Predicted copolymer compositions are shown in **Figure 3.15B** and compared to the experimental values as obtained by  $^1\text{H-NMR}$ .

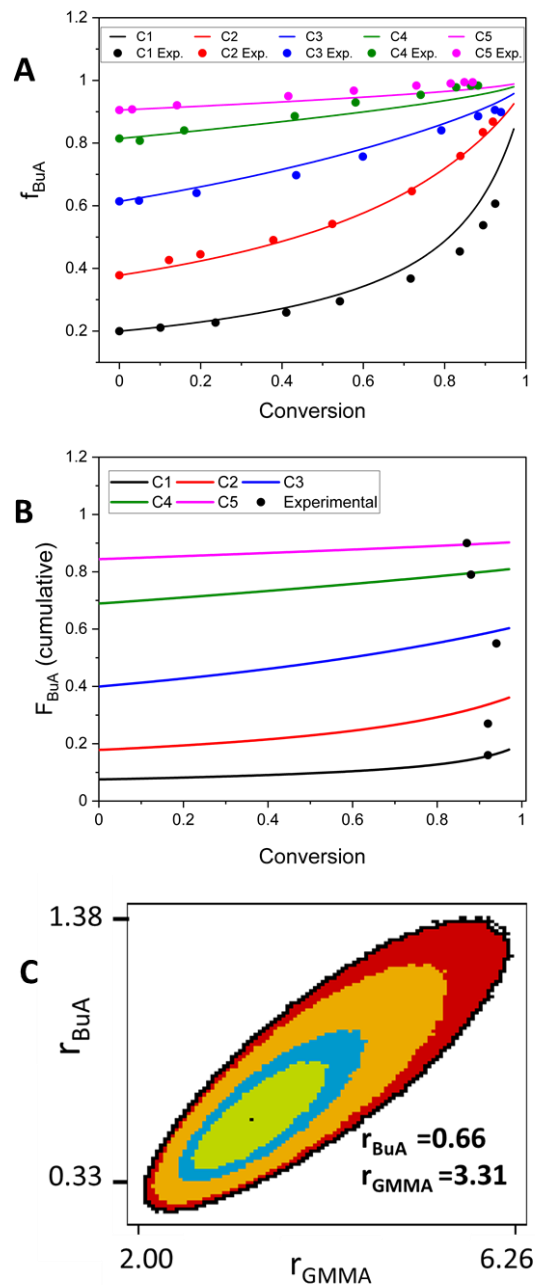


**Figure 3.15** Monomer fraction  $f_{\text{BuA}}$  and copolymer fraction  $F_{\text{BuA}}$ , and joint confidence plots. Figures A and B compare the monomer fraction  $f_{\text{BuA}}$  and copolymer fraction  $F_{\text{BuA}}$  as a function of conversion with the corresponding experimental values obtained by NMR for the copolymerization of the system GMMA/BuA. Figure C shows joint confidence regions for the estimated reactivity ratios. Green 50%, blue 70%, orange 90% and red 95% probabilities joint confidence regions for the estimated reactivity ratios.  $r_{\text{BuA}}=0.66$  and  $r_{\text{GMMA}}=3.31$

Regarding the instantaneous sequence length distribution, it can be observed that the proportion of sequences in which BuA monomer appears as GMMA-BuA-GMMA (13%) is comparable to other sequences such as dyads (11.3%), triads (9.9%), tetrads (8.6%), pentads (7.5%), hexads (6.5%) and heptads (5.6%) for a  $f_{\text{BuA},0} = 0.91$  (sample C5). As  $f_{\text{BuA},0}$  decreases, the percentage of GMMA-BuA-GMMA sequences considerably increases up to a value of 85.8% for a  $f_{\text{BuA},0} = 0.20$  (sample C1, **Figure 3.16A**). On the other hand, the distribution of GMMA sequences in which GMMA appears as BuA-GMMA-BuA is the most abundant (75.3%) for a  $f_{\text{BuA},0} = 0.91$  (sample C5, **Figure 3.16A**) and decreases down to 7% for a  $f_{\text{BuA},0} = 0.20$  (sample C1, **Figure 3.16A**). For the former value of  $f_{\text{BuA},0}$ , other observed instantaneous sequences are dyads (18.6%), triads (4.6%), tetrads (1.1%), pentads (0.3%), hexads (0.1%) and heptads (0%) (see **Figure 3.16B**). However, as the value of  $f_{\text{BuA},0}$  decreases (*i.e.*, GMMA increases) other sequences become more significant in particular for dyads, triads and tetrads (see **Figure 3.16B**).

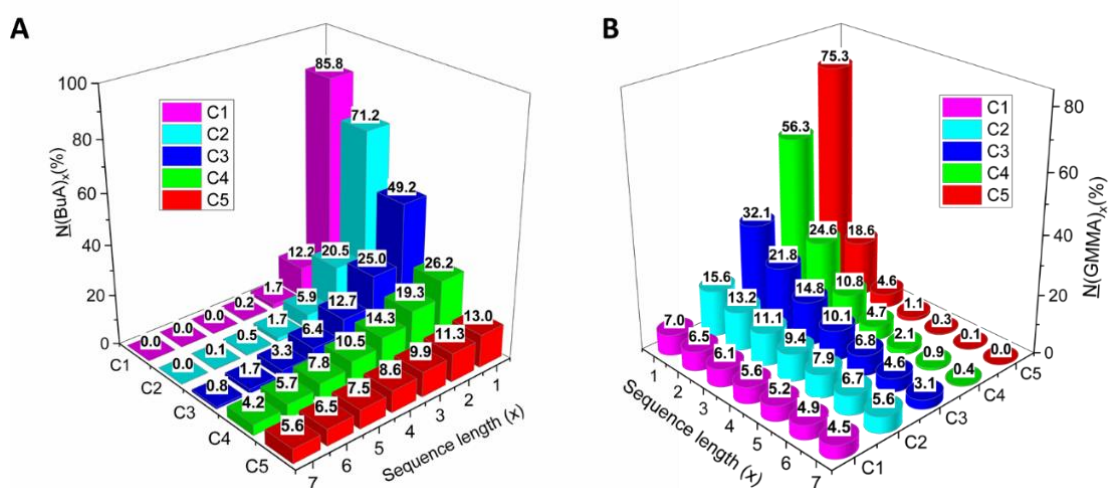


**Figure 3.16** Sequence length distribution for the copolymerization of the system GMMA/BuA at different monomers fractions  $f_0(\text{BuA})$ . The vertical axis represents the percentage of a determined mean sequence length  $\underline{N}$  (Figure A for BuA and Figure B for GMMA) in percentage and one of the horizontal axes the corresponding sequence of length  $x$ . Please note that sequences are only shown up to heptads but other sequences could be present.

### 3.4.3 DSC investigations and theoretical estimations of $T_g$ .

The  $T_g$  of copolymers is mainly governed by the copolymer composition, stereo configuration, and size and nature of the monomeric repeating units.[175] In this context, the incorporation of monomers with pendant groups such as hydroxyl or carbonyl groups may provide the possibility to form hydrogen-bonds between the copolymer chains, which, in turn, may increase the  $T_g$  of these materials.[101,176,177] In this investigation,

copolymers B1-B5 and C1-C5 (Table 2.1) were subjected to a DSC analysis; copolymers A1-A5 were discarded in this respect because changes in the slope of the corresponding DSC thermograms were too small to be detected in a reliable manner at the investigated experimental conditions. The  $T_g$  experimental values recorded for homopolymers PGMA (sample B0 in Table 2.1) and PNIPAM (sample B6 in Table 1) were 108 °C and 132 °C respectively. As expected, the  $T_g$  of P(GMA-*stat*-NIPAM) copolymers increased with the NIPAM content (see **Figure 3.17A**). In this investigation, the  $T_g$  of PBuA (sample C1 in Table 1) was recorded at -52.4 °C; for the case of P(BuA-*stat*-GMA) copolymers (samples C1-C5 in Table 1) the  $T_g$  values increased with the GMA content (see **Figure 3.17C**). This behavior can be correlated to the increase in the GMA composition and the incorporation of additional methyl groups into the polymer backbone, which might induce rotational restrictions in the copolymer chains.[175] In addition, the DSC thermograms of PGMA homopolymer (sample B0 in Table 1) and copolymers B1-B5 revealed a signal around 20 °C (see **Figure 3.17B**), whose integral value decreases with the incorporation of NIPAM monomer units according to **Figure 3.18**. It is worth noting that this transition was not observed in the respective BuA-based copolymer. The observed transition could be ascribed to intermolecular interactions between hydroxyl-hydroxyl and hydroxyl-carbonyl groups present in the copolymer chains as suggested in a previous report on the hydrolysis of poly(solketal methacrylate) to obtain PGMA.[101] For a full elucidation of the nature of these intermolecular interactions, additional investigations involving (co)polymers of different molar mass might be necessary in future research in this topic.

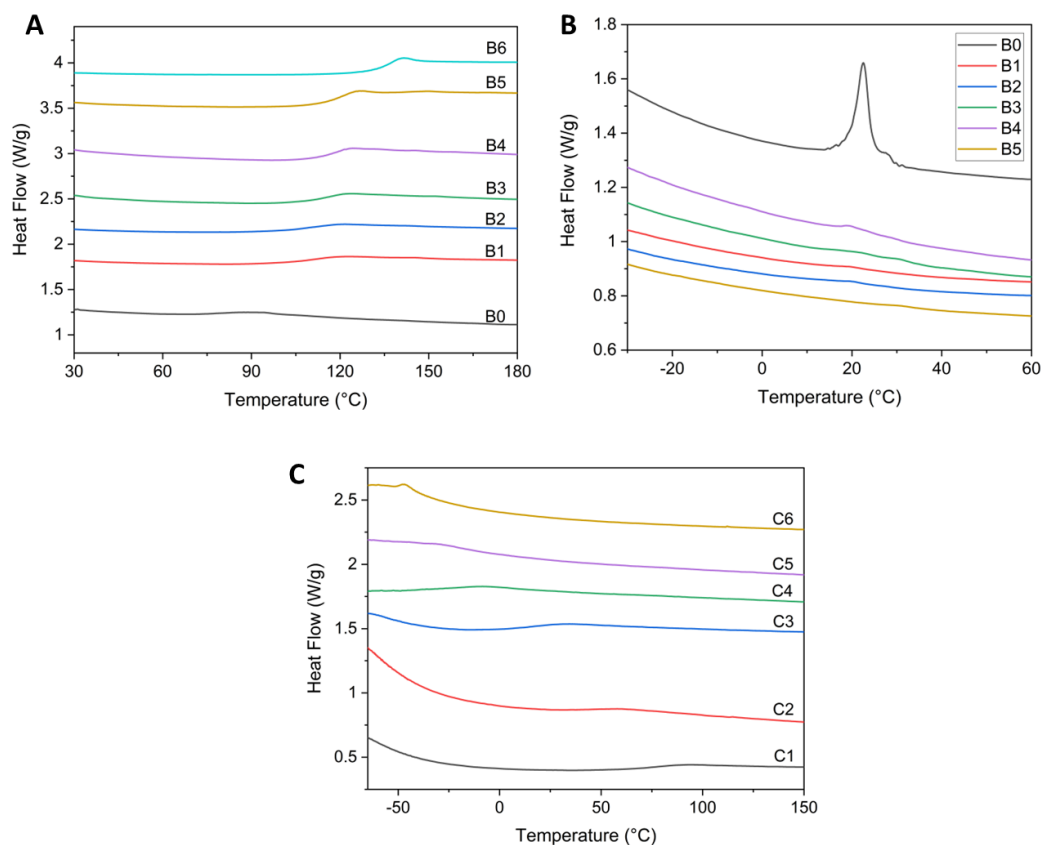


**Figure 3.17** DSC Analysis of B0-B6 and C1-C6 copolymers. A) DSC thermograms of homopolymers B0 and B6, and copolymers B1-B5, determination of the  $T_g$ . B) Thermodynamic transition observed around 20 °C. C) DSC thermograms of C6 homopolymer and C1-C5 copolymers. The DSC curves have been shifted (y-axis) to facilitate their interpretation.

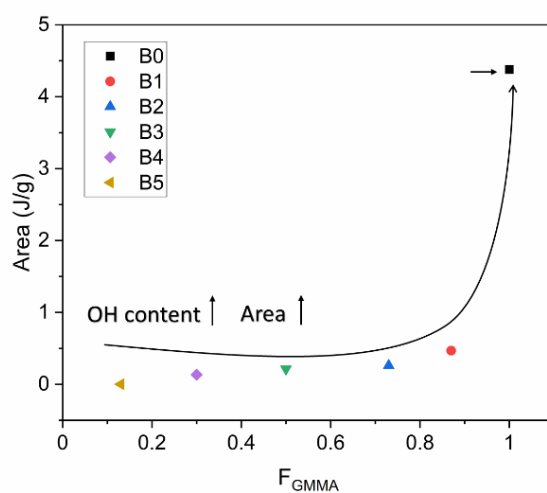


**Figure 3.18** Area values (J/g) of polymers B0-B5 calculated by integration of DSC thermograms at the transition around 20 °C.

In addition, theoretical values of  $T_g$  for all the investigated copolymer systems were calculated utilizing the Fox equation (Eq.3.4), [178] commonly employed in binary polymer blends and statistical copolymers. Complementarily to this, the  $T_g$  values were also estimated using the Bristow equation (Eq.3.5) [179] and the Kwei equation (Eq.3.6) [177], which considers deviations from linearity related to copolymer composition using fitting parameters. As reported elsewhere, the “q” constant in the Kwei model represents the contribution of potential hydrogen bonds. [177]

$$\frac{1}{T_{g(\text{copolymer})}} = \frac{x_1}{T_{g1}} + \frac{1-x_1}{T_{g2}} \dots \dots \dots (3.4)$$

$$T_{g(\text{copolymer})} = x_1 T_{g1} + (1-x_1) T_{g2} + x_1(1-x_1) \times [a_0 + a_1(2x_1-1) + a_2(2x_1-1)^2 + a_3(2x_1-1)^3] \dots \dots \dots (3.5)$$

$$T_{g(\text{copolymer})} = \frac{x_1 T_{g1} + k_{kwei}(1-x_1) T_{g2}}{x_1 + k_{kwei}(1-x_1)} + q x_1(1-x_1) \dots \dots \dots (3.6)$$

Where,  $T_{g(\text{copolymer})}$ ,  $T_{g1}$  and  $T_{g2}$  correspond to the  $T_g$  of the copolymer, component 1 (as homopolymer) and component 2 (as homopolymer), respectively.  $x_1$  is the weight fraction of component 1, and  $k_{kwei}$ ,  $q$  and  $a_i$  are fitting parameters determined from experimental curves.

In this contribution, P(GMMA-*stat*-NIPAM) copolymers have a "q" value higher than the other investigated copolymer system ( $q^{\text{GMMA-NIPAM}} = 18.7$  and  $q^{\text{GMMA-BuA}} = 4.55$ ), which suggests that the observed intermolecular interactions may be of a hydrogen bonding nature. Furthermore, **Figure 3.19A** shows that the  $T_{g,\text{DSC}}$  of P(GMMA-*stat*-NIPAM) copolymers is a nonlinear function of copolymer composition, thus the Fox equation might not be a suitable model to accurately describe this particular copolymer system; a similar situation to this latter was observed when using the Kwei equation. However, a good agreement between the Bristow model and the experimentally recorded  $T_g$  values could be observed. In the case of copolymers C1-C5, theoretical  $T_g$  values with the three abovementioned equations were close to the experimentally recorded  $T_g$  values as depicted in **Figure 3.19B**. All in all, the GMMA/NIPAM copolymer displayed a nonlinear behavior as a function of NIPAM composition and the parabolic representation provided by the Bristow equation was the most appropriate model to describe this copolymer system; in contrast, the  $T_g$  values of the hydrophobic copolymer system involving BuA monomer were well described by all three selected models.

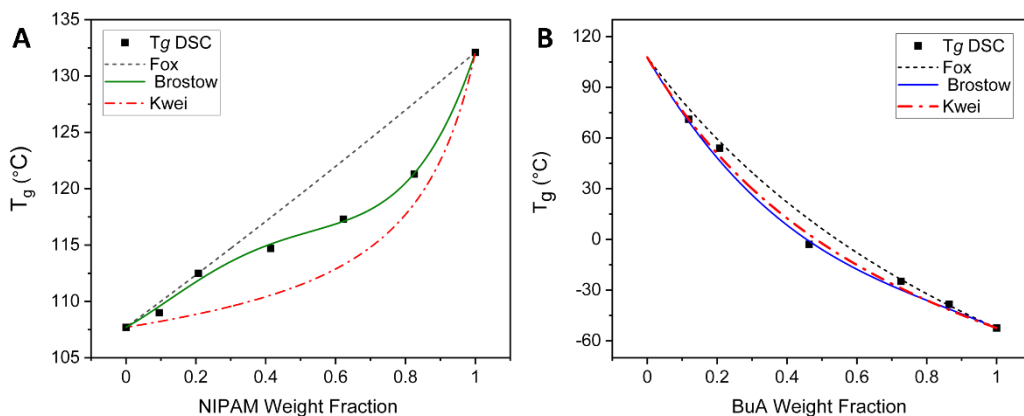


**Figure 3.19** Experimental  $T_g$  values and  $T_g$  values estimated with the Fox, Kwei, and Brostow equations **A)** homopolymers B0 and B6 and copolymers B1-B5,  $K_{kwei} = 5.92$ ,  $q^{GMA-NIPAM} = 18.70$ ,  $a_0 = -15.82$ ,  $a_1 = -30.56$  and  $a_2 = -21.82$ . **B)** homopolymers C0 and C6 and copolymers C1-C5,  $K_{kwei} = 0.45$ ,  $q^{GMA-BuA} = 4.55$ ,  $a_0 = 134.34$  and  $a_1 = 61.09$ .

#### 3.4.4 TGA investigations

The decomposition temperature ( $T_d$ ) of the investigated copolymers was determined by TGA. P(GMMA-*stat*-NIPAM) and P(GMMA-*stat*-NHSMA) copolymers exhibited a  $T_d$  between 200 and 250 °C at a 5 wt. % mass loss, whereas P(GMMA-*stat*-BuA) copolymers the recorded  $T_d$  values were in the range from 270 to 300 °C (see  $T_d$  values in **Tables 3.2 to 3.4**). Previous thermal decomposition studies of methacrylate monomers bearing OH pendant groups revealed that the decomposition process involves two main reactions. The first one corresponds to a depolymerization process, whereas the second one can be ascribed to side reactions involving ester groups.[180,181] Furthermore, previous PGMMA degradation investigations by means of derivative thermogravimetric analysis (DTG) suggested that this process is performed in two overlapped steps starting at 220 °C; however, this kind of degradation processes cannot be fully elucidated by conventional TGA.[101] In this regard, the TGA thermograms displayed on **Figure 3.20A** revealed a two-step degradation for P(GMMA-*stat*-NHSMA) copolymers, whereas **Figure 3.20B** shows a single-step degradation process for P(GMMA-*stat*-NIPAM) and P(GMMA-*stat*-BuA) copolymers. Nevertheless, an overlapping multi-step degradation could not be fully discarded from the recorded conventional TGA thermograms and additional DTG measurements could be necessary in future investigations for a more detailed elucidation of the decomposition mechanisms of these materials.

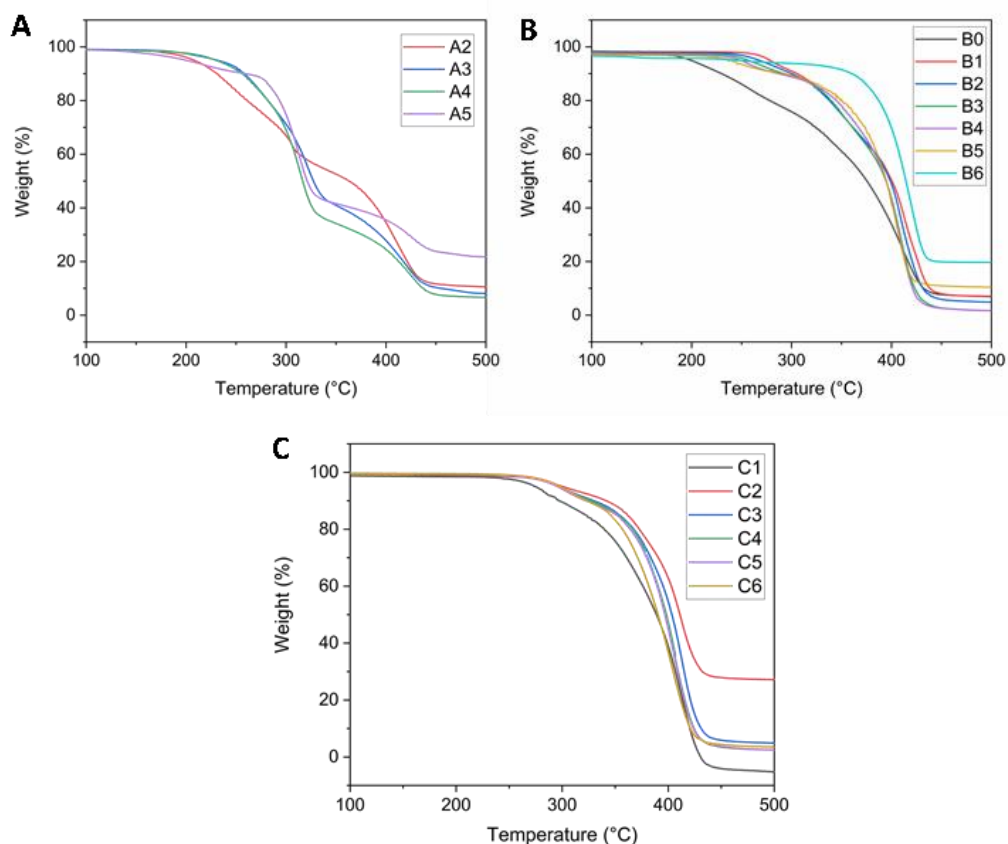


**Figure 3.20** TGA thermograms of A) homopolymer A5 and copolymers A2-A4; B) homopolymers B0 and B6, and copolymers B1-B5; C) homopolymers C6 and copolymers C1-C5.

### 3.4.5 Light transmission measurements and cell viability

PNIPAM is one of the most investigated thermo-responsive polymers in aqueous media with a LCST around 32 °C. At this temperature, a conformational change occurs in the dissolved polymer chains provoking a loss of hydrophilicity, which turn them insoluble.[182,183] This behavior can be modulated by modifying the molar mass and/or end groups of the polymer chains, or via copolymerization reaction with other comonomers.[184,185] To understand the influence of incorporating GMMA as a comonomer on the LCST of P(GMMA-*stat*-NIPAM) aqueous solutions (copolymers B1-B5 in Table 3.3), light transmission measurements were performed to determine their corresponding  $T_{cp}$ .

**Figure 3.21A** shows the changes of light transmittance (%) as a function of temperature for aqueous solutions of homopolymer B6 (PNIPAM) and copolymers B4-B5



(P(GMMA-*stat*-NIPAM)) in Table 3.3. Note that aqueous solution of copolymers with a higher content of GMMA (copolymers B1-B3 in Table 3.3) did not show any thermal response in the investigated temperature range (results not shown). This suggests that the presence of an observable thermal response in aqueous solutions of these copolymers is limited by the NIPAM composition ( $F_{\text{NIPAM}} \geq 0.74$ ). Hence, the experimentally recorded  $T_{\text{cp}}$  of copolymers B4, B5 and B6 aqueous solutions were 38.5, 33.1 and 34.1 °C, respectively. Copolymers B5 ( $F_{\text{GMMA}} = 0.13$ ) and B6 ( $F_{\text{GMMA}} = 0$ ) did not show a significant difference in the measured  $T_{\text{cp}}$  values, which can be ascribed to the relatively small difference between the respective GMMA composition in these materials. On the other hand, an increase in  $T_{\text{cp}}$  was more pronounced for copolymer B4 ( $F_{\text{GMMA}} = 0.3$ ) aqueous solution, whose GMMA content is larger than copolymer B5, which enhance the hydrophilicity of this sample by incorporating more OH groups into the polymer chains. A similar behavior has been reported when NIPAM was copolymerized with other comonomers bearing hydrophilic groups.[174,185]

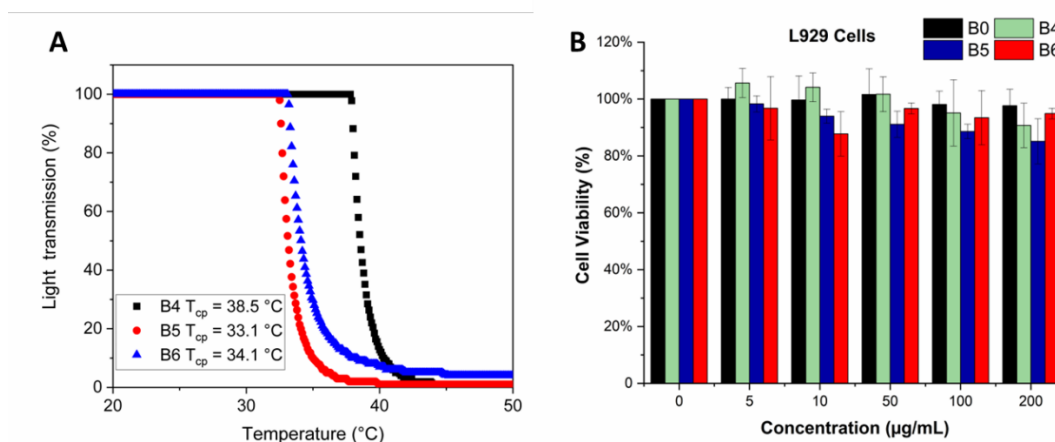


**Figure 3.21** A) Light transmission measurements of homopolymer B6 and copolymers B4-B5. B) Cell viability of homopolymers B0 and B6 and copolymers B4-B5.

Last but not least, the cytotoxicity of copolymers B4 and B5 and homopolymers B0 and B6 was investigated using the presto blue assay in mouse fibroblast cells (L929) for 24 h. All these samples displayed a cell viability higher than 80 % up to a polymer concentration of 200  $\mu\text{g mL}^{-1}$  (see **Figure 3.21B**), which suggests that these materials could be suitable candidates for biomedical applications being copolymer B4 of a

particular interest because exhibited a  $T_{cp} = 38.5$  °C (a value close to the physiological temperature) and cell viability of 90 % at a polymer concentration of  $200 \mu\text{g mL}^{-1}$ .

### 3.5 Conclusions and outlook

Three series of statistical copolymer systems with varying copolymer composition and based on GMMA comonomer were synthesized. The measured reactivity ratios of these copolymer systems confirmed that GMMA prefers undergoing homopolymerization reactions rather than cross-propagation with the other investigated comonomers (*i.e.*, BuA and NIPAM), which favors the formation of “gradient-like” copolymers rich in GMMA at the initial stages of the respective copolymerization reactions. On the other hand, it was confirmed that GMMA is more susceptible to cross-propagate when copolymerized with NHSMA. DSC measurements of the obtained copolymers enabled the construction of data-fitting curves of well-established mathematical models (*i.e.*, Fox, Kwei and Brostow equations) to predict  $T_g$  of these materials when varying comonomer composition. The  $T_g$  of copolymers bearing the hydrophobic BuA comonomer were successfully described by the three models, whereas the copolymer system containing NIPAM showed a better fit to the Brostow equation. The LCST of aqueous solution containing GMMA-*stat*-NIPAM copolymers increases with the content of OH groups supplied by an increase of GMMA comonomer content; however, this observed thermoresponsive behavior was limited to aqueous solutions containing a NIPAM composition  $F_{NIPAM} \geq 0.74$ . Finally, a GMMA-*stat*-NIPAM copolymer (copolymer B4 in Tale 1) exhibited a  $T_{cp} = 38.5$  °C (a value close to the human body temperature) and a cell viability higher than 90 %, which turns this particular material into an interesting potential candidate for further investigations in biomedical applications.

## Chapter 4 Bioconjugation of amphiphilic copolymers with peptides derived from HA protein.

### 4.1 Introduction

In this research project, we investigated three peptide sequences derived from the HA1 subunit of the HA protein of the Influenza A virus obtained from the vaccine strain A/California/07/2009 (H1N1pdm09). The HA1 subunit contains the receptor binding site (RBS) that interacts with  $\alpha$ -sialic acid linked to saccharides located on the membrane of host cells [186]; the RBS is mainly formed by a pocket of three conserved elements, the 130 and 220 loops and the 190 helix, as well as several conserved amino acids at the bottom of the pocket. [77]

The peptide sequences of the RBS may differ depending on the virus subtype; however, most of them have a similar conformation.[187] Hence, cytotoxicity and some physicochemical properties of three relevant peptide sequences were initially investigated in this chapter. For this purpose, each peptide sequence was functionalized with a fluorescent tryptophan residue (W) as an end group to enable monitoring by fluorescence spectroscopy. In addition, the peptide analogues of the 130 and 220-loops were also telechelically functionalized with a fluorescent marker (5FAM). Thus, the final sequence of the investigated peptides can be summarized as DSNKGVTAACPW, DQQLYQNAW, RPKVRDQEGRMW, 5FAM-DSNKGVTAACPW, and 5FAM-RPKVRDQEGRMW, and were denominated as PC1, PC2, PC3, PC1-5FAM and PC3-5FAM, respectively. The three synthetic peptides sequences selected for this investigation *i.e.*, DSNKGVTAACPW, DQQLYQNAW and RPKVRDQEGRMW are based on the 130-loop, 190-helix and 220-loop of the HA1 subunit of the HA protein, respectively.

RAFT polymerization is a versatile technique that enables the access to different polymer architectures, including block copolymers. Furthermore, it is possible to access a wide range of topologies via various synthetic approaches based on the RAFT technique; for example, RAFT agents can be functionalized via post-modification reactions for bioconjugation purposes including peptide-bioconjugate polymers. In this work, PC1 and PC3 peptides sequences were conjugated with block copolymers via two synthetic routes based on ester activation.

## 4.2 Experimentation

### 4.2.1 Synthesis of PFP-CPAD.

Pentafluorophenyl-(4-phenylthiocarbonylthio-4-cyanovalerate) (PFP-CPAD) was synthesized as described in the literature.[188,189] CPAD (1.4 g, 5 mmol), PF (1.014 g, 5.5 mmol) and DMAP (62 mg, 0.5 mol) were dissolved in anhydrous dichloromethane (DCM, 70 mL). The solution was stirred and cooled down to 0°C using an ice bath. Thereafter, DIC (0.697 g, 5.5 mmol) was added dropwise under vigorous stirring into 10 mL of DCM, the obtained solution was kept cool for 2 h and, subsequently, stored at room temperature overnight. This solution was filtered to remove urea impurities and was concentrated using a rotary evaporator. The obtained mixture was purified via column chromatography using silica gel as a packing material and chloroform as an eluent. The obtained pink oil was dried and cooled for crystallization. Yield: 1.201 g (53 %). Elem. Anal.: theory C: 51.23 %, H: 2.72 %, N: 3.14 %, S: 14.40 %; found C: 51.71 %, H: 2.70 %, N: 3.30 %, S: 14.20 %. ESI-MS: Calculated, 445.43 g·mol<sup>-1</sup>; found 445.02 g·mol<sup>-1</sup>. The structure was confirmed by <sup>1</sup>H-NMR, 300 MHz CDCl<sub>3</sub>: δ =7.95 (d, 2 H, *o*-Ar), 7.61 (t, 1 H, *p*-Ar), 7.43 (t, 2H, *m*-Ar), 3.13-3.04 (m, 2H, O=C-CH<sub>2</sub>), 2.86- 2.71 (m, 1H, O=CH<sub>2</sub>-CHH), 2.65-2.5(m, 1H, O=CH<sub>2</sub>-CHH) 2.06-1.97 (s, 3H, CH<sub>3</sub>). <sup>19</sup>F NMR, CDCl<sub>3</sub>, 400 MHz: δ = -152.5 (d, 2F, *o*-C<sub>6</sub>F<sub>5</sub>), -157.3 (t, 1F, *p*-C<sub>6</sub>F<sub>5</sub>), -161.9 (t, 2F, *m*-C<sub>6</sub>F<sub>5</sub>).

### 4.2.2 Synthesis of P(OEGMEMA -*stat*-FLUMA) with PFP-CPAD (P10 macro RAFT agent).

OEGMEMA (14 g, 28 mmol), was polymerized in 41 mL of 1,4-dioxane using PFP-CPAD (360 mg, 0.8 mmol) as CTA, AIBN (13.3 mg, 0.08 mmol) as initiator (OEGMEMA:CTA:AIBN 35:1:0.1 mole ratio) and 1,3,5-trioxane (251 mg, 2.8 mmol) as an internal standard to estimate monomer conversion via <sup>1</sup>H-NMR analysis. The polymerization mixture was initially degassed for 30 min by sparging N<sub>2</sub> gas and, subsequently, placed into an oil bath preheated at 65 °C. After 4 h, 2 mL of a 1,4-dioxane solution containing FLUMA monomer (70 mg, 0.17 mmol) corresponding to 0.5 wt % with respect to the utilized OEGMEMA monomer was added. The reaction proceeded for 4 h more at 65°C to allow the copolymerization of FLUMA; thereafter, the reaction was quenched by cooling into an ice bath. The obtained copolymer was precipitated into cold diethyl ether (x4) and dried under vacuum at 40°C for 48 h. OEGMEMA conversion was

57 % as determined by the integral value of the signals ascribed to the vinyl proton at 5.5 and 6.1 ppm from the corresponding  $^1\text{H-NMR}$  spectrum. The degree of polymerization (DP) and molar mass of the purified polymer was also calculated via  $^1\text{H-NMR}$  by comparing the integral value of the signals ascribed to the aromatic protons of the PFP-CPAD at 7.3-7.8 ppm with that of the methoxy protons of the P(OEGMEMA-*stat*-FLUMA) at 4.1 ppm (DP 25,  $M_{n,NMR}$  13,000  $\text{g}\cdot\text{mol}^{-1}$ ,  $M_{n,theo}$  10,500  $\text{g}\cdot\text{mol}^{-1}$ ,  $M_{n,sec}$  8,800  $\text{g}\cdot\text{mol}^{-1}$  and  $\bar{D}$  1.14). The presence of fluorine signals was confirmed by  $^{19}\text{F-NMR}$  using  $\text{CDCl}_3$  as an analysis solvent and a 400 MHz equipment:  $\delta$  (ppm) = -152.54 (d, 2F, *o*- $\text{C}_6\text{F}_5$ ), -157.50 (t, 1F, *p*- $\text{C}_6\text{F}_5$ ), -162.01 (t, 2F, *m*- $\text{C}_6\text{F}_5$ ).

#### 4.2.3 Synthesis of block copolymer P(OEGMEMA-*stat*-FLUMA)-*b*-P(BMA) (P20).

The P(OEGMEMA-*stat*-FLUMA)-*b*-P(BMA) block copolymer was prepared from a previously purified and dried P10 macro-CTA. The P10 macro-CTA (25 repeating units, 1.048 g, 0.081 mmol), BMA monomer (1.40 g, 9.84 mmol), V88 radical initiator (1.9 mg, 0.008 mmol) and 1,3,5-trioxane internal standard (94 mg, 1.03 mmol) were dissolved into 9.5 mL of 1,4-dioxane. This reaction mixture was degassed by sparging  $\text{N}_2$  gas for 30 min and, subsequently, placed into an oil bath preheated at 90 °C for 17 h. The obtained copolymer was precipitated into cold hexane (x3) and dried under reduced pressure at 40°C for 48 h. The monomer conversion was 62 % as determined via  $^1\text{H-NMR}$  by comparing the integral value of the signals ascribed to the vinyl protons at 5.5 and 6 ppm with that of the signal ascribed to the protons of 1,3,5-trioxane. DP and  $M_n$  values were also determined via  $^1\text{H-NMR}$  by comparing the integral values of the signals ascribed to the methoxy protons ( $\text{CH}_2$ - $\text{CH}_2$ - $\text{COO}$ -) of P(OEGMEMA-*stat*-FLUMA) at 4.28-4.02 ppm with that of the signal related to the methylene protons of the P(BuA) segment at 1.70-1.54 ppm.  $M_{n,NMR}$  was 23500  $\text{g}\cdot\text{mol}^{-1}$  while DP of BMA was 49. SEC analysis of the diblock copolymer yielded an  $M_{n,sec}$  and  $\bar{D}$  of 18200  $\text{g}\cdot\text{mol}^{-1}$  and 1.12, respectively. The fluorine presence was verified via  $^{19}\text{F-NMR}$  analysis, whose signals were identical to those observed for P10.

#### 4.2.4 Synthesis of P(BMA) macro-CTA (P30).

A homopolymer of BMA was synthesized as follows: BMA monomer (30 g, 210.97 mmol) and CPAD (0.47 g, 1.68 mmol) as RAFT agent, V88 (25.8 mg, 0.105 mmol) (BMA: CTA: V88 125:1:0.06 mole ratio) and 1,3,5-trioxane (1.9 g, 21.10 mmol) were added into a 100 mL round-bottom flask. This solution was degassed by sparging  $\text{N}_2$  gas

for 30 min and, subsequently, placed into an oil bath preheated at 90 °C for 8 h. After this time elapsed, the reaction mixture was cooled into an ice bath for quenching and the round-bottom flask was open. The obtained polymer was precipitated into methanol (x4) and dried under vacuum at 40°C for 48 h. The DP and  $M_n$  values of the purified polymer were estimated via <sup>1</sup>H-NMR analysis by comparing the integral value of the signals ascribed to the aromatic protons of the CPAD at 7.3-7.8 ppm with that of the signal ascribed to the methyl protons of the P(BMA) at 0.07-1.14 ppm (obtained monomer conversion: 50 %, DP: 68,  $M_{n,NMR}$  9900 g·mol<sup>-1</sup>,  $M_{n,theo}$  9100 g·mol<sup>-1</sup>,  $M_{n,sec}$  9000 g·mol<sup>-1</sup> and  $D$ : 1.07).

#### 4.2.5 Synthesis of *P(BMA)-b-P(GMMA)-b-P(GMMA-stat-NHSMA-stat-FLUMA)* (P40).

The *P(BMA)-b-P(GMMA)-b-P(GMMA-stat-NHSMA-stat-FLUMA)* was prepared from the previously purified and dried P30 homopolymer. The P30 macro-CTA (68 repeating units, 1.92 g, 0.194 mmol), GMMA monomer (1.87 g, 11.7 mmol), ACVA radical initiator (10.5 mg, 0.038 mmol) and 1,3,5-trioxane internal standard (117 mg, 1.32 mmol) were dissolved into 13 mL of DMF. This reaction mixture was cooled and degassed by sparging N<sub>2</sub> gas for 30 min and, subsequently, placed into an oil bath preheated 70 °C for 3.5 h. After this time elapsed, 2 mL of a solution of DMF containing NHSMA (255 mg, 1.39 mmol) and FLUMA (22 mg, 0.055 mmol) (previously degassed by sparging N<sub>2</sub> gas for 20 min) were added into the polymerization reaction. The reaction proceeded for 6.5 h more at 70°C to allow the copolymerization of NHSMA and FLUMA monomers; thereafter the copolymerization reaction was quenched by cooling into an ice bath. The obtained polymer was dialyzed against acetone, recovered and dried under vacuum at 40°C for 48 h. The monomer conversions, as estimated via <sup>1</sup>H-NMR analysis, were 58 and 65 % for GMMA and NHSMA, respectively; these values were determined by comparing the integral value of the signals ascribed to the vinyl protons at 5.5 and 6.4 ppm for GMMA and 5.8 and 6.8 ppm for NHSMA with that of the signal ascribed to the proton of 1,3,5-trioxane. NHSMA units contained in the copolymer chains were additionally estimated via elemental analysis by monitoring nitrogen content in the copolymer sample, which yielded a content of ~2.7 (2.68) NHSMA units per chain. GMMA units contained in the copolymer chains were determined via a quantitative <sup>13</sup>C-NMR method (Inverse-Gated Decoupling) using DMF-d<sub>7</sub> by comparing the integral values of the signals ascribed to BMA at 64.69 ppm ( $-COO-\underline{C}H_2-CH_2-$ ) with that of the signals ascribed to GMMA at 63.60 ppm ( $-COO-CH_2-CHOH-\underline{C}H_2OH$ ), 66.78 ppm ( $-$

COO-CH<sub>2</sub>-CHOH-CH<sub>2</sub>OH) and 69.88 ppm (-COO-CH<sub>2</sub>-CHOH-CH<sub>2</sub>OH), DP<sub>G<sub>MMMA</sub></sub> = 31.  $M_{n, NMR} = 15400 \text{ g}\cdot\text{mol}^{-1}$  was determined using the DP values obtained for GMMA and NHSMA comonomers.  $M_{n, theo} = 16500 \text{ g}\cdot\text{mol}^{-1}$  was calculated using monomer conversion as obtained via <sup>1</sup>H-NMR analysis. SEC analysis of the diblock copolymer yielded  $M_{n, sec}$  and Đ values of 20500 g·mol<sup>-1</sup> and 1.13, respectively.

#### 4.2.6 Synthesis of peptide-bioconjugated copolymer.

PC1 (DSNKGVTAACPW) and PC3 (RPKVRDQEGRMW) peptides were conjugated to copolymers P20 and P40 via an ester activation strategy. First, the corresponding peptide and triethylamine (5 μL, 35.86 μmol for P20 conjugates and 15 μL, 107.64 μmol for P40 conjugates) were dissolved in 2 mL of DMF in a microwave vial. This solution was degassed for 15 min by sparging argon and, subsequently, added dropwise into another microwave vial containing the corresponding copolymer dissolved in 1 mL of DMF (previously degassed) and kept under magnetic stirring. The polymer-peptide solution was placed into an oil bath preheated at 50 °C for 24 h. After this time, amino-2-propanol (8 μL, 103 μmol) was added and the reaction further proceeded for 12 h. Thereafter, the unreacted peptide was removed via dialysis against a solvent/water mixture for 2 days. In a final step, the polymer-peptide bioconjugates were dried by lyophilization.

“Grafting to” with P20 copolymer. The general procedure described above was utilized for peptides PC1 (13 mg, 10.42 μmol) and PC3 (16.4 mg, 10.53 μmol) to bind to copolymer P20 (250 mg, 10.63 μmol, which contained a pentafluorophenyl ester functional unit at the end of each copolymer chain) in DMF. After reaction, the obtained mixture was dialyzed against acetone/water for 2 days; the obtained conjugates were dried by lyophilization.

“Grafting to” with P40 copolymer. The general procedure described above was carried out using peptides PC1 (21.8 mg, 17.51 μmol) and PC3 (18.7 mg, 12.05 μmol) to link to copolymer P40 (200 mg, 37.66 μmol, which contained reactive NHSMA comonomer units along the copolymer chains) in DMF. After reaction, the obtained mixture was precipitated into hexane (x2) and re-dissolved in ethanol for dialysis against ethanol/water for 2 days; the obtained polymer-peptide bioconjugates were dried by lyophilization.

#### 4.2.7 *Evaluations of potential cytotoxic effects of peptides and peptide-polymer conjugates*

The potential cytotoxicity of the investigated materials was evaluated using the Madin-Darby Canine Kidney (MDCK), HuH7 and HEPG2 cell lines following the standardized procedure described in the ISO10993-5 guideline. For the HuH7 cell line, the D10 low + HEPES was utilized as a cell medium, whereas for the MDCK and HEPG2 cell lines, the Dulbecco's Modified Eagle Medium (DMEM) Nutrient Mixture F12 supplemented with 10% fetal calf serum, 100 U mL<sup>-1</sup> penicillin, and 100 mg mL<sup>-1</sup> streptomycin (Biochrom, Berlin, Germany) was used as a culture medium. Cells were routinely cultured at 37°C in a humidified atmosphere containing 5% CO<sub>2</sub>. Cells were plated at a density of 10<sup>4</sup> cells per well in 96-well plates and grown for 24 h. After 24 h, the culture medium was replaced with a fresh one containing the dissolved peptides or the polymer-conjugates. Control cells were also incubated with a fresh culture medium. After additional 24 h of incubation, the medium was removed, cells were washed with PBS, and subsequently treated with PrestoBlue reagent diluted in culture medium according to the instructions of the manufacturer (Invitrogen, Germany). After 45 min of incubation at 37°C, fluorescence of the medium was measured at the wavelengths of Ex 560/Em 590 nm. Samples displaying a cell viability value higher than 70% were considered as non-cytotoxic. Experiments were performed in sextuplicate.

- *Evaluations of potential cytotoxic effects of peptides and peptide-polymer conjugates in the absence of DMSO.*

Several concentrations of nanoformulations containing each peptide or peptide-polymer conjugate (in the range from 0 up to 500 µg mL<sup>-1</sup> for peptides and from 0 up to 100 µg mL<sup>-1</sup> for polymer-conjugate) were prepared in the respective cell medium and 100 µL of each dilution were added into different wells containing cells; control cells were also incubated with fresh culture medium.

- *Cytotoxic evaluation of peptide-polymer conjugates in the presence of DMSO.*

The analyzed samples were also dissolved in mixtures containing DMSO; DMSO was also analyzed as a control sample to demonstrate that the utilized amounts of this compound have a negligible effect on the evaluated cytotoxicity.



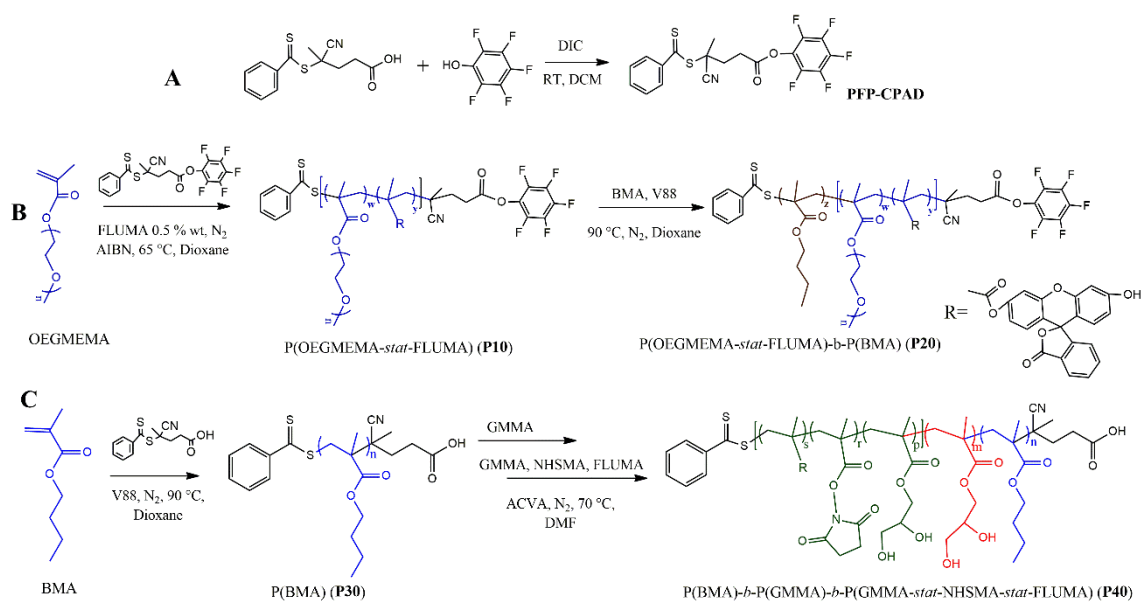
#### *4.2.8 Cell-uptake experiments and flow cytometry quantification*

Cellular uptake of the bioconjugates was determined via flow cytometry using MDCK cells plated in 12-well plates at a density of  $10^5$  cells per well. After 24 h, the culture medium was replaced by fresh medium containing the dissolved peptides or the peptide-polymer conjugates. Control cells were also incubated with fresh culture medium. All cells were incubated for additional 24 h, washed with PBS, harvested by trypsinization and re-suspended in PBS supplemented with 10% fetal calf serum. To determine the relative uptake of the peptide-polymer bioconjugates,  $10^4$  cells were quantified via flow cytometry using a Cytoflex S (Beckman Coulter) and a 488 nm laser for excitation and a FITC filter-set for detection of the emission signal.

For microscopic analysis, the cell nuclei were additionally stained with medium containing Hoechst 33342 dye ( $10 \text{ mg mL}^{-1}$ ) for 10 min, subsequently washed with medium, and immediately subjected to fluorescence imaging.

### 4.3 Synthesis and characterization of amphiphilic block copolymers based on GMMA and OEGMEMA

The P(OEGMEMA-*stat*-FLUMA)-*b*-P(BMA) (P20) block copolymer was synthesized via the RAFT polymerization technique according to **Scheme 4.1**. First, the synthesis involves the esterification of the corresponding RAFT agent to incorporate an active ester functional group derived from pentafluorophenol (PFP-CPAD) as depicted in **Scheme 4.1A**. The successful incorporation of the pentafluorophenyl ester was confirmed via  $^{19}\text{F}$ -NMR as is shown in **Figure 4.1A**. Next, a P(OEGMEMA-*stat*-FLUMA) macro-RAFT denominated as P10 was prepared using the previously synthesized PFP-CPAD RAFT agent (**Scheme 4.1B**); monomer conversion was kept relatively low (ca. 57 %) to maximize the living character of the synthesized polymer chains. The utilized content of fluorescent comonomer (FLUMA) was ~0.6 % mol relative to the content of OEGMEMA.  $^1\text{H}$ -NMR analysis of P10 revealed a DP of 25 and a  $M_{n,\text{NMR}}$  of  $13,000 \text{ g}\cdot\text{mol}^{-1}$  (see **Figure 4.2**), whereas SEC analysis yielded values of  $M_{n,\text{sec}}$  of  $8,800 \text{ g}\cdot\text{mol}^{-1}$  and  $\bar{D}$  of 1.14 (see **Figure 4.8A**). After this synthesis, a chain extension of the macro-RAFT with BMA monomer was performed to obtain the amphiphilic copolymer P20. The chemical structure of copolymer P20 was confirmed by  $^1\text{H}$ -NMR analysis using  $\text{CDCl}_3$  as solvent; **Figures 4.2** and **4.3** display the  $^1\text{H}$ -NMR spectra of P10 and P20, respectively. The fluorine signals ascribed to the presence of the pentafluorophenyl ester end group in P10 and P20 were analyzed via  $^{19}\text{F}$ -NMR (**Figures 4.1B and C**); the signals at -152.5 (*ortho*), -157.4 (*para*) and -161.9 (*meta*) ppm ascribed to the PFP-CPAD end-functional group were observed for both polymers. The monomer repeating units of OEGMEMA and BMA were 25 and 49 as determined via  $^1\text{H}$ -NMR analysis, respectively. The  $M_n$  and  $\bar{D}$  of copolymer P20 were 18.2 kDa and 1.1 as determined via SEC analysis (see **Figure 4.8A**), respectively; the  $M_n$  value obtained via  $^1\text{H}$ -NMR analysis was 23.5 kDa.



**Scheme 4.1** Scheme 4.1. Synthesis of amphiphilic block copolymers via RAFT Polymerization (A) Synthesis of functionalized PFP-CTAP RAFT agent. (B) Synthesis of P(OEGMEMA-*stat*-FLUMA)-*b*-P(BMA) (P20), (C) Synthesis of P(BMA)-*b*-P(GMMA)-*b*-P(GMMA-*stat*-NHSMA-*stat*-FLUMA) (P40).

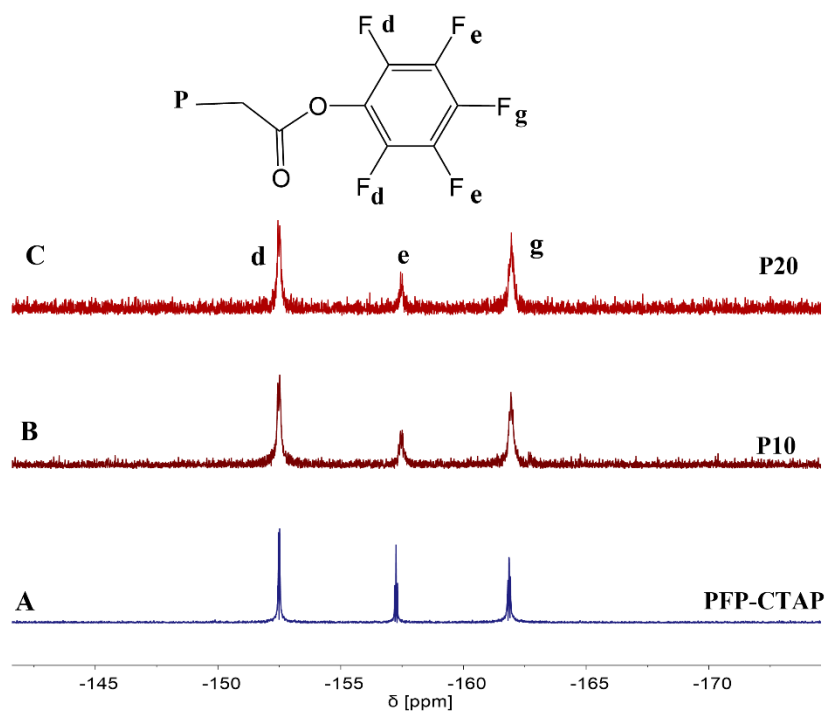


**Figure 4.1.**  $^{19}\text{F}$ -NMR spectra of (A) purified PFP-CTAP, (B) P10 and (C) P20 in  $\text{CDCl}_3$  (300 MHz).

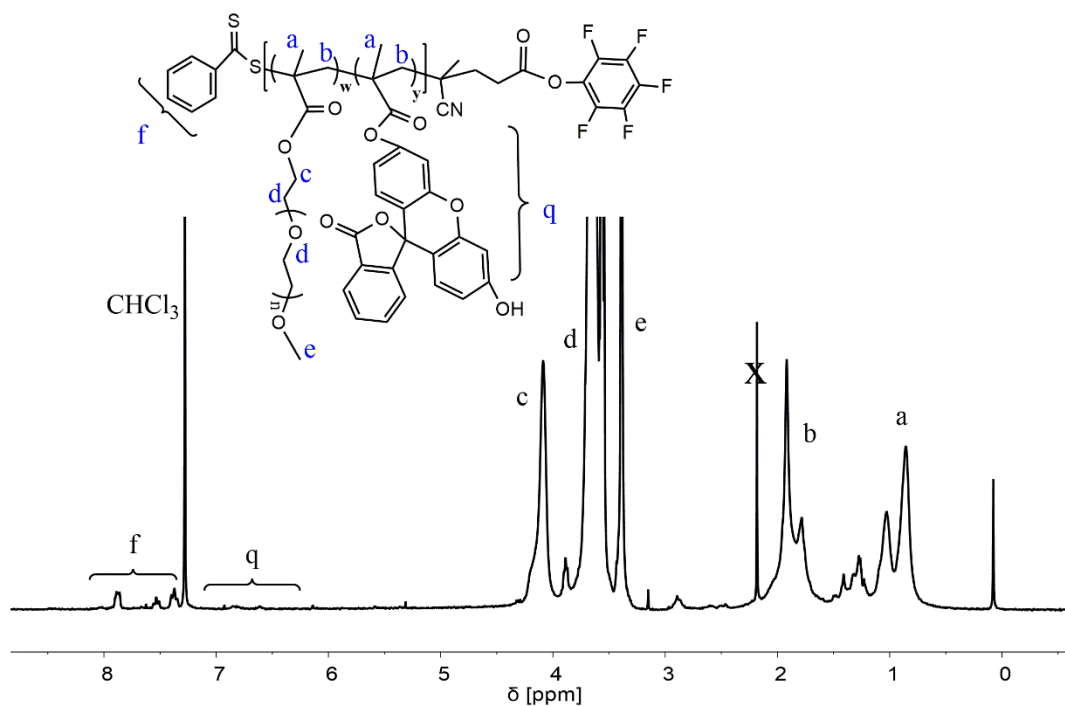


**Figure 4.2.**  $^1\text{H-NMR}$  spectrum of the synthesized P(OEGMEMA-*stat*-FLUMA) (copolymer P10) in  $\text{CDCl}_3$  (300 MHz).

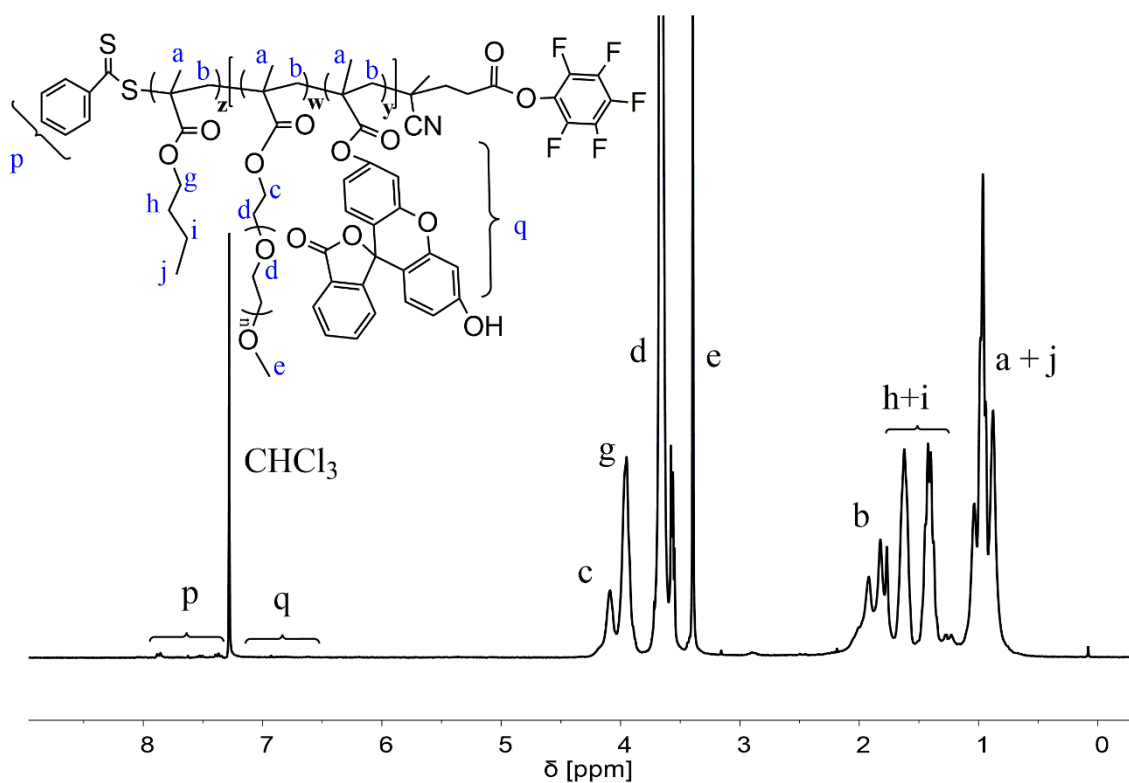


**Figure 4.3**  $^1\text{H-NMR}$  spectrum of the synthesized P(OEGMEMA-*stat*-FLUMA)-*b*-P(BMA) (copolymer P20) in  $\text{CDCl}_3$  (300 MHz).

The RAFT polymerization technique was also utilized to prepare the second polymer system investigated in this work. A P(BMA) (P30) macro-CTA was first synthesized and subsequently, chain-extended with a hydrophilic segment (**Scheme 4.1C**). The synthesis of P30 was achieved at 50 % of BMA conversion.  $^1\text{H-NMR}$  analysis of P30 revealed a DP of 68 and a  $M_{n,\text{NMR}}$  of  $9900 \text{ g}\cdot\text{mol}^{-1}$  (see **Figure 4.4**), whereas SEC analysis yielded values of  $M_{n,\text{sec}}$  of  $9000 \text{ g}\cdot\text{mol}^{-1}$  and  $\mathcal{D}$  of 1.07 (see **Figure 4.8B**). For the second step of the synthesis, the monomer feeding during the chain extension reaction was carried out in two steps. Firstly, the polymerization of pure GMMA proceeded up to 41% monomer conversion. Subsequently, NHSMA and FLUMA comonomers were added into the polymerization reaction mixture to enable the incorporation of the reactive amino and fluorescent groups towards the end of the copolymer chains. Previous reports from our group (see also Chapter 3) demonstrated that during the copolymerization of the comonomers NHSMA and GMMA, a radical chain ending with a NHSMA unit has no preference to add either a NHSMA or GMMA monomer units.[190] Hence, the chemical structure of copolymer P40 was confirmed by  $^1\text{H-NMR}$ ; however, some signals ascribed to the GMMA and NHSMA moieties overlap in the spectrum, which potentially complicates a quantitative analysis (see **Figure 4.5**). Therefore, a  $^{13}\text{C-NMR}$  spectrum recorded using the inverse-gated decoupling (IGD) technique (see **Figure 4.6**) was utilized to estimate the content of repeating units of GMMA. For this purpose, the integral value of the signal ascribed to the BMA units at 64.69 ppm ( $-\text{COO}-\underline{\text{C}}\text{H}_2-\text{CH}_2-$ ) was compared with that of the signals ascribed to the GMMA units at 63.60 ppm ( $-\text{COO}-\text{CH}_2-\underline{\text{C}}\text{HOH}-\text{CH}_2\text{OH}$ ), 66.78 ppm ( $-\text{COO}-\underline{\text{C}}\text{H}_2-\text{CHOH}-\text{CH}_2\text{OH}$ ) and 69.88 ppm ( $-\text{COO}-\text{CH}_2-\underline{\text{C}}\text{HOH}-\text{CH}_2\text{OH}$ ); the results obtained from this analysis were  $\text{DP}_{\text{GMMA}}$  of 31 and  $\text{DP}_{\text{BMA}}$  of 68. Regarding the content of NHSMA in copolymer P40, a  $\text{DP}_{\text{NHSAMA}}$  value of 2.68 was estimated based on the content of nitrogen in the copolymer as determined via the elemental analysis technique (see **Figure 4.7**). Note that a difference between the  $M_{n,\text{NMR}}$  ( $15400 \text{ g}\cdot\text{mol}^{-1}$ ) and  $M_{n,\text{sec}}$  ( $20500 \text{ g}\cdot\text{mol}^{-1}$ ) of P40 was found, which has also been reported in previous investigations also utilizing a SEC system employing DMAc + 0.21 wt% LiCl as an eluent;[190] however, the utilization of such solvent mixture is preferred due to its ability to solubilize different amphiphilic block copolymer systems. **Figure 4.8B** displays the SEC chromatograms of polymers P10 to P40; all the chromatograms revealed a monomodal distribution and a low  $\mathcal{D}$  value. The  $M_{n,\text{NMR}}$ ,  $M_{n,\text{sec}}$  and  $\mathcal{D}$  values recorded for all the polymers described in this chapter (P10, P20, P30 and P40) are summarized in **Table 4.1**

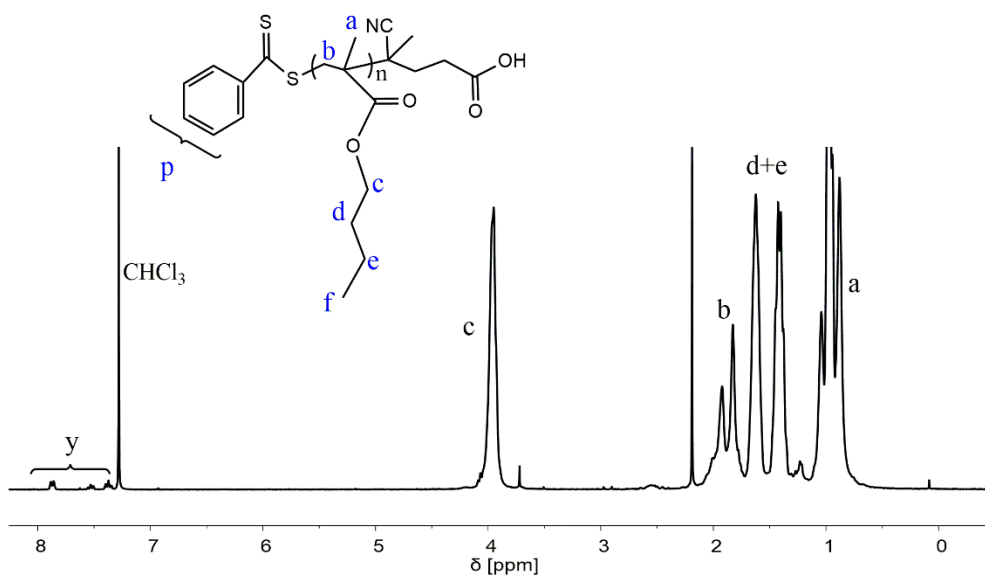


**Figure 4.4.**  $^1\text{H-NMR}$  spectrum of synthesized PBMA (homopolymer P30) in  $\text{CDCl}_3$  (300 MHz)

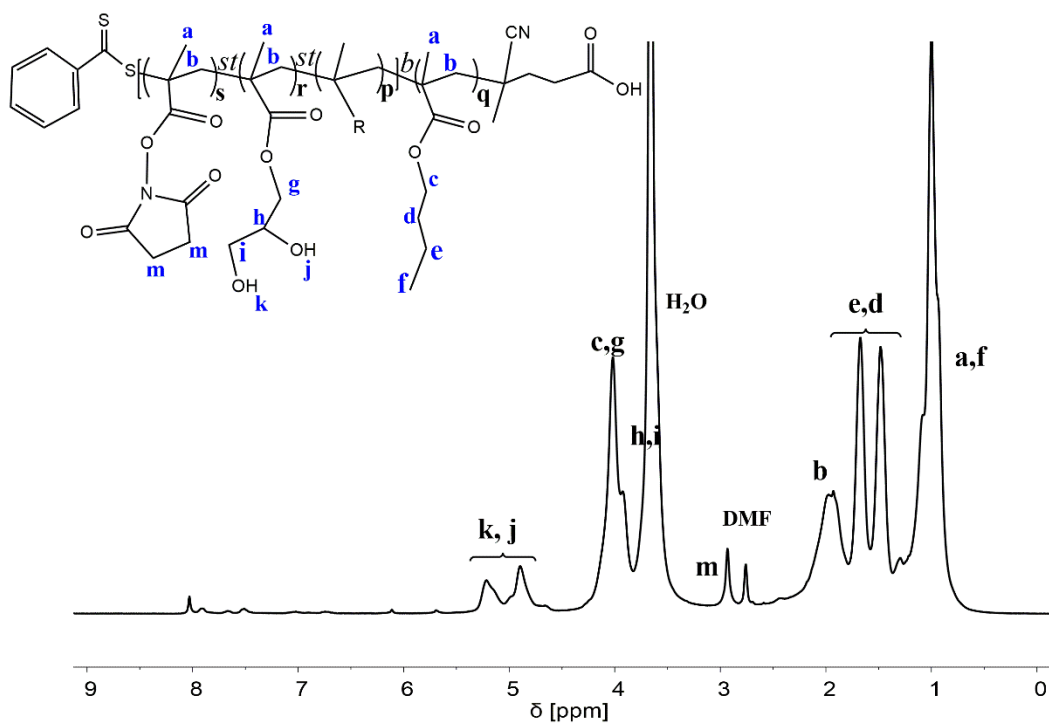


**Figure 4.5**  $^1\text{H-NMR}$  spectrum of P(BMA)-*b*-P(GMMA)-*b*-P(GMMA-*stat*-NHSMA-*stat*-FLUMA) (copolymer P40) in  $\text{DMF-d}_7$  (300 MHz).

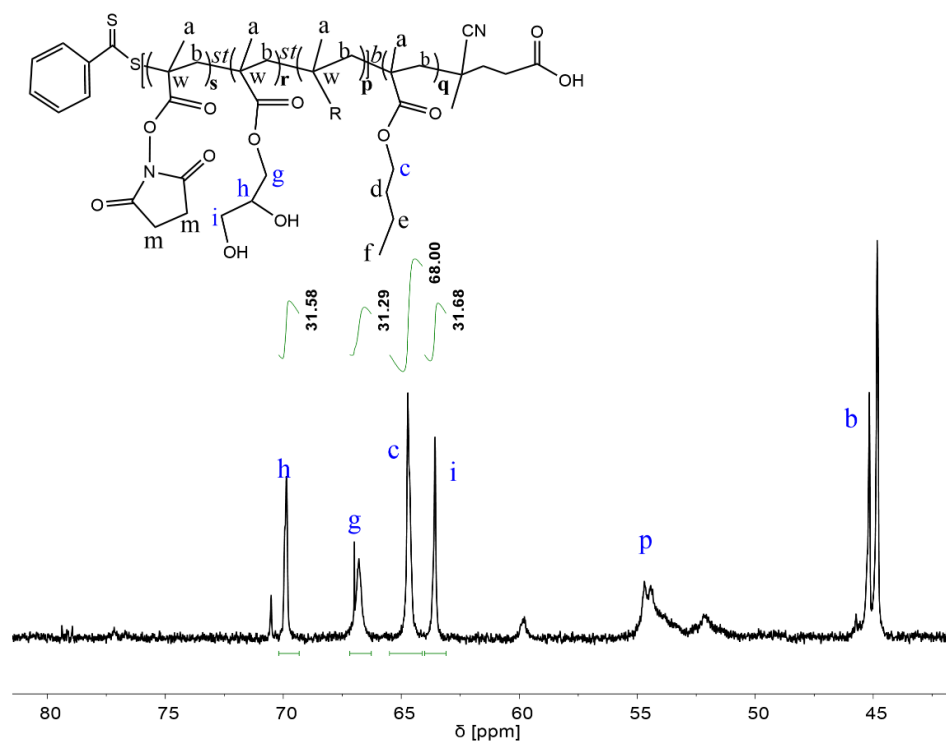


**Figure 4.6** <sup>13</sup>C NMR spectrum (using the Inverse-Gated Decoupling technique) of P(BMA)-*b*-P(GMMA)-*b*-P(GMMA-*stat*-NHSMA-*stat*-FLUMA) (copolymer P40) in DMF-*d*7 utilized for a quantitative analysis.

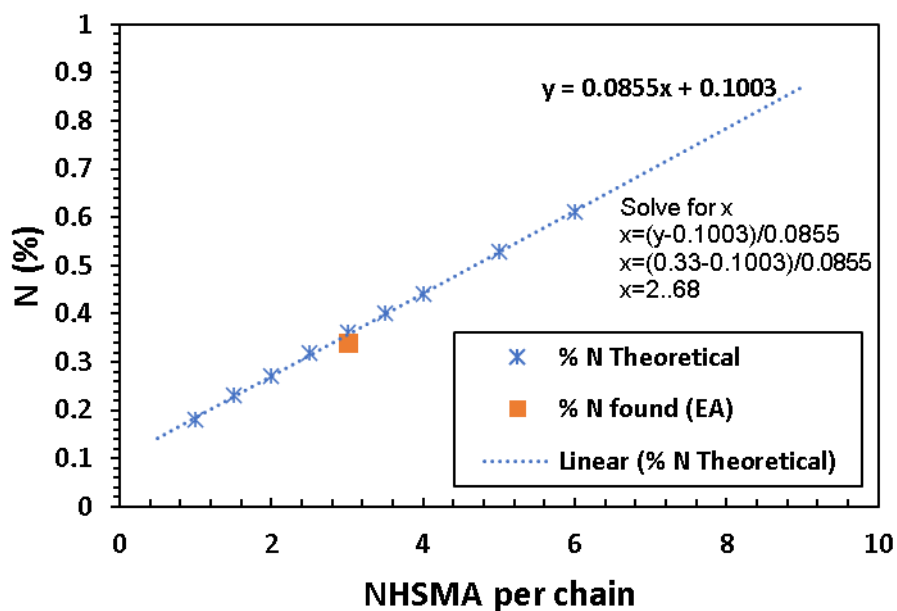


**Figure 4.7** Elemental analysis results for copolymer P40.

**Table 4.1** Summary of some physicochemical properties of polymers P10 to P40.

Entry	Composition [mol %]					AEC	$M_n^{b,theo}$ (kDa)	$M_n^c,NMR$ (kDa)	$M_n^d,SEC$ (kDa)	$D^d$
	M1	M2	M3	M4	M5					
P10	99.6	0.4	-	-	-	1	10.5	13.0	8.8	1.14
P20	25.1	0.1	74.7	-	-	1	23.8	23.5	18.2	1.12
P30	-	-	100	-	-	-	9.1	9.9	9.0	1.07
P40	-	0.1	66.6	30.4	2.68 <sup>e</sup>	2.68 <sup>f</sup>	16.5	15.4	20.5	1.13

Where M1: OEGMEMA, M2: FLUMA, M3: BMA, M4: GMA and M5: NHSMA. <sup>a</sup> Calculated using DP or NMR signal integration of each comonomer obtained from <sup>1</sup>H-NMR and/or <sup>13</sup>C-NMR analysis. <sup>b</sup>  $M_{n,theo} = ([Monomer]_0/[CTA]_0 \times Conv. \times M_M) + M_{CTA}$ , where  $[Monomer]_0$  and  $[CTA]_0$  are the initial concentrations of monomer and CTA, respectively. Conv. is the monomer conversion and  $M_M$  and  $M_{CTA}$  are the molar mass of monomer and RAFT agent, respectively. <sup>c</sup>  $M_{n,NMR} = (DP \times M_M + M_{CTA})$ . <sup>d</sup> Determined by SEC with an eluent of DMAc + 0.21 % LiCl, refractive index (RI) detection and a calibration curve prepared from poly(methyl methacrylate) (PMMA) standards of narrow dispersity. <sup>e</sup> Obtained by elemental analysis, from  $y=0.0855x + 0.1003$ , Solve for x,  $x=(y-0.1003)/0.0855$ ,  $y=0.33$ ,  $x=2.68$ . AEC: Activated ester per chain.

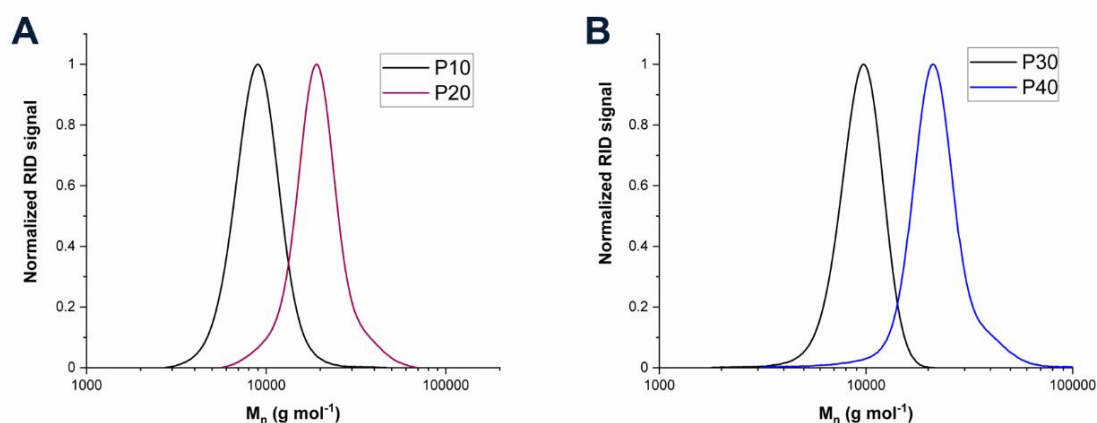


**Figure 4.8** SEC chromatograms of the investigated polymers A) P10 copolymer and corresponding P20 block copolymer. B) P30 macro-RAFT and corresponding P40 copolymer. The SEC equipment utilized DMAc + 0.21 wt% LiCl was used as an eluent, refractive index (RI) detection and a calibration curve prepared from P(methyl methacrylate) (PMMA) standards of narrow dispersity.

## 4.4 Characterization of peptides PC1-PC3

### 4.4.1 Physicochemical properties of PC1-PC3 peptides

Theoretical physicochemical properties of PC1-PC3 peptides were estimated using the ProtParam tool in the ExPASy server (<https://web.expasy.org/protaram/>). These properties are pI, instability index, aliphatic index, and GRAVY (summarized in **Table 4.2**). The theoretical pI is the pH value where the net charge is zero; generally, close to this pH value, the solubility of the corresponding protein or peptide decreases.[131] In this study,



the pI value of PC1 to PC3 peptides ranges from 3.8 to 10.74. The instability index (II) relates to the stability of a certain amino acid sequence where values higher than 40 are considered unstable.[133] Given that, the II value obtained for PC1 and PC2 were higher than 40, whereas PC3 yielded a value of 24.17 being the only peptide (from the ones investigated in this work) considered as stable. Likewise, the GRAVY value for each peptide was calculated using the hydropathy values from Kyte and Doolittle.[127] Positive and negative values relate to the hydrophobic and hydrophilic nature of the corresponding protein or peptide, respectively. The negative GRAVY value obtained for all the investigated peptides suggests a rather hydrophilic nature. Finally, the aliphatic index considers the relative volume occupied by the aliphatic side chains (alanine, valine, isoleucine, leucine, etc.) of a certain peptide. A high value of aliphatic index suggests an increase in the thermo-stability of globular proteins.[134] The aliphatic index value obtained for the analyzed peptides follow the order PC2 > PC1 > PC3, which suggests that the PC2 compound is the most thermostable of the three pristine peptides (see **Table 4.2**).

**Table 4.2** Theoretical physicochemical properties of peptides PC1-PC3, PC1-5FAM, and PC3-5FAM.

Entry	Sequence	M <sub>w</sub> (g mol <sup>-1</sup> )	n	pI***	Aliphatic index	Instability index	GRAVY
PC1	NH2-DSNKGVTAAACPW (P220)	1247.4	12	5.83	40.83	81.07	-0.417
PC2	NH2-DQQSLYQNAW (P190)	1251.4	10	3.8	49	72.2	-1.49
PC3	NH2-RPKVRDQEGRMW (P130)	1557.2	12	10.74	24.17	34.19	-2.058
PC1-5FAM	5FAM-DSNKGVTAAACPW	1606.1	12	-	-	-	-
PC3-5FAM	5FAM-RPKVRDQEGRMW	1915.8	12	-	-	-	-

**Figure 4.9** depicts predictions of the secondary structure of PC1, PC2 and PC3 linear peptides generated by two online computational tools, PEP-FOLD3[191] and I-TASSER[192]. These secondary structure predictions and confidence scores were simulated using the I-TASSER server; the values obtained for the confidence scores range from 0 to 9 (a high value suggests a higher confidence in the predicted structure of the corresponding sequence of amino acids). A coiled conformation was revealed in all the investigated peptides; however, the  $\alpha$ -helical conformation predominated for peptide PC2. The 3D peptide structures predicted by the PEP-FOLD3 platform were taken from Model 1. In our case, an  $\alpha$ -helical conformation was dominant for PC2 and in a considerable segment of PC3 but absent in PC1. The local structure prediction generated by PEP-FOLD3 is a graphical representation of the probabilities of structural alphabet[193] (*i.e.*, set of 27 letters to describe protein conformation as a series of overlapping fragments of four amino acids) at each position of the sequence.[194] This graphical representation is

displayed with a color code corresponding to red: helical, green: extended, and blue: coil. The results of this graphical representation also revealed that the probability of generating a helical structure is higher in PC2 as compared to peptides PC1 and PC3, where a coil conformation predominates. As explained above, peptides PC1-PC3 correspond to amino acid sequences derived from the HA protein of the influenza A virus. PC1 and PC3 peptides in the HA protein acquire a coil conformation, whereas PC2 is part of an  $\alpha$ -helix conformation. In this investigation, computational analysis revealed that most of the segments of PC1 and PC2 peptides reveal a conformation similar to that found in the HA protein, in contrast, only a part of the PC3 peptide undergoes a conformational change to adopt an  $\alpha$ -helix structure.

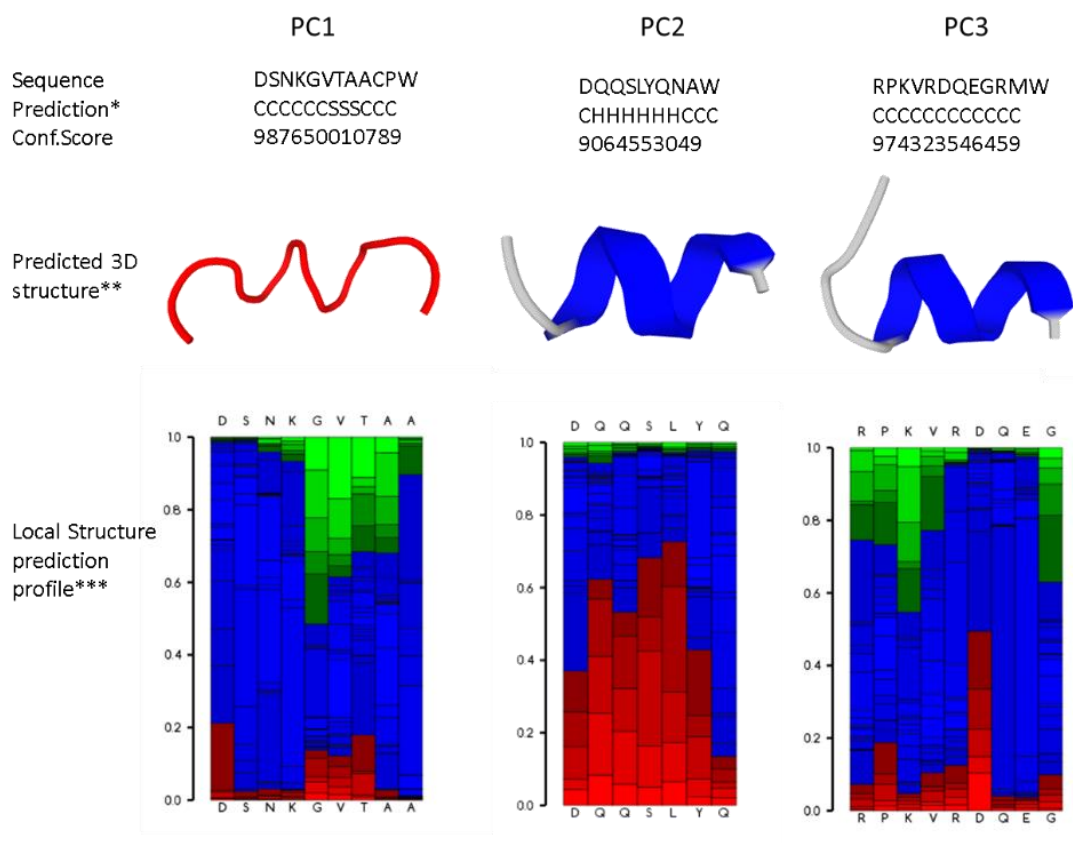


**Figure 4.9** Secondary structure of the investigated peptides generated with the PEP-FOLD3 and I-TASSER platforms. \* Prediction of secondary structure and confidence scores were computed by the iterative threading assembly refinement (I-TASSER) server, H: Helix; S: Strand; C: Coil. (Zhang Lab, University of Michigan (2018) I-TASSER Protein Structure and Function Predictions [Internet]. <https://zhanglab.cmb.med.umich.edu/I-TASSER/>. Accessed 06 December 2021) \*\* Three-dimensional (3D) models were predicted by the PEP-FOLD3 platform using 100 simulations. \*\*\*The local structure predictions were generated with PEP-FOLD3 platform; the color code corresponds to red: helical, green: extended, and blue: coil.

#### 4.4.2 Characterization of PC1-PC3, PC1-5FAM and PC3-5FAM peptides by NMR

The chemical structure of each peptide was also investigated via NMR spectroscopy. **Figures 5.1 to 5.5 in Appendix** display the  $^1\text{H}$ -NMR spectrum of PC1, PC1-5FAM, PC2, PC3 and PC3-5FAM peptides in DMSO-*d*<sub>6</sub>, respectively. Peptides with a 5FAM-ending contain a 5-carboxyfluorescein terminal unit. Although PC1 and PC1-5FAM peptides show similar signals in the upfield region, differences are more evident downfield (from 7.5 ppm onwards) due to the presence of the fluorescein moiety (5FAM). Moreover, an increase in the intensity of the signals ascribed to the vinyl protons was observed in the 5-7 ppm region. Likewise, similar signals were observed for PC3 and PC3-5FAM peptides from 0 to ~7.5 ppm; however, and similar to PC1-5FAM, new signals arose for PC3-5FAM in the 6.5 to 9 ppm region.

#### 4.4.3 Fluorescence properties of the investigated peptides

Fluorescence properties of PC1-PC3, PC1-5FAM, and PC3-5FAM peptides were scrutinized using three-dimensional excitation-emission matrix (3D-EEM) fluorescence spectroscopy, which allows scanning the fluorescence intensity at different excitation and emission wavelengths and provides valuable information about the fluorescence distribution.[195] In this investigation, we combined tryptophan residues with each peptide sequence to evaluate their conjugation. Hence, all the investigated peptides contain a tryptophan (Trp) residue; nevertheless, only PC1-5FAM and PC3-5FAM peptides bear a covalently attached fluorescein dye moiety.

Trp, an amino acid with a high quantum yield, is primarily responsible for the fluorescence properties of several proteins.[116,196,197] The ultraviolet light absorption of Trp in an aqueous solution is characterized by two bands with excitation wavelengths centered at 220 and 280 nm, and due to the presence of two electronic absorption transitions ( $^1\text{L}_a$  and  $^1\text{L}_b$  states).[198] Additionally,  $^1\text{L}_a$  and  $^1\text{L}_b$  transitions are highly impacted by the polarity of their surroundings. In nonpolar environments, the  $^1\text{L}_b$  state dominates emission; nevertheless, in polar solvents that promote hydrogen bonds, emission is dominated by the  $^1\text{L}_a$  state that shifts to a longer wavelength (red shift) and a decrease in intensity is normally observed[115,116,199] In aqueous medium, the maximum emission occurs around 357 nm when excitation takes place at 280 nm.[198]

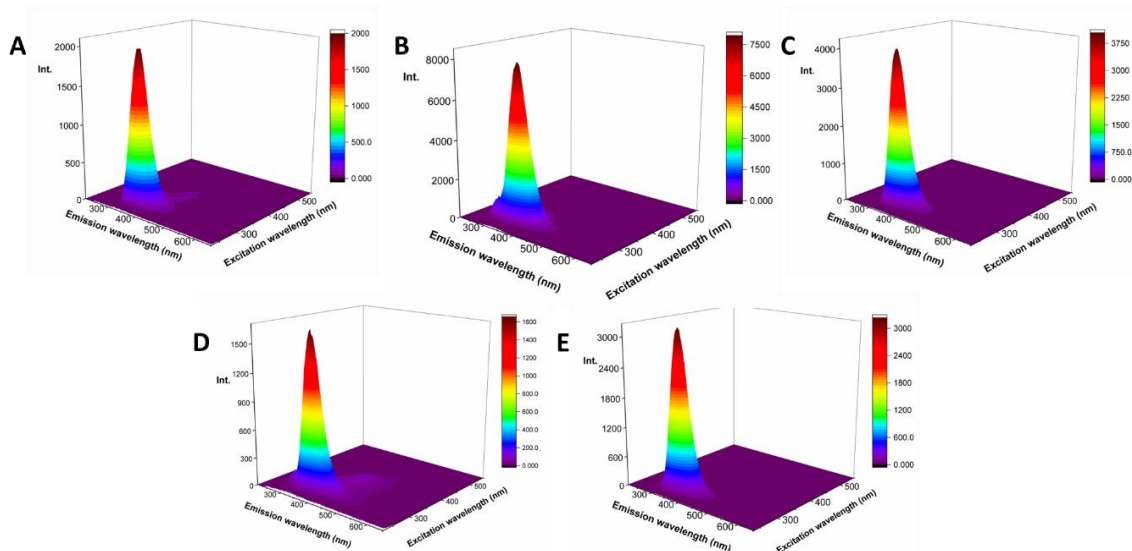


**Figure 4.10** 3D Fluorescence spectra plots of the investigated peptides in DMSO at  $T = 25\text{ }^{\circ}\text{C}$ . A) PC1 ( $1.6\text{ }\mu\text{M}$ ;  $0.002\text{ mg mL}^{-1}$ ). B) PC2 ( $3.2\text{ }\mu\text{M}$ ;  $0.004\text{ mg mL}^{-1}$ ). C) PC3 ( $2.57\text{ }\mu\text{M}$ ;  $0.004\text{ mg mL}^{-1}$ ). D) PC1-5FAM ( $2.49\text{ }\mu\text{M}$ ;  $0.002\text{ mg mL}^{-1}$ ). E) PC3-5FAM ( $2.09\text{ }\mu\text{M}$ ;  $0.004\text{ mg mL}^{-1}$ ).

**Table 4.3** Summary of  $\lambda_{\text{ex}} / \lambda_{\text{em}}$  signal of the investigated peptides in DMSO and PBS.

Peptide	Signal 1		Signal 2		Solvent
	$\lambda_{\text{ex}} / \lambda_{\text{em}}$ , nm/nm	F, a.u.	$\lambda_{\text{ex}} / \lambda_{\text{em}}$ , nm/nm	F, a.u.	
PC1	285/342.5	1868	-	-	DMSO
PC1	220/353.5	967	280/351	921	PBS
PC2	285/347.5	8002	-	-	DMSO
PC3	285/339	4111	-	-	DMSO
PC3	225/359	1418	280/359	1492	PBS
PC1-5FAM	285/342	2136	-	-	DMSO
PC1-5FAM*	240/524.5	8549	320/525	3639	PBS
PC3-5FAM	285/341	3232	-	-	DMSO
PC3-5FAM	240/521.5	9405	325/521.5	4261	PBS

The experiments were performed at room temperature, the concentration of the samples was  $4\text{ }\mu\text{g mL}^{-1}$ , except for PC1-5FAM\* ( $2\text{ }\mu\text{g mL}^{-1}$ ).

**Table 4.3** summarizes maximum excitation and emission values of the investigated peptides in DMSO and PBS. As observed in **Figure 4.10**, the 3D-EEM plots of all the peptides in DMSO apparently have a single Trp fluorescence signal with the same excitation maximum located at 285 nm, whereas the wavelength for the recorded maximum emission values differed for each compound. As aforementioned, the indole chromophore present in the Trp molecule is sensitive to microenvironmental and conformational changes.[200][201] In this study, PC2 peptide exhibited an emission maxima at longer wavelengths than that of PC1 and PC3; PC2 also revealed the highest aliphatic index value and a major proportion of an  $\alpha$ -helical conformation (see **Table 4.2**). Hence, one can speculate that the Trp residue in the  $\alpha$ -helical conformation of PC2 is

prone to form hydrogen bonds and/or to establish other non-covalent interactions with the surroundings, which may lead to slight changes in the emission maximum.

On the other hand, fluorescein derivatives contain dissociable carboxyl and aryl hydroxy groups that are sensitive to pH and to solvent polarity. For instance, fluorescence intensity decreases as the hydrogen bonding strength decreases.[117] Fluorescein in aqueous medium can exist in cationic, neutral, monoanionic and dianionic forms; this ionization equilibrium also involves the formation of a non-fluorescent neutral lactone.[202] As observed in **Figures 4.10D** and **E**, no signal ascribed to fluorescein (5FAM) could be detected in DMSO (although there are contrary reports in the literature in this regard [117]).

The non-fluorescent lactone form is typically found in non-polar solvents, such as isopropanol and cyclohexane.[118][116] Nonetheless, DMSO is a hydroscopic solvent, whose water content has an impact on its polarity and solvation response.[203][201][117] In this research, anhydrous DMSO was used, which may promote a decrease in fluorescence ascribed to fluorescein due to the “absence” of hydrogen bonds; however, the presence of the non-fluorescent lactone form cannot be discarded.

**Figure 4.11** shows excitation-emission contour plots of PC1, PC1-5FAM, and PC3-5FAM in PBS (PC2 was discarded due to its low solubility in PBS), whereas the corresponding 3D-EEM plots are displayed in **Figure 4.12**. Two signals ascribed to Trp can be observed in the corresponding contour plots of PC1 and PC3 in PBS (see **Figures 4.11 A** and **C**); however, only one signal was detected in DMSO (see **Figures 4.13 A** and **C**). The shift to longer wavelengths from PBS to DMSO, and the visualization of a single fluorescent signal in DMSO can be correlated to a change in solvent polarity, which affects the  $^1L_a$  and  $^1L_b$  transitions.[114]

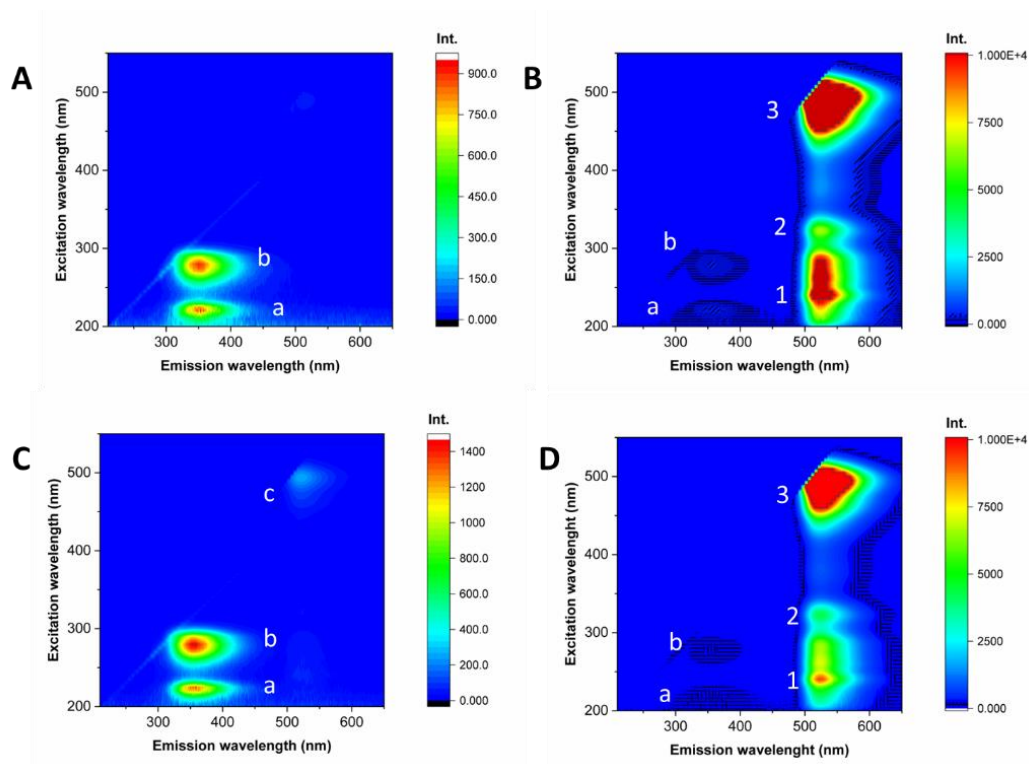


**Figure 4.11** Excitation-emission contour plots of investigated peptides in physiological solution at pH 7.4 (PBS) and  $T = 25\text{ }^{\circ}\text{C}$ . A) PC1 ( $3.21\text{ }\mu\text{M}$ ). B) PC1-5FAM ( $2.49\text{ }\mu\text{M}$ ). C) PC3 ( $2.57\text{ }\mu\text{M}$ ). D) PC3-5FAM ( $2.09\text{ }\mu\text{M}$ ).

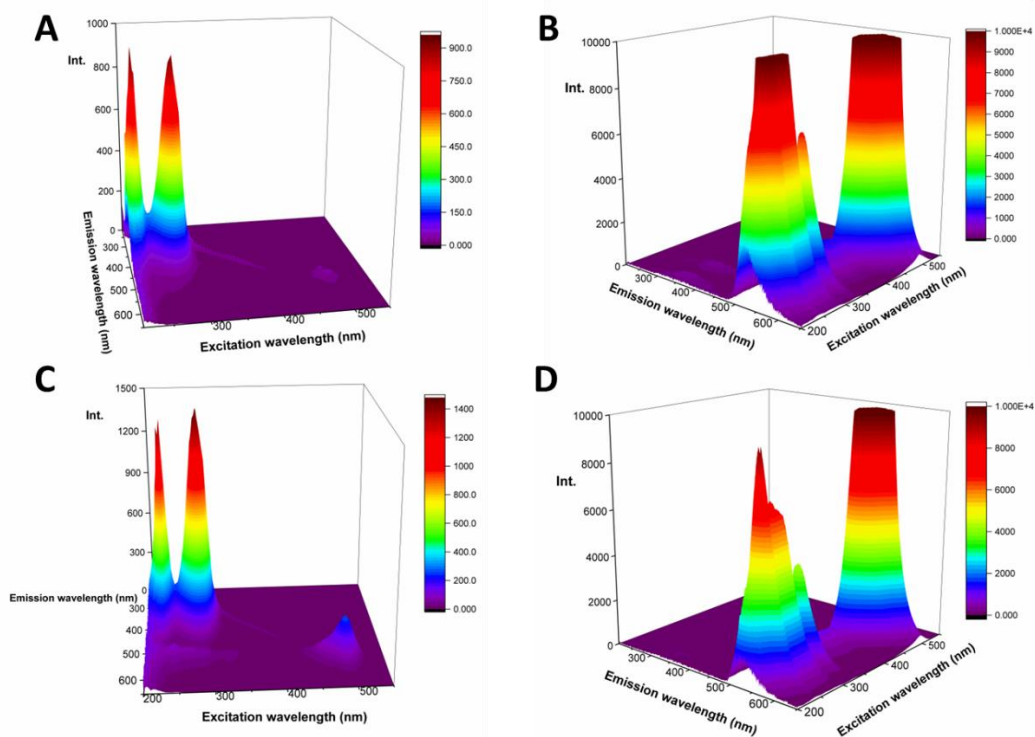


**Figure 4.12** Fluorescence spectra of investigated peptides in PBS at  $T = 25\text{ }^{\circ}\text{C}$  and  $4\text{ }\mu\text{g mL}^{-1}$ . A) PC1 ( $3.2\text{ }\mu\text{M}$ ). B) PC1-5FAM ( $2.5\text{ }\mu\text{M}$ ). C) PC3 ( $2.57\text{ }\mu\text{M}$ ) and D) PC3-5FAM ( $2.1\text{ }\mu\text{M}$ ).

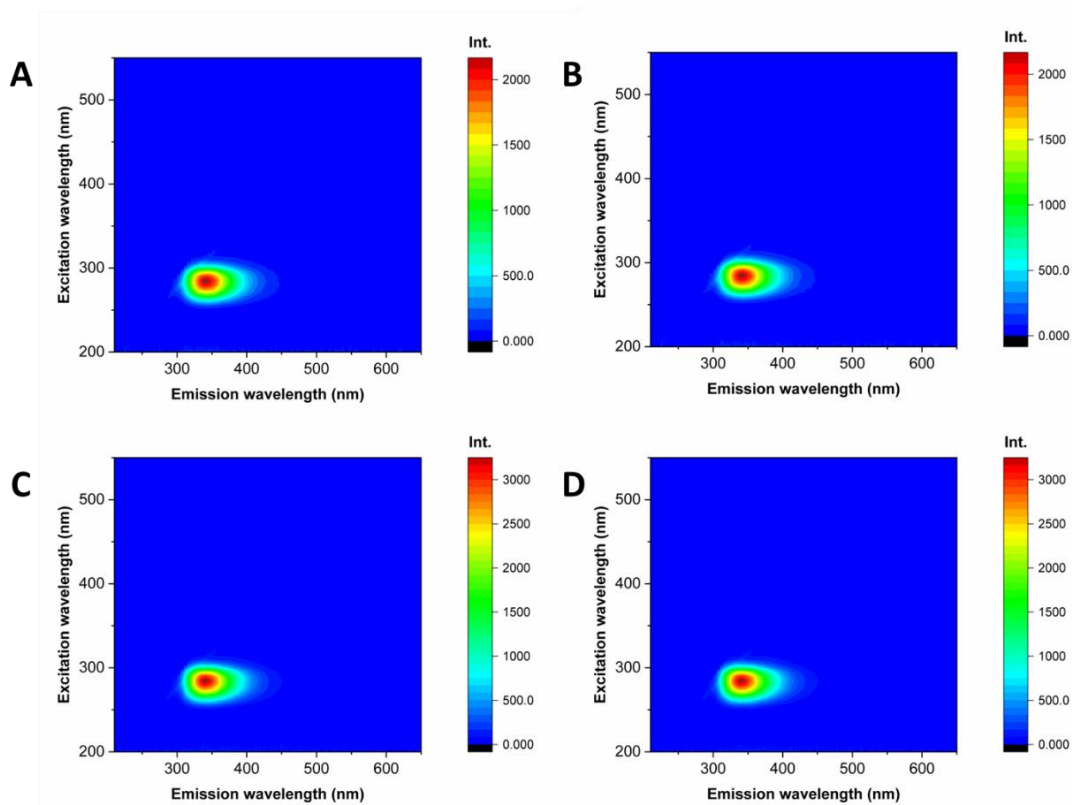


**Figure 4.13** Excitation-emission contour plots of investigated peptides in DMSO at  $4 \mu\text{g mL}^{-1}$  and  $T=25^\circ\text{C}$ . A) PC1. B) PC1-5FAM. C) PC3. D) PC3-5FAM.

**Figures 4.11 B** and **C** display the excitation-emission contour plots of PC1-5FAM and PC3-5FAM in PBS, signals “a” and “b” are ascribed to the Trp residue. Signal “c” (a non-fluorescence signal) in **Figure 4.11C** refers to the Rayleigh scattering ( $\lambda_{\text{ex}}=\lambda_{\text{em}}$ ).[197,198,204]. The values of signals “1” ( $\sim 240 \text{ nm}$ ) and “2” ( $\sim 320\text{-}325 \text{ nm}$ ) in the UV region, which relate to 5FAM absorption, are similar to those previously reported for the dianion form,[120] whereas signal “3” is attributed to the fluorescence of 5FAM ( $\sim 520 \text{ nm}$ ). Absorption and fluorescence signals were relatively wide due to the contribution of different fluorescein forms; at pH 7.4, the dianion form is dominant and followed by the monoanionic form.[119] The large difference in intensity between Trp and 5FAM moieties is associated with their corresponding quantum yield value (i.e., 0.13 and 0.95, respectively).[116] Moreover, Marmé et al.[121] reported the formation of a non-fluorescent complex between Trp and fluorescein in a buffer solution of pH value 7.4; the presence of this complex could also contribute to fluorescence quenching both Trp and 5FAM moieties in the peptides. [205,206] However, it would be necessary to perform additional experiments in order to confirm that hypothesis. Furthermore, fluorescence intensity curves (**Figure 4.19**) of peptides PC1 to PC3 in anhydrous DMSO

were recorded using a  $\lambda_{\text{ex}} = 360 \text{ nm}$  at different concentrations; the corresponding calibration plots of fluorescence intensity vs. concentration are also shown in **Figure 4.19**.

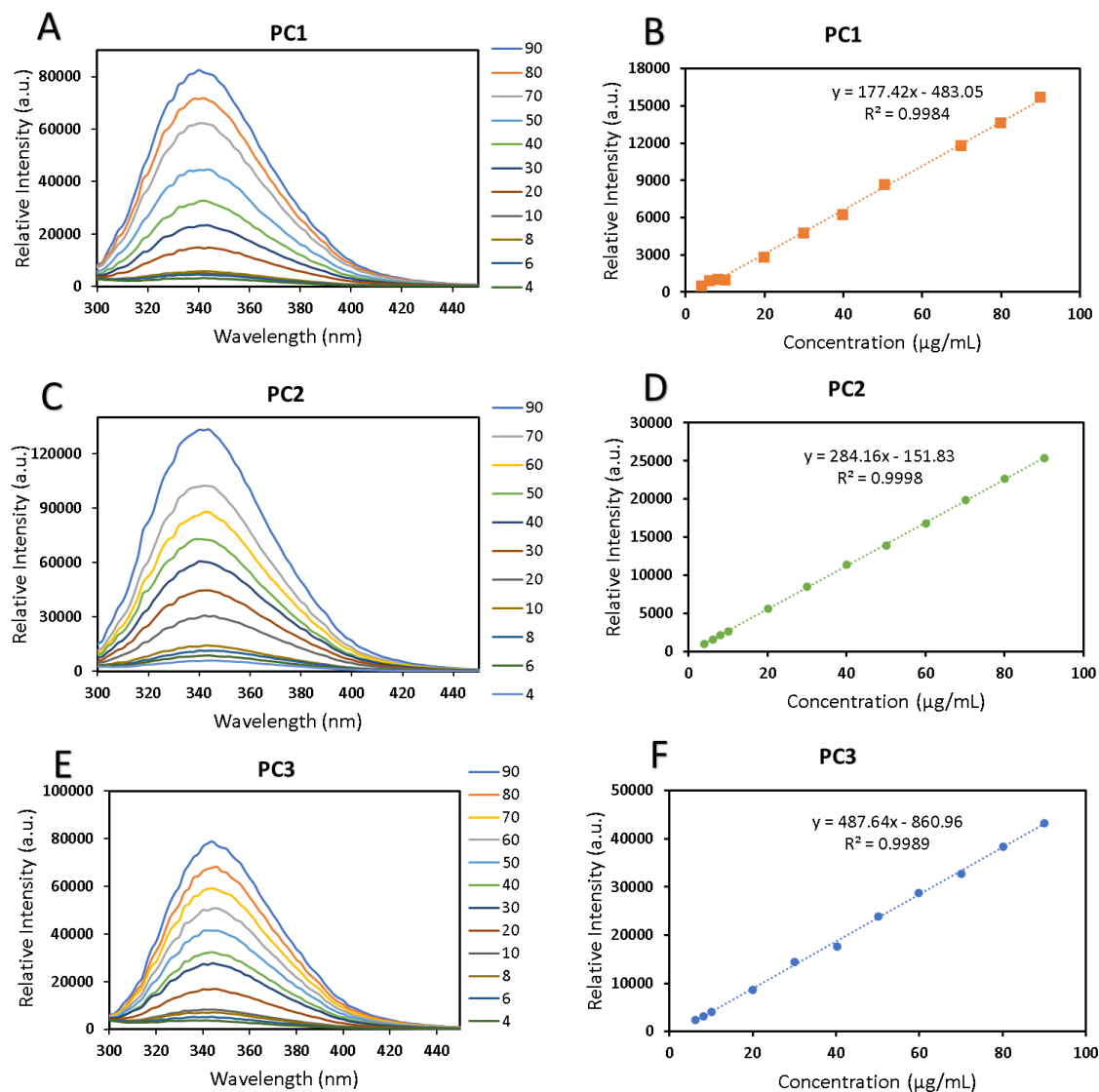
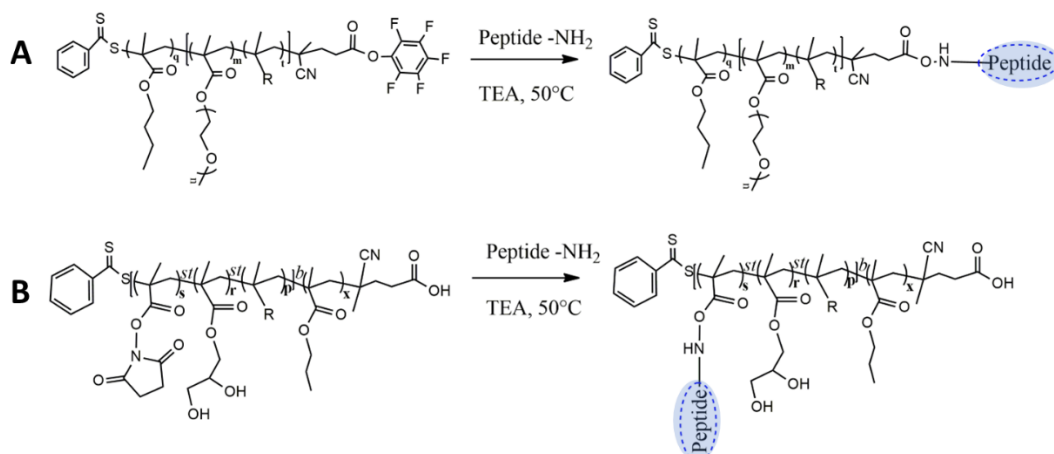


**Figure 4.14** Fluorescence spectra of peptides PC1 to PC3 in anhydrous DMSO using a  $\lambda_{\text{ex}} = 360 \text{ nm}$  at different concentrations (ca 90.04, 80.03, 70.18, 60.13, 50.13, 40.06, 29.91, 20.18, 10.18, 8.11, 6.13 and 3.99  $\mu\text{g mL}^{-1}$ ) (A, C and E). Generated calibration calibration plots of fluorescence intensity vs concentration (B, D and F).



## 4.5 Conjugation of peptides with amphiphilic block copolymers



**Scheme 4.2** Conjugation route of peptides derived from HA and amphiphilic block copolymers. A) Aminolysis of PFP-CTAP in P(OEGMEMA-*stat*-FLUMA)-*b*-P(BMA) (P20) and peptides. B) Synthesis of P(BMA)-*b*-P(GMMA)-*b*-P(GMMA-*stat*-NHSMA-*stat*-FLUMA)-peptide (P40-peptide) conjugate via aminolysis of NHSMA. C) Scheme of peptide-polymer conjugation.

Herein, PC1 and PC3 peptides were coupled to P20 and P40 copolymers through an amidation reaction as illustrated in **Scheme 4.2**. Conjugation aims to increase the internalization capacity and decrease the cytotoxicity of NPs (biological assays are described in the paragraphs of the following sections). Firstly, the “grafting to” strategy was explored using OEGMEMA copolymer (P20) with a RAFT agent with pentafluorophenyl ester terminal (See **Scheme 4.2A**); for this research we discarded the copolymerization of OEGMEMA and pentafluorophenyl ester monomers due to low conjugation yield previously observed by Alex *et al.*[207] On the other hand, the “grafting-to” method was also considered for the second system (See **Scheme 4.2B**); in this regard, inspired by a promising statistical copolymer of GMMA and NHSMA previously reported by Lamm *et al.* for coupling C-terminal lysine of fibrin-binding peptide to the NHSMA comonomer.[112,208] Due to the potential application of P(GMMA-*st*-NHSMA) copolymers in nanomedicine, we synthesized amphiphilic copolymers of this system for HA-peptide conjugation. The polymer conjugates are listed in **Table 4.4**; in total, four peptide-polymer conjugates were obtained.

**Table 4.4** Summary of the properties of bioconjugates and peptides

Entry	Copolymer	Peptide	$D \times 10^{-11}$ ( $\text{m}^2 \cdot \text{s}^{-1}$ ) <sup>a</sup>	% of modified AEC <sup>b</sup>	$\lambda_{\text{Ex}}$ (nm) <sup>b</sup>	$\lambda_{\text{Em}}$ (nm) <sup>b</sup>
PC1	-	PC1	19.72	-	285	343
PC2	-	PC2	21.98	-	285	348
PC3	-	PC3	21.63	-	285	343
P20	P20	-	12.73	-	275	328
P40	P40	-	7.50	-	275	326
B1	P20	PC1	9.09	40	285	342
B2	P20	PC3	8.99	55	285	347
B3	P40	PC1	8.51	98.1	285	339
B4	P40	PC3	9.02	31.5	280	334

<sup>a</sup> Calculated from the corresponding 2D DOSY spectrum with the chemical shift along the F2 axis and  $D$  along the F1 axis; log  $D$  values were converted to  $\text{m}^2 \cdot \text{s}^{-1} \times 10^{-11}$  (for instance, for PC3, log  $D = -9.664$  (as obtained from the recorded spectrum) becomes  $D = 10^{-9.664} = 21.6 \times 10^{-11} \text{ m}^2 \cdot \text{s}^{-1}$ ). <sup>b</sup> Determined from fluorescence spectroscopy in DMSO; concentration of peptide =  $4 \mu\text{g} \cdot \text{ml}^{-1}$ , and polymer and conjugates =  $0.2 \text{ mg} \cdot \text{ml}^{-1}$ , AEC: Activated ester per chain.

Diffusion Ordered Spectroscopy (DOSY) is an NMR method that can directly measure the diffusion coefficient ( $D$ ) for every single resonance in a  $^1\text{H}$ -NMR spectrum.[209] Molecules of different size decay at different rates and show dissimilar  $D$  values. The Stokes-Einstein equation is used as an ideal basis for calculating  $D$  of spherical objects/molecules, but it shows limitations for different shapes. Furthermore, molecules diffusing across a liquid medium are wetted by a monomolecular layer of solvent that is not taken into account for the calculation of the object radius; however, several empirical correction factors have been proposed in the literature for this limitation.[210] In this regard, DOSY experiments have been used to investigate the conjugation of polymer materials with biomolecules. During a DOSY measurement, a biomolecule (e.g., peptides, proteins, nucleic acids etc.) might show a  $D$  value different to that featured either by the polymer precursor or the corresponding polymer conjugate.[211]

DOSY spectra of B1-B4 conjugates, P20 and P40 copolymers, and PC1 and PC3 peptides are displayed in **Figures 4.15-4.17**. The  $D$ 's obtained from DOSY experiments are summarized in **Table 4.4**. The presence of the resonance signals of B1-B4 conjugates ascribed to the corresponding peptide in the 6.6 - 8.4 ppm region suggests that the covalent binding between the peptide and the corresponding polymer precursor. In addition, the absence of free peptide in B1-B4 conjugates was corroborated with the absence of the NMR signals ascribed to PC1 or PC3 peptide at the  $D$  values of  $19.72 \times 10^{-11}$

<sup>11</sup> or  $21.63 \times 10^{-11} \text{ m}^2 \cdot \text{s}^{-1}$ . On the other hand, the  $D$  value of B1 and B2 conjugates decreased as compared to their polymer precursor (P20), which may be related to changes in the hydrodynamic radius (*i.e.*, an increase in hydrodynamic radius due to the incorporation of the peptide moieties).[211] In contrast, the recorded  $D$  value of B3 and B4 were slightly higher than its polymer precursor P40. This can be explained by a decrease in the hydrodynamic radius due to the incorporation of the peptide moieties.

The results of the DOSY experiments varied depending on the utilized polymer precursor system. This suggests that  $D$  values are not only influenced by the molar mass of the macromolecule but also by variations in the solvophilic/solvophobic nature of the corresponding conjugates due to the incorporation of the respective peptides (*i.e.* changes in the hydrodynamic radius in DMF).

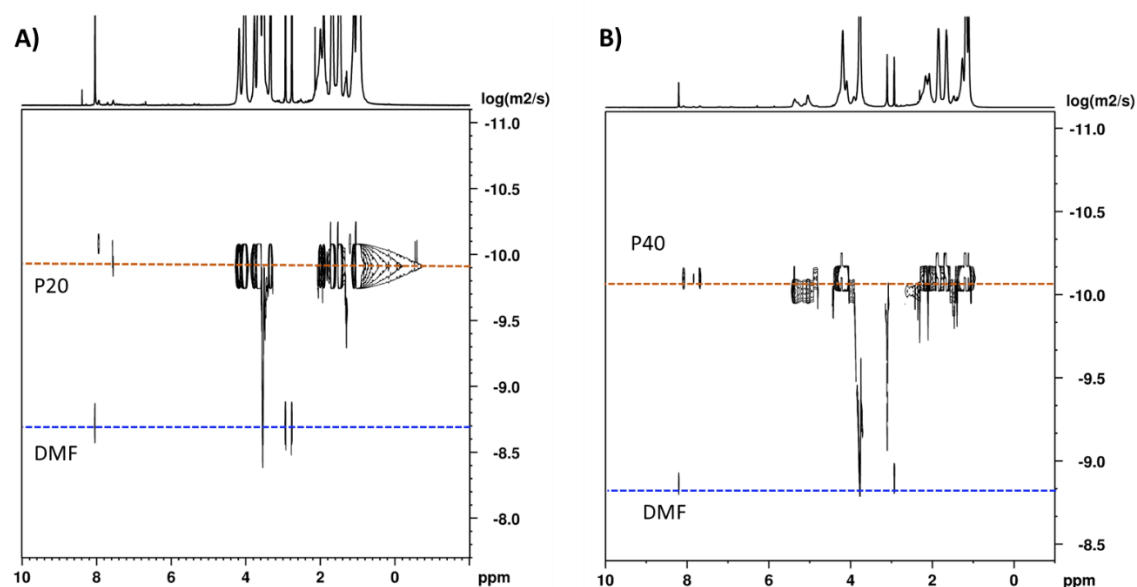


**Figure 4.15** 2D DOSY spectra of A) P20 and B) P40 in DMF-d<sub>7</sub> (400 MHz, RT).

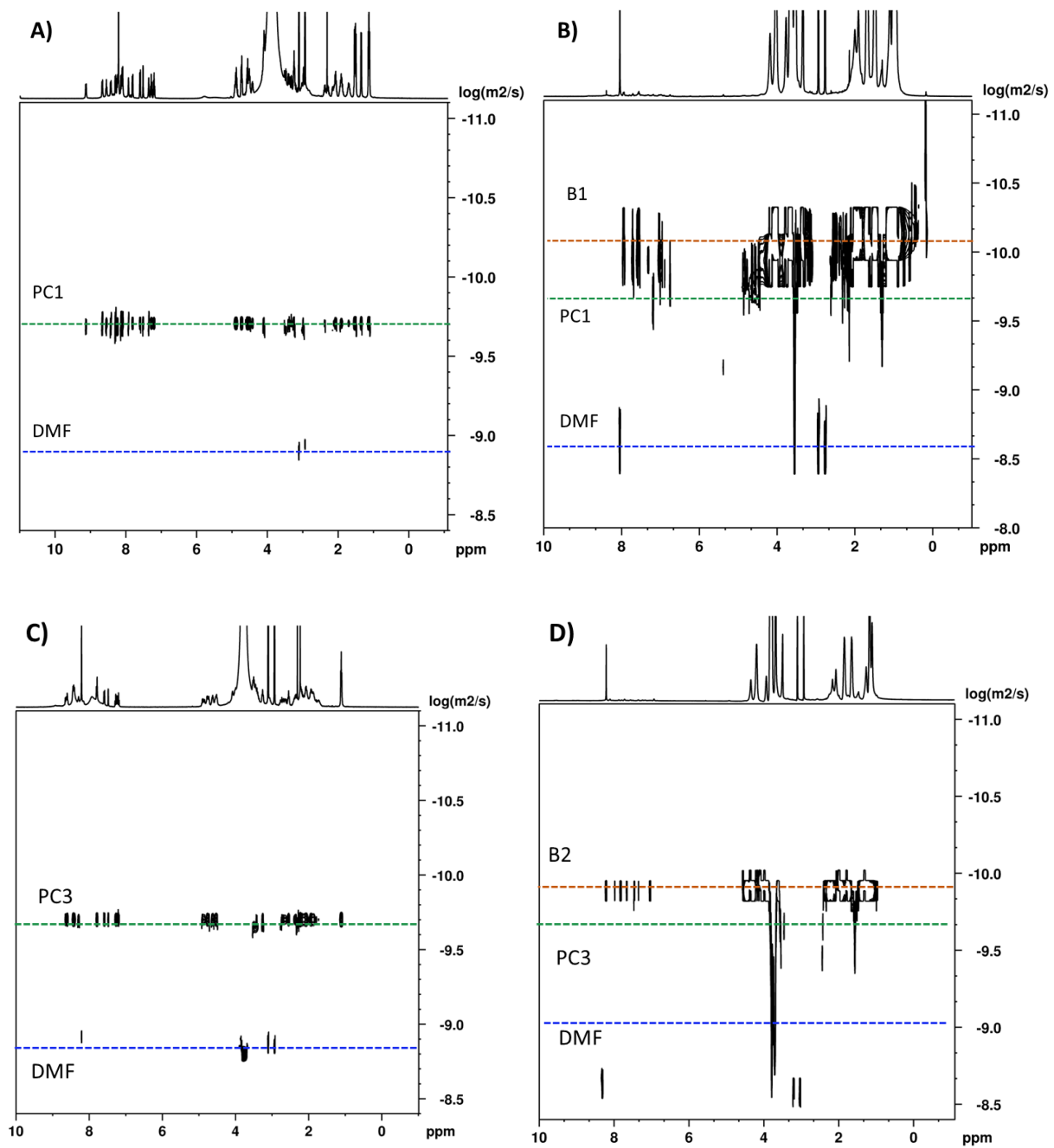


**Figure 4.16** 2D DOSY spectra in DMF-d<sub>7</sub> (400 MHz, RT). A) PC1 peptide, b) B1 conjugate, C) PC3 peptide and D) B2 conjugate.

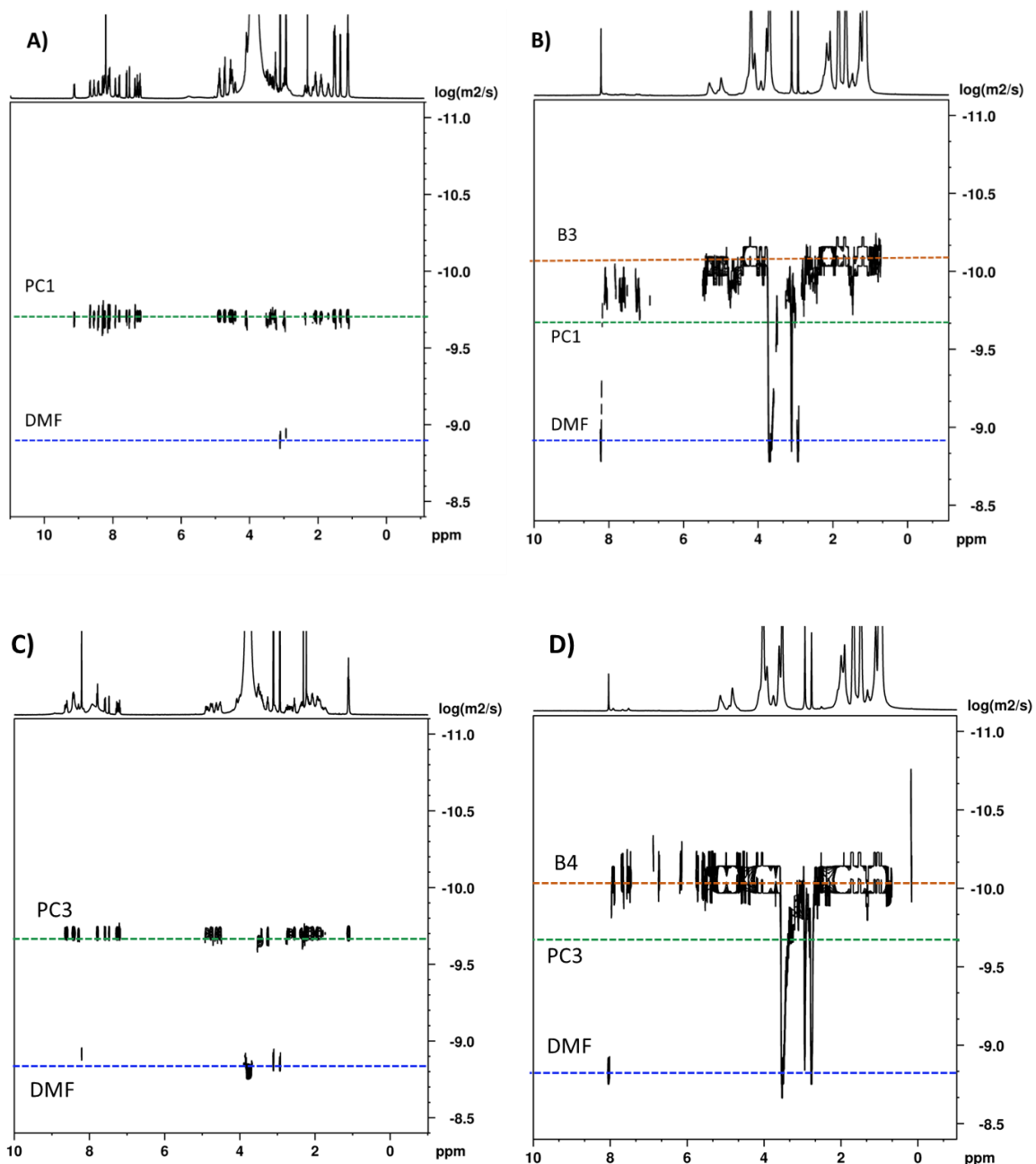


**Figure 4.17** 2D DOSY spectra in DMF- $d_7$  (400 MHz, RT). A) PC1 peptide, b) B3 conjugate, C) PC3 peptide and D) B4 conjugate.

To monitor the conjugation process via confocal microscopy, we incorporated a terminal unit of tryptophan into the investigated peptide sequences (PC1 and PC3), as well as fluorescein O-methacrylate (FLUMA) dye into the copolymer chains. The 3D-fluorescence spectra of block copolymers P20 and P40, and conjugates B1 to B4 in DMSO are displayed in **Figures. 4.18 and 4.19**, and the  $\lambda_{Ex}$  and  $\lambda_{Em}$  values summarized in **Table 4.4**. Note that in this study, a fluorescence signal near 1000 u.a. was observed in DMSO at  $\lambda_{Em}$  323 nm, which was ascribed to impurities, such as stabilizers, present in

the commercial solvent. Copolymers P20 and P40 revealed a fluorescence signal around 326-327 nm in the DMSO, which was also ascribed to impurities present in the utilized DMSO solvent as aforementioned (see **Figure 4.20**).

Furthermore, the intensity of the signal ascribed to the fluorescence of the dye at 513 nm in copolymers P20 and P40, and conjugates B1-B4 increased in PBS as compared to DMSO, which can be attributed to the increment of hydrogen bonds in PBS,[117] as previously discussed above for the study of peptide fluorescence (See **Figure 4.18A** and **Figure 4.19A**).

On the other hand, the shift of  $\lambda_{Em}$  from 326-327 nm to 339-347 nm observed from unmodified copolymers to polymer-peptide conjugates, may be attributed to the presence of Trp residue in the conjugates. The content of peptide into the corresponding polymer-peptide conjugates was estimated using the prepared fluorescence calibration curve for each peptide at the corresponding  $\lambda_{Em}$  (PC1:  $y = 177.42 x - 483.05$ ; and PC3:  $y = 487.64 x - 860.96$ ; where “x” is the peptide concentration and “y” the relative intensity; see **Figure 4.14** and example below). Likewise, these estimations were performed considering the increase in fluorescence intensity observed in the conjugates as compared to pristine copolymer precursors and the utilized solvent. The content of peptide in both investigated copolymer systems is summarized in **Table 4.4**. The % of modified NHSMA grafted units of P40 was higher for PC1 than for PC3 (conjugates B3 and B4, respectively), in contrast, for P20 system the % of modified pentafluorophenyl end-groups was higher for PC3 than for PC1 (conjugates B2 and B1, respectively). The lower incorporation of PC3 in B4 may be attributed to the potential deactivation of the amino-reactive groups in the NHSMA units due to a nucleophilic attack of the hydroxyl groups of the GMMA comonomer units.[112]

#### **Calculation example for the determination of % of modified pentafluorophenyl end-groups into the copolymer chains. P20 system.**

$y$  ( $E_m$  347 nm) = 264 using  $200 \mu\text{g mL}^{-1}$  of B1 conjugate; (experimentally measured value).

- Using the previously prepared calibration curve for PC1.

$$y = 177.42x - 483.05$$

- Solving for x

$$x = (264 + 483.05) / 177.42 = 4.21 \mu\text{g mL}^{-1} \text{ of PC1}$$

- Conversion of x units from  $\mu\text{g mL}^{-1}$  to  $\text{g L}^{-1}$

$$x = 4.21 \mu\text{g mL}^{-1} = 4.21 \times 10^{-3} \text{g L}^{-1} \text{ of PC1 peptide}$$

- Using the molar mass ( $M_w$ ) of PC1 =  $1247.4 \text{ g mol}^{-1}$

$$C_{\text{PC1}} = 4.21 \times 10^{-3} \text{g L}^{-1} / 1247.4 \text{g mol}^{-1} = 3.38 \times 10^{-6} \text{ M}$$

- Conversion of  $C_{\text{PC1}}$  to  $\mu\text{M}$  ( $\mu\text{ mol L}^{-1}$ ) is:

$$C_{\text{PC1}} = 3.38 \times 10^{-6} \text{ M} = 3.38 \mu\text{M} \text{ (experimentally determined concentration of PC1 in the B1 conjugate solution)}$$

- Calculation of the molar mass considering the available reactive units

$$\text{Concentration of B1 conjugate (200 } \mu\text{g mL}^{-1}\text{) expressed in } \mu\text{g L}^{-1} \text{ is } 200000 \mu\text{g L}^{-1}$$

$$\text{Calculation of the } M_n \text{ of the pentafluorophenyl end-functionalized copolymer (based on a 100 \% functionalization efficiency) = } 200000 \mu\text{g L}^{-1} / 3.38 \mu\text{ mol L}^{-1} = 59250 \text{ g mol}^{-1}$$

- Calculation of the actually modified pentafluorophenyl end-groups.

$$M_n \text{ of P20 (as determined via NMR analysis) = } 23500 \text{ g mol}^{-1}$$

$$\% \text{ of modified pentafluorophenyl end-groups} = (23500 \text{ g mol}^{-1} / 59250 \text{ g mol}^{-1}) \times 100 = 39.7 \%$$

$y$  ( $E_m$  343 nm) = 2700.3 using  $200 \mu\text{g mL}^{-1}$  of B2 conjugate; (experimentally measured value).

- Using the previously prepared calibration curve for PC3.

$$y = 487.64x - 860.96$$

- Solving for x

$$x = (2700.3 + 860.96) / 487.64 = 7.303 \mu\text{g mL}^{-1} \text{ of PC3}$$

- Conversion of x units from  $\mu\text{g mL}^{-1}$  to  $\text{g L}^{-1}$

$$x = 7.303 \mu\text{g mL}^{-1} = 7.303 \times 10^{-3} \text{g L}^{-1} \text{ of PC3 peptide}$$

- Using the molar mass ( $M_w$ ) of PC3 =  $1557.2 \text{ g mol}^{-1}$

$$C_{\text{PC3}} = 7.303 \times 10^{-3} \text{g L}^{-1} / 1557.2 \text{g mol}^{-1} = 4.689 \times 10^{-6} \text{ M}$$

- Conversion of  $C_{\text{PC3}}$  to  $\mu\text{M}$  ( $\mu\text{ mol L}^{-1}$ ) is:

$$C_{\text{PC3}} = 4.689 \times 10^{-6} \text{ M} = 4.69 \mu\text{M} \text{ (experimentally determined concentration of PC3 in the B2 conjugate solution)}$$

- Calculation of the molar mass considering the available reactive units

$$\text{Concentration of B2 conjugate (200 } \mu\text{g mL}^{-1}\text{) expressed in } \mu\text{g L}^{-1} \text{ is } 200000 \mu\text{g L}^{-1}$$

Calculation of the  $M_n$  of the pentafluorophenyl end-functionalized copolymer (based on a 100 % functionalization efficiency) =  $200000 \mu\text{g L}^{-1} / 4.69 \mu\text{mol L}^{-1} = 42645 \text{ g mol}^{-1}$

- Calculation of the actually modified pentafluorophenyl end-groups.

$M_n$  of P20 (as determined via NMR analysis) =  $23500 \text{ g mol}^{-1}$

% of modified pentafluorophenyl end-groups =  $(23500 \text{ g mol}^{-1} / 42645 \text{ g mol}^{-1}) \times 100 = 55 \%$

**Calculation example for the determination of % of modified NHSMA grafted units into the copolymer chains. P40 system.**

$y$  ( $E_m$  339 nm) = 569 using  $200 \mu\text{g mL}^{-1}$  of B3 conjugate; (experimentally measured value).

- Using the previously prepared calibration curve for PC1.

$$y = 177.42x - 483.05$$

- Solving for  $x$

$$x = (569 + 483.05) / 177.42 = 5.929 \mu\text{g mL}^{-1} \text{ of PC1}$$

- Conversion of  $x$  units from  $\mu\text{g mL}^{-1}$  to  $\text{g L}^{-1}$

$$x = 5.929 \mu\text{g mL}^{-1} = 5.929 \times 10^{-3} \text{ g L}^{-1} \text{ of PC1}$$

- Using the molar mass ( $M_w$ ) of PC1 =  $1247.4 \text{ g mol}^{-1}$

$$C_{\text{PC1}} = 5.929 \times 10^{-3} \text{ g L}^{-1} / 1247.4 \text{ g mol}^{-1} = 4.754 \times 10^{-6} \text{ M}$$

- Conversion of  $C_{\text{PC1}}$  to  $\mu\text{M}$  ( $\mu\text{mol L}^{-1}$ ) is:

$C_{\text{PC1}} = 4.754 \times 10^{-6} \text{ M} = 4.754 \mu\text{M}$  (experimentally determined concentration of PC1 in the B3 conjugate solution)

- Calculation of the molar mass considering the reactive units

Concentration of B2 conjugate ( $200 \mu\text{g mL}^{-1}$ ) expressed in  $\mu\text{g L}^{-1}$  is  $200000 \mu\text{g L}^{-1}$

Calculation of the  $M_n$  of the NHSMA-based copolymer (based on a 100 % functionalization efficiency) =  $200000 \mu\text{g L}^{-1} / 4.754 \mu\text{mol L}^{-1} = 42070 \text{ g mol}^{-1}$

- Calculation  $M_n$  of the NHSMA-based copolymer the considering 2.68 NHSMA grafted units in the copolymer chain.

Calculation of the  $M_n$  of the NHSMA-based copolymer considering 2.68 NHSMA units per chain =  $42070 \text{ g mol}^{-1} / 2.68 = 15698 \text{ g mol}^{-1}$

- Calculation of the actually modified NHSMA grafted units.

$M_n$  of P40 (as determined via NMR analysis) =  $15400 \text{ g mol}^{-1}$

% of modified NHSMA grafted units =  $(15400 \text{ g mol}^{-1} / 15698 \text{ g mol}^{-1}) \times 100 = 98.1 \%$



---

$y$  ( $E_m$  334 nm) = 298.3 using 200  $\mu\text{g mL}^{-1}$  of **B4** conjugate; (experimentally measured value).

- Using the previously prepared calibration curve for PC3.

$$y = 487.64x - 860.96$$

- Solving for  $x$

$$x = (298.3 + 860.96) / 487.64 = 2.377 \mu\text{g mL}^{-1} \text{ of PC3}$$

- Conversion of  $x$  units from  $\mu\text{g mL}^{-1}$  to  $\text{g L}^{-1}$

$$x = 2.377 \mu\text{g mL}^{-1} = 2.377 \times 10^{-3} \text{ g L}^{-1} \text{ of PC3}$$

- Using the molar mass ( $M_w$ ) of PC3 =  $1557.2 \text{ g mol}^{-1}$

$$C_{\text{PC3}} = 2.377 \times 10^{-3} \text{ g L}^{-1} / 1557.2 \text{ mol}^{-1} = 1.526 \times 10^{-6} \text{ M}$$

- Conversion of  $C_{\text{PC3}}$  to  $\mu\text{M}$  ( $\mu\text{ mol L}^{-1}$ ) is:

$$C_{\text{PC3}} = 1.526 \times 10^{-6} \text{ M} = 1.526 \mu\text{M} \text{ (experimentally determined concentration of PC1 in the B3 conjugate solution)}$$

- Calculation of the molar mass considering the reactive units

Concentration of pBGF-PC3 conjugate ( $200 \mu\text{g mL}^{-1}$ ) expressed in  $\mu\text{g L}^{-1}$  is  $200000 \mu\text{g L}^{-1}$

Calculation of the  $M_n$  of the NHSMA-based copolymer (based on a 100 % functionalization efficiency) =  $200000 \mu\text{g L}^{-1} / 1.526 \mu\text{ mol L}^{-1} = 131062 \text{ g mol}^{-1}$

- Calculation  $M_n$  of the NHSMA-based copolymer the considering 2.68 NHSMA grafted units in the copolymer chain.

Calculation of the  $M_n$  of the NHSMA-based copolymer considering 2.68 NHSMA units per chain =  $131062 \text{ g mol}^{-1} / 2.68 = 48904 \text{ g mol}^{-1}$

- Calculation of the actually modified NHSMA grafted units.

$M_n$  of P40 (as determined via NMR analysis) =  $15400 \text{ g mol}^{-1}$

% of modified NHSMA grafted units =  $(15400 \text{ g mol}^{-1} / 48904 \text{ g mol}^{-1}) \times 100 = 31.5 \%$

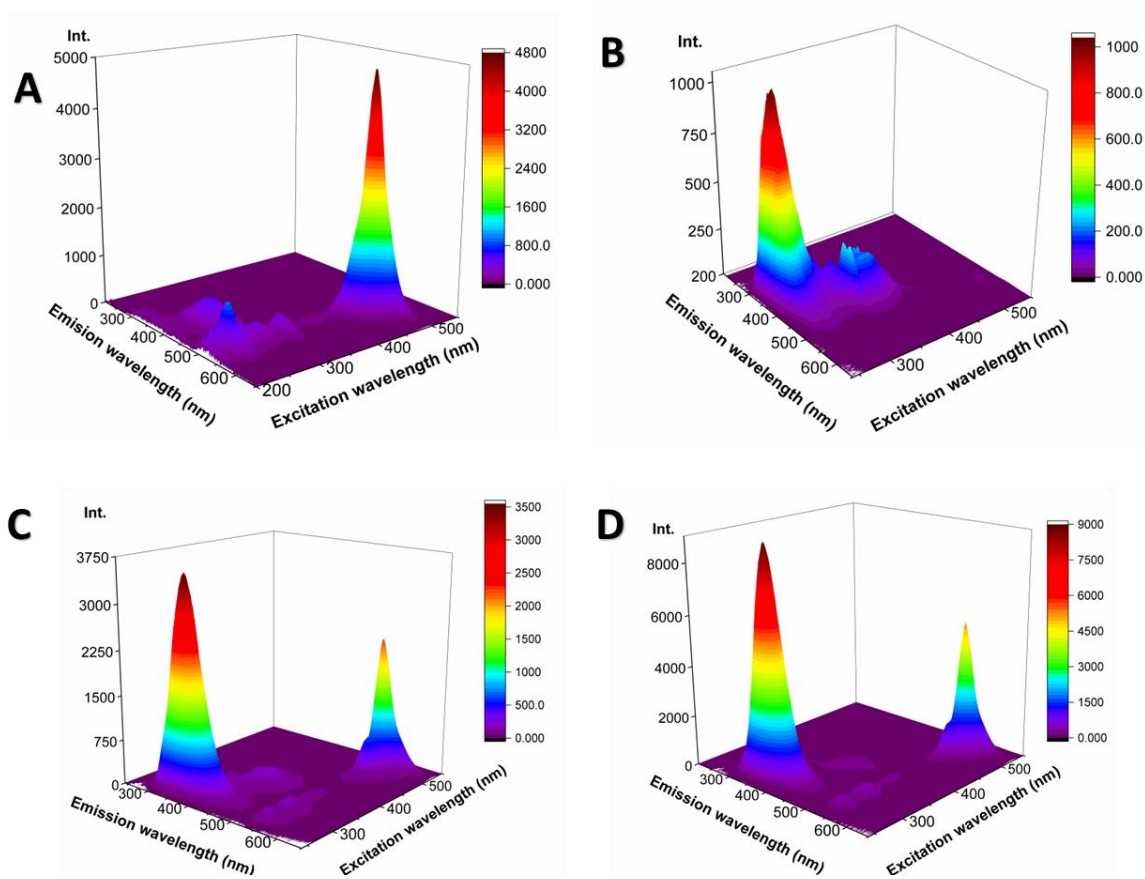


**Figure 4.18.** 3D fluorescence spectra at 0.2 mg mL<sup>-1</sup> of A) P20 copolymer in PBS, B) P20 copolymer in DMSO, C) conjugate B1 in DMSO and D) conjugate B2 in DMSO.

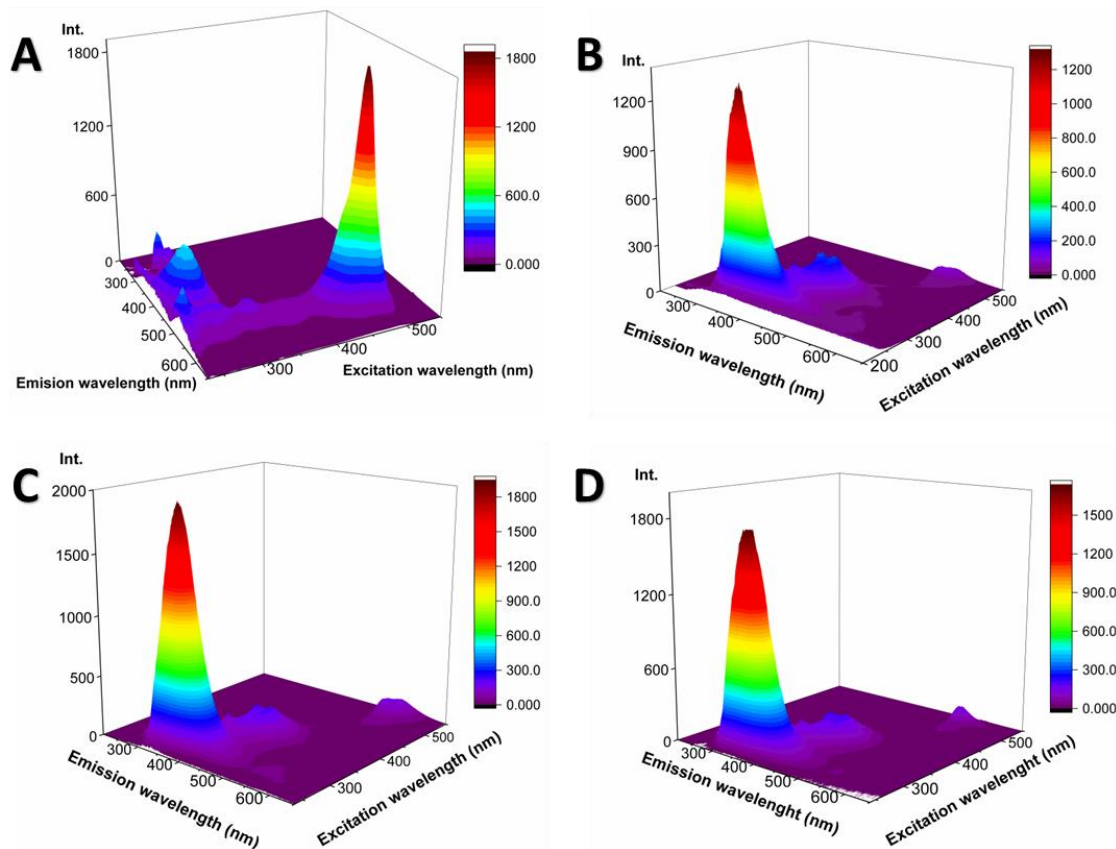


**Figure 4.19.** 3D- fluorescence spectra at 0.2 mg mL<sup>-1</sup> of A) P40 copolymer in PBS, B) P40 copolymer in DMSO, C) conjugate B3 in DMSO and D) conjugate B4 in DMSO.

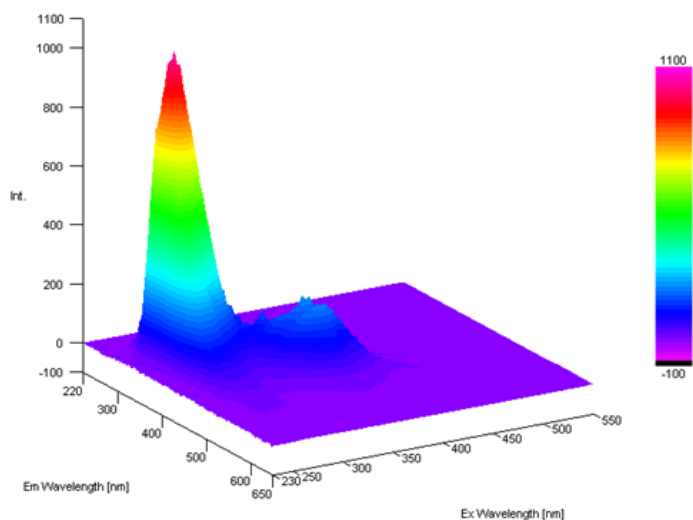


**Figure 4.20.** 3D fluorescence spectrum of the utilized DMSO solvent.

## 4.6 Polymer nanoparticles decorated with peptides derived from the HA protein of the influenza A virus

Experimental data obtained from DLS and cryo-TEM characterizations are summarized in **Table 4.5**, which suggests that copolymers P20 and P40 self-assemble into nanostructures in aqueous medium (see **Figures 4.21 to 4.23**). In the case of copolymer P20 (containing the OEGMEMA comonomer), the values of the particle size estimated via DLS (i.e., hydrodynamic diameters ( $D_h$ )) and cryo-TEM at copolymer concentration values of 2.5 and 0.4 mg mL<sup>-1</sup> were 21.6 and 22.1 nm, respectively. These results are in good agreement with a previous report by Rozen et al., who investigated spherical nanostructures of brush copolymers based on OEGMEMA, BMA and diethylaminoethyl methacrylate (DEAEMA) comonomers (i.e., reported sizes as estimated via TEM measurements were in the 24-28 nm range).[212] In contrast, a bimodal distribution was observed when a higher copolymer concentration (~ 5 mg mL<sup>-1</sup>) was utilized for the analysis. The second population arose around ~370 and ~71 nm as determined via DLS and TEM, respectively (see **Figure 4.21A**). The significant difference observed between these recorded sizes may be related to (1) the main distribution at lower  $D_h$  values may mainly correspond to single random-coil polymer chains or individual particles of small size, which contrasts to the minor distribution at higher  $D_h$  values featuring particle aggregates of larger size,[213,214] and/or (2) the intrinsic limitations of the DLS technique to resolve polydisperse samples[215,216] as it has been reported that DLS tends to overestimate the average size in polydisperse samples.[217–219] Furthermore, the morphology of the nanoparticles recorded via cryo-TEM reveals a change from micelles to vesicles by increasing copolymer concentration. Thus, spherical micelles are only observed at a copolymer concentration of 1 mg mL<sup>-1</sup>, whereas a co-existence of micelles and vesicles was revealed at a concentration of 5 mg mL<sup>-1</sup> (see **Figures 4.22 A, 4.22 B and 4.23A**).

**Table 4.5 Physicochemical properties of the investigated copolymer and conjugates derived thereof.**

Physicochemical properties of the investigated copolymer and conjugates derived thereof.

Entry	<sup>a</sup> $D_h$ (nm) DLS	<sup>a</sup> PDI	Conc. DLS (mg/mL)	<sup>b</sup> D (nm) TEM	<sup>b</sup> Morphology	Conc. TEM (mg/mL)
P20	21	0.211	2.5	22	Micelles	0.4
P20	17 (82 %) / 371 (18 %)	0.329	5	18/71	Micelles & vesicles	5
B1	11 (82 %)/328 (12 %)	0.326	3	14	Micelles	5
B2	23 (51 %)/206 (49 %)	0.503	3	-	-	-
P40	79	0.145	0.5	29	Worms, micelles & vesicles	0.5
P40	111	0.078	1.5	96/171	Vesicles	1.5
B3	12 (9 %) / 316 (91 %)	0.615	2	41	Micelles	1.5
B4	190	0.25	2	-	-	-

<sup>a</sup> DLS in deionized water, hydrodynamic diameter ( $D_h$ ) corresponding to mean value; for bimodal distributions, the mean value of every peak was considered. <sup>b</sup> Observed by TEM, particle diameter (D) was calculated as the average of vesicles and micelles considering a spherical morphology.

Conjugates B1 and B2 maintained a bimodal distribution by DLS even though the peptide changed (**Figure 4.21A**), whereas cryo-TEM images of conjugate B1 displayed in **Figure 4.27 C** revealed micellar structures of a smaller size than that one shown by its precursor copolymer P20.

DLS studies of the GMMA-based copolymer P40 showed a monomodal distribution and an increase in  $D_h$  from 79 to 111 nm at copolymer concentrations of 0.5 and 1.5 mg mL<sup>-1</sup>, respectively (see **Figure 4.21 B**). **Figures. 4.22D and E, and 4.23B and C** revealed morphological changes by showing the co-existence of vesicles, micelles and worms with increasing copolymer concentration. Two populations of vesicles at a copolymer concentration of 1.5 mg mL<sup>-1</sup> were observed via cryo-TEM with a mean diameter length of 95 and 171 nm, respectively. The obtained DLS and TEM results suggest that  $D_h$  increases with increasing copolymer concentration due to the formation of vesicles as other co-existent nanostructures with morphologies such as micelles and worms merge. However, at higher copolymer concentrations, the increase in size of the vesicles may be ascribed to aggregation of different vesicles of smaller size. Armes et al.[169,220] reported that GMMA-based copolymers prepared via emulsion and polymerization-induced self-assembly (PISA) methods can yield nanostructures featuring diverse morphologies.

Concerning the size of the nanostructures derived from conjugates based on copolymer P40, conjugate B4 maintains a monomodal distribution as compared to its material precursor. However, conjugate B3 revealed an additional population of a smaller size (i.e., 12 nm (9 %)). Interestingly, the cryo-TEM micrographs of conjugate B3 showed uniform micelles of a mean diameter of 41 nm (see **Figure 4.22F**). Conjugate B4 exhibited a monomodal distribution with a mean diameter of 190.2 nm as determined via DLS, which, based on the results obtained for copolymer P40, suggests that its morphology may correspond to vesicles. In general, the differences observed between both characterization methods can be mainly ascribed to three limitations of the DLS technique. 1) Hydrodynamic diameter values are calculated from the Stokes-Einstein equation, which assumes spherical particles. 2) Fluctuations in the scattered light intensity are relative to the Brownian motion of the particles in the solvent where larger particles and agglomerates have a considerably higher intensity than their smaller counterparts, which has a strong impact on the calculation of the  $D$  and diameter values,[221–225] 3) The particle size is estimated from different mathematical approaches used to determine a correlation function, for instance, the cumulants algorithm fits a single exponential to the correlation function and is considered appropriate for monomodal samples because it takes into account only one population of particles (i.e., single average  $D$  and a single standard deviation). In contrast, the non-negative least squares (NNLS) method fits a multiple exponential to obtain the distribution of particle sizes, which results more suitable for multimodal samples. Due to the fact that these mentioned methods feature several limitations, the results derived thereof must be taken and/or considered with care.[226] Herein, the reported particle size of monodisperse samples derived from the cumulants algorithm, whereas that corresponding to multimodal samples from NNLS method.

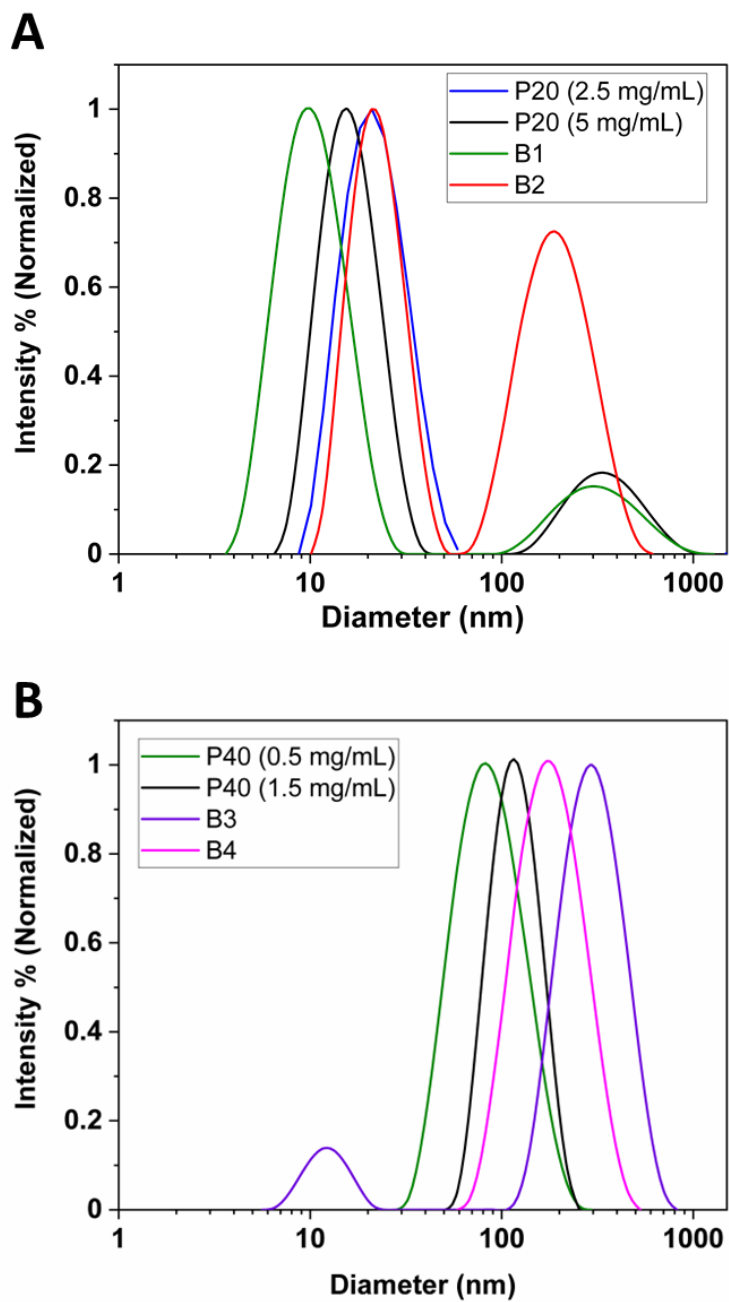


**Figure 4.21.** DLS size distribution plots, measurements performed using deionized water at room temperature. A) DLS plots of copolymer P20 (1 and 5 mg mL<sup>-1</sup>), and conjugates B1 (3 mg mL<sup>-1</sup>) and B2 (3 mg mL<sup>-1</sup>). B) DLS plots of copolymer P40 (0.5 and 1.5 mg mL<sup>-1</sup>), and conjugates B3 (2 mg mL<sup>-1</sup>), and B4 (2 mg mL<sup>-1</sup>).

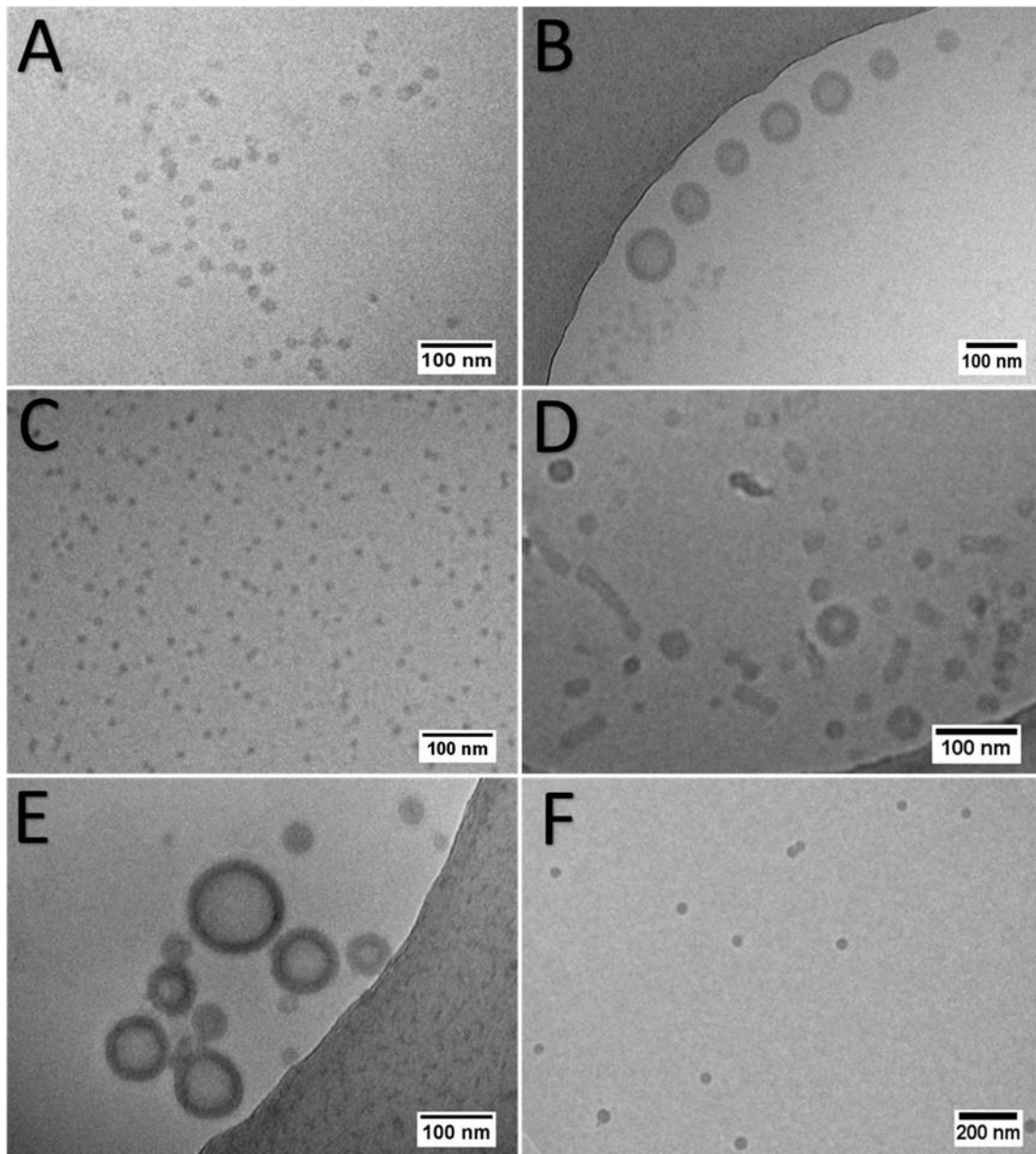


**Figure 4.22.** Cryo-TEM micrographs of copolymers P20 and P40 and their corresponding conjugates; the analysis was performed using deionized water at room temperature. Shape changes from micelles to vesicles were observed with an increase in P20 concentration. A) Copolymer P20 at  $0.4 \text{ mg mL}^{-1}$ . B) Copolymer P20 at  $5 \text{ mg mL}^{-1}$ . Conjugate of P20 with PC1 peptide forms micelle in aqueous media. C) Conjugate B1 at  $5 \text{ mg mL}^{-1}$ . Shape changes from worms, micelles and vesicles to vesicles were observed with an increase in P40 concentration. D) Copolymer P40 at  $0.5 \text{ mg mL}^{-1}$ . E) Copolymer P40 at  $1.5 \text{ mg mL}^{-1}$ . Conjugate of P40 with PC1 peptide forms mainly micelle nanostructure F) Conjugate B3 at  $2 \text{ mg mL}^{-1}$ .



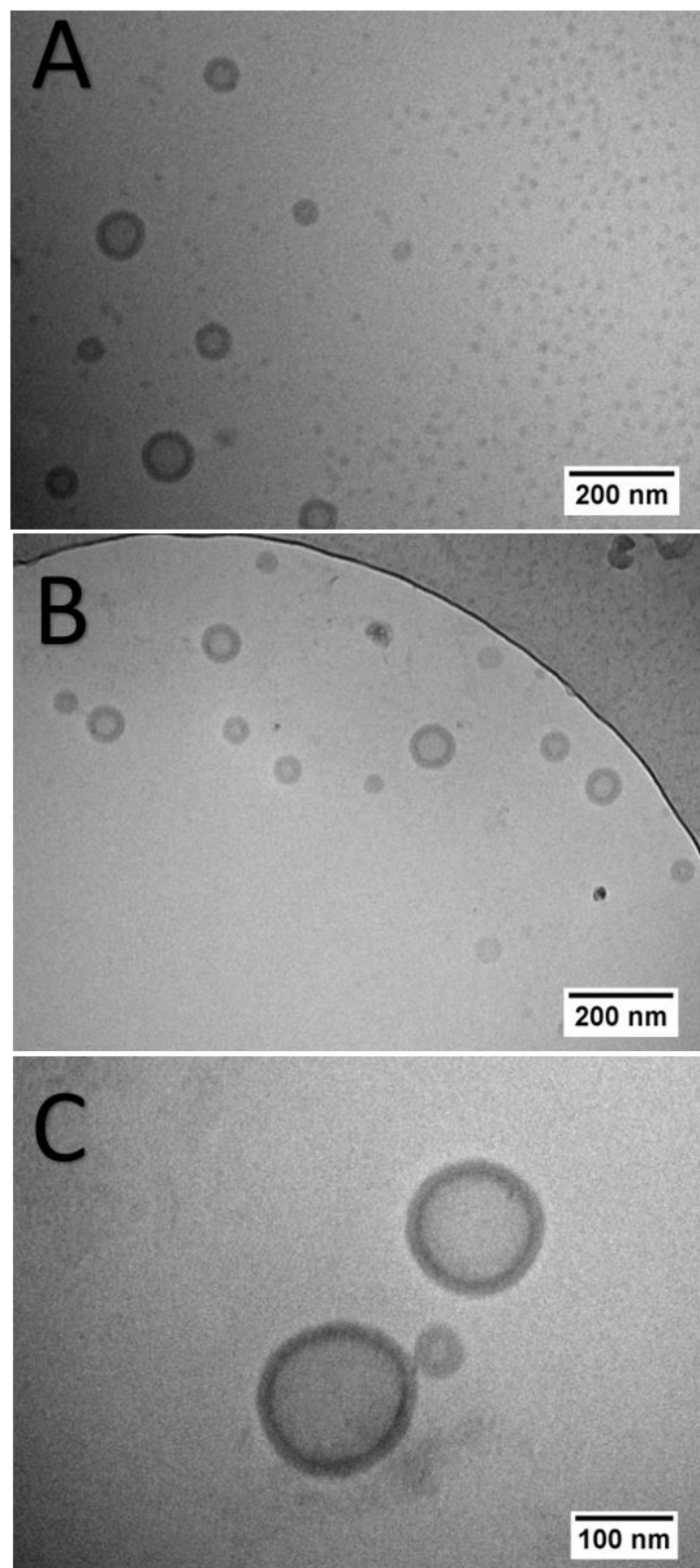


**Figure 4.23** Cryo-TEM micrographs of copolymers P20 and P40 in aqueous media. A) Co-existence of vesicles and micelles using P20 at  $5 \text{ mg mL}^{-1}$ . B-C) Formation of vesicles using P40 at  $1.5 \text{ mg mL}^{-1}$ .

## 4.7 Cell viability and cellular internalization of polymer nanoparticles decorated with peptides derived from the HA protein of the influenza virus

### 4.7.1 Cell viability and internalization of peptides in MDCK cell line

Glycosylated proteins located at the cell surface are the main target for influenza viruses to adhere and translocate across epithelial host cells.[78][77] The Madin-Darby Canine Kidney (MDCK) epithelial cell line is generally utilized as a model to study viral infections, such as influenza, due to the expression of sialylated proteins at the cell membrane.[227] In this investigation, cytotoxic effects of peptides PC1-PC3, PC1-5FAM and PC3-5FAM on the MDCK cell line were assessed using the presto blue assay. In this regard, **Figure 4.24A** reveals cell viability % values of 82, 71 and 78 for PC2, PC1 and PC1-5FAM, respectively; in turn, peptides PC3 and PC3-5FAM displayed cell viability values higher than 80 % up to a peptide concentration of  $250 \mu\text{g mL}^{-1}$ . At the highest peptide concentration tested (i.e.,  $500 \mu\text{g mL}^{-1}$ ), the cell viability follows the order PC3-5FAM > PC3 > PC1-5FAM > PC1 > PC2. The 5FAM-labeled peptides featured slightly higher cell viability values (> 4 %) than their precursor counterparts, which suggests that the presence of the dye label does not have a significant effect on the investigated cell viability.

Cell internalization capacities of the peptides were assessed via flow cytometry and confocal microscopy. For these investigations, PC2 was discarded due to its relatively high cytotoxicity. To better understand the mechanism of internalization, additional cellular fluorescence (autofluorescence) was quenched using Trypan Blue (TB); such assay does not influence the fluorescence featured by the internalized peptides / particles.[228][229] The fluorescence intensity of peptides quenched with Trypan Blue did not displayed a significant difference as compared to that of the unquenched counterparts (see **Figure 4.24B**), indicating that the measured fluorescence mainly derives from the presence of the peptides in the investigated cells. The recorded fluorescent intensity ratio of [Control]:[PC1-5FAM]:[PC3-5FAM] was [1]:[89.7]:[138.6], respectively. Peptides PC1-5FAM and PC3-5FAM displayed higher cellular uptake values for the MDCK cell line; however, peptide PC3-5FAM showed a better internalization capacity (ca. 64% higher than peptide PC1-5FAM). Different internalization mechanisms have been proposed for cell penetrating peptides being a direct penetration across the

plasma membrane and an endosomal uptake the most common ones.[230] The micrographs of **Figure 4.24C** show that both peptides spread all over the cells, including the cytoplasm and nucleus (**overlay and Hoechst dye**). This suggests that the main uptake of the peptide occurred via a direct penetration; in addition, peptide aggregates of a relatively small size were observed in the cytoplasm, which may correspond to vesicles or vacuoles derived from an endocytosis process. To understand in more detail the cell internalization process of the investigated peptides, further experiments at various concentrations and in other epithelial cells might be necessary in future research work.

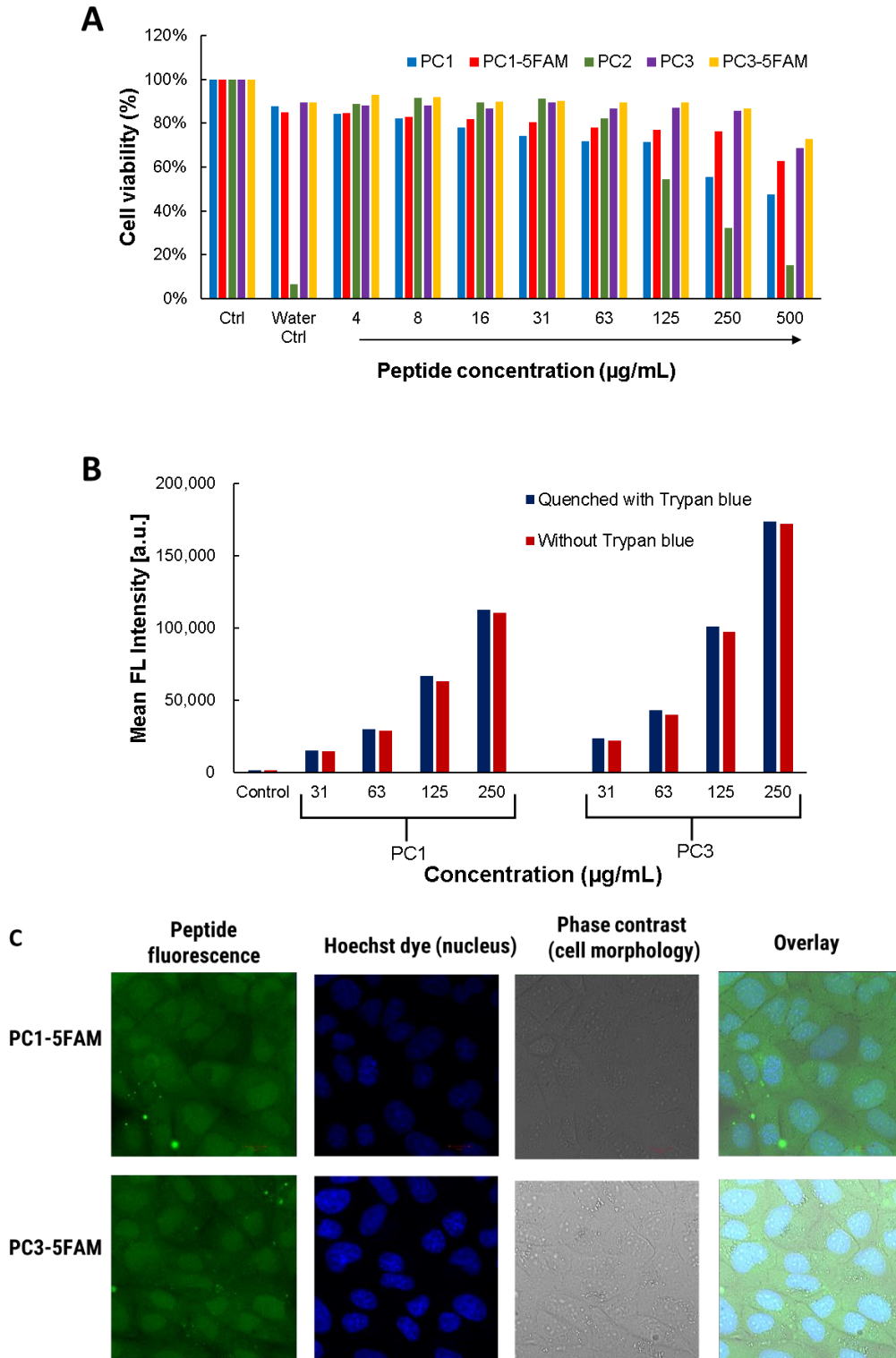


**Figure 4.24.** A) Relative cell viability of MDCK cells in the presence of 4-500  $\mu\text{g mL}^{-1}$  of PC1-PC3, PC1-5FAM, and PC3-5FAM as determined by Alamar Blue measurements after 24 h. Microscope was used at Ex 560/Em 590 nm. B) Cellular uptake peptides-labeled 5FAM at different concentrations ( $n = 4$ ) quenched by trypan blue and without pretreatment. C) Confocal images of the MDCK cells exposed to PC1-5FAM and PC3-5FAM peptides ( $250 \mu\text{g mL}^{-1}$ ), the nuclei of the cells were stained with Hoechst dye.

The cell viability of the investigated copolymers and their counterparts conjugated with the peptides PC1 and PC3 were assessed via the presto blue assay in the MDCK cell line using methodologies A and B, and a copolymer concentration of  $100 \mu\text{g mL}^{-1}$  (see **Figure 4.25A**). For method A, the materials were dissolved in DMSO before addition into the cell medium, whereas for method B, the materials were used in the form of nanoparticles formulated in aqueous solutions (as described in **section 4.2.7**). Only small differences were found in the cell viability results between the two utilized methods. Copolymer P20 and its conjugate counterparts displayed an increase in cell viability of ca. 5 to 10% when method A was used, whereas copolymer P40 and its conjugate derivatives featured a decrease of ca. 4 to 9 % (see **Figure 4.25A**). In general, cell viability values higher than 80% prevailed for all the investigated copolymers and corresponding conjugates at a material concentration of  $100 \mu\text{g mL}^{-1}$  regardless of the utilized methodology.

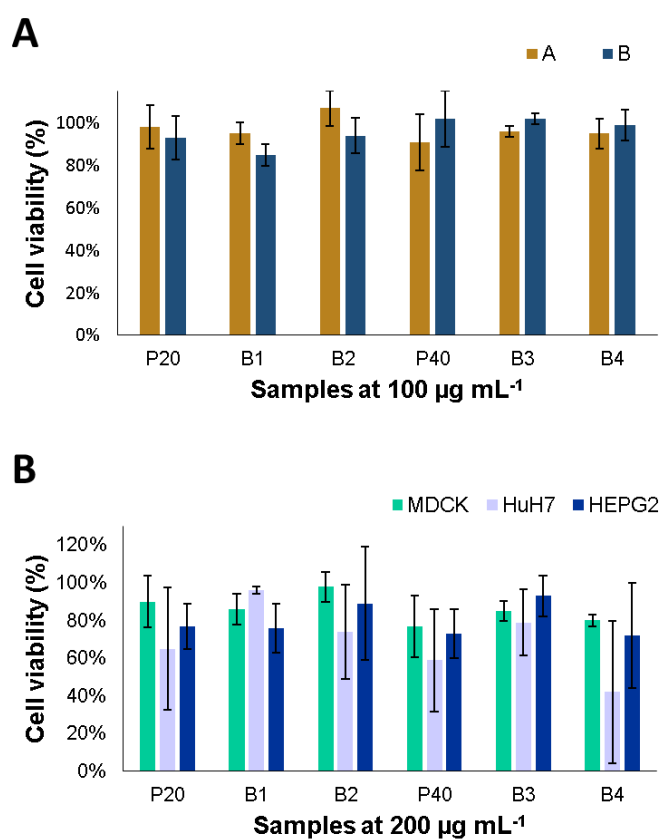


**Figure 4.25.** A) Relative cell viability of MDCK cells exposed at a polymer / nanoparticle concentration of  $100 \mu\text{g mL}^{-1}$  as determined by Alamar Blue measurements after 24 h using wavelengths of Ex 560/ Em 590 nm, and methodologies A and B for the analyses. B) Cell viability of MDCK, HuH7 and HEPG2 cell lines in the presence of copolymers P20 and P40 and conjugates B1-B4 at a material concentration of  $200 \mu\text{g mL}^{-1}$ .

#### 4.7.2 Comparison of cell viability of the MDCK cell line vs HuH7 and HEPG2 cell lines in the presence of the investigated copolymers and derivative conjugates.

The cell viability of the MDCK cell line was compared to those assessed in HuH7 and HEPG2 epithelial cell lines in the presence of investigated copolymers and corresponding conjugates using methodology A (see **Figures 4.25B** and **4.26**).

Regarding cell viability, an increase in cell viability of ca. 8-12% was observed for the case of conjugate B2 as compared to copolymer P20 in the three investigated cell lines. In addition, conjugate B1 had a significant impact on the cell viability of HuH7 cells where an increase of 31% was detected when compared to copolymer P20. Nevertheless, this increase was not observed in the evaluations involving the MDCK and HEPG2 cell lines. Copolymer P40 and its conjugates B3 and B4 were also evaluated. The cell viability at 200  $\mu\text{g mL}^{-1}$  of polymer sample recorded for the case of conjugate B3 increased up to 20% in HuH7 and HEPG2 cell lines when compared to its corresponding copolymer precursor P40, whereas an 8% increase was detected in the MDCK cell line. These latter increases in cell viability were not observed for the case of conjugate B4. In summary, the highest cell viability values in the MDCK, HuH7 and HEPG2 cell lines were obtained in the presence of conjugates B2, B1 and B3, respectively. The differences in the cell viability results between the three utilized cell lines observed in this investigation may be ascribed to the different nature and characteristics of these cell lines. [227,231–234]

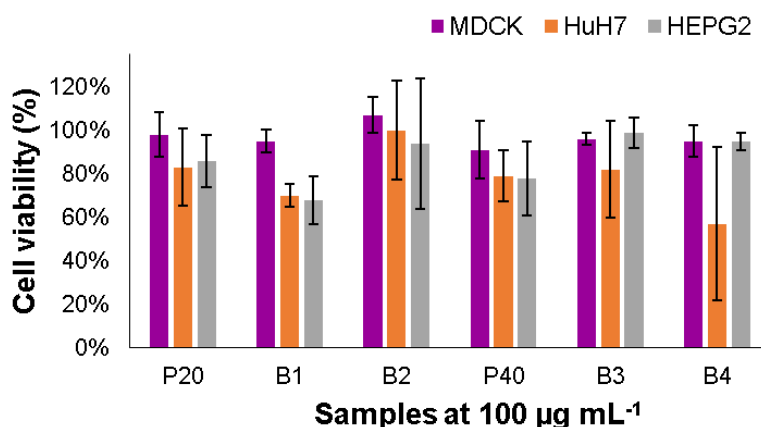


**Figure 4.26.** Cell viability of the MDCK, HuH7 and HEPG2 cell lines in presence of copolymers P20 and P40, and conjugates B1-B4 at a material concentration of  $100 \mu\text{g mL}^{-1}$ .

Regarding the cellular internalization of the conjugated NPs investigated via flow cytometry, the following observations can be mentioned (see **Figure 4.27**). (i) OEGMEMA-based copolymers (P20 series) featured a better internalization capacity than GMMA-based copolymers (P40 series). (ii) Regarding the fluorescence evaluations of cells quenched with trypan blue, copolymer P20 coupled to peptide PC1 (conjugate B1) featured a higher cellular internalization as compared to the copolymer precursor (P20); the obtained fluorescence ratio [P20]:[B1] was [1]:[1.16] at a material concentration of  $100 \mu\text{g mL}^{-1}$ . (iii) The impact of the peptide conjugation was more significant for nanoparticles bearing GMMA monomer units; the obtained fluorescence ratios [P40]:[P40-PC1] and [P40]:[P40-PC3] were [1]:[5.00] and [1]:[1.94], respectively, at a material concentration of  $50 \mu\text{g mL}^{-1}$ . As was described before (**Section 4.5**), the GMMA-based conjugates bear more units of PC1 peptide than their OEGMEMA counterparts, which can be correlated to the higher cellular uptake observed for conjugates based on copolymer P40. This suggests that the incorporation of more peptide units into the copolymer chains might promote a higher cellular uptake of the corresponding NPs. In general, the incorporation peptide units can improve the cellular internalization of NPs; this was particularly observed for peptide PC1 in this investigation. Nonetheless, this phenomenon will depends on multiple factors including the characteristics of the polymeric system utilized as nanocarrier.

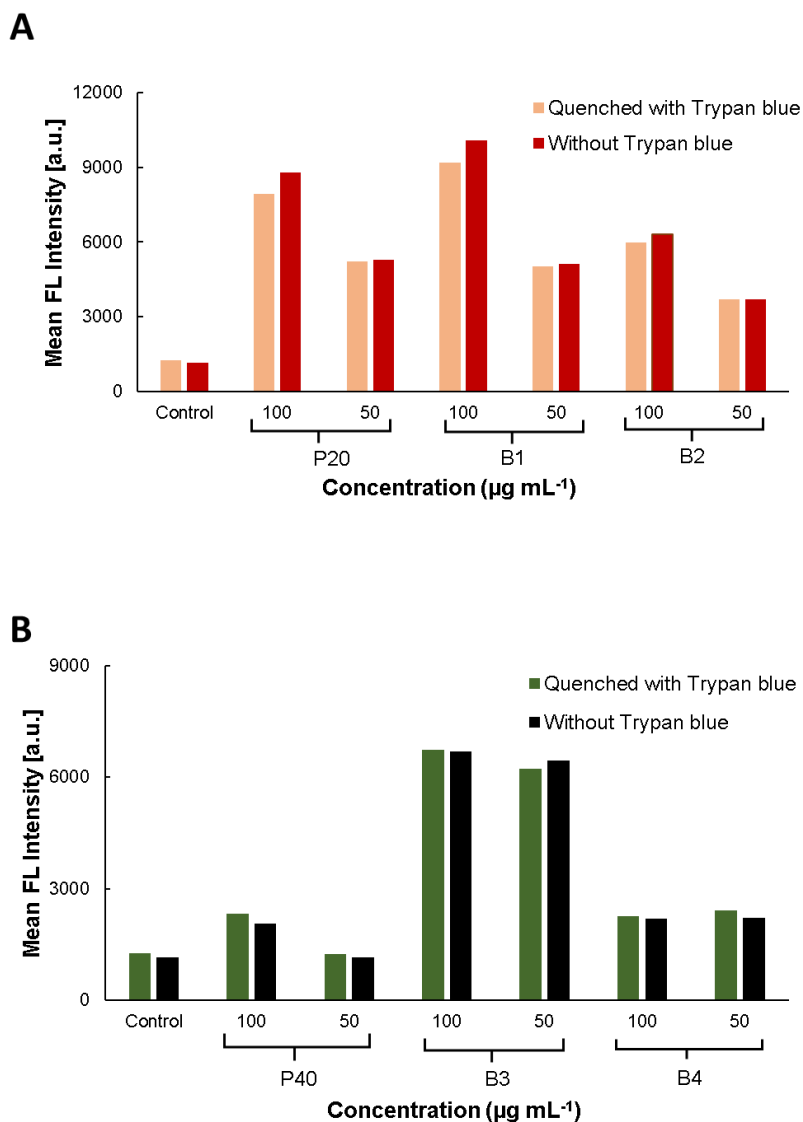


**Figure 4.27.** Cellular uptake of block copolymers conjugated with peptides PC1 and PC3 quenched by trypan blue and without pretreatment at material concentrations of 50 and 100 µg mL<sup>-1</sup>. A) Copolymer P20 and its corresponding conjugates B1 and B2. B) Copolymer P40 and its corresponding conjugates B3 and B4.

## 4.8 Conclusion and outlook

Herein was described for the first time the synthesis of P(BMA)-*b*-P(GMMA-NHSMA) (P40) block copolymer and its self-assembly in aqueous media; in addition, the preparation of the standard P(OEGMEMA)-*b*-P(BMA) (P20) was performed. In both polymer systems, a morphological transition from micelles to vesicles was observed by TEM in water. The cell viability of the MDCK cell line was evaluated in the presence of the peptides PC1-PC3, PC1-5FAM and PC3-5FAM; significant differences were observed in cytotoxicity according to the type of peptide. The hydrophobic PC2 affected cell viability in a greater proportion than PC1 and PC3; hence, PC1 and PC3 were selected



for confocal microscopy and internalization studies, the combination of both methods indicates that HA-derived peptides have the ability to access the nucleus of MDCK cells; based on the studies we suggest that the uptake of the peptide was by direct penetration.

Bioconjugation has been used to improve the internalization of polymer particles into the cells; in our case, PC1 and PC3 peptides were covalently attached to P40 and P20 block copolymers. Fluorescence of Tryptophan residue and DOSY were used to confirm the peptides binding into the copolymers.

The cell viability of the epithelial cell lines MDCK, HuH7 and HEPG2 was compared, and the results indicate a dependence not only on the peptide but also on the polymeric system used, with B2 (P20 copolymer with PC3 peptide) exhibiting the highest value. Overall, an improvement in cell viability is noted with the incorporation of the peptide. Finally, flow cytometry analysis confirmed the internalization of the bioconjugates in the MDCK cell line. Bioconjugates with PC1 peptide showed better internalization capacity.

## Chapter 5 Conclusions, recommendations publications- congresses and references.

### 5.1 Conclusions

The reactivity ratios of three GMMA copolymers were determined. (1)  $r_{\text{GMMA}}=0.32$  and  $r_{\text{NHSMA}}=1.01$ , (2)  $r_{\text{GMMA}}=3.31$  and  $r_{\text{BuA}}=0.66$ , (3)  $r_{\text{GMMA}}=2.55$   $r_{\text{NIPAM}}=0.11$ . GMMA prefers to undergo homopolymerization reactions when is copolymerized with BuA and NIPAM. However, GMMA is more prone to cross-propagate when copolymerized with NHSMA.

Data-fitting curves were constructed to predict the  $T_g$  of GMMA copolymers was performed from DSC measurements. Copolymerization with the hydrophobic monomer BuA showed the best agreement with the mathematical models.

For conjugation purposes, two amphiphilic block copolymers were successfully synthesized by RAFT. The structure of the polymer was confirmed from NMR spectra. The active ester groups were included in the polymeric platforms and by  $^{19}\text{F}$ -NMR or elemental analysis. RAFT technique allowed good control of chain extension reactions; however, SEC characterization of amphiphilic copolymers may deviate from predicted values and/or an ideal behavior. For GMMA copolymers, SEC results are affected by the high hydrophobicity of GMMA monomer units and their potential interactions with both the solvent system and the chromatographic columns of a given SEC instrument.

The “grafting to” conjugation strategy was investigated to incorporate peptide moieties derived from the HA protein of the Influenza A virus into the copolymer chains via activated esters derived from PFP and NHS units. For this purpose, a copolymer of OEGMEMA (P20) with a pentafluorophenyl ester-terminated RAFT agent and a statistical copolymer of GMMA and NHSMA (P40), both containing a BMA hydrophobic block segment, were used.

The self-assembly of these block copolymers was confirmed by means of the TEM and DLS techniques where micellar and vesicular nanostructures were obtained in aqueous media. This enabled the preparation of polymer nanoparticles conjugated with the investigated peptides, which was also confirmed via TEM and DLS. In addition, the incorporation of PC1 and PC3 peptides was quantified by means of fluorescence spectroscopy; the DOSY technique was complementarily utilized to further elucidate the functionalization process of the copolymer chains with the selected peptides.

The cell viability of the epithelial cell lines MDCK, HuH7, and HEPG2 in presence of P20 and P40 conjugates was analyzed. For the P20 conjugate series, an increase in cell viability was observed on the three cell lines when the PC3 peptide was added, whereas PC1 incorporation decreased cell viability. In the case of the P40 conjugates, the PC1 and PC3 peptides improved the cell viability in the MDCK and HEPG2 cell lines, but not in the HuH7 cell line. In general, it was concluded that the cell viability results were not only influenced by the peptide but also by the polymer system and the utilized cell line.

Internalization into cells for P20 and P40 and their respective conjugates, as determined via flow cytometry, suggests that the incorporation of peptide PC1 increases internalization for both polymer systems when compared to PC3.

## 5.2 Recommendations

1. Significant effects have been observed in the cell internalization of GMMA-based conjugates as compared to their non-conjugated counterparts. In general, copolymer systems containing a larger amount of NHSMA comonomer is recommended to increase the incorporation of peptide units and, consequently, its effect on the corresponding conjugated materials.
2. The synthesis of copolymer systems containing a suitable amount of FLUMA comonomer is necessary to investigate the cell internalization of the conjugates via confocal microscopy.
3. Flow cytometry investigations of the conjugated polymer systems provide evidence of their cell internalization in the MDCK cell line; nevertheless, different cell lines must be evaluated using this technique in future work.

## 5.3 Publications and congresses

### Publication as first author

1. C. Ventura-Hunter, G. Ayora-Talavera, P. Quintana-Owen, C. Kellner, S. Hoepfner, N. C. Roesner, D. Pretzel, U.S. Schubert, P. Quintana-Owen, G. Ayora-Talavera, E. Saldívar-Guerra, S. Fedeli, C. Guerrero-Sánchez. Haemagglutinin-derived peptides and their conjugation with block copolymers. Submitted for publication to Journal of Materials Chemistry B 2024.
2. C. Ventura-Hunter, V.D. Lechuga-Islas, J. Ulbrich, C. Kellner, U.S. Schubert, E. Saldívar-Guerra, M. Rosales-Guzmán, C. Guerrero-Sánchez. Glycerol methacrylate-based copolymers: Reactivity ratios, physicochemical characterization and cytotoxicity.

### **Publications as a co-author**

3. R. Pérez-Isidoro, F.J. Guevara-Pantoja, C. Ventura-Hunter, C. Guerrero-Sánchez, J.C. Ruiz-Suárez, U.S. Schubert, E. Saldívar-Guerra, Fluidized or not fluidized? Biophysical characterization of biohybrid lipid/protein/polymer liposomes and their interaction with tetracaine. *Biochimica et Biophysica Acta - General Subjects* 2023, 1867, 2. <https://doi.org/10.1016/j.bbagen.2022.130287>
4. Í. Terzioğlu, C. Ventura-Hunter, J. Ulbrich, E. Saldívar-Guerra, U.S. Schubert, C. Guerrero-Sánchez. Automated Parallel Dialysis for Purification of Polymers. *Polymers* 2022, 14, 4835. <https://doi.org/10.3390/polym14224835>

### **Participation in congresses**

5<sup>th</sup> US-Mexico-Canada Symposium on Advances in Polymer Science MACROMEX 2021. oral presentation. ID247, Title: “Bioconjugation of polymers with peptides derived from hemagglutinin protein.” By C. Ventura-Hunter, E. Saldívar-Guerra, C. Guerrero-Sánchez.

Conference of the CRC POLY-TARGET 2020. Cell specific strategies against inflammation-transferring basic research into application. 7-8 September 2020. Jena, Germany.

## 5.4 Appendix

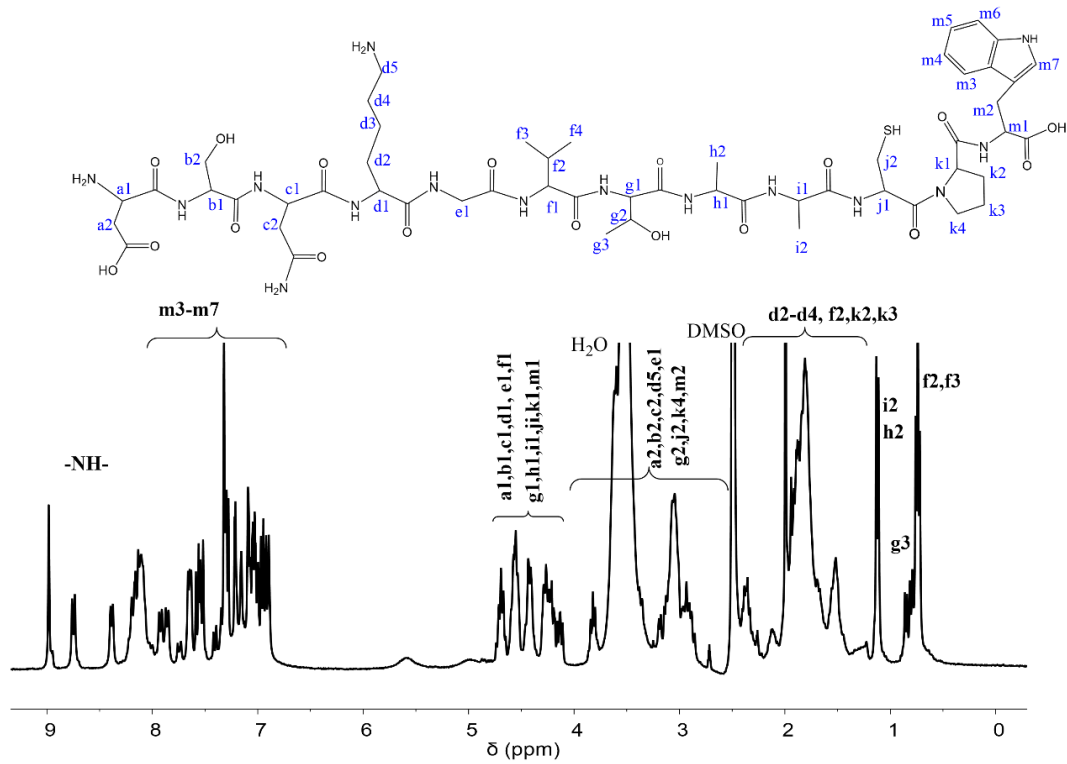


**Figure 5.1**  $^1\text{H-NMR}$  spectrum of PC1 (in  $\text{DMSO-}d_6$ , 300 MHz)

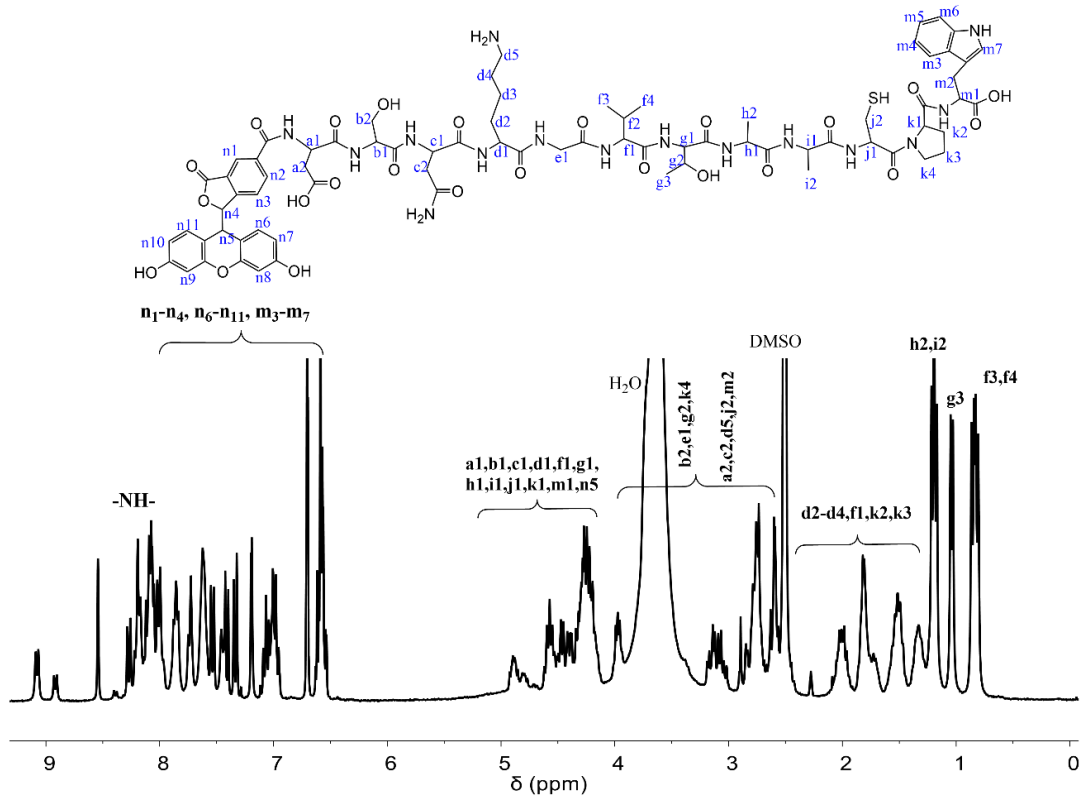


**Figure 5.2**  $^1\text{H-NMR}$  spectrum of PC1-5FAM (in  $\text{DMSO-}d_6$ , 300 MHz)

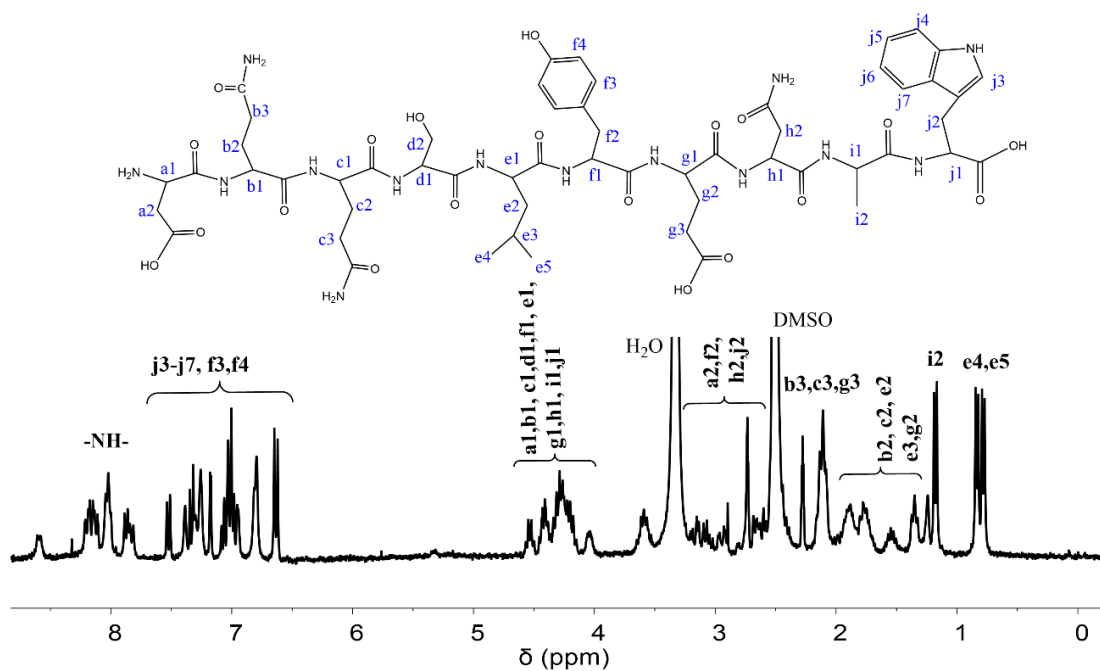


**Figure 5.3**  $^1\text{H-NMR}$  spectrum of PC2 (in  $\text{DMSO-}d_6$ , 300 MHz)

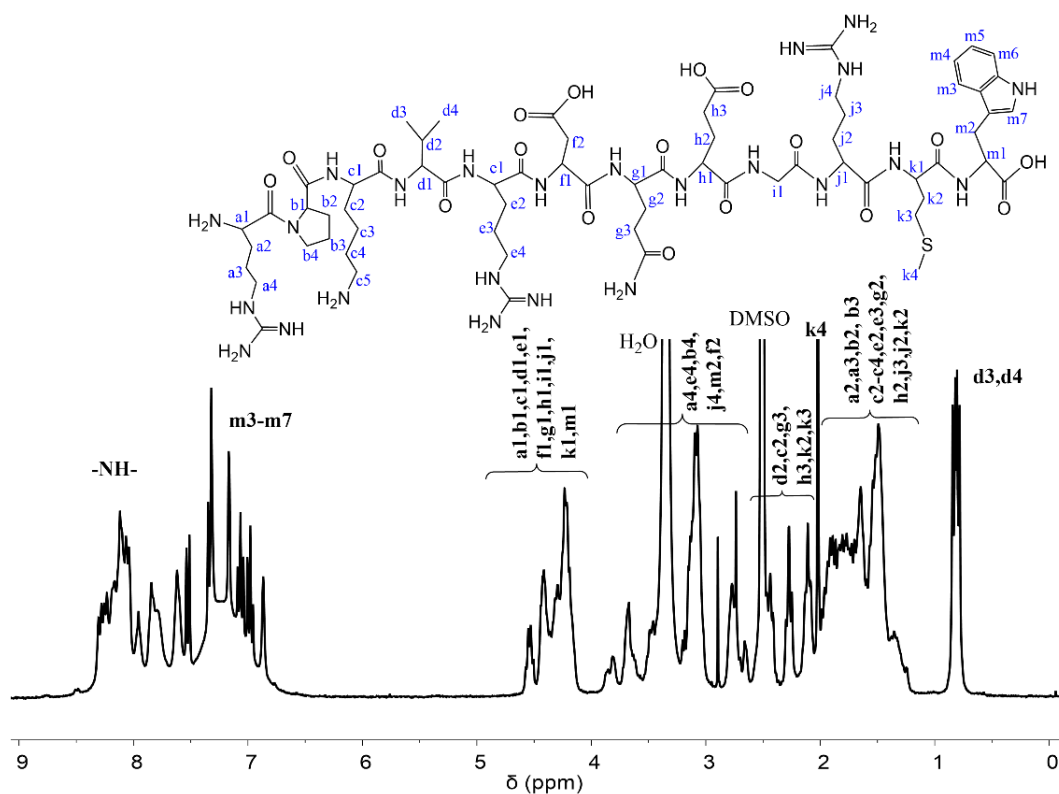


**Figure 5.4**  $^1\text{H-NMR}$  spectrum of PC3 (in  $\text{DMSO-}d_6$ , 300 MHz)

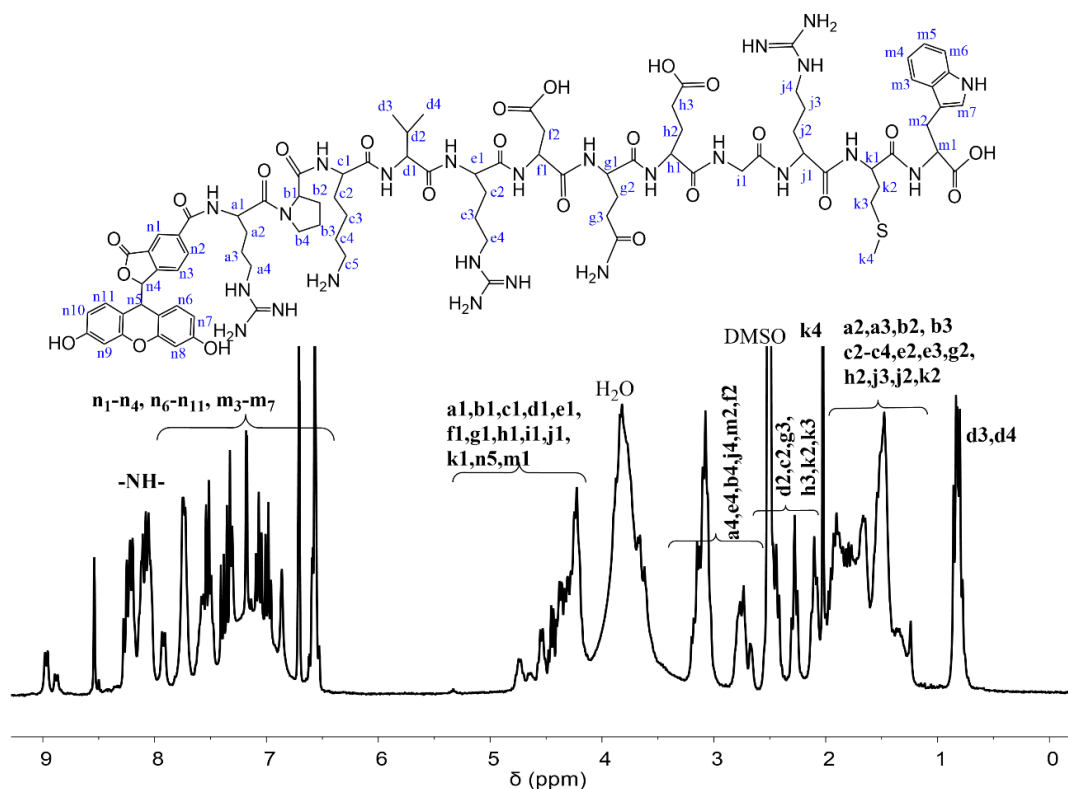


**Figure 5.5**  $^1\text{H-NMR}$  spectrum of PC3-5FAM (in  $\text{DMSO-}d_6$ , 300 MHz)

## 5.5 References

- [1] T.R. Darling, T.P. Davis, M. Fryd, A.A. Gridnev, D.M. Haddleton, S.D. Ittel, R.R. Matheson, G. Moad, E. Rizzardo, Living polymerization: Rationale for uniform terminology, *J. Polym. Sci. Part A Polym. Chem.* 38 (2000) 1706–1708. [https://doi.org/10.1002/\(SICI\)1099-0518\(20000515\)38:10<1706::AID-POLA20>3.0.CO;2-5](https://doi.org/10.1002/(SICI)1099-0518(20000515)38:10<1706::AID-POLA20>3.0.CO;2-5).
- [2] G. Moad, E. Rizzardo, S.H. Thang, Living radical polymerization by the RAFT process a third update, *Aust. J. Chem.* 65 (2012) 985–1076. <https://doi.org/10.1071/CH12295>.
- [3] S. Perrier, 50th Anniversary Perspective : RAFT Polymerization - A User Guide, *Macromolecules*. 50 (2017) 7433–7447. <https://doi.org/10.1021/acs.macromol.7b00767>.
- [4] V. Sciannamea, R. Jérôme, C. Detrembleur, In-situ nitroxide-mediated radical polymerization (NMP) processes: Their understanding and optimization, *Chem. Rev.* 108 (2008) 1104–1126. <https://doi.org/10.1021/cr0680540>.
- [5] K. Matyjaszewski, Atom Transfer Radical Polymerization (ATRP): Current status and future perspectives, *Macromolecules*. 45 (2012) 4015–4039. <https://doi.org/10.1021/ma3001719>.
- [6] M.R. Hill, R.N. Carmean, B.S. Sumerlin, Expanding the Scope of RAFT Polymerization: Recent Advances and New Horizons, *Macromolecules*. 48 (2015) 5459–5469. <https://doi.org/10.1021/acs.macromol.5b00342>.
- [7] C.L. Moad, G. Moad, Fundamentals of reversible addition–fragmentation chain transfer (RAFT), *Chem. Teach. Int.* 3 (2021) 3–17. <https://doi.org/10.1515/cti-2020-0026>.
- [8] K. Nakabayashi, H. Mori, Recent progress in controlled radical polymerization of N-vinyl monomers, *Eur. Polym. J.* 49 (2013) 2808–2838. <https://doi.org/10.1016/j.eurpolymj.2013.07.006>.

- [9] M. Destarac, On the critical role of RAFT agent design in reversible addition-fragmentation chain transfer (RAFT) polymerization, *Polym. Rev.* 51 (2011) 163–187. <https://doi.org/10.1080/15583724.2011.568130>.
- [10] D.J. Keddie, G. Moad, E. Rizzardo, S.H. Thang, RAFT agent design and synthesis, *Macromolecules*. 45 (2012) 5321–5342. <https://doi.org/10.1021/ma300410v>.
- [11] H. Mori, Living Radical Polymerization: Reversible Addition-Fragmentation Chain Transfer (RAFT) Polymerization, in: S. Kobayashi, K. Müllen (Eds.), *Encycl. Polym. Nanomater.*, Springer Berlin Heidelberg, Berlin, Heidelberg, 2015: pp. 1148–1155. <https://doi.org/10.1007/978-3-642-29648-2>.
- [12] G. Odian, Chain Copolymerization, in: *Princ. Polym.*, Fourth, John Wiley & Sons, Inc., Hoboken, NJ, USA, 2004: pp. 464–543. <https://doi.org/10.1002/047147875X.ch6>.
- [13] compiled by A.D.M. and A. Wilkinson, *The IUPAC Compendium of Chemical Terminology*, 2nd, International Union of Pure and Applied Chemistry (IUPAC), Research Triangle Park, NC, 1997. <https://doi.org/10.1351/goldbook>.
- [14] A. Gregory, M.H. Stenzel, Complex polymer architectures via RAFT polymerization: From fundamental process to extending the scope using click chemistry and nature’s building blocks, *Prog. Polym. Sci.* 37 (2012) 38–105. <https://doi.org/10.1016/j.progpolymsci.2011.08.004>.
- [15] N. Hadjichristidis, H. Iatrou, M. Pitsikalis, J. Mays, Macromolecular architectures by living and controlled/living polymerizations, *Prog. Polym. Sci.* 31 (2006) 1068–1132. <https://doi.org/10.1016/j.progpolymsci.2006.07.002>.
- [16] C. Feng, Y. Li, D. Yang, J. Hu, X. Zhang, X. Huang, Well-defined graft copolymers: From controlled synthesis to multipurpose applications, *Chem. Soc. Rev.* 40 (2011) 1282–1295. <https://doi.org/10.1039/b921358a>.
- [17] N. Corrigan, K. Jung, G. Moad, C.J. Hawker, K. Matyjaszewski, C. Boyer, Reversible-deactivation radical polymerization (Controlled/living radical polymerization): From discovery to materials design and applications, *Prog. Polym. Sci.* 111 (2020). <https://doi.org/10.1016/j.progpolymsci.2020.101311>.
- [18] J.N. Israelachvili, D.J. Mitchell, B.W. Ninham, Theory of self-assembly of hydrocarbon amphiphiles into micelles and bilayers, *J. Chem. Soc. Faraday Trans. 2.* 72 (1976) 1525. <https://doi.org/10.1039/f29767201525>.
- [19] C. Lu, M.W. Urban, Stimuli-responsive polymer nano-science: Shape anisotropy, responsiveness, applications, *Prog. Polym. Sci.* 78 (2018) 24–46. <https://doi.org/10.1016/j.progpolymsci.2017.07.005>.
- [20] C. Guerrero-Sanchez, D. Wouters, C.A. Fustin, J.F. Gohy, B.G.G. Lohmeijer, U.S. Schubert, Structure-property study of diblock copolymer micelles: Core and corona radius with varying composition and degree of polymerization, *Macromolecules*. 38 (2005) 10185–10191. <https://doi.org/10.1021/ma051544u>.
- [21] F. Sciortino, Entropy in self-assembly, *Riv. Del Nuovo Cim.* 42 (2019) 511–548. <https://doi.org/10.1393/ncr/i2019-10165-1>.
- [22] L. Zhang, A. Eisenberg, Multiple morphologies and characteristics of “crew-cut” micelle-like aggregates of polystyrene-b-poly(acrylic acid) diblock copolymers in aqueous solutions, *J. Am. Chem. Soc.* 118 (1996) 3168–3181. <https://doi.org/10.1021/ja953709s>.
- [23] S. Schubert, J.T. Delaney, Jr, U.S. Schubert, Nanoprecipitation and nanoformulation of polymers: from history to powerful possibilities beyond poly(lactic acid), *Soft Matter*. 7 (2011) 1581–1588. <https://doi.org/10.1039/C0SM00862A>.
- [24] G. Riess, Micellization of block copolymers, *Prog. Polym. Sci.* 28 (2003) 1107–1170. [https://doi.org/10.1016/S0079-6700\(03\)00015-7](https://doi.org/10.1016/S0079-6700(03)00015-7).
- [25] F. Asghari, M. Samiei, K. Adibkia, A. Akbarzadeh, S. Davaran, Biodegradable and biocompatible polymers for tissue engineering application: a review, *Artif. Cells, Nanomedicine Biotechnol.* 45



- (2017) 185–192. <https://doi.org/10.3109/21691401.2016.1146731>.
- [26] P. Sharma, P. Negi, N. Mahindroo, Recent advances in polymeric drug delivery carrier systems, *Adv. Polym. Biomed. Appl.* (2018) 369–388.
- [27] A.J. Nathanael, T.H. Oh, Biopolymer coatings for biomedical applications, *Polymers (Basel)*. 12 (2020) 1–26. <https://doi.org/10.3390/polym12123061>.
- [28] M.F. Maitz, Applications of synthetic polymers in clinical medicine, *Biosurface and Biotribology*. 1 (2015) 161–176. <https://doi.org/10.1016/j.bsbt.2015.08.002>.
- [29] F. Vert, M.; Doi, Y.; Hellwich, K.; Hess, M.; Hodge, P.; Kubisa, P.; Rinaudo, M.; Schue, Terminology for biorelated polymers and applications (IUPAC Recommendations 2012), *Pure Appl. Chem.* 84 (2012) 377–410. <https://doi.org/10.1351/PAC-REC-10-12-04>.
- [30] D.F. Williams, On the mechanisms of biocompatibility, *Biomaterials*. 29 (2008) 2941–2953. <https://doi.org/10.1016/j.biomaterials.2008.04.023>.
- [31] T.L. Riss, R.A. Moravec, Use of multiple assay endpoints to investigate the effects of incubation time, dose of toxin, and plating density in cell-based cytotoxicity assays, *Assay Drug Dev. Technol.* 2 (2004) 51–62. <https://doi.org/10.1089/154065804322966315>.
- [32] W. LI, J. ZHOU, Y. XU, Study of the in vitro cytotoxicity testing of medical devices, *Biomed. Reports*. 3 (2015) 617–620. <https://doi.org/10.3892/br.2015.481>.
- [33] D.J. Snodin, A primer for pharmaceutical process development chemists and analysts in relation to impurities perceived to be mutagenic or “genotoxic,” *Org. Process Res. Dev.* 24 (2020) 2407–2427. <https://doi.org/10.1021/acs.oprd.0c00343>.
- [34] L.A. Poole-Warren, A.J. Patton, Introduction to biomedical polymers and biocompatibility, Elsevier Ltd, 2016. <https://doi.org/10.1016/B978-1-78242-105-4.00001-8>.
- [35] V. Bulmus, RAFT polymerization mediated bioconjugation strategies, *Polym. Chem.* 2 (2011) 1463–1472. <https://doi.org/10.1039/c1py00039j>.
- [36] J.F. Lutz, H.G. Börner, Modern trends in polymer bioconjugates design, *Prog. Polym. Sci.* 33 (2008) 1–39. <https://doi.org/10.1016/j.progpolymsci.2007.07.005>.
- [37] F. Li, R.I. Mahato, Bioconjugate Therapeutics: Current Progress and Future Perspective, *Mol. Pharm.* 14 (2017) 1321–1324. <https://doi.org/10.1021/acs.molpharmaceut.7b00263>.
- [38] C. Chen, D.Y.W. Ng, T. Weil, Polymer bioconjugates: Modern design concepts toward precision hybrid materials, *Prog. Polym. Sci.* 105 (2020) 101241. <https://doi.org/10.1016/j.progpolymsci.2020.101241>.
- [39] J. Nicolas, G. Mantovani, D.M. Haddleton, Living Radical Polymerization as a Tool for the Synthesis of Polymer-Protein / Peptide Bioconjugates, (2006) 1083–1111. <https://doi.org/10.1002/marc.200700112>.
- [40] A. Das, P. Theato, Activated Ester Containing Polymers: Opportunities and Challenges for the Design of Functional Macromolecules, *Chem. Rev.* 116 (2016) 1434–1495. <https://doi.org/10.1021/acs.chemrev.5b00291>.
- [41] P. Ferruti, A. Bettelli, A. Fere, High polymers of acrylic and methacrylic esters of N-hydroxysuccinimide as polyacrylamide and polymethacrylamide precursors, *Polymer (Guildf)*. 13 (1972) 462–464.
- [42] M. Eberhardt, R. Mruk, R. Zentel, P. Théato, Synthesis of pentafluorophenyl(meth)acrylate polymers: New precursor polymers for the synthesis of multifunctional materials, *Eur. Polym. J.* 41 (2005) 1569–1575. <https://doi.org/10.1016/j.eurpolymj.2005.01.025>.
- [43] J. Alex, J. Ulbrich, M. Rosales-Guzmán, C. Weber, U.S. Schubert, C. Guerrero-Sanchez, Kinetic investigations on homo- and co-polymerizations of pentafluorophenyl (meth)acrylates, *Eur. Polym. J.* 143 (2021). <https://doi.org/10.1016/j.eurpolymj.2020.110175>.
- [44] M. Sobczak, C. Debek, E. Oledzka, R. Kozłowski, Polymeric systems of antimicrobial peptides-

- strategies and potential applications, *Molecules*. 18 (2013) 14122–14137. <https://doi.org/10.3390/molecules181114122>.
- [45] Z. Kang, Q. Meng, K. Liu, Peptide-based gene delivery vectors, *J. Mater. Chem. B*. 7 (2019) 1824–1841. <https://doi.org/10.1039/C8TB03124J>.
- [46] W. jin Jeong, J. Bu, L.J. Kubiawicz, S.S. Chen, Y.S. Kim, S. Hong, Peptide–nanoparticle conjugates: a next generation of diagnostic and therapeutic platforms?, *Nano Converg.* 5 (2018) 1–18. <https://doi.org/10.1186/s40580-018-0170-1>.
- [47] R. He, B. Finan, J.P. Mayer, R.D. DiMarchi, Peptide conjugates with small molecules designed to enhance efficacy and safety, *Molecules*. 24 (2019) 11–14. <https://doi.org/10.3390/molecules24101855>.
- [48] B. Albada, N. Metzler-Nolte, Organometallic–Peptide Bioconjugates: Synthetic Strategies and Medicinal Applications, *Chem. Rev.* 116 (2016) 11797–11839. <https://doi.org/10.1021/acs.chemrev.6b00166>.
- [49] S.A.A. Rizvi, A.M. Saleh, Applications of nanoparticle systems in drug delivery technology, *Saudi Pharm. J.* 26 (2018) 64–70. <https://doi.org/10.1016/j.jsps.2017.10.012>.
- [50] G. Guidotti, L. Brambilla, D. Rossi, Cell-Penetrating Peptides: From Basic Research to Clinics, *Trends Pharmacol. Sci.* 38 (2017) 406–424. <https://doi.org/10.1016/j.tips.2017.01.003>.
- [51] K. Desale, K. Kuche, S. Jain, Cell-penetrating peptides (CPPs): An overview of applications for improving the potential of nanotherapeutics, *Biomater. Sci.* 9 (2021) 1153–1188. <https://doi.org/10.1039/d0bm01755h>.
- [52] M. Green, M. Ishino, P.M. Loewenstein, Mutational analysis of HIV-1 Tat minimal domain peptides: Identification of trans-dominant mutants that suppress HIV-LTR-driven gene expression, *Cell*. 58 (1989) 215–223. [https://doi.org/10.1016/0092-8674\(89\)90417-0](https://doi.org/10.1016/0092-8674(89)90417-0).
- [53] P.A. Wender, D.J. Mitchell, K. Pattabiraman, E.T. Pelkey, L. Steinman, J.B. Rothbard, The design, synthesis, and evaluation of molecules that enable or enhance cellular uptake: Peptoid molecular transporters, *Proc. Natl. Acad. Sci. U. S. A.* 97 (2000) 13003–13008. <https://doi.org/10.1073/pnas.97.24.13003>.
- [54] J.C. Mai, H. Shen, S.C. Watkins, T. Cheng, P.D. Robbins, Efficiency of protein transduction is cell type-dependent and is enhanced by dextran sulfate., *J. Biol. Chem.* 277 (2002) 30208–30218. <https://doi.org/10.1074/jbc.M204202200>.
- [55] A. Joliot, C. Pernelle, H. Deagostini-Bazin, A. Prochiantz, Antennapedia homeobox peptide regulates neural morphogenesis, *Proc. Natl. Acad. Sci. U. S. A.* 88 (1991) 1864–1868. <https://doi.org/10.1073/pnas.88.5.1864>.
- [56] T. Jiang, Z. Zhang, Y. Zhang, H. Lv, J. Zhou, C. Li, L. Hou, Q. Zhang, Dual-functional liposomes based on pH-responsive cell-penetrating peptide and hyaluronic acid for tumor-targeted anticancer drug delivery, *Biomaterials*. 33 (2012) 9246–9258. <https://doi.org/10.1016/j.biomaterials.2012.09.027>.
- [57] S. El-Andaloussi, H.J. Johansson, T. Holm, Ü. Langel, A novel cell-penetrating peptide, M918, for efficient delivery of proteins and peptide nucleic acids, *Mol. Ther.* 15 (2007) 1820–1826. <https://doi.org/10.1038/sj.mt.6300255>.
- [58] H.J. Johansson, S. El-Andaloussi, T. Holm, M. Mäe, J. Jänes, T. Maimets, Ü. Langel, Characterization of a novel cytotoxic cell-penetrating peptide derived from p14ARF protein, *Mol. Ther.* 16 (2008) 115–123. <https://doi.org/10.1038/sj.mt.6300346>.
- [59] G. Elliott, P. O’Hare, Intercellular trafficking and protein delivery by a herpesvirus structural protein, *Cell*. 88 (1997) 223–233. [https://doi.org/10.1016/S0092-8674\(00\)81843-7](https://doi.org/10.1016/S0092-8674(00)81843-7).
- [60] M. Pooga, M. Hällbrink, M. Zorko, Ü. Langel, Cell penetration by transportan, *FASEB J.* 12 (1998) 67–77. <https://doi.org/10.1096/fsb2fasebj.12.1.67>.
- [61] M.C. Morris, S. Deshayes, F. Heitz, G. Divita, Cell-penetrating peptides: from molecular mechanisms to therapeutics, *Biol. Cell*. 100 (2008) 201–217. <https://doi.org/10.1042/bc20070116>.

- [62] A. Elmquist, M. Lindgren, T. Bartfai, Ü. Langel, Ve-cadherin-derived cell-penetrating peptide, pVEC with carrier functions, *Exp. Cell Res.* 269 (2001) 237–244. <https://doi.org/10.1006/excr.2001.5316>.
- [63] J. Oehlke, A. Scheller, B. Wiesner, E. Krause, M. Beyermann, E. Klauschenz, M. Melzig, M. Bienert, Cellular uptake of an  $\alpha$ -helical amphipathic model peptide with the potential to deliver polar compounds into the cell interior non-endocytically, *Biochim. Biophys. Acta - Biomembr.* 1414 (1998) 127–139. [https://doi.org/10.1016/S0005-2736\(98\)00161-8](https://doi.org/10.1016/S0005-2736(98)00161-8).
- [64] M.C. Morris, P. Vidal, L. Chaloin, F. Heitz, G. Divita, A new peptide vector for efficient delivery of oligonucleotides into mammalian cells, *Nucleic Acids Res.* 25 (1997) 2730–2736. <https://doi.org/10.1093/nar/25.14.2730>.
- [65] J. Oehlke, E. Krause, B. Wiesner, M. Beyermann, M. Bienert, Extensive cellular uptake into endothelial cells of an amphipathic  $\beta$ -sheet forming peptide, *FEBS Lett.* 415 (1997) 196–199. [https://doi.org/10.1016/S0014-5793\(97\)01123-X](https://doi.org/10.1016/S0014-5793(97)01123-X).
- [66] C.L. Watkins, P. Brennan, C. Fegan, K. Takayama, I. Nakase, S. Futaki, A.T. Jones, Cellular uptake, distribution and cytotoxicity of the hydrophobic cell penetrating peptide sequence PFVYLI linked to the proapoptotic domain peptide PAD, *J. Control. Release.* 140 (2009) 237–244. <https://doi.org/10.1016/j.jconrel.2009.04.028>.
- [67] F. Nakayama, T. Yasuda, S. Umeda, M. Asada, T. Imamura, V. Meineke, M. Akashi, Fibroblast growth factor-12 (FGF12) translocation into intestinal epithelial cells is dependent on a novel cell-penetrating peptide domain: Involvement of internalization in the in vivo role of exogenous FGF12, *J. Biol. Chem.* 286 (2011) 25823–25834. <https://doi.org/10.1074/jbc.M110.198267>.
- [68] S. Gao, M.J. Simon, C.D. Hue, B. Morrison, S. Banta, An unusual cell penetrating peptide identified using a plasmid display-based functional selection platform, *ACS Chem. Biol.* 6 (2011) 484–491. <https://doi.org/10.1021/cb100423u>.
- [69] A. Mousavizadeh, A. Jabbari, M. Akrami, H. Bardania, Cell targeting peptides as smart ligands for targeting of therapeutic or diagnostic agents: a systematic review, *Colloids Surfaces B Biointerfaces.* 158 (2017) 507–517. <https://doi.org/10.1016/j.colsurfb.2017.07.012>.
- [70] D.A. Cheresch, R.C. Spiro, Biosynthetic and functional properties of an Arg-Gly-Asp-directed receptor involved in human melanoma cell attachment to vitronectin, fibrinogen, and von Willebrand factor, *J. Biol. Chem.* 262 (1987) 17703–17711. [https://doi.org/10.1016/s0021-9258\(18\)45436-1](https://doi.org/10.1016/s0021-9258(18)45436-1).
- [71] Q.K. Lin, Y. Hou, K.F. Ren, J. Ji, Selective endothelial cells adhesion to Arg-Glu-Asp-Val peptide functionalized polysaccharide multilayer, *Thin Solid Films.* 520 (2012) 4971–4978. <https://doi.org/10.1016/j.tsf.2012.03.041>.
- [72] Z. Meng, Z. Kang, C. Sun, S. Yang, B. Zhao, S. Feng, Q. Meng, K. Liu, Enhanced gene transfection efficiency by use of peptide vectors containing laminin receptor-targeting sequence YIGSR, *Nanoscale.* 10 (2018) 1215–1227. <https://doi.org/10.1039/c7nr05843h>.
- [73] S. Urnauer, A.M. Müller, C. Schug, K.A. Schmohl, M. Tutter, N. Schwenk, W. Rödl, S. Morys, M. Ingrisich, J. Bertram, P. Bartenstein, D.A. Clevert, E. Wagner, C. Spitzweg, EGFR-targeted nonviral NIS gene transfer for bioimaging and therapy of disseminated colon cancer metastases, *Oncotarget.* 8 (2017) 92195–92208. <https://doi.org/10.18632/oncotarget.21028>.
- [74] M. Demeule, A. Regina, C. Ché, J. Poirier, T. Nguyen, R. Gabathuler, J.P. Castaigne, R. Béliveau, Identification and design of peptides as a new drug delivery system for the brain, *J. Pharmacol. Exp. Ther.* 324 (2008) 1064–1072. <https://doi.org/10.1124/jpet.107.131318>.
- [75] F. Maruta, A.L. Parker, K.D. Fisher, M.T. Hallissey, T. Ismail, D.C. Rowlands, L.A. Chandler, D.J. Kerr, L.W. Seymour, Identification of FGF receptor-binding peptides for cancer gene therapy, *Cancer Gene Ther.* 9 (2002) 543–552. <https://doi.org/10.1038/sj.cgt.7700470>.
- [76] J. Yang, X. Hao, Q. Li, M. Akpanyung, A. Nejjari, A.L. Neve, X. Ren, J. Guo, Y. Feng, C. Shi, W. Zhang, CAGW Peptide- and PEG-Modified Gene Carrier for Selective Gene Delivery and Promotion of Angiogenesis in HUVECs in Vivo, *ACS Appl. Mater. Interfaces.* 9 (2017) 4485–4497. <https://doi.org/10.1021/acsami.6b14769>.

- [77] N. Sriwilaijaroen, Y. Suzuki, Molecular basis of the structure and function of H1 hemagglutinin of influenza virus, *Proc. Japan Acad. Ser. B.* 88 (2012) 226–249. <https://doi.org/10.2183/pjab.88.226>.
- [78] G. Neumann, Y. Kawaoka, Transmission of influenza A viruses, *Virology.* 479–480 (2015) 234–246. <https://doi.org/10.1016/j.virol.2015.03.009>.
- [79] N.K. Garcia, M. Guttman, J.L. Ebner, K.K. Lee, Dynamic changes during acid-induced activation of influenza hemagglutinin, *Structure.* 23 (2015) 665–676. <https://doi.org/10.1016/j.str.2015.02.006>.
- [80] M. Murata, Y. Sugahara, S. Takahashi, S. ichi Ohnishi, Ph-dependent membrane fusion activity of a synthetic twenty amino acid peptide with the same sequence as that of the hydrophobic segment of influenza virus hemagglutinin, *J. Biochem.* 102 (1987) 957–962. <https://doi.org/10.1093/oxfordjournals.jbchem.a122137>.
- [81] C. Plank, B. Oberhauser, K. Mechtler, C. Koch, E. Wagner, The influence of endosome-disruptive peptides on gene transfer using synthetic virus-like gene transfer systems., *J. Biol. Chem.* 269 (1994) 12918–12924. [https://doi.org/10.1016/S0021-9258\(18\)99963-1](https://doi.org/10.1016/S0021-9258(18)99963-1).
- [82] P. Midoux, A. Kichler, V. Boutin, J.C. Maurizot, M. Monsigny, Membrane permeabilization and efficient gene transfer by a peptide containing several histidines, *Bioconjug. Chem.* 9 (1998) 260–267. <https://doi.org/10.1021/bc9701611>.
- [83] M. Sisteré-Oró, J. Vergara-Alert, T. Stratmann, S. López-Serrano, S. Pina-Pedrero, L. Córdoba, M. Pérez-Maillo, P. Pleguezuelos, E. Vidal, V. Veljkovic, J. Segalés, J. Nielsen, A. Fomsgaard, A. Darji, Conserved HA-peptide NG34 formulated in pCMV-CTLA4-Ig reduces viral shedding in pigs after a heterosubtypic influenza virus SwH3N2 challenge, *PLoS One.* 14 (2019) 1–18. <https://doi.org/10.1371/journal.pone.0212431>.
- [84] S. López-Serrano, L. Cordoba, M. Pérez-Maillo, P. Pleguezuelos, E.J. Remarque, T. Ebensen, C.A. Guzmán, D. Christensen, J. Segalés, A. Darji, Immune responses to pandemic h1n1 influenza virus infection in pigs vaccinated with a conserved hemagglutinin HA1 peptide adjuvanted with CAF®01 or CDA/αGalCerMPEG, *Vaccines.* 9 (2021). <https://doi.org/10.3390/vaccines9070751>.
- [85] X. Ge, V. Tan, P.L. Bollyky, N.E. Standifer, E.A. James, W.W. Kwok, Assessment of Seasonal Influenza A Virus-Specific CD4 T-Cell Responses to 2009 Pandemic H1N1 Swine-Origin Influenza A Virus, *J. Virol.* 84 (2010) 3312–3319. <https://doi.org/10.1128/jvi.02226-09>.
- [86] N. Lohia, M. Baranwal, Highly conserved hemagglutinin peptides of H1N1 influenza virus elicit immune response, *3 Biotech.* 8 (2018) 1–10. <https://doi.org/10.1007/s13205-018-1509-3>.
- [87] F.M. Veronese, G. Pasut, PEGylation, successful approach to drug delivery, *Drug Discov. Today.* 10 (2005) 1451–1458. [https://doi.org/10.1016/S1359-6446\(05\)03575-0](https://doi.org/10.1016/S1359-6446(05)03575-0).
- [88] L.H. Belén, C. De Oliveira Rangel-Yagui, J.F. Beltrán Lissabet, B. Effer, M. Lee-Estevez, A. Pessoa, R.L. Castillo, J.G. Fariás, From synthesis to characterization of site-selective pegylated proteins, *Front. Pharmacol.* 10 (2019) 1–16. <https://doi.org/10.3389/fphar.2019.01450>.
- [89] F.M. Veronese, Peptide and protein PEGylation, *Biomaterials.* 22 (2001) 405–417. [https://doi.org/10.1016/s0142-9612\(00\)00193-9](https://doi.org/10.1016/s0142-9612(00)00193-9).
- [90] J. Milton Harris, N.E. Martin, M. Modi, Pegylation: A novel process for modifying pharmacokinetics, *Clin. Pharmacokinet.* 40 (2001) 539–551. <https://doi.org/10.2165/00003088-200140070-00005>.
- [91] M.S. Thompson, T.P. Vadala, M.L. Vadala, Y. Lin, J.S. Riffle, Synthesis and applications of heterobifunctional poly(ethylene oxide) oligomers, *Polymer (Guildf).* 49 (2008) 345–373. <https://doi.org/10.1016/j.polymer.2007.10.029>.
- [92] J. Li, W.J. Kao, Synthesis of polyethylene glycol (PEG) derivatives and PEGylated - Peptide biopolymer conjugates, *Biomacromolecules.* 4 (2003) 1055–1067. <https://doi.org/10.1021/bm034069l>.
- [93] D. Hutanu, M.D. Frishberg, L. Guo, C.C. Darie, Recent Applications of Polyethylene Glycols (PEGs) and PEG Derivatives, *Mod. Chem. Appl.* 02 (2014) 2–7. <https://doi.org/10.4172/2329->

6798.1000132.

- [94] J. Alex, K. González, T. Kindel, P. Bellstedt, C. Weber, T. Heinekamp, T. Orasch, C. Guerrero-Sanchez, U.S. Schubert, A.A. Brakhage, Caspofungin Functionalized Polymethacrylates with Antifungal Properties, *Biomacromolecules*. 21 (2020) 2104–2115. <https://doi.org/10.1021/acs.biomac.0c00096>.
- [95] M. Beija, Y. Li, A.B. Lowe, T.P. Davis, C. Boyer, Factors influencing the synthesis and the post-modification of PEGylated pentafluorophenyl acrylate containing copolymers, *Eur. Polym. J.* 49 (2013) 3060–3071. <https://doi.org/10.1016/j.eurpolymj.2013.05.003>.
- [96] R. Haigh, S. Rimmer, N.J. Fullwood, Synthesis and properties of amphiphilic networks. 1: The effect of hydration and polymer composition on the adhesion of immunoglobulin-G to poly(laurylmethacrylate-stat-glycerolmonomethacrylate-stat-ethylene-glycol-dimethacrylate) networks, *Biomaterials*. 21 (2000) 735–739. [https://doi.org/10.1016/S0142-9612\(99\)00245-8](https://doi.org/10.1016/S0142-9612(99)00245-8).
- [97] G. Robert-Nicoud, R. Evans, C.D. Vo, C.J. Cadman, N. Tirelli, Synthesis, self-assembly and (absence of) protein interactions of poly(glycerol methacrylate)-silicone macro-amphiphiles, *Polym. Chem.* 4 (2013) 3458–3470. <https://doi.org/10.1039/c3py00273j>.
- [98] C. Giacomelli, V. Schmidt, R. Borsali, Nanocontainers formed by self-assembly of poly(ethylene oxide)-b-poly(glycerol monomethacrylate) - Drug conjugates, *Macromolecules*. 40 (2007) 2148–2157. <https://doi.org/10.1021/ma062562u>.
- [99] M. Save, J.V.M. Weaver, S.P. Armes, P. Mckenna, Atom Transfer Radical Polymerization of Hydroxy-Functional Methacrylates at Ambient Temperature: Comparison of Glycerol Monomethacrylate with 2-Hydroxypropyl Methacrylate, *Macromolecules*. 35 (2002) 1152–1159.
- [100] L.P.D. Ratcliffe, A. Blanz, C.N. Williams, S.L. Brown, S.P. Armes, RAFT polymerization of hydroxy-functional methacrylic monomers under heterogeneous conditions: Effect of varying the core-forming block, *Polym. Chem.* 5 (2014) 3643–3655. <https://doi.org/10.1039/c4py00203b>.
- [101] S.O. Kyeremateng, E. Amado, J. Kressler, Synthesis and characterization of random copolymers of (2,2-dimethyl-1,3-dioxolan-4-yl)methyl methacrylate and 2,3-dihydroxypropyl methacrylate, *Eur. Polym. J.* 43 (2007) 3380–3391. <https://doi.org/10.1016/j.eurpolymj.2007.04.048>.
- [102] F. D'Agosto, J. Rieger, M. Lansalot, RAFT-Mediated Polymerization-Induced Self-Assembly, *Angew. Chemie - Int. Ed.* 59 (2020) 8368–8392. <https://doi.org/10.1002/anie.201911758>.
- [103] S. Chatterjee, P. Upadhyay, M. Mishra, M. Srividya, M.R. Akshara, N. Kamali, Z.S. Zaidi, S.F. Iqbal, S.K. Misra, Advances in chemistry and composition of soft materials for drug releasing contact lenses, *RSC Adv.* 10 (2020) 36751–36777. <https://doi.org/10.1039/d0ra06681h>.
- [104] Y. Ma, H. Gao, W. Gu, Y.W. Yang, Y. Wang, Y. Fan, G. Wu, J. Ma, Carboxylated poly(glycerol methacrylate)s for doxorubicin delivery, *Eur. J. Pharm. Sci.* 45 (2012) 65–72. <https://doi.org/10.1016/j.ejps.2011.10.025>.
- [105] P. De Leonardis, F. Cellesi, N. Tirelli, Tuning the properties of hybrid SiO<sub>2</sub>/ poly(glycerol monomethacrylate) nanoparticles for enzyme nanoencapsulation, *Colloids Surfaces A Physicochem. Eng. Asp.* 580 (2019) 123734. <https://doi.org/10.1016/j.colsurfa.2019.123734>.
- [106] C. Wang, B. Yu, B. Knudsen, J. Harmon, F. Moussy, Y. Moussy, Synthesis and performance of novel hydrogels coatings for implantable glucose sensors, *Biomacromolecules*. 9 (2008) 561–567. <https://doi.org/10.1021/bm701102y>.
- [107] K. Mequanint, A. Patel, D. Bezuidenhout, Synthesis, swelling behavior, and biocompatibility of novel physically cross-linked polyurethane-block-poly(glycerol methacrylate) hydrogels, *Biomacromolecules*. 7 (2006) 883–891. <https://doi.org/10.1021/bm0507047>.
- [108] M. Patenaude, T. Hoare, Injectable, degradable thermoresponsive poly(nisopropylacrylamide) hydrogels, *ACS Macro Lett.* 1 (2012) 409–413. <https://doi.org/10.1021/mz200121k>.
- [109] I. Canton, N.J. Warren, A. Chahal, K. Amps, A. Wood, R. Weightman, E. Wang, H. Moore, S.P. Armes, Mucin-inspired thermoresponsive synthetic hydrogels induce stasis in human pluripotent stem cells and human embryos, *ACS Cent. Sci.* 2 (2016) 65–74.

<https://doi.org/10.1021/acscentsci.5b00370>.

- [110] E. Patrucco, S. Ouasti, D.V. Cong, P. De Leonardis, A. Pollicino, S.P. Armes, M. Scandola, N. Tirelli, Surface-initiated ATRP modification of tissue culture substrates: Poly(glycerol monomethacrylate) as an antifouling surface, *Biomacromolecules*. 10 (2009) 3130–3140. <https://doi.org/10.1021/bm900856r>.
- [111] L. Ragupathy, D.G. Millar, N. Tirelli, F. Cellesi, An orthogonal click-chemistry approach to design poly(glycerol monomethacrylate)-based nanomaterials for controlled immunostimulation, *Macromol. Biosci*. 14 (2014) 1528–1538. <https://doi.org/10.1002/mabi.201400146>.
- [112] R.J. Lamm, T.J. Pichon, F. Huyen, X. Wang, A.N. Prossnitz, K.T. Manner, N.J. White, S.H. Pun, Optimizing the Polymer Chemistry and Synthesis Method of PolySTAT, an Injectable Hemostat, *ACS Biomater. Sci. Eng.* 6 (2020) 7011–7020. <https://doi.org/10.1021/acsbiomaterials.0c01189>.
- [113] M. Sauer, J. Hofkens, J. Enderlein, *Handbook of Fluorescence Spectroscopy and Imaging*, WILEY-VCH Verlag GmbH & Co. KGaA, Weinheim, Germany, 2011. <https://doi.org/10.1002/9783527633500>.
- [114] J. Diagram, E. Transitions, *Fluorescence Spectroscopy Principles*, in: *Princ. Appl. Fluoresc. Spectrosc.*, Wiley, 2007: pp. 88–114. <https://doi.org/10.1002/9780470692059.ch7>.
- [115] A.B.T. Ghisaidoobe, S.J. Chung, Intrinsic tryptophan fluorescence in the detection and analysis of proteins: A focus on Förster resonance energy transfer techniques, *Int. J. Mol. Sci.* 15 (2014) 22518–22538. <https://doi.org/10.3390/ijms151222518>.
- [116] J.R. Lakowicz, *Principles of Fluorescence Spectroscopy*, Third Edit, Springer US, Boston, MA, 2006. <https://doi.org/10.1007/978-0-387-46312-4>.
- [117] M.M. Martin, Hydrogen bond effects on radiationless electronic transitions in xanthene dyes, *Chem. Phys. Lett.* 35 (1975) 105–111. [https://doi.org/10.1016/0009-2614\(75\)85598-9](https://doi.org/10.1016/0009-2614(75)85598-9).
- [118] Z.G. Zhao, T. Shen, H.J. Xu, The absorption and structure of fluorescein and its ethyl derivatives in various solutions, *Spectrochim. Acta Part A Mol. Spectrosc.* 45 (1989) 1113–1116. [https://doi.org/10.1016/0584-8539\(89\)80189-8](https://doi.org/10.1016/0584-8539(89)80189-8).
- [119] D.M. Tosashi, B. Szczupak, A.G. Ryder, A. Calvet, M. O’Loughlin, Erratum: Investigating tryptophan quenching of fluorescein fluorescence under protolytic equilibrium (*Journal of Physical Chemistry* (2009) 113 (2757)), *J. Phys. Chem. A*. 113 (2009) 7981. <https://doi.org/10.1021/jp904494p>.
- [120] R. Sjöback, J. Nygren, M. Kubista, Absorption and fluorescence properties of fluorescein, *Spectrochim. Acta Part A Mol. Spectrosc.* 51 (1995) L7–L21. [https://doi.org/10.1016/0584-8539\(95\)01421-P](https://doi.org/10.1016/0584-8539(95)01421-P).
- [121] N. Marmé, J.P. Knemeyer, M. Sauer, J. Wolfrum, Inter- and Intramolecular Fluorescence Quenching of Organic Dyes by Tryptophan, *Bioconjug. Chem.* 14 (2003) 1133–1139. <https://doi.org/10.1021/bc0341324>.
- [122] A.C. Vaiana, H. Neuweiler, A. Schulz, J. Wolfrum, M. Sauer, J.C. Smith, Fluorescence Quenching of Dyes by Tryptophan: Interactions at Atomic Detail from Combination of Experiment and Computer Simulation, *J. Am. Chem. Soc.* 125 (2003) 14564–14572. <https://doi.org/10.1021/ja036082j>.
- [123] Ö.S. Aslantürk, In Vitro Cytotoxicity and Cell Viability Assays: Principles, Advantages, and Disadvantages, in: *Genotoxicity - A Predict. Risk to Our Actual World*, InTech, Rijeka, 2018: p. Ch. 1. <https://doi.org/10.5772/intechopen.71923>.
- [124] L. Boulos, M. Prévost, B. Barbeau, J. Coallier, R. Desjardins, LIVE/DEAD® BacLight(TM): Application of a new rapid staining method for direct enumeration of viable and total bacteria in drinking water, *J. Microbiol. Methods*. 37 (1999) 77–86. [https://doi.org/10.1016/S0167-7012\(99\)00048-2](https://doi.org/10.1016/S0167-7012(99)00048-2).
- [125] W. Strober, Trypan blue exclusion test of cell viability., *Curr. Protoc. Immunol. Appendix 3* (2001) 2–3. <https://doi.org/10.1002/0471142735.ima03bs21>.

- [126] O. Braissant, M. Astasov-Frauenhoffer, T. Waltimo, G. Bonkat, A Review of Methods to Determine Viability, Vitality, and Metabolic Rates in Microbiology, *Front. Microbiol.* 11 (2020) 1–25. <https://doi.org/10.3389/fmicb.2020.547458>.
- [127] M. Xu, D.J. McCanna, J.G. Sivak, Use of the viability reagent PrestoBlue in comparison with alamarBlue and MTT to assess the viability of human corneal epithelial cells, *J. Pharmacol. Toxicol. Methods.* 71 (2015) 1–7. <https://doi.org/10.1016/j.vascn.2014.11.003>.
- [128] N. Lall, C.J. Henley-Smith, M.N. De Canha, C.B. Oosthuizen, D. Berrington, Viability reagent, prestoblue, in comparison with other available reagents, utilized in cytotoxicity and antimicrobial assays, *Int. J. Microbiol.* 2013 (2013). <https://doi.org/10.1155/2013/420601>.
- [129] C.M. Martín-Navarro, A. López-Arencibia, I. Sifaoui, M. Reyes-Battle, A.M. Cabello-Vílchez, S. Maciver, B. Valladares, J.E. Piñero, J. Lorenzo-Morales, PrestoBlue® and AlamarBlue® are equally useful as agents to determine the viability of *Acanthamoeba* trophozoites, *Exp. Parasitol.* 145 (2014) S69–S72. <https://doi.org/10.1016/j.exppara.2014.03.024>.
- [130] C.N. Pace, G.R. Grimsley, J.M. Scholtz, Protein ionizable groups: pK values and their contribution to protein stability and solubility, *J. Biol. Chem.* 284 (2009) 13285–13289. <https://doi.org/10.1074/jbc.R800080200>.
- [131] K.L. Shaw, G.R. Grimsley, G.I. Yakovlev, A.A. Makarov, C.N. Pace, The effect of net charge on the solubility, activity, and stability of ribonuclease Sa, *Protein Sci.* 10 (2001) 1206–1215. <https://doi.org/10.1110/ps.440101>.
- [132] J. Kyte, R.F. Doolittle, A simple method for displaying the hydropathic character of a protein, *J. Mol. Biol.* 157 (1982) 105–132. [https://doi.org/10.1016/0022-2836\(82\)90515-0](https://doi.org/10.1016/0022-2836(82)90515-0).
- [133] K. Guruprasad, B.V.B. Reddy, M.W. Pandit, Correlation between stability of a protein and its dipeptide composition: A novel approach for predicting in vivo stability of a protein from its primary sequence, *Protein Eng. Des. Sel.* 4 (1990) 155–161. <https://doi.org/10.1093/protein/4.2.155>.
- [134] A. Ikai, Thermostability and aliphatic index of globular proteins, *J. Biochem.* 88 (1980) 1895–1898. <https://doi.org/10.1093/oxfordjournals.jbchem.a133168>.
- [135] E. Wenande, L.H. Garvey, Immediate-type hypersensitivity to polyethylene glycols: a review, *Clin. Exp. Allergy.* 46 (2016) 907–922. <https://doi.org/10.1111/cea.12760>.
- [136] P. Sellaturay, S. Nasser, S. Islam, P. Gurugama, P.W. Ewan, Polyethylene glycol (PEG) is a cause of anaphylaxis to the Pfizer/BioNTech mRNA COVID-19 vaccine, *Clin. Exp. Allergy.* 51 (2021) 861–863. <https://doi.org/10.1111/cea.13874>.
- [137] K. Wylon, S. Dölle, M. Worm, Polyethylene glycol as a cause of anaphylaxis, *Allergy, Asthma Clin. Immunol.* 12 (2016) 10–12. <https://doi.org/10.1186/s13223-016-0172-7>.
- [138] E. Pedone, X. Li, N. Koseva, O. Alpar, S. Brocchini, An information rich biomedical polymer library, *J. Mater. Chem.* 13 (2003) 2825–2837. <https://doi.org/10.1039/b306857a>.
- [139] G. Gody, P.B. Zetterlund, S. Perrier, S. Harrisson, The limits of precision monomer placement in chain growth polymerization, *Nat. Commun.* 7:10514 (2016) 1–8. <https://doi.org/10.1038/ncomms10514>.
- [140] J. Zhang, B. Farias-Mancilla, M. Destarac, U.S. Schubert, D.J. Keddie, C. Guerrero-Sanchez, S. Harrisson, Asymmetric Copolymers: Synthesis, Properties, and Applications of Gradient and Other Partially Segregated Copolymers, *Macromol. Rapid Commun.* 39 (2018) 1–22. <https://doi.org/10.1002/marc.201800357>.
- [141] M. Rosales-Guzmán, O. Pérez-Camacho, R. Torres-Lubián, S. Harrisson, U.S. Schubert, C. Guerrero-Sánchez, E. Saldívar-Guerra, Kinetic and Copolymer Composition Investigations of the Free Radical Copolymerization of 1-Octene with Glycidyl Methacrylate, *Macromol. Chem. Phys.* 219 (2018) 1–10. <https://doi.org/10.1002/macp.201800084>.
- [142] H. Priya James, R. John, A. Alex, K.R. Anoop, Smart polymers for the controlled delivery of drugs – a concise overview, *Acta Pharm. Sin. B.* 4 (2014) 120–127.

<https://doi.org/10.1016/j.apsb.2014.02.005>.

- [143] Q. Zhang, C. Weber, U.S. Schubert, R. Hoogenboom, Thermoresponsive polymers with lower critical solution temperature : from fundamental aspects turbidimetry conditions †, *Mater. Horizons*. 4 (2017) 109–116. <https://doi.org/10.1039/c7mh00016b>.
- [144] J. Madsen, G. Madden, E. Themistou, N.J. Warren, S.P. Armes, pH-Responsive diblock copolymers with two different fluorescent labels for simultaneous monitoring of micellar self-assembly and degree of protonation, *Polym. Chem.* 9 (2018) 2964–2976. <https://doi.org/10.1039/c8py00111a>.
- [145] R. Engineering, C. Waterloo, Deteruination of reactivity ratios in copolymerization, *Makromol. Chem. Macromol. Symp.* 10 (1987) 355–374. <https://doi.org/10.1002/masy.19870100118>.
- [146] A.L. Polic, T.A. Duever, A. Penlidis, Case studies and literature review on the estimation of copolymerization reactivity ratios, *J. Polym. Sci. Part A Polym. Chem.* 36 (1998) 813–822. [https://doi.org/10.1002/\(SICI\)1099-0518\(19980415\)36:5<813::AID-POLA14>3.0.CO;2-J](https://doi.org/10.1002/(SICI)1099-0518(19980415)36:5<813::AID-POLA14>3.0.CO;2-J).
- [147] C. Guerrero-Sanchez, D.J. Keddie, S. Saubern, J. Chiefari, Automated parallel freeze-evacuate-thaw degassing method for oxygen-sensitive reactions: RAFT polymerization, *ACS Comb. Sci.* 14 (2012) 389–394. <https://doi.org/10.1021/co300044w>.
- [148] A. Tselepy, T.L. Schiller, S. Harrisson, C. Guerrero-Sanchez, G. Moad, D.J. Keddie, Effect of Scandium Triflate on the RAFT Copolymerization of Methyl Acrylate and Vinyl Acetate Controlled by an Acid/Base “Switchable” Chain Transfer Agent, *Macromolecules*. 51 (2018) 410–418. <https://doi.org/10.1021/acs.macromol.7b02104>.
- [149] M. Rosales-Guzmán, O. Pérez-Camacho, C. Guerrero-Sánchez, S. Harrisson, R. Torres-Lubián, J. Vitz, U.S. Schubert, E. Saldívar-Guerra, Semiautomated Parallel RAFT Copolymerization of Isoprene with Glycidyl Methacrylate, *ACS Comb. Sci.* 21 (2019) 771–781. <https://doi.org/10.1021/acscombsci.9b00110>.
- [150] V.D. Lechuga-Islas, G. Festag, M. Rosales-Guzmán, O.E. Vega-Becerra, R. Guerrero-Santos, U.S. Schubert, C. Guerrero-Sánchez, Quasi-block copolymer design of quaternized derivatives of poly(2-(dimethylamino)ethyl methacrylate): Investigations on thermo-induced self-assembly, *Eur. Polym. J.* 124 (2020) 109457. <https://doi.org/10.1016/j.eurpolymj.2019.109457>.
- [151] P.R. Judzewitsch, L. Zhao, E.H.H.H. Wong, C. Boyer, High-Throughput Synthesis of Antimicrobial Copolymers and Rapid Evaluation of Their Bioactivity, *Macromolecules*. 52 (2019) 3975–3986. <https://doi.org/10.1021/acs.macromol.9b00290>.
- [152] A.A.A. Smith, K. Zuwala, M.B.L. Kryger, B.M. Wohl, C. Guerrero-Sanchez, M. Tolstrup, A. Postma, A.N. Zelikin, Macromolecular prodrugs of ribavirin: towards a treatment for co-infection with HIV and HCV, *Chem. Sci.* 6 (2015) 264–269. <https://doi.org/10.1039/C4SC02754J>.
- [153] T. Yildirim, I. Yildirim, R. Yañez-Macias, S. Stumpf, C. Fritzsche, S. Hoepfener, C. Guerrero-Sanchez, S. Schubert, U.S. Schubert, Dual pH and ultrasound responsive nanoparticles with pH triggered surface charge-conversional properties, *Polym. Chem.* 8 (2017) 1328–1340. <https://doi.org/10.1039/C6PY01927G>.
- [154] C. Chen, F. Richter, J. Zhang, C. Guerrero-Sanchez, A. Traeger, U.S. Schubert, A. Feng, S.H. Thang, Synthesis of functional miktoarm star polymers in an automated parallel synthesizer, *Eur. Polym. J.* 160 (2021) 110777. <https://doi.org/10.1016/j.eurpolymj.2021.110777>.
- [155] G. Ng, M. Li, J. Yeow, K. Jung, C.W. Pester, C. Boyer, Benchtop Preparation of Polymer Brushes by SI-PET-RAFT: The Effect of the Polymer Composition and Structure on Inhibition of a Pseudomonas Biofilm, *ACS Appl. Mater. Interfaces*. 12 (2020) 55243–55254. <https://doi.org/10.1021/acami.0c15221>.
- [156] D.J. Keddie, A guide to the synthesis of block copolymers using reversible-addition fragmentation chain transfer (RAFT) polymerization, *Chem. Soc. Rev.* 43 (2013) 496–505. <https://doi.org/10.1039/C3CS60290G>.
- [157] RAFT: Choosing the Right Agent to Achieve Controlled Polymerization, (n.d.).



- [158] D.A.L. Otte, D.E. Borchmann, C. Lin, M. Weck, K.A. Woerpel, 13 C NMR Spectroscopy for the Quantitative Determination of Compound Ratios and Polymer End Groups, *Org. Lett.* 16 (2014) 1566–1569. <https://doi.org/10.1021/ol403776k>.
- [159] L.P.D. Ratcliffe, A.J. Ryan, S.P. Armes, From a Water-Immiscible Monomer to Block Copolymer Nano- Objects via a One-Pot RAFT Aqueous Dispersion Polymerization Formulation, *Macromolecules.* 46 (2013) 769–777. <https://doi.org/10.1021/ma301909w>.
- [160] S. Monge, D.M. Haddleton, Synthesis of precursors of poly (acryl amides) by copper mediated living radical polymerization in DMSO, *Eur. Polym. J.* 40 (2004) 37–45. <https://doi.org/10.1016/j.eurpolymj.2003.08.003>.
- [161] Y.K. Schilli, C.; Mueller, A.H.E.; Thang, San H.; Rizzardo, Ezio; Chong, Controlled radical polymerization of N-isopropylacrylamide and of activated esters for the synthesis of polymer-protein and polymer-drug conjugates, *Am. Chem. Soc. Polym. Prepr. Div. Polym. Chem.* 43 (2002) 687–688.
- [162] M.J. Yanjarappa, K. V Gujraty, A. Joshi, A. Saraph, R.S. Kane, Synthesis of Copolymers Containing an Active Ester of Methacrylic Acid by RAFT : Controlled Molecular Weight Scaffolds for Biofunctionalization, *Biomacromolecules.* 7 (2006) 1665–1670.
- [163] A. Favier, F.D. Agosto, M.-T. Charreyre, C. Pichot, Synthesis of N -acryloxysuccinimide copolymers by RAFT polymerization , as reactive building blocks with full control of composition and molecular weights, *Polymer (Guildf).* 45 (2004) 7821–7830. <https://doi.org/10.1016/j.polymer.2004.09.042>.
- [164] R. Paula, M.-T. Charreyre, J.P.S. Farinha, J.M.G. Martinho, C. Pichot, Well-defined polymer precursors synthesized by RAFT polymerization of N , N -dimethylacrylamide / N -acryloxysuccinimide : random and block copolymers, *Polymer (Guildf).* 45 (2004) 8639–8649. <https://doi.org/10.1016/j.polymer.2004.10.056>.
- [165] E. Sjöholm, K. Gustafsson, B. Eriksson, W. Brown, A. Colmsjö, Aggregation of cellulose in lithium chloride/N,N-dimethylacetamide, *Carbohydr. Polym.* 41 (2000) 153–161. [https://doi.org/10.1016/S0144-8617\(99\)00080-6](https://doi.org/10.1016/S0144-8617(99)00080-6).
- [166] M.L. Dias, E.B. Mano, C. Azuma, Size exclusion behavior of polymers in amide solvents — III. Elution characteristics of acrylic polymers in N,N-dimethylformamide, *Eur. Polym. J.* 33 (1997) 559–564. [https://doi.org/10.1016/S0014-3057\(96\)00186-3](https://doi.org/10.1016/S0014-3057(96)00186-3).
- [167] M. Strlič, J. Kolar, Size exclusion chromatography of cellulose in LiCl/N,N-dimethylacetamide, *J. Biochem. Biophys. Methods.* 56 (2003) 265–279. [https://doi.org/10.1016/S0165-022X\(03\)00064-2](https://doi.org/10.1016/S0165-022X(03)00064-2).
- [168] Y. Ono, K. Furihata, N. Isobe, T. Saito, A. Isogai, Solution-state structures of the cellulose model pullulan in lithium chloride / N , N -dimethylacetamide, *Int. J. Biol. Macromol.* 107 (2018) 2598–2603. <https://doi.org/10.1016/j.ijbiomac.2017.10.141>.
- [169] C.P. Jesson, V.J. Cunningham, M.J. Smallridge, S.P. Armes, Synthesis of High Molecular Weight Poly(glycerol monomethacrylate) via RAFT Emulsion Polymerization of Isopropylidene glycerol Methacrylate, *Macromolecules.* 51 (2018) 3221–3232. <https://doi.org/10.1021/acs.macromol.8b00294>.
- [170] O.A. El Seoud, H. Nawaz, E.P.G. Arêas, Chemistry and Applications of Polysaccharide Solutions in Strong Electrolytes/Dipolar Aprotic Solvents: An Overview, *Molecules.* 18 (2013) 1270–1313. <https://doi.org/10.3390/molecules18011270>.
- [171] M. Van Den Brink, A.M. Van Herk, A.L. German, Nonlinear regression by visualization of the sum of residual space applied to the integrated copolymerization equation with errors in all variables. I. Introduction of the model, simulations and design of experiments, *J. Polym. Sci. Part A Polym. Chem.* 37 (1999) 3793–3803. [https://doi.org/10.1002/\(SICI\)1099-0518\(19991015\)37:20<3793::AID-POLA8>3.0.CO;2-Q](https://doi.org/10.1002/(SICI)1099-0518(19991015)37:20<3793::AID-POLA8>3.0.CO;2-Q).
- [172] G. Odian, Principles of polymerization, 4th ed., Wiley-Interscience, Hoboken, N.J., 2004. <https://search.library.wisc.edu/catalog/999960211002121>.

- [173] R. Yañez-Macias, I. Kulai, J. Ulbrich, T. Yildirim, P. Sungur, S. Hoepfener, R. Guerrero-Santos, U.S. Schubert, M. Destarac, C. Guerrero-Sanchez, S. Harrisson, Thermosensitive spontaneous gradient copolymers with block- and gradient-like features, *Polym. Chem.* 8 (2017) 5023–5032. <https://doi.org/10.1039/c7py00495h>.
- [174] K. Bauri, S.G. Roy, S. Arora, R.K. Dey, A. Goswami, G. Madras, P. De, Thermal degradation kinetics of thermoresponsive poly(N-isopropylacrylamide-co-N,N-dimethylacrylamide) copolymers prepared via RAFT polymerization, *J. Therm. Anal. Calorim.* 111 (2013) 753–761. <https://doi.org/10.1007/s10973-012-2344-0>.
- [175] Ulf W. Gedde, *Polymer Physics*, First, Chapman & Hall, 2–6 Boundary Row, London, 1995.
- [176] S. Kuo, W. Liu, F. Chang, Effect of Hydrolysis on the Strength of Hydrogen Bonds and T<sub>g</sub> of Poly(vinylphenol-co-acetoxystyrene), *Macromolecules.* 36 (2003) 5165–5173. <https://doi.org/10.1021/ma0341824>.
- [177] T.K. Kwei, The Effect of Hydrogen Bonding on the Glass Transition Temperatures of Polymer Mixtures Introduction, *Polym. Lett. Ed.* 22 (1984) 307–313.
- [178] T. Fox, Influence of Diluent and of Copolymer Composition on the Glass Temperature of a Polymer System, *Bull. Am. Phys. Soc.* 1 (1956) 123–128.
- [179] W. Brostow, R. Chiu, I.M. Kalogeras, A. Vassilikou-Dova, Prediction of glass transition temperatures: Binary blends and copolymers, *Mater. Lett.* 62 (2008) 3152–3155. <https://doi.org/10.1016/j.matlet.2008.02.008>.
- [180] K. Demirelli, M.F. Coşkun, E. Kaya, M. Coşkun, Investigation of the thermal decomposition of poly(2-hydroxypropyl methacrylate), *Polym. Degrad. Stab.* 78 (2002) 333–339. [https://doi.org/10.1016/S0141-3910\(02\)00182-9](https://doi.org/10.1016/S0141-3910(02)00182-9).
- [181] K. Demirelli, M. Coşkun, E. Kaya, A detailed study of thermal degradation of poly(2-hydroxyethyl methacrylate), *Polym. Degrad. Stab.* 72 (2001) 75–80. [https://doi.org/10.1016/S0141-3910\(00\)00204-4](https://doi.org/10.1016/S0141-3910(00)00204-4).
- [182] A. Halperin, M. Kröger, F.M. Winnik, Poly(N-isopropylacrylamide) Phase Diagrams: Fifty Years of Research, *Angew. Chemie Int. Ed.* 54 (2015) 15342–15367. <https://doi.org/10.1002/anie.201506663>.
- [183] E.S. Gil, S.M. Hudson, Stimuli-responsive polymers and their bioconjugates, *Prog. Polym. Sci.* 29 (2004) 1173–1222. <https://doi.org/10.1016/j.progpolymsci.2004.08.003>.
- [184] Q. Xingping, K. Tsuyoshi, T. Fumihiko, W. M. Françoise, New insights into the effects of molecular weight and end group on the temperature-induced phase transition of poly(N-isopropylacrylamide) in water, *Sci. China Chem.* 56 (2013) 56–64. <https://doi.org/10.1007/s11426-012-4781-9>.
- [185] M.M. Fares, A.A. Othman, Lower Critical Solution Temperature Determination of Smart, Thermosensitive N – Isopropylacrylamide-alt-2 – Hydroxyethyl Methacrylate Copolymers: Kinetics and Physical Properties, *J. Appl. Polym. Sci.* 110 (2008) 2815–2825. <https://doi.org/10.1002/app.28840>.
- [186] M. Luo, Influenza Virus Entry, in: M.G. Rossmann, V.B. Rao (Eds.), *Viral Mol. Mach.*, Springer US, Boston, MA, 2012: pp. 201–221. [https://doi.org/10.1007/978-1-4614-0980-9\\_9](https://doi.org/10.1007/978-1-4614-0980-9_9).
- [187] M. De Graaf, R.A.M. Fouchier, Role of receptor binding specificity in influenza A virus transmission and pathogenesis, *EMBO J.* 33 (2014) 823–841. <https://doi.org/10.1002/embj.201387442>.
- [188] P.J. Roth, K.T. Wiss, R. Zentel, P. Theato, Synthesis of reactive telechelic polymers based on pentafluorophenyl esters, *Macromolecules.* 41 (2008) 8513–8519. <https://doi.org/10.1021/ma801681b>.
- [189] N. Vanparijs, S. Maji, B. Louage, L. Voorhaar, D. Laplace, Q. Zhang, Y. Shi, W.E. Hennink, R. Hoogenboom, B.G. De Geest, Polymer-protein conjugation via a “grafting to” approach—a comparative study of the performance of protein-reactive RAFT chain transfer agents, *Polym.*

Chem. 6 (2015) 5602–5614. <https://doi.org/10.1039/c4py01224k>.

- [190] C. Ventura-Hunter, V.D. Lechuga-Islas, J. Ulbrich, C. Kellner, U.S. Schubert, E. Saldívar-Guerra, M. Rosales-Guzmán, C. Guerrero-Sánchez, Glycerol methacrylate-based copolymers: Reactivity ratios, physicochemical characterization and cytotoxicity, *Eur. Polym. J.* 178 (2022) 111478. <https://doi.org/10.1016/j.eurpolymj.2022.111478>.
- [191] A. Lamiable, P. Thevenet, J. Rey, M. Vavrusa, P. Derreumaux, P. Tuffery, PEP-FOLD3: faster denovo structure prediction for linear peptides in solution and in complex, *Nucleic Acids Res.* 44 (2016) W449–W454. <https://doi.org/10.1093/nar/gkw329>.
- [192] A. Roy, A. Kucukural, Y. Zhang, I-TASSER: a unified platform for automated protein structure and function prediction, *Nat. Protoc.* 5 (2010) 725–738. <https://doi.org/10.1038/nprot.2010.5>.
- [193] A.C. Camproux, R. Gautier, P. Tufféry, A hidden Markov model derived structural alphabet for proteins, *J. Mol. Biol.* 339 (2004) 591–605. <https://doi.org/10.1016/j.jmb.2004.04.005>.
- [194] J. Maupetit, P. Derreumaux, P. Tuffery, PEP-FOLD: An online resource for de novo peptide structure prediction, *Nucleic Acids Res.* 37 (2009) 498–503. <https://doi.org/10.1093/nar/gkp323>.
- [195] J. Yu, K. Xiao, W. Xue, Y. xiao Shen, J. Tan, S. Liang, Y. Wang, X. Huang, Excitation-emission matrix (EEM) fluorescence spectroscopy for characterization of organic matter in membrane bioreactors: Principles, methods and applications, *Front. Environ. Sci. Eng.* 14 (2020). <https://doi.org/10.1007/s11783-019-1210-8>.
- [196] M. Bhattacharyya, U. Chaudhuri, R.K. Poddar, Evidence for cooperative binding of chlorpromazine with hemoglobin: equilibrium dialysis, fluorescence quenching and oxygen release study., *Biochem. Biophys. Res. Commun.* 167 (1990) 1146–1153.
- [197] Y. Liu, Y.Z. Zhang, B. Zhou, C.X. Zhou, X.L. Ding, Y.X. Liu, Fluorescence study on the interaction of bovine serum albumin with P-aminoazobenzene, *J. Fluoresc.* 18 (2008) 109–118. <https://doi.org/10.1007/s10895-007-0247-4>.
- [198] K.R. Grigoryan, H.A. Shilajyan, Fluorescence 2D and 3D spectra analysis of tryptophan, tyrosine and phenylalanine, *Chem. Biol.* 51 (2017) 3–7.
- [199] Y. Xiong, C. Shi, L. Li, Y. Tang, X. Zhang, S. Liao, B. Zhang, C. Sun, C. Ren, A review on recent advances in amino acid and peptide-based fluorescence and its potential applications, *New J. Chem.* 45 (2021) 15180–15194. <https://doi.org/10.1039/d1nj02230j>.
- [200] K.T. O’Neil, H.R. Wolfe, S. Erickson-Viitanen, W.F. DeGrado, Fluorescence properties of calmodulin-binding peptides reflect alpha-helical periodicity, *Science* (80-. ). 236 (1987) 1454–1456. <https://doi.org/10.1126/science.3589665>.
- [201] J. Malicka, M. Groth, J. Karolczak, C. Czaplewski, A. Liwo, W. Wicz, Influence of solvents and leucine configuration at position 5 on tryptophan fluorescence in cyclic enkephalin analogues, *Biopolymers.* 58 (2001) 447–457. [https://doi.org/10.1002/1097-0282\(20010405\)58:4<447::AID-BIP1020>3.0.CO;2-4](https://doi.org/10.1002/1097-0282(20010405)58:4<447::AID-BIP1020>3.0.CO;2-4).
- [202] L. Ferrari, L. Rovati, P. Fabbri, F. Pilati, Disposable Fluorescence Optical pH Sensor for Near Neutral Solutions, *Sensors.* 13 (2012) 484–499. <https://doi.org/10.3390/s130100484>.
- [203] S. Roy, B. Bagchi, Solvation dynamics of tryptophan in water-dimethyl sulfoxide binary mixture: In search of molecular origin of composition dependent multiple anomalies, *J. Chem. Phys.* 139 (2013). <https://doi.org/10.1063/1.4813417>.
- [204] A. Bortolotti, Y.H. Wong, S.S. Korsholm, N.H.B. Bahring, S. Bobone, S. Tayyab, M. Van De Weert, L. Stella, On the purported “backbone fluorescence” in protein three-dimensional fluorescence spectra, *RSC Adv.* 6 (2016) 112870–112876. <https://doi.org/10.1039/c6ra23426g>.
- [205] A.C. Vaiana, H. Neuweiler, A. Schulz, J. Wolfrum, M. Sauer, J.C. Smith, Fluorescence Quenching of Dyes by Tryptophan: Interactions at Atomic Detail from Combination of Experiment and Computer Simulation, *J. Am. Chem. Soc.* 125 (2003) 14564–14572. <https://doi.org/10.1021/ja036082j>.
- [206] D.M. Togashi, B. Szczupak, A.G. Ryder, A. Calvet, M. O’Loughlin, Investigating Tryptophan

- Quenching of Fluorescein Fluorescence under Protolytic Equilibrium, *J. Phys. Chem. A.* 113 (2009) 7981–7981. <https://doi.org/10.1021/jp904494p>.
- [207] G. V. Lowry, R.J. Hill, S. Harper, A.F. Rawle, C.O. Hendren, F. Klaessig, U. Nobbmann, P. Sayre, J. Rumble, Guidance to improve the scientific value of zeta-potential measurements in nanoEHS, *Environ. Sci. Nano.* 3 (2016) 953–965. <https://doi.org/10.1039/c6en00136j>.
- [208] R.J. Lamm, E.B. Lim, K.M. Weigandt, L.D. Pozzo, N.J. White, S.H. Pun, Peptide valency plays an important role in the activity of a synthetic fibrin-crosslinking polymer, *Biomaterials.* 132 (2017) 96–104. <https://doi.org/10.1016/j.biomaterials.2017.04.002>.
- [209] P. Groves, Diffusion ordered spectroscopy (DOSY) as applied to polymers, *Polym. Chem.* 8 (2017) 6700–6708. <https://doi.org/10.1039/c7py01577a>.
- [210] J.T. Edward, Molecular volumes and the Stokes-Einstein equation, *J. Chem. Educ.* 47 (1970) 261. <https://doi.org/10.1021/ed047p261>.
- [211] J. Nguyen, X. Xie, M. Neu, R. Dumitrascu, R. Reul, J. Sitterberg, U. Bakowsky, R. Schermuly, L. Fink, T. Schmehl, T. Gessler, W. Seeger, T. Kissel, Effects of cell-penetrating peptides and pegylation on transfection efficiency of polyethylenimine in mouse lungs, *J. Gene Med.* 10 (2008) 1236–1246. <https://doi.org/10.1002/jgm.1255>.
- [212] N. Cohen, L. Binyamin, Y. Levi-Kalishman, G.Y. Berguig, A. Convertine, P. Stayton, R. Yerushalmi-Rozen, PH and Salt Effects on Surface Activity and Self-Assembly of Copolymers Containing a Weak Polybase, *Langmuir.* 32 (2016) 9286–9292. <https://doi.org/10.1021/acs.langmuir.6b02452>.
- [213] L.M. Alhaidari, S.G. Spain, Synthesis of 5-Fluorouracil Polymer Conjugate and <sup>19</sup>F NMR Analysis of Drug Release for MRI Monitoring, *Polymers (Basel).* 15 (2023) 1778. <https://doi.org/10.3390/polym15071778>.
- [214] T. Senthilkumar, S.K. Asha, Selective and Sensitive Sensing of Free Bilirubin in Human Serum Using Water-Soluble Polyfluorene as Fluorescent Probe, *Macromolecules.* 48 (2015) 3449–3461. <https://doi.org/10.1021/acs.macromol.5b00043>.
- [215] C.M. Maguire, M. Rösslein, P. Wick, A. Prina-Mello, Characterisation of particles in solution – a perspective on light scattering and comparative technologies, *Sci. Technol. Adv. Mater.* 19 (2018) 732–745. <https://doi.org/10.1080/14686996.2018.1517587>.
- [216] F. Varenne, A. Makky, M. Gaucher-Delmas, F. Violleau, C. Vauthier, Multimodal Dispersion of Nanoparticles: A Comprehensive Evaluation of Size Distribution with 9 Size Measurement Methods, *Pharm. Res.* 33 (2016) 1220–1234. <https://doi.org/10.1007/s11095-016-1867-7>.
- [217] W. Anderson, D. Kozak, V.A. Coleman, Å.K. Jämting, M. Trau, A comparative study of submicron particle sizing platforms: Accuracy, precision and resolution analysis of polydisperse particle size distributions, *J. Colloid Interface Sci.* 405 (2013) 322–330. <https://doi.org/10.1016/j.jcis.2013.02.030>.
- [218] M.A. Al-Khafaji, A. Gaál, A. Wacha, A. Bóta, Z. Varga, Particle size distribution of bimodal silica nanoparticles: A comparison of different measurement techniques, *Materials (Basel).* 13 (2020). <https://doi.org/10.3390/ma13143101>.
- [219] D. Mahl, J. Diendorf, W. Meyer-Zaika, M. Eppe, Possibilities and limitations of different analytical methods for the size determination of a bimodal dispersion of metallic nanoparticles, *Colloids Surfaces A Physicochem. Eng. Asp.* 377 (2011) 386–392. <https://doi.org/10.1016/j.colsurfa.2011.01.031>.
- [220] A. Blanazs, A.J. Ryan, S.P. Armes, Predictive phase diagrams for RAFT aqueous dispersion polymerization: Effect of block copolymer composition, molecular weight, and copolymer concentration, *Macromolecules.* 45 (2012) 5099–5107. <https://doi.org/10.1021/ma301059r>.
- [221] Y. Dieckmann, H. Cölfen, H. Hofmann, A. Petri-Fink, Particle size distribution measurements of manganese-doped ZnS nanoparticles, *Anal. Chem.* 81 (2009) 3889–3895. <https://doi.org/10.1021/ac900043y>.

- [222] F. Caputo, J. Clogston, L. Calzolari, M. Rösslein, A. Prina-Mello, Measuring particle size distribution of nanoparticle enabled medicinal products, the joint view of EUNCL and NCI-NCL. A step by step approach combining orthogonal measurements with increasing complexity, *J. Control. Release.* 299 (2019) 31–43. <https://doi.org/10.1016/j.jconrel.2019.02.030>.
- [223] C.M. Maguire, M. Rösslein, P. Wick, A. Prina-Mello, Characterisation of particles in solution—a perspective on light scattering and comparative technologies, *Sci. Technol. Adv. Mater.* 19 (2018) 732–745. <https://doi.org/10.1080/14686996.2018.1517587>.
- [224] G.G. Stokes, On the Effect of the Internal Friction of Fluids on the Motion of Pendulums, *Math. Phys. Pap.* (2010) 1–10. <https://doi.org/10.1017/cbo9780511702266.002>.
- [225] F. Varenne, A. Makky, M. Gaucher-Delmas, F. Violleau, C. Vauthier, Multimodal Dispersion of Nanoparticles: A Comprehensive Evaluation of Size Distribution with 9 Size Measurement Methods, *Pharm. Res.* 33 (2016) 1220–1234. <https://doi.org/10.1007/s11095-016-1867-7>.
- [226] N. Farkas, J.A. Kramar, Dynamic light scattering distributions by any means, *J. Nanoparticle Res.* 23 (2021) 120. <https://doi.org/10.1007/s11051-021-05220-6>.
- [227] J.D. Dukes, P. Whitley, A.D. Chalmers, The MDCK variety pack: choosing the right strain, *BMC Cell Biol.* 12 (2011) 43. <https://doi.org/10.1186/1471-2121-12-43>.
- [228] R. Bjerknes, C.F. Bassøe, Phagocyte C3-mediated attachment and internalization: Flow cytometric studies using a fluorescence quenching technique, *Blut.* 49 (1984) 315–323. <https://doi.org/10.1007/BF00320205>.
- [229] F. Illien, N. Rodriguez, M. Amoura, A. Joliot, M. Pallerla, S. Cribier, F. Burlina, S. Sagan, Quantitative fluorescence spectroscopy and flow cytometry analyses of cell-penetrating peptides internalization pathways: optimization, pitfalls, comparison with mass spectrometry quantification, *Sci. Rep.* 6 (2016) 36938. <https://doi.org/10.1038/srep36938>.
- [230] I. Ruseska, A. Zimmer, Internalization mechanisms of cell-penetrating peptides, *Beilstein J. Nanotechnol.* 11 (2020) 101–123. <https://doi.org/10.3762/bjnano.11.10>.
- [231] M. Kawamoto, T. Yamaji, K. Saito, Y. Shirasago, K. Satomura, T. Endo, M. Fukasawa, K. Hanada, N. Osada, Identification of Characteristic Genomic Markers in Human Hepatoma HuH-7 and Huh7.5.1-8 Cell Lines, *Front. Genet.* 11 (2020) 1–10. <https://doi.org/10.3389/fgene.2020.546106>.
- [232] D.P. Aden, A. Fogel, S. Plotkin, I. Damjanov, B.B. Knowles, Controlled synthesis of HBsAg in a differentiated human liver carcinoma-derived cell line, *Nature.* 282 (1979) 615–616. <https://doi.org/10.1038/282615a0>.
- [233] Y. Cao, A. Merling, P.R. Crocker, R. Keller, R. Schwartz-Albiez, Differential expression of  $\beta$ -galactoside  $\alpha$ 2, 6 sialyltransferase and sialoglycans in normal and cirrhotic liver and hepatocellular carcinoma, *Lab. Invest.* 82 (2002) 1515–1524. <https://doi.org/10.1097/01.LAB.0000038503.34655.98>.
- [234] Y. Wang, H. Chen, Protein glycosylation alterations in hepatocellular carcinoma: function and clinical implications, *Oncogene.* 42 (2023) 1970–1979. <https://doi.org/10.1038/s41388-023-02702-w>.